Beam optics transport and fundamental processes involving a charge breeder in the upgraded SIRAL1 facility

Arun Annaluru

THESE

Pour obtenir le diplôme de doctorat

Spécialité PHYSIQUE

Préparée au sein de « l'Université de Caen Normandie »

Beam optics transport and fundamental processes involving a charge breeder in the upgraded SPIRAL1 facility

Présentée par
Arun Tejaswee ANNALURU

Thèse soutenue publiquement le 30/09/2019 devant le jury composé de		
M. GAMMINO SANTO	Directeur de recherche – INFN-LNS	Rapporteur
Mme LACOSTE ANA	Professeur des universités – INP - ENSE3 à Grenoble	Rapporteur
Mme LAMOUR EMILY	Professeur des universités – Université Paris 6 Pierre et Marie Curie	Examinateur
M. ANGELIQUE JEAN CLAUDE	Professeur des universités – 14 ENSI de Caen	Examinateur
M. DELAHAYE PIERRE	Chargé de recherche au CNRS – 14 GANIL de CAEN	Examinateur
M. MAUNOURY LAURENT	Ingénieur de recherche – 14 GANIL de CAEN	Directeur de thèse

Thèse dirigée par LAURENT MAUNOURY, Grand Accélérateur National d'Ions Lourds (GANIL)

UNIVERSITÉ CAEN NORMANDIE

ED PSIME

GANIL spiral2
laboratoire commun CEA/DRF   CNRS/IN2P3

Acknowledgements

The work reported in this thesis has been carried out at Grand Accélérateur National d'Ions Lourds (GANIL), Caen, during the years 2016–2019. I want to sincerely thank my supervisor Dr. Laurent Maunoury for all the guidance and insight into the world of ECR ion source physics that I have been privileged to receive during the years working in the ion source group. I wish to thank him not only for professional help but also for all the cheerful moments that we have spent together in work, free time and international conferences. I wish to extend my thanks also to Dr. Pierre Delahaye, who has not only been a constant source of information and valuable instructions, but whose enthusiasm for physics has also been a major source of inspiration to my work. I wish to express my gratitude to the members of the Jury for taking their time to estimate my work. I would like to thank Dr. Santo Gammino, Prof. Ana Lacoste and Prof. Emily Lamour for reviewing my thesis and providing me with comments and suggestions which helped to improve it. My thanks to Prof. Jean-Claude Angelique for having accepted to preside over this jury.

I would like to express my most sincere thanks to all the technicians, who helped me to perform the experimental work described in this thesis. I am grateful for all the discussions with the former and current Ph.D students and postdocs. I would also like to thank all the members of the ion source group that I have been privileged to work with, especially Mr. Mickael Dubois, Dr. Pascal Jardin, Dr. Barue Christophe, Mr. Frigot Romain, Mr. Lechartier Nicolas, Mr. Alexandre Leduc, and Mr. Kuchi Venkateswarlu, for years of collaboration in an inspirational and enjoyable working environment.

I owe the biggest debt of gratitude to my loving wife Prathima Rachapudi, my parents and my brother, who have always supported me in my activities. Without them this work would not have been possible.

Caen, September 2019

Arun Annaluru

Abstract

The thesis describes with a great deal of details the efforts done to understand the physical processes inside the SPIRAL1 ECR charge breeder. This device accepts the mono-charged ion beams of different masses and charge bred them to higher charge states. In the framework of the SPIRAL1 upgrade, the R&D of charge breeding technique is of primary interest for optimizing the yields of radioactive ion beams (RIBs). In this context, the thesis begins with a theoretical discussion dealing with the different Target Ion Sources (TIS) at upgraded SPIRAL1 facility, Low Energy Beam Transport system and fundamentals of plasma physics relevant for the production of highly charged ions in ECR ion source plasmas. This is followed by description of the technological issues affecting the 1+/N+ charge breeding technique. In the final chapter, the effect of axial magnetic field gradient, position of deceleration tube and 1+ beam emittance were studied to understand their influence on the performance of the SP1 CB (charge breeding efficiency). The optimization of axial magnetic field gradient shows that the charge breeding efficiency is strongly influenced by the variation of the two soft iron rings positions around the permanent magnet hexapole. It has been deduced from the observations that the charge breeding efficiency improves when the emittance of 1+ beam is smaller and the position of deceleration tube is close to the entrance of SP1 CB. At the same time, the charge breeding times of K charge states (1+,2+,4+ and 9+) were estimated by pulsing the injected K^{1+} beam. The results from these investigations revealed the optimum SP1 CB tuning parameters that can minimize the value of charge breeding time and maximize the charge breeding efficiency of the high charge states of K.

In order to investigate the 1+ ion beam transport (shooting through mode) through the SP1 ECR charge breeder and the fundamental physical mechanisms involved in charge breeding process, several experiments were carried out in the framework of this thesis (the interaction of 1+ ion beam of different masses (Na^+ and K^+) in different background plasma species (He and O_2)). The data from these experiments (potentials, emittance of 1+ beam, deceleration tube position, magnetic field and pressures) were collected and given as inputs to the numerical simulation tools (SIMION, TraceWin and MCBC). The simulations were performed in three steps: i) simulation of the 1+ beam transmission through the breeder to verify the ion losses and showed good agreement with the experimental results. ii) Simulation of 1+ beam transmission through a potential map that reflects the presence of the ECR plasma (without collisions) and reproduced the ΔV curves of 1+ and 2+. It also revealed the role of Coulomb collisions in the charge breeding process leading to a necessary detailed analysis using Monte-Carlo Charge Breeding code (MCBC). iii) MCBC models Coulomb collisions of the injected 1+ ion beam in an ECR plasma and atomic processes which includes ionization and charge exchange. Finally, the code can reproduce the low charge state (1+ and 2+) experimental trends by a novel simulation strategy that has been developed to estimate the plasma parameters from charge breeding simulations. Finally, Simulations demonstrated that the ion temperature, the plasma density and 1+ ion beam quality as critical parameters influencing the 1+ ion capture and the reasons for the difference in charge breeding efficiencies between Na^{q+} (in Helium plasma) and K^{q+} (in Helium and Oxygen plasma) species were discussed.

Key words: Fundamental processes in ion source, plasma, ECR charge breeder ion source, production of highly charged ions, ion beam optics.

résumé

La thèse décrit avec beaucoup de détails les efforts déployés pour comprendre les processus physiques à l'intérieur du Booster de Charge SPIRAL1 (SP1 CB). Cet appareil accepte les faisceaux d'ions mono-chargés de différentes masses et augmente leur charge vers des états plus élevés. Dans le cadre de la mise à niveau de SPIRAL1, la R&D autour de la technique 1+/N+ présente un intérêt primordial pour optimiser les rendements des faisceaux d'ions radioactifs (RIB). Dans ce contexte, la thèse commence par une présentation théorique des ensembles cible-source de l'installations SPIRAL1, de la ligne de transport de faisceaux à basse énergie et des principes de la physique des plasmas pour la production d'ions fortement chargés dans les plasmas de source d'ions RCE (Résonance Cyclotronique Electronique). Ensuite, il y a une description des enjeux technologiques concernant la technique d'augmentation de charge 1+/ N+. Dans le chapitre suivant, les effets du gradient de champ magnétique axial, de la position du tube de décélération et de l'émittance du faisceau1+ ont été étudiés pour comprendre leur influence sur les performances du SP1 CB (efficacité de la transformation). L'optimisation du gradient de champ magnétique axial montre que l'efficacité du processus est fortement influencée par la position des deux anneaux en fer doux autour de l'hexapole. Il a été également déduit des observations que l'efficacité de la transformation s'améliore lorsque l'émittance du faisceau 1+ est faible et que la position du tube de décélération est proche de l'entrée du SP1 CB. En parallèle, les temps de la transformation 1+/N+ pour le potassium (1 +, 2+, 4 + et 9+) ont été mesurés en pulsant le faisceau de K^{1+} injecté. Les résultats de cette campagne expérimentale ont permis d'extraire les paramètres de réglage optimaux du SP1 CB qui permettent de minimiser la valeur du temps de la transformation tout en maximisant son efficacité.

Afin d'étudier le transport du faisceau d'ions 1+ à travers le SP1 CB et les mécanismes physiques fondamentaux impliqués dans le processus d'augmentation de charges, plusieurs expériences ont été menées dans le cadre de cette thèse : interaction de faisceaux d'ions 1+ de différentes masses (Na^+ et K^+) dans deux plasmas RCE fait d'He et d'O_2. Les données de ces expériences (potentiels, émittance du faisceau 1+, position du tube de décélération, champ magnétique et pressions) ont été collectées et utilisées en tant que données d'entrée dans les outils de simulations numériques suivants :SIMION 3D, TraceWin et MCBC. Les simulations ont été effectuées en trois étapes: i) simulation de la transmission du faisceau 1+ à travers le SP1 CB pour chercher les lieux des pertes des ions, elle a montré un bon accord avec les résultats expérimentaux. ii) simulation de la transmission du faisceau1+ à travers une carte de potentiel reflétant la présence du plasma RCE (sans collisions) ; ça a permis de reproduire les courbes ΔV pour les états de charge 1+ et 2+. Elle a également révélé le rôle important joué par les collisions coulombiennes dans le processus d'augmentation de charge, concluant à une analyse plus détaillée nécessaire à l'aide d'un code type Monte-Carlo (MCBC). iii) Code MCBC incluant les collisions coulombiennes du faisceau d'ions 1+ injecté dans un plasma RCE et les processus atomiques incluant l'ionisation simple et l'échange de charge. Le modèle peut reproduire les courbes expérimentales impliquant les faibles états de charge (1+ et 2+) en faisant varier chaque paramètre du plasma (densité électronique et ionique, température des ions et température des électrons) de manière indépendante. Une nouvelle stratégie de simulation a été développée pour estimer les paramètres du plasma à partir de ce code et des comparaisons avec les mesures expérimentales. Le résultat de ces simulations a démontré que la température des ions, la densité du

plasma et la qualité du faisceau d'ions 1+ sont les paramètres critiques influant fortement sur la capture des ions 1+ et ils expliquent les différentes efficacités mesurées de la transformation 1+/N+ des Na^{q+} et K^{q+} dans le SP1 CB.

Mots clés : Procédés fondamentaux des source d'ions, plasma RCE, booster de charge type RCE, production d'ions fortement chargés, optique de faisceaux ioniques.

Contents

version française

Résumé de la thèse " Transport de faisceaux d'ions à basse énergie et processus fondamentaux impliquant un booster de charge disposé dans l'installation SPIRAL1" par Arun Annaluru

A. Introduction

Le GANIL est un laboratoire d'accueil qui reçois chaque année environ 700 expérimentateurs nationaux et internationaux. Ce laboratoire a pour mission première d'exploiter une Très Grand Infrastructure de Recherche (TGIR) dédiée à la production et l'accélération d'ions lourds stables comme radioactifs afin d'en faire bénéficier les communautés françaises et européennes de Physique Nucléaire, Physique Astrophysique, Physique atomique et Physique des matériaux ainsi qu'un certain nombre d'Industriels (implantation, espace, irradiation etc…). L'installation SPIRAL1 (Système de Production d'Ions Accélérés en Ligne) est dédiée à la production d'ions radioactifs de masse < 90 u.m.a. Elle a été mise en service en 2001 et a permis la délivrance d'environ 35 faisceaux d'ions radioactifs (FIR) différents issus de 7 éléments différents : He, N, O, F, Ne, Ar et Kr. Récemment, cette installation a subi une transformation majeure afin d'élargir sa palette de faisceaux aux éléments condensables pour répondre aux besoins des physiciens. Trois ingrédients majeurs caractérisent cette mise à niveau : utilisation de nouvelles réactions nucléaires pour créer les atomes radioactifs (fragmentation de la cible, fusion-évaporation) ; réalisation de nouveaux ensembles cible-source dédiés à des familles d'élément chimiques et la mise en œuvre d'un booster de charge. La thèse s'inscrit dans ce cadre et plus particulièrement s'attache à comprendre les pertes de faisceaux dues à la mise en place du booster de charge (SP1_CB) et quels sont les paramètres de celui-ci permettant d'optimiser la production des faisceaux d'ions radioactifs sur la cible du physicien.

B. L'installation SPIRAL1

Présentation de l'installation

Comme écrit dans l'introduction, l'extension de la production d'atomes radioactifs nécessite la mise en œuvre de nouveaux ensembles cible-source qui ont la particularité de produire essentiellement des ions monochargés. Or, le post-accélérateur de l'installation est un cyclotron qui a besoin d'ions multichargés pour fonctionner dans sa gamme d'énergie. Il est donc indispensable d'utiliser un appareil qui permet cette augmentation d'état de charge : c'est le booster de charge (SP1_CB). L'installation SPIRAL1 est composée maintenant de trois éléments qui, combinés ensemble, vont permettre d'élargir considérablement la palette des FIR accessibles par les physiciens :

- De nouvelles réactions de production d'atomes radioactifs : fragmentation de la cible et fusion-évaporation
  Jusqu'à présent la cible était composée uniquement de carbone et le faisceau primaire était le paramètre variable (du C à l'U) d'où la fragmentation du projectile. Maintenant il va être possible de faire l'inverse c'est-à-dire avoir un faisceau primaire fixe (^{12}C@95MeV/u) mais des cibles différentes (SiC, Nb, etc…) ceci afin de produire de nouveaux isotopes jusqu'au Z=42. La fusion évaporation est une réaction nucléaire qui est réalisée à plus basse énergie. Le faisceau primaire interagit avec les noyaux d'une cible mince, ils vont pouvoir fusionner et émettre de nouveaux atomes qui vont être radioactifs. L'avantage de cette méthode est de pouvoir avoir accès à des atomes

radioactifs ayant des temps de demi-vie très courte (<100ms) et d'optimiser également les taux de production.

- Le nouvel ensemble cible-source FEBIAD

  Le nouvel ensemble cible source FEBIAD est basé sur la cible de carbone utilisée auparavant mais couplée à une source FEBIAD (Force Electron Beam Ion Arc Discharge) de type VADIS développée au CERN/ISOLDE (fig.1). Cette source a l'avantage de fonctionner aussi bien en mode plasma qu'en mode ionisation de surface et d'avoir un corps de source à très haute température permettant ainsi aux éléments condensables d'être ionisés et extraits sans qu'ils se collent sur les parois.

- Le booster de charge SP1_CB

  Il a été développé initialement au LPSC pour répondre à des besoins similaires mais le projet au LPSC n'a pas abouti, seul le développement du booster de charge a été mené à son terme. Le SP1_CB est basé sur une source d'ions multichargés classiques de type RCE (Résonance Cyclotronique Electronique) à laquelle a été enlevée la partie injection pour permettre aux ions monochargés de pouvoir atteindre le plasma RCE. Il est composé de trois bobines où circule un fort courant électrique pour créer le champ magnétique (en rouge fig.1 b), d'une carcasse de fer doux (en bleu fig.1 b), d'un double ensemble d'injection HF (en marron foncé fig.1 b) et d'une chambre plasma délimitée par l'électrode plasma percée en son centre d'un trou de 6mm de diamètre (en blanc crème fig.1 b).

Figure 1 : Ensemble cible source FEBIAD (gauche) et booster de charge SPIRAL1 (droite)
a) Ensemble d'injection des ions monochargés b) Booster de charge c) Ensemble d'extraction des ions multichargés
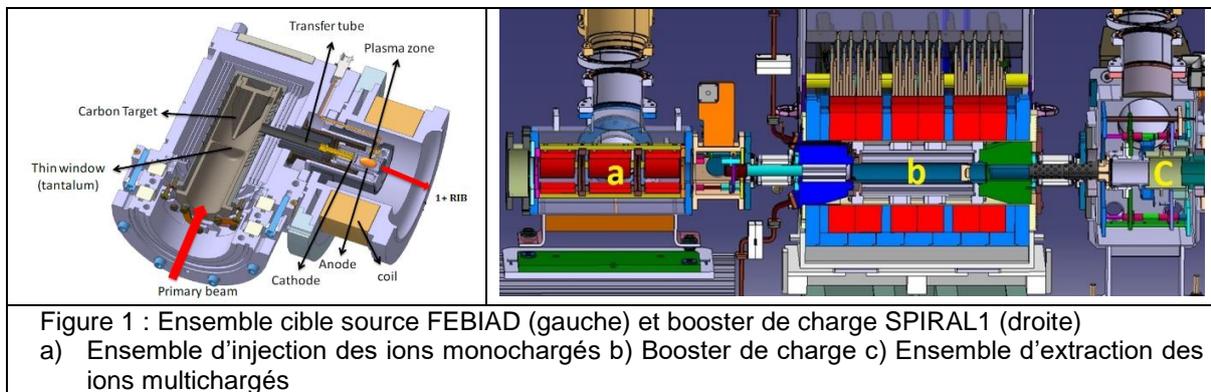
Comme on peut le voir sur la figure 2, de nombreuses possibilités s'offrent au physicien pour réaliser des expériences de Physique sur l'installation SPIRAL1 :

- Le mode NANOGANIII radioactif

  Une des contraintes à respecter pour le projet d'upgrade de SPIRAL1 était la possibilité d'utiliser le précédent ensemble cible-source NANOGANIII qui produit des FIR multichargés ou monochargés comme pour les éléments légers type l'He. Dans ce cas, le FIR doit passer à travers le SP1_CB avec la plus grande transmission possible.

- Le mode 1+ radioactif

Un ensemble cible-source comme l'ensemble cible-source FEBIAD produit un FIR monochargé, il doit traverser le SP1_CB sans perdre d'intensité puis celui va être utilisé directement par l'installation de basse énergie LIRAT et ultérieurement par l'installation DESIR ; on appellera ce mode « passage à travers » par la suite.

🞣 Le mode 1+ stable
Une source d'ions a été développée pour le commissionning de l'installation et pour pouvoir régulièrement faire des études machines de la nouvelle installation. Elle est appelée Canon à ions (fig.2 gauche). Cette source est basée sur l'utilisation d'un pellet de la société HeatWave qui permet la production d'ions stables alcalins dans une gamme d'intensité allant de quelques pA à quelques dizaines de µA.

🞣 Le mode 1+/n+
Le mode 1+/n+ est le mode recherché (fig.2 droite). Un ensemble cible-source FEBIAD produit un FIR mais monochargé, il est ensuite analysé en masse par le dipôle D1P pour être injecté dans le SP1_CB. Les ions radioactifs vont y être capturés, multi-ionisés puis extraits et transportés par la ligne basse énergie n+. Le dipôle D3P va permettre de choisir l'espèce d'intérêt par sa sélection en A/Q avant l'envoi vers le post-accélérateur CIME.

🞣 Le mode SP1_CB comme injecteur
Le SP1_CB est, de par sa construction, une source d'ions de type RCE qui peut être utilisée comme injecteur d'ions stables pour le cyclotron CIME. De par ses performances en terme de production d'ions de haut états de charge avec des intensités utilisables par CIME, ceci donne accès à de nouvelles énergies difficilement accessibles jusqu'à ce jour. Pour le moment seuls les faisceaux d'ions de type gaz y sont produits.

Figure 2 : Source d'ions Canon à Ions (gauche) et schéma de principe de l'installation SPIRAL1 (droite)
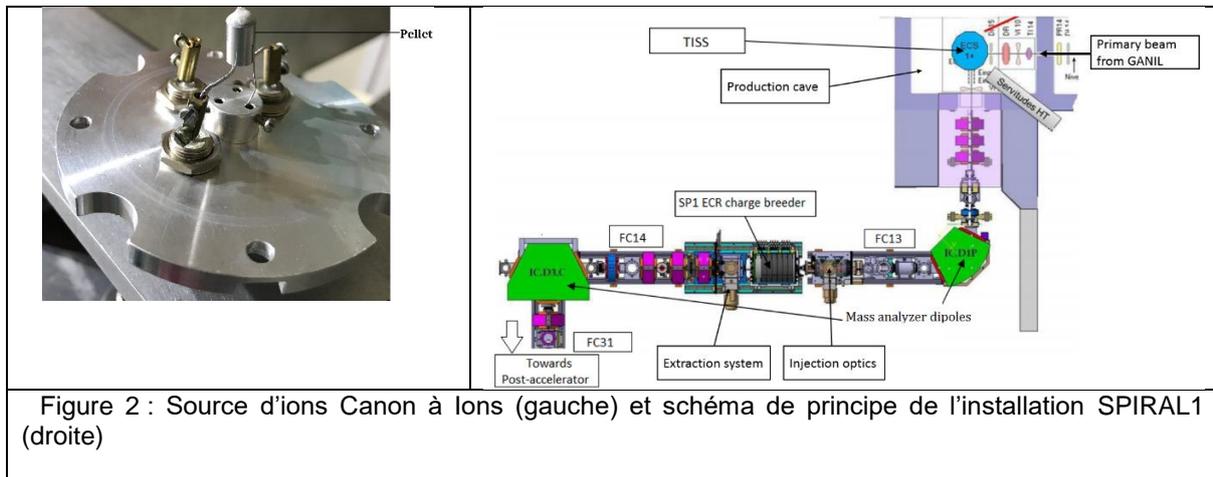
Mesures caractéristiques avec le SP1_CB

Il est indispensable de définir les trois mesures qui vont être utilisées tout le long de cette thèse avec le SP1_CB : Efficacité de la transformation 1+/n+ ; Temps de la transformation 1+/n+ ; Courbe ΔV.

L'efficacité de la transformation 1+/n+ se calcule comme le rapport du nombre d'ions extraits dans l'état de charge Q divisé par le nombre d'ions injectés monochargés et l'efficacité globale correspond à la somme des efficacités individuelles pour chaque état de charge :

$$\varepsilon_Q = \frac{I_Q/_Q}{I_{1+}} \qquad \varepsilon_g = \frac{\Sigma_Q\, I_Q/_Q}{I_{1+}}$$

Le temps de la transformation 1+/n+ se mesure en pulsant le faisceau 1+ à l'aide d'un pulseur de faisceau (fig.3 en haut gauche courbe noire). La réponse à ce signal est la mesure du courant d'ions multichargés après le dipôle d'analyse D3P (fig.3 en haut gauche courbe rouge). Il est communément admis dans la communauté que le temps de la transformation 1+/n+ est égal à la différence en temps entre le front de montée du signal du pulseur et le temps où le signal de réponse atteint 90% du signal saturé.

Finalement, la dernière mesure importante de cette thèse est l'enregistrement des courbes dite ΔV. Cette courbe exprime la variation de l'efficacité de la transformation 1+/n+ (ordonnée en unité arbitraire) en fonction de l'énergie des ions (abscisse en ΔV (V)) avant de pénétrer le plasma RCE (fig.3 en haut droite). Il est important pour la suite de bien comprendre cette mesure qui est explicitée sur le schéma de la figure 3 en bas. La source « Canon à ions » ou l'ensembles cible-source est liée au SP1_CB par la même haute tension qui permet de transporter les ions dans les lignes de faisceaux avec une bonne efficacité (> 80%). Concernant la source « Canon à ions » ou les ensembles cible-source, une légère tension additionnelle appelée ΔV est appliquée afin de donner une énergie suffisante aux ions monochargés pour passer la barrière de potentiel plasma appelé V_p. Sur les courbes ΔV de la fig.3 droite, trois exemples sont donnés qui démontrent les principales différences selon l'état de charge des ions extraits du SP1_CB :

- La courbe en noire représente les ions monochargés => il y a une augmentation du signal avec l'augmentation du ΔV jusqu'à 50V puis ensuite une oscillation autour d'une valeur moyenne. Cette courbe représente les ions monochargés qui n'ont pas été capturés par le plasma et les oscillations sont dues au transport de ce faisceau dans un champ magnétique très intense (1.4 T au maximum).
- La courbe en bleu représente les ions doublement chargés => il y a une augmentation du signal avec l'augmentation du ΔV jusqu'à 18V puis une diminution continue. Cette courbe montre une fenêtre en énergie assez large car les ions doublement chargés sont issus de deux processus différents : capture des ions monochargés puis ionisation par impact électronique ou ionisation en vol des ions monochargés par la haute densité électronique présente.
- La courbe en violet représente les ions très chargés => il y a une augmentation rapide du signal avec l'augmentation du ΔV jusqu'à 7V puis une diminution rapide et un retour à zéro après 60V. Cette dernière courbe démontre qu'il existe une fenêtre en énergie très réduite où les ions 1+ sont capturés puis multi-ionisés et extraits.

Figure 3 : Mesure du temps de la transformation 1+/n+ (en haut gauche) ; courbe ∆V pour trois états de charge du sodium :1+,2+ et 3+ (en haut droite) ; principe de la mesure des courbes ∆V (en bas)
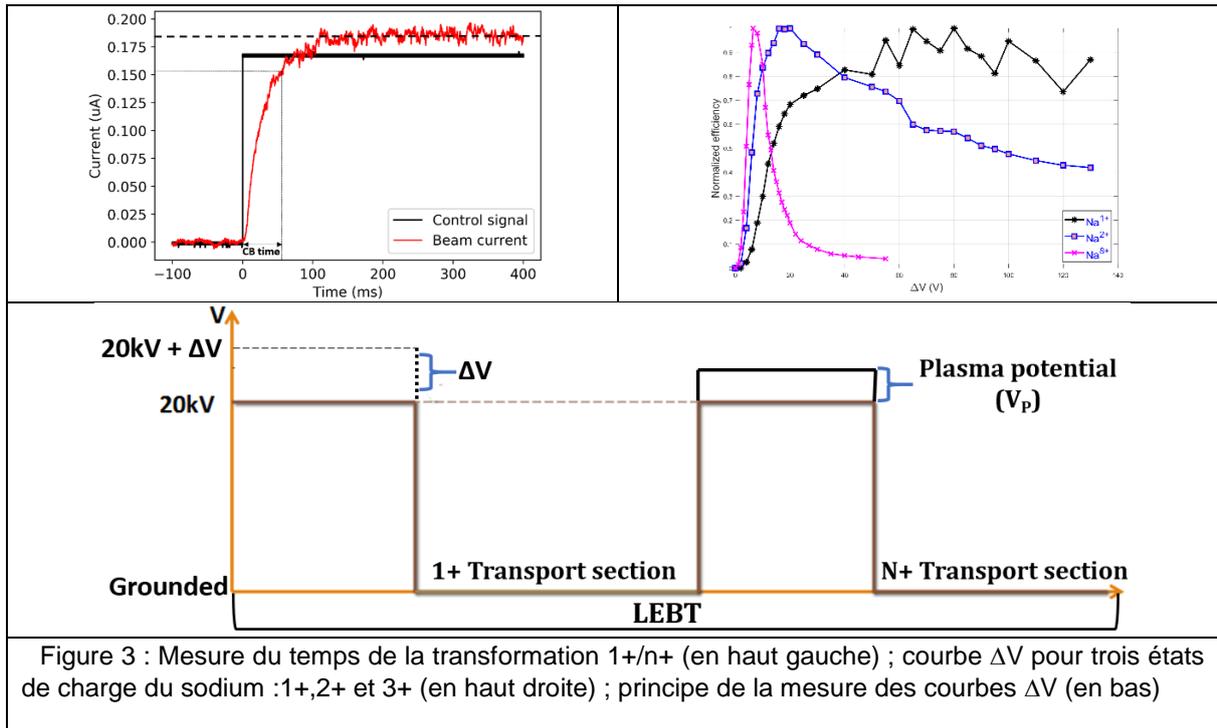
C. Les outils de calculs – modèles Physiques

SIMION 3D

Deux logiciels vont être utilisés pour comprendre et interpréter les résultats des mesures expérimentales : SIMION 3D et MCBC. Le logiciel SIMION 3D, initialement développé par David A. Dahl à l'Idaho National Engineering Laboratory USA, est distribué par la société BCP Instruments. Il permet de calculer les champs électriques d'un système d'optique ionique et des champs magnétiques externes peuvent être inclus. Ainsi des ions peuvent se propager en tenant compte des forces dues aux champs électromagnétiques ci-dessus nommés. Une interface utilisateur simple et un codage en LUA permet facilement de suivre les ions, enregistrer leurs caractéristiques à un moment t donné où à un endroit bien précis. Il permet de faire des simulations en 3D.

MCBC (Monte Carlo Charge Breeding code)

Ce logiciel a été développé par le société FAR-TECH Inc. en collaboration avec le laboratoire Argone National Laboratory USA. Le but de ce code est de reproduire les phénomènes physiques existant dans un booster de charge allant de l'injection d'un faisceau d'ions 1+, sa capture, son ionisation jusqu'à son extraction. Il utilise un modèle simple de plasma avec l'implémentation de deux processus atomiques fondamentaux : l'ionisation par impact électronique et l'échange de charge. Pour la capture, il utilise le processus de collision coulombienne à longue portée pour ralentir les ions 1+ par les ions du plasma. Il est à noter que le processus de ralentissement des ions étant beaucoup plus efficace sur les ions du plasma que sur les électrons libres ; l'interaction

coulombienne ions 1+ - e- est négligée. C'est un code qui fonctionne en 3D. Pour faire fonctionner le code, l'utilisateur doit l'alimenter avec différentes données qui vont former son plasma : le profil de densité électronique et ionique ; les températures électroniques et ioniques du plasma ; les caractéristiques du faisceau d'ions 1+ (taille, divergence) ; le profil du champ magnétique ; le profil des champs électriques formant le potentiel plasma et potentiel dipolaire. C'est l'utilisateur qui engendre son plasma ; pour se faire le plasma du booster de charge inclus dans ce code est basé sur les recherches de V. Mironov, Dubna, Russie et A. Galata, Legnaro, Italie. A ce stade, il est important de regarder les limites de ce code de calcul :

- Ce code ne comprend pas les processus atomiques tels que la double ionisation, les recombinaisons radiatives et diélectroniques. Mais ces processus sont inférieurs d'un facteur 3 à plusieurs ordres de grandeur en section efficace comparativement à l'ionisation par impact électronique et à l'échange de charge
- Le code utilise une densité et température uniforme des neutres injectés, ce qui n'est pas le cas concernant la densité dans la réalité
- Les ions 1+ rencontrent des ions dans le plasma qui correspondent à une distribution d'états de charge (q=1 à 8 dans le cas d'un plasma d'oxygène). Comme simplification, le code remplace cette distribution d'états de charge par une charge moyenne et les ions 1+ ne collisionne qu'avec cette charge moyenne.
- Les ions 1+ sont injectés nom pas continument mais comme une fonction de DIRAC donc il n'est pas possible d'étudier les hauts états de charge qui nécessitent d'injecter en continu les ions 1+ pour qu'ils soient piégés dans le plasma RCE et multi-ionisés

Modèles Physiques pour les temps de confinement

Le temps de confinement des ions multichargés dans un plasma RCE peut être décrit par trois modèles : le modèle « potentiel dipolaire » ; le modèle « diffusion ambipolaire » et le « modèle marche aléatoire ». Dans le modèle « potentiel dipolaire », les électrons chauds chauffés par la zone RCE sont piégés au centre et par la même vont créer un puit de potentiel négatif comme sur la fig.4 gauche. Ce potentiel retient les ions multichargés et on peut en déduite la formule suivante pour le temps de confinement :

$$\tau_q = R \frac{L\sqrt{\pi}}{\sqrt{kT_i/m_i}} e^{\frac{|qe\Delta\varphi|}{kT_i}}$$

Dans le modèle « diffusion ambipolaire », le potentiel plasma créé un champ électrique qui fait diffuser les ions hors du plasma, dans ce cas le temps de confinement est :

$$\tau_q = 7.1 \times 10^{-20} Lq\ln\Lambda\sqrt{A_i} \frac{n_e Z_{eff}}{T_i^{3/2} E}$$

Finalement, dans le modèle « marche aléatoire », les ions subissent une diffusion aléatoire vers les zones de plus basse densité d'où le temps de confinement suivant :

$$\tau_q = 7.1 \times 10^{-20} L^2 q^2 \ln\Lambda\sqrt{A_i} \frac{n_e Z_{eff}}{T_i^{5/2}}$$

La fig.4 droite représente l'évolution du temps de confinement de l'ion K[9+] dans un plasma d'hélium en fonction de la température des ions de ce plasma. Comme on peut le constater, les trois modèles donnent des résultats très différents avec le modèle « potentiel dipolaire » qui diverge très rapidement lorsque la température des ions du plasma devient très faible.

Figure 4 : Schéma du potentiel dipolaire créé au centre du plasma RCE (gauche) – Temps de confinement d'un ion K[9+] en fonction de la température des ions hélium pour les 3 modèles
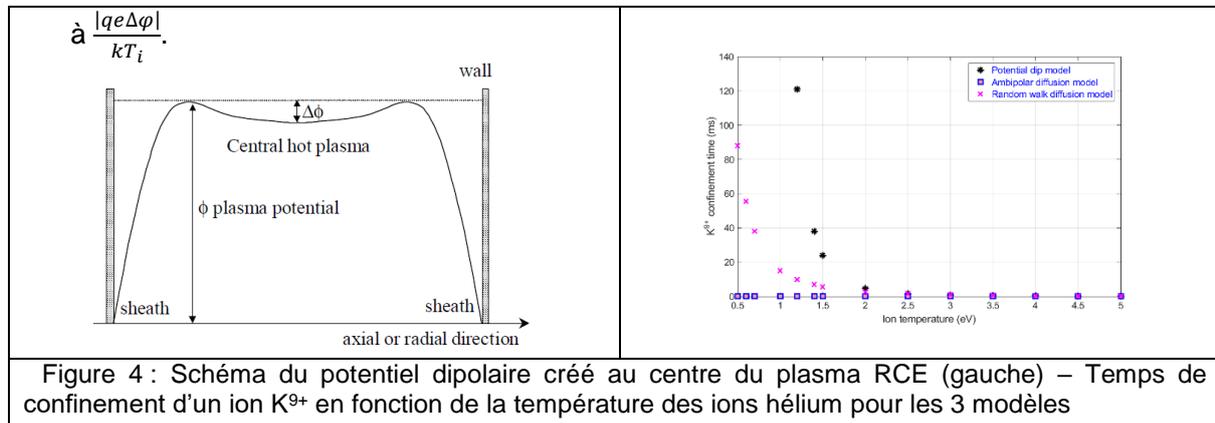
D. **Les mesures expérimentales**

Deux modes de fonctionnement du SP1_CB sont étudiés : le mode « passage à travers » et le mode «1+/n+». Dans la suite de ce paragraphe, 4 mesures vont être présentées et les codes de calculs ou modèles vont être des outils pour interpréter les résultats obtenus.

Mode « passage à travers » - mesure de la transmission

Dans le mode « passage à travers », le SP1_CB est arrêté (pas d'onde HF envoyée), seuls ses bobines sont utilisées comme solénoïdes pour guider le faisceau d'ions. Les tests ont été réalisés sur un faisceau de Na+@20keV et K+@15keV avec une émittance de 50 π.mm.mrad. Les transmissions mesurées sont de 78% et 80% respectivement. Le code commercial SIMION 3D a été utilisé pour comprendre où se situaient les pertes. Des transmissions très proches de la mesure ont été reproduites soit 79% et 82% pour chacun des 2 cas ci-dessus. Il s'avère que les ions se perdent pour 15% autour du trou de l'électrode plasma (ϕ=6mm) et 5% dans l'extraction du booster de charge (fig.5). Le champ magnétique des 2 solénoïdes de la source provoque une propagation en forme d'onde dans la source et il faut placer le minimum sur le trou de l'électrode plasma pour maximiser la transmission.

Figure 5 : Na+@20keV transmis à travers le SP1_CB jusqu'à la sortie de l'extraction
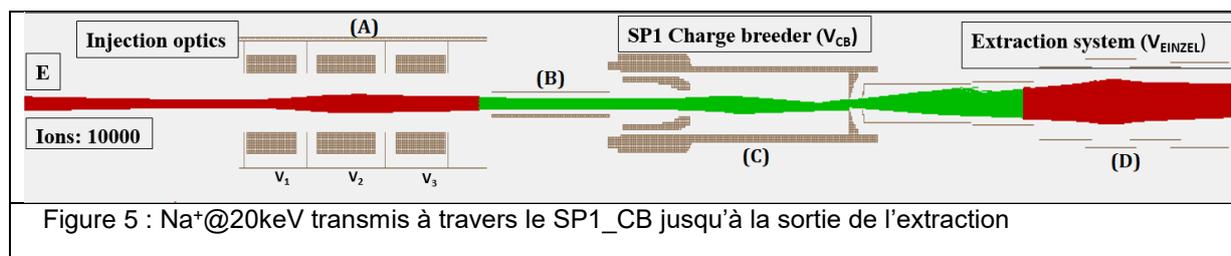
Mode « 1+/n+ » - optimisation du SP1_CB

Dans le mode «1+/n+», deux campagnes expérimentales ont été effectuées. Une première campagne est dédiée à la recherche de paramètres du SP1_CB qui permettent de maximiser l'efficacité de la transformation 1+/n+ tout en minimisant le temps de cette transformation. Le cas choisi est celui du K^+@20keV avec un plasma d'hélium à 270W de puissance hyperfréquence (HF) injectée. Le réglage du SP1_CB se fait sur la charge 9+ définissant un premier jeu de paramètres : champ magnétique, puissance HF, I_{1+}, ΔV. A partir de ce jeu, un seul paramètre est varié en gardant les autres constants et les efficacités comme les temps de la transformation sont enregistrés. Un exemple est donné sur la fig.6 où le champ magnétique est modifié et surtout le champ magnétique de la trappe ionique (bobine médiane du SP1_CB). Pour chaque état de charge, il existe un maximum concernant l'efficacité de la transformation par contre l'évolution du temps de la transformation est plus variable ; il semble avoir une tendance à la diminution de ce temps lorsque le ratio B_{min}/B_{ecr} augmente. Il est clair également que ce temps transformation augmente drastiquement avec les états de charge puisqu'on passe de ≈0.4ms pour le 4+ à ≈120ms pour le 9+. En conclusion, sur cette fig.6 bas droite, la valeur B_{min}/B_{ecr} = 0.81 est la meilleure configuration pour le K^{9+}@180keV afin de remplir les objectifs. D'autres travaux de recherche ont démontré que ce ratio est normalement préférable pour les performances des sources d'ions de type RCE. Ce type de variation est faite pour les autres paramètres tels que la puissance HF injectée, l'intensité d'ions 1+ injectée et la variation d'énergie du faisceau incident avec le paramètre ΔV. Les paramètres du SP1_CB permettant d'atteindre nos objectifs sont donc les suivant :

B_{min}/B_{ecr} = 0.81 – Puissance HF de 270W – Intensité d'ions 1+ injectés 180nA – ΔV = 5.3V
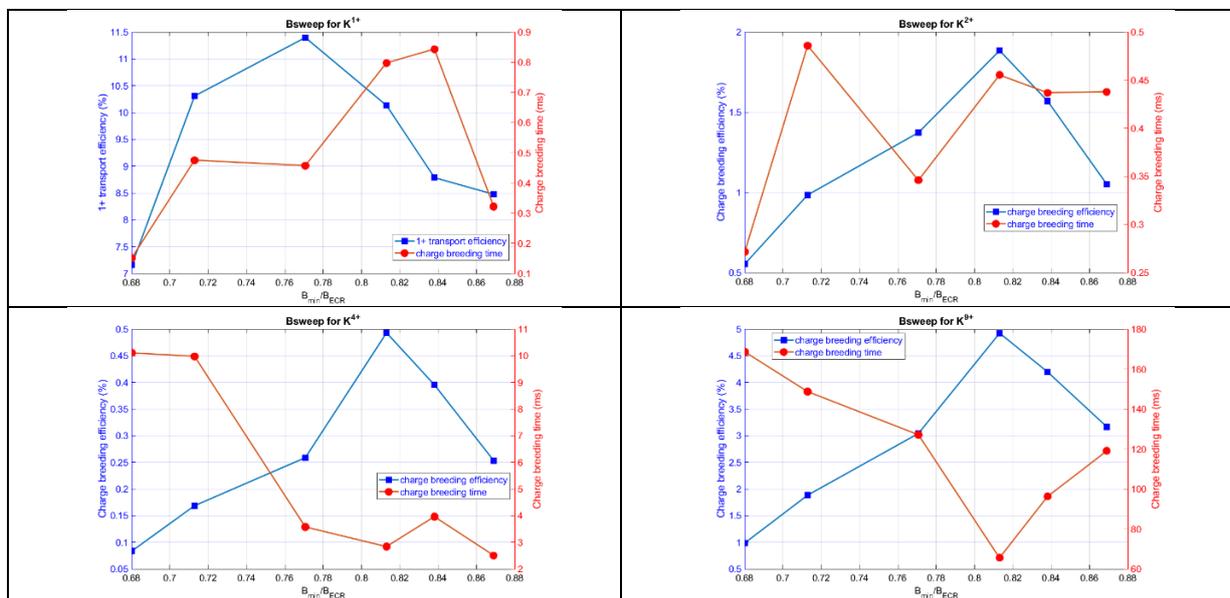
Figure 6 : Mesures des temps de la transformation 1+/n+ pour le K^{9+} dans un plasma d'hélium en fonction du B_{min}/B_{ECR} et ceci pour 4 états de charge : 1+ (haut gauche) 2+ (haut droite) 4+ (bas gauche) 9+ (bas droite)

<u>Mode « 1+/n+ » - mesures des courbes ΔV</u>

L'autre campagne expérimentale est consacrée à l'utilisation d'un faisceau d'ions monochargés comme sonde du plasma type RCE créé dans le SP1_CB. Pour ce faire trois systèmes ont été étudiées : Na+ + plasma He ; K+ + plasma He et K+ + plasma O_2 et ceci pour les ions 1+ et 2+. Une étude optique au préalable a permis de déterminer les caractéristiques optiques du faisceau d'ions 1+ dans chacun de ces cas (tableau 1). Ces caractéristiques ont été déduites de mesures faites sur le faisceau lui-même.

Caractéristiques faisceaux (paramètres de Twiss)	$^{23}Na^+$@20keV	$^{39}K^+$@15keV
α	-1.438	-1.079
β (mm/mrad)	0.482	0.362
ε_{RMS} (π.mm.mrad) [norm]	0.0148	0.0177
Tableau 1 : Caractéristiques faisceaux utilisés dans les cas d'étude Na+ et K+		

Un premier essai de reproduction des données est réalisé avec le logiciel SIMION 3D. Dans ce cas, les champs magnétiques et électrostatiques sont reproduits pour réaliser un plasma RCE sans particules, seuls les champs électromagnétiques sont inclus imitant la présence d'un plasma. La fig.8 gauche prouve qu'avec un modèle aussi brut, il est possible de reproduire la courbe ΔV expérimentale dans le cas de l'injection d'ions $^{23}Na^+$@20keV. Les oscillations au-delà d'un ΔV=50V sont reproduites preuve qu'elles sont majoritairement dues au transport des ions dans un fort champ magnétique. Il y a un décalage de ≈7-8V au départ entre la courbe expérimentale et calculée nécessitant l'utilisation d'un potentiel plasma de 10V pour reproduire au mieux les données expérimentales. Concernant la courbe ΔV du $^{23}Na^{2+}$, la tendance est reproduite mais avec un accord beaucoup moins bon ; ici la transformation de l'ion $^{23}Na^+$en ion $^{23}Na^{2+}$ se fait aléatoirement tout le long du SP1_CB. De ce premier modèle, il s'avère qu'une modélisation impliquant les processus fondamentaux atomiques se produisant dans un plasma doit être réalisé. Ceci sera le cas avec le code MCBC.

Figure 8 : Comparaison des courbes mesurées (noir) avec les courbes obtenues par MCBC (bleu) pour les états de charge 1+ (gauche) et 2+ (droite).

Une stratégie particulière a été développée pour utiliser le code MCBC (fig.9). D'abord le faisceau d'ions 1+ est transporté avec le logiciel SIMION 3D du point de définition du faisceau à travers le triplet électrostatique jusqu'à l'entrée du SP1_CB. En ce point, le rayon du faisceau ainsi que sa divergence deviennent des données d'entrée pour MCBC. Une fois la simulation terminée,

le code crée un fichier rassemblant les vitesses et positions des particules sortant d'un orifice faisant l'analogie avec le trou de l'électrode plasma. Ce fichier devient alors le fichier d'entrée pour le logiciel SIMION 3D pour le transport à travers le système d'extraction du SP1_CP.

Figure 9 : Stratégie utilisée pour l'utilisation du code MCBC aux données expérimentales
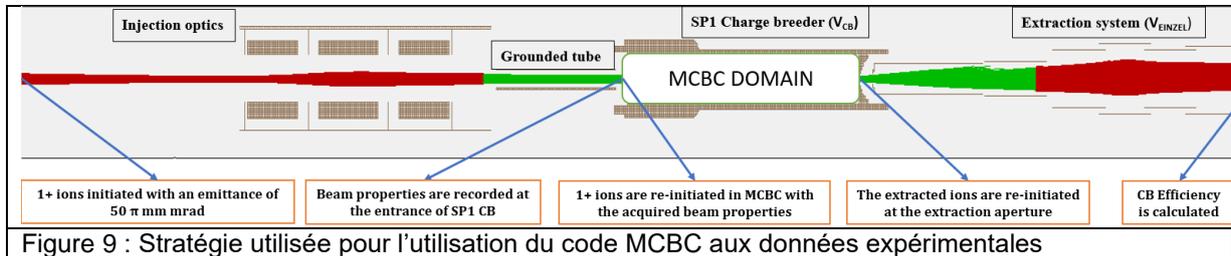
Donnons l'exemple du $^{23}Na^+$ dans un plasma d'hélium. Un premier jeu de paramètres permet d'obtenir une première courbe calculée. Le test du χ^2 de K. Pearson va être appliqué aux données pour extraire les paramètres plasma tels que densité électronique, densité ionique, température électronique et température ionique. Tour à tour, chaque variable du jeu de paramètre est variée en gardant constante les autres (fig.10) et le χ^2 est ainsi calculé. Deux exemples sont montrés sur la fig.10 : à gauche les variations avec la densité électronique (donc la densité ionique) et à droite celle avec la température des ions du plasma d'hélium. Comme on peut le constater, ces deux paramètres sont très sensibles et les courbes calculées peuvent vite s'éloignées de celle mesurée. Une fois chaque variable du jeu de paramètres optimisée, une deuxième courbe calculée (fig.11 gauche violet) est obtenue. Le processus est reconduit une seconde fois pour affiner les résultats finaux (fig.10 gauche violet). Cette méthodologie va être appliquée aux deux autre cas de l'étude.
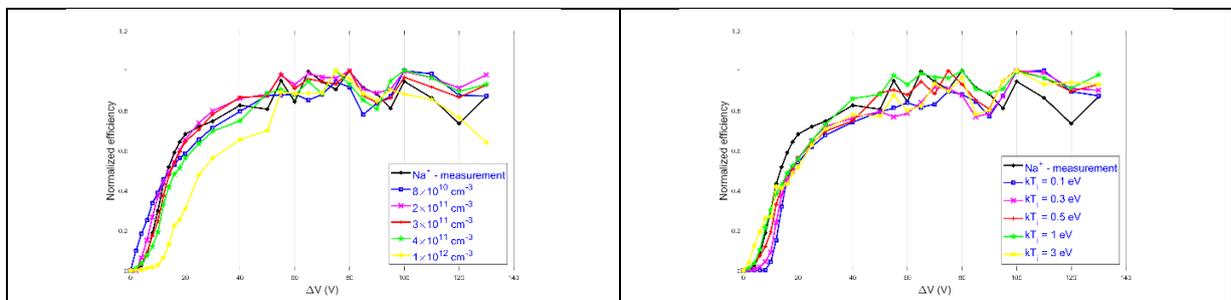
Figure 10 : Courbe ΔV calculée en faisant varier une variable tout en gardant les autres constantes (gauche variable est la densité électronique – droite variable est la température des ions du plasma
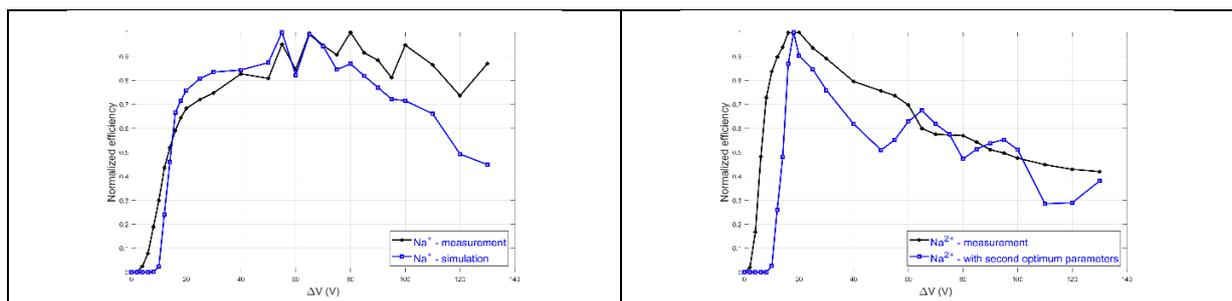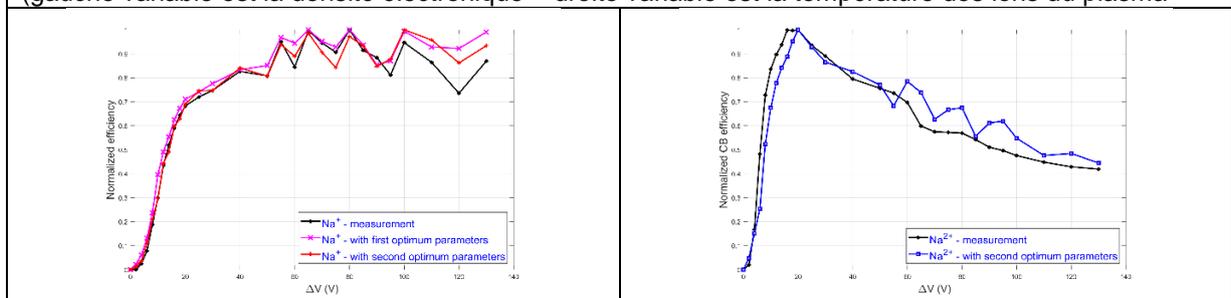

Figure 11 : Comparaison des courbes mesurées avec les courbes obtenues par MCBC pour les états de charge 1+ (gauche) et 2+ (droite).

Par conséquent, les paramètres plasma ont été déduits et sont mis dans le tableau 2 avec en plus l'efficacité globale de capture des ions 1+ calculée par le code MCBC et les caractéristiques faisceaux avant pénétration dans le plasma. La fig.12 gauche montre l'évolution des émittances des faisceaux d'ions $^{23}Na^+$@20keV et $^{39}K^+$@20keV avant de pénétrer dans le SP1_CB. Le faisceau de $^{39}K^+$@20keV est plus concentré sur l'axe que celui de $^{23}Na^+$@20keV. La fig.12 droite montre l'évolution des ions Na^+ à l'intérieur du SP1_CB pour 2 temps (30µs et 90µs) et 4 émittances : 10, 30, 50 et 80π.mm.mrad. Plus l'émittance diminue, plus les ions 1+ atteignent le plasma RCE et plus le pourcentage de capture globale augmente (Tableau 2).

Dans le tableau 2, intéressons-nous aux fréquences de collisions ν_{ii}^{1+} et distance moyenne de capture des ions 1+. Pour le cas du $^{39}K + O_2$, ces deux dernières valeurs sont la plus petite et la plus grande respectivement signifiant que l'ion $^{39}K^{1+}$ nécessite une distance plus grande pour être capturé correspondant à une moindre interaction avec le plasma d'oxygène et par conséquent la plus faible efficacité globale de capture. Si maintenant on compare le cas des ions $^{23}Na^{1+}$ et $^{39}K^{1+}$ dans un plasma d'He, les deux ont sensiblement les mêmes valeurs de ν_{ii}^{1+} et λ_{ii}^{1+} pour des valeurs d'efficacité globale de capture très différentes : 16.44% et 24.52%. La majeure différence est dans les caractéristiques du faisceau qui est plus concentré en taille dans le cas du $^{39}K^{1+}$ (r = 4.25mm) que dans le cas du $^{23}Na^{1+}$ (r = 4.9mm) avec des divergences similaires. Ceci démontre que les caractéristiques optiques du faisceau d'ions 1+ jouent un rôle majeur dans l'efficacité globale de capture.

De ces mesures et en recoupant avec, d'une part les emplacements des pertes des ions 1+ dans la chambre plasma du SP1_CP et d'autre part, les mesures d'évolution de l'efficacité de la transformation 1+/n+ en fonction de l'émittance du faisceau d'ions 1+, les conclusions suivantes peuvent être faites :

✓ Les qualités optiques du faisceau d'ions 1+ sont primordiales pour avoir une efficacité de capture importante ($^{23}Na^{1+}$ + He, $^{39}K^{1+}$ + He).
✓ Les courbes théoriques des courbes ΔV sont très sensibles à deux paramètres plasma : densité électronique (affecte l'ionisation) et température ionique (affecte la capture des ions 1+).
✓ L'énergie des ions injectés une fois dans le plasma est quasi constante alors qu'elle devrait dépendre selon la théorie de $T_{ion\_plasma}*(M_{1+}/M_{ion\_plasma})$, résultats mesurés plusieurs fois pour ces éléments et le SP1_CP.
✓ Le potentiel plasma est très faible par rapport à une source RCE standard où les valeurs sont plutôt de la dizaine de volts.

	Na + He	K + He	K + O₂
Rayon du faisceau d'ions 1+ (mm)	4.90	4.25	4.25
Divergence du faisceau d'ions 1+ (mrad)	17.83	17.29	17.29
Puissance HF injectée (W)	470	209	207
$e\Delta V_{exp}$ (eV)	6.5	7.5	6.5
$E_{inj} = e(\Delta V_{exp}-V_p)$ (eV)	5.0	6.5	5.5
Température ionique He (eV)	0.9 – 1.1	0.7 – 0.8	1.5 – 2.5

Température électronique (keV)	1 - 2	1 - 2	2 - 3
Densité électronique (cm^{-3})	3.3 -3.7 10^{11}	1.5 -2.5 10^{11}	1.0 -2.0 10^{11}
Potentiel plasma Vp (V)	1.5	1	1
eΔV$_{simulation}$ (eV)	7.5	8.5	8.5
E$_{inj}$ = e(ΔV$_{simulation}$-Vp) (eV)	6	7.5	7.5
Efficacité globale de capture des ions 1+ calculée par MCBC (%)	16.44	24.52	7.26
ν_{ii}^{1+} (kHz)	182	163	109
λ_{ii}^{1+} (mm)	37.8	34.63	47.52

Tableau 2 : Récapitulatif des principaux paramètres plasma déduits des comparaisons avec le code MCBC
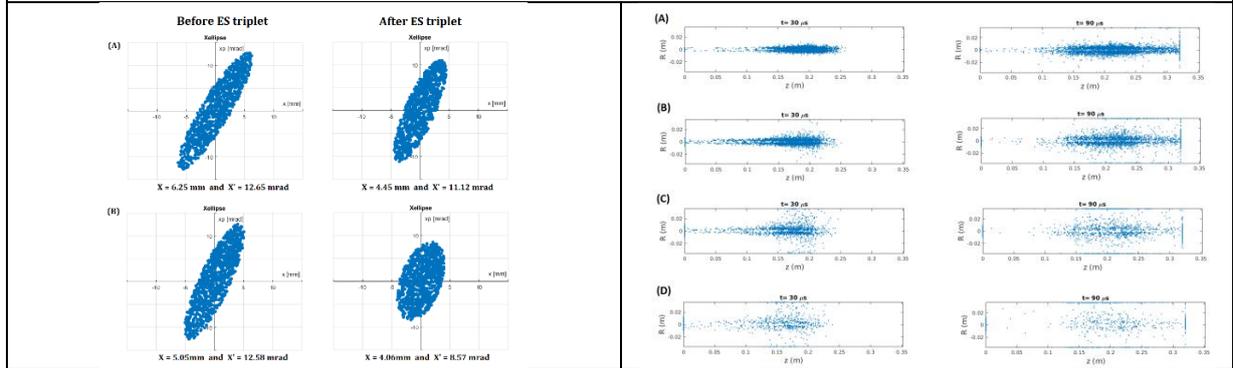
Figure 12 - Gauche : Evolution du faisceau d'ions 1+ avant d'entrer dans le SP1_CB (A) ^{23}Na$^+$@20keV et (B) ^{39}K$^+$@15keV pour la même émittance de 50π.mm.mrad
- Droite : Distribution des ions ^{23}Na$^+$ calculée avec MCBC après 30 µs (colonne de droite) et 90 µs (colonne de gauche) pour des émittances croissantes (A 10π.mm.mrad - B 30π.mm.mrad - C 50π.mm.mrad - B 80π.mm.mrad)

Mode « 1+/n+ » - mesures du temps de la transformation

Finalement une tentative a été faite pour mieux comprendre quel modèle peut reproduire le mieux le temps de confinement des ions dans la trappe que constitue le plasma RCE pour les ions ayant des états de charge élevés. Il doit être précisé ici que le temps de la transformation 1+/n+ comprend le temps pour que l'ions 1+ soit capturé, multi-ionisé (temps de confinement) puis extrait de la source. Pour les ions moyennement à très chargés, ces deux temps (capture et extraction) représentent moins de 15% du temps total mesuré. Dans le modèle « marche aléatoire », le temps de confinement est proportionnel à $\frac{q^2}{T_i^{5/2}}$ tandis que dans le modèle « potentiel dipolaire », il est proportionnel exponentiellement à $\frac{|qe\Delta\varphi|}{kT_i}$. En regardant la fig.4 et en utilisant les températures ioniques déduites dans ce travail de thèse, il est possible de reproduire avec les deux modèles les résultats de mesures de 2016 comme 2018. La seule conclusion possible est que les deux modèles décrivent une partie du problème et que les temps de confinement des ions dans la trappe plasma sont une combinaison des deux modèles soit :

$$\tau_{q+} = \alpha\tau_{potentiel\ dip} + \beta\tau_{marche\_aléatoire}$$
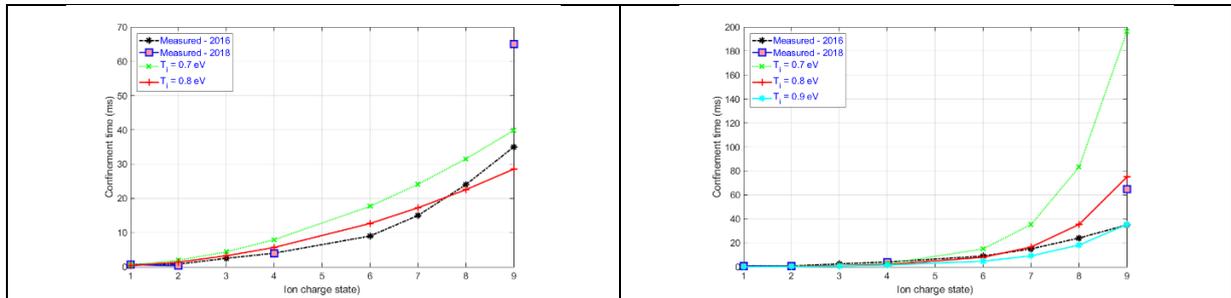
Figure 13 : Comparaison des mesures de temps de la transformation 1+/n+ avec le modèle « marche aléatoire » (gauche) et « potentiel dip » à droite pour les ion K^{q+} mesurés lors de ce travail et dans des conditions similaires en 2016 au LPSC.

E. **Conclusions et perspectives**

Cette thèse présente les résultats de travaux expérimentaux appliqués au booster de charge de l'installation SPIRAL1. Les cas étudiés concernent les éléments alcalins de masse légères (^{23}Na et ^{39}K) injectés dans deux type de plasma différents à savoir plasma d'He et plasma d'O$_2$. Ces études ont été menées en parallèle du commissionning de l'installation après sa modification portant sur l'implémentions de la méthode 1+/n+ afin d'élargir la palette des ions radioactifs à délivrer aux physiciens.

La mesure du temps de la transformation 1+/n+ combinée à celle de l'efficacité de cette transformation a permis de dégager un ensemble de paramètres fonctionnels (B_{min}/B_{ecr} – Puissance HF – Intensité d'ions 1+ injectés – ΔV) applicable au cas du $^{39}K^{9+}$ pour répondre à la condition suivante : maximisation de l'efficacité de la transformation tout en minimisant le temps de cette transformation. Cette mesure ayant été réalisée pour un seul cas, il faudrait en perspective appliquer cette méthode à d'autres M/Q pour en extraire un ensemble plus large de paramètres fonctionnels débouchant sur des lois empiriques.

La reproduction des courbes expérimentales ΔV pour les trois cas suivant : $^{23}Na^{1+}$ + He, $^{39}K^{1+}$ + He, $^{39}K^{1+}$ + O$_2$ a permis d'extraire un ensemble de paramètres plasma caractéristiques du fonctionnement d'un booster de charge. Ces résultats ont permis de mettre en avant la sensibilité de l'efficacité de la transformation 1+/n+ à la densité électronique comme à la température des ions du plasma (He ou O$_2$). De même, il a été démontré dans ce travail de thèse que les qualités optiques du faisceau 1+ sont primordiales pour avoir une bonne efficacité. Au regard des énergies d'injections des ions 1+ arrivant dans le cœur du plasma RCE, une question se pose toujours : pourquoi la température des ions du plasma RCE s'adapte toujours quel que soit l'espèce injectée (ΔV constant) ? Pour répondre à cette question, d'autres mesures sont nécessaires notamment avec des espèces ayant des masses plus élevées comme le Rb, Cs dans un plasma d'He et d'O$_2$.

English version

1 Introduction

The understanding of the properties of the exotic nuclei far from stability valley necessitates the production of RIBs with high intensities. Re-accelerated RIBs permits a number of studies ranging from nuclear structure to the standard model, and its foremost importance for nuclear astrophysics. In late 1980's, the first post accelerated RIBs were produced with ISOL technique at Cyclotron Resource Centre (CRC) - Université catholique de Louvain (UCL), Louvain-La-Neuve, Belgium. Following the same principle, different facilities are equipped with post-accelerators to produce the RIBs for the nuclear physics experiments near the Coulomb barrier: ISOLDE (CERN), SPIRAL1 at GANIL (France), TRIUMF (Canada), ANL (USA), GSI/FAIR (Germany), RIKEN (Japan), NSCL at MSU (USA), and JINR at FLNR (Dubna). These major installations use different targets, ion sources, different energies, intensities and different production methods. These installations try to produce the RIBs as intense as possible to answer and explore the new regions of nuclide chart. The technical framework of this Ph.D. is the SPIRAL1 facility at GANIL.

Originally, two techniques are currently being used to produce the good quality of RIBs,: the isotope separation on line (ISOL) technique and in-flight separation technique (see figure 1.1).
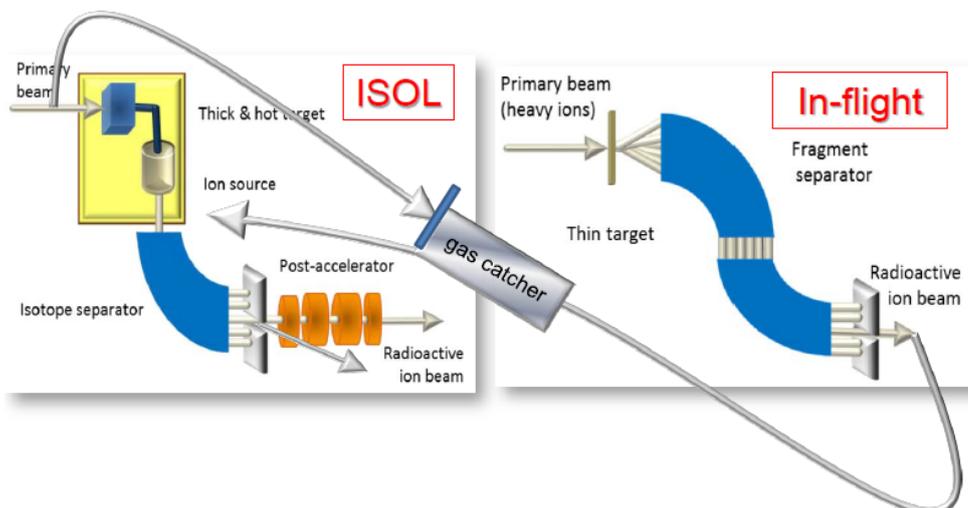

FIGURE 1.1: A schematic drawing of the ISOL and in-flight techniques for the production of radioactive ion beams. Figure reproduced from [1].

The in-flight technique uses thin production targets to create the fragments with energies close to the projectile one. They are in-flight separated by a magnetic separator

and transported to various experimental areas. This technique allows the production of very short-lived isotopes. In the ISOL technique, the radioactive isotopes are produced during the interaction of primary beams with thick target material. The produced secondary particles from the interaction diffuse out of the target and effuse into an ion source which is coupled to the target. The multi-ionized ions are extracted and accelerated to the experimental areas. Finally, the production sequence followed in these techniques should possess the following properties: should be very efficient, should achieve high production rate, should be fast to avoid the decay losses and should be selective.

The use of ISOL as well as high energy projectile fragmentation methods for exploring the structure of nuclei far from stability with medium energy beams (1 - 90 MeV/u) became one of the major activities at GANIL (Grand Accélérateur National d'Ions Lourds). The primary light-or heavy ion beam accelerated by the GANIL cyclotrons permit a wide range of radioactive nuclei by impinging on a hot production target located in the SPIRAL1 facility. The radioactive atoms produced by the nuclear reactions are released from the target and effused through a cold transfer tube into a ion source (e.g. full permanent magnet ECRIS - NANOGAN III), which is connected to the target. This combination of target and ion source is usually called Target Ion Source System (TISS). The radioactive atoms are ionized and extracted as multi-charged radioactive ion beam. After extraction from the TISS, the low-energy RIB (accelerated up to 34 keV) are selected by means of mass analyzer dipole and sent to the low energy experimental areas (LIRAT or in the future DESIR) or injected into a compact cyclotron CIME (K = 265) for post-acceleration. Since 2001, 35 radioactive beams of gaseous elements (He, Ne, Ar, Kr, O, N and F) were produced using NANOGAN III and delivered to numerous experiments. Because of the cold assembly of transfer tube and the ECR ion source, the ionization technique prevents the effusion and ionization of condensable elements. Therefore, a major upgrade has been undertaken in 2014 [2], with the aim to extend the production capabilities of SPIRAL1 facility to a number of condensable elements. To this intent, a FEBIAD TISS has been chosen for the production of singly charged condensable RIBs with high yields.

In order to study the properties of exotic nuclei, the post accelerated RIBs are expected to have high energies (few MeV/u to GeV/u). In order to reach highest energies, the charge state of the RIBs from the new TISS has to match the injection characteristics of the CIME cyclotron. For this purpose, the 1+/N+ method has been put into practice by installing a **charge breeder** between the target ion source system (TISS) and the CIME cyclotron. The device accepts the 1+ RIBs from the TISS, boosts its charge state and extracts the highly charged ions (N+) very quickly and efficiently. In addition, the integration of 1+/N+ method allows the use of versatile 1+ source for the acceleration of a wide range of elements. Since the first work of Tamburella et al. [3], the charge breeding technique in Electron Cyclotron Resonance Ion Source (ECRIS) and Electron Beam Ion Source (EBIS) has been nicely developed. In the framework of EURISOL and EURONS, the two charge breeding techniques were studied and compared with regards to their performances and were found to be complementary. Considering the continuous mode of operation and the intrinsic resolving power of the cyclotron CIME, an ECRIS based charge breeder has been found better suitable than an EBIS. Therefore, the SPIRAL1 ECR charge breeder (SP1 CB), based on a LPSC Phoenix ECRIS, was installed in the Low Energy Beam Transport (LEBT) during the SPIRAL1 upgrade. The advantages of this technique are the high acceptance of injected 1+ current and emittance, the reliability and the ability

to produce high charge states continuous and pulsed beams.

Based on the conclusion of the EMILIE collaboration studies [4], the SP1 CB has gone through several modifications [5] to improve its performance. Generally, the performance of the charge breeder is mainly characterized by charge breeding efficiency and charge breeding time. The efficiency is defined as the ratio between the extracted particle current at the given charge state and the injected particle current. Since the RIB production yield is very low (typically 10^4 - 10^8 pps), the charge breeding efficiency for a given charge state should be as high as possible. At SPIRAL1, the RIBs having a short half-life (on the order of 1s or less) are delivered for many physics experiments. Therefore, the charge breeding time is a key parameter that has to be short (to be able to produce elements with half life $T_{1/2} \leq 100$ ms) to avoid decay losses of the radioactive ions during the charge breeding stage. These parameters are always measured during the experiments.

Considering the operating range of CIME, charge breeding will be required for condensable elements ranging from Na to Y. The recent SP1 CB experimental results showed modest efficiencies for light alkali ions (Na and K) in Helium and Oxygen plasma. The reasons behind these results were argued as: a mismatch between the velocity of 1+ injected ion and plasma ion, resulting in a weaker slowing down force and therefore a lower charge breeding efficiency and poor 1+ injection beam optics. Moreover, large variations between the charge breeding efficiency and charge breeding time were observed when the SP1 CB was optimized with different buffer gas (H_2 and He) with similar operating conditions. In order to understand these two important aspects, a deeper understanding of the Physics involved in the charge breeding process is necessary and the work presented in this thesis goes in this direction.

The thesis consists of a series of experimental studies performed with Na and K ions in Helium and Oxygen plasma. Initially, the SP1 CB has been optimized to improve the charge breeding efficiency. The experiments allowed studying the influence of injection and source tuning parameters that mainly affect the performance of the SP1 CB. The experimental results also provided a strong motivation to investigate the ion losses during the transmission of 1+ beam through the SP1 CB (shooting through mode). Following the optimization, a series of experiments were performed to study the interaction of 1+ beam in an ECR plasma and therefore, to understand the reason for the difference in charge breeding efficiencies of Na and K. This work has been carried out using a Monte-Carlo code, which models the capture of 1+ injected ions and atomic physics processes in an ECR plasma. Concerning the second important aspect, the dependence of charge breeding efficiencies and charge breeding times of low and high charge states of K (in Helium plasma) on SP1 CB tuning parameters has been investigated in collaboration with the ion source team from JYFL. The goal of these measurements is to understand the influence of each tuning parameter on the SP1 CB performance and finally, to gain control over these parameters to improve the performance of SP1 CB.

The thesis is divided in the following way: Chapter 2 gives a short introduction about the SPIRAL1 facility, different TISSs installed in the upgraded SPIRAL1 facility and describes different charge breeding techniques, underlining the reasons for the particular choice adopted for the upgraded SPIRAL1. It also discusses the ion optics associated to the LEBT and introduces the ion beam motion and related concepts, as the beam emittance, which is crucial to understand the topics discussed along this thesis work. Chapter 3 focuses on the basic plasma physics for the production of

highly charged ions and the principles of ECR ion sources. Chapter 4 is dedicated to the SP1 CB: the main components of the device and the SP1 CB beam line are discussed. It recalls the Physics involved in the beam capture in ECR plasma and conclude with a short description of two different simulation tools (SIMION 3D and MCBC) used in chapter 5 to investigate the beam transport and 1+ ion beam capture in an ECR plasma. In chapter 5, the experimental and numerical activities performed with SP1 CB are presented: the influence of axial magnetic field modifications and the injection optics on charge breeding efficiencies are discussed. In addition to that, the experimental results from the charge breeding time investigations are presented. A computational study has been undertaken using the two simulations tools to understand the ion transport through SP1 CB and interaction of injected 1+ beam in ECR plasma. Finally, in chapter 6 the conclusions of the work are drawn.

2 Ion sources and Low Energy Beam Transport

GANIL (Grand Accélérateur National d'Ions Lourds), a nuclear installation located at Caen, is one of the international laboratories dedicated for fundamental research in nuclear physics, atomic physics, radiobiology, material irradiation and R&D for detectors and associate instrumentation. The layout of GANIL facility is shown in the figure 2.1. The facility delivers a wide range of high intense primary beams (i.e. ^{12}C to ^{238}U), which can be accelerated up to 95 MeV/A using three cascade cyclotrons (C01 or C02 (K = 30), CSS1 and CSS2 (K = 380)) [6].
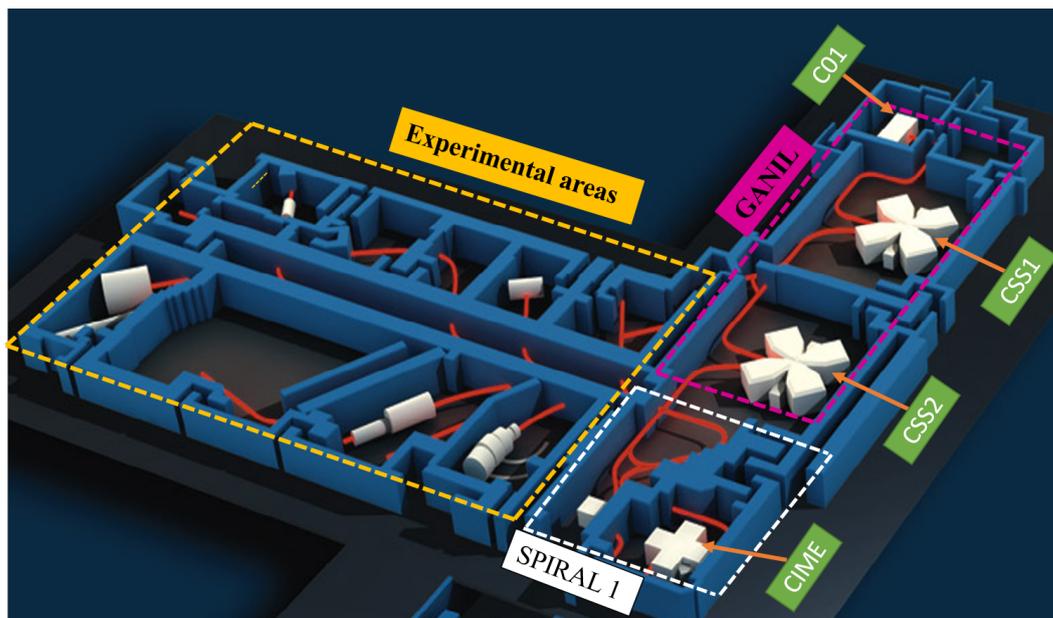
FIGURE 2.1: Layout of GANIL facility.

The SPIRAL1 (Systéme de Production d'Ions Radioactifs Accélérés en Ligne) facility shown in the figure 2.1 is dedicated to produce and accelerate stable and radioactive ion beams which are delivered to physicist for nuclear physics experiments. This facility is based on ISOL (Isotope Separation On-Line) technique [7], where the radioactive atoms are produced by fragmentation of high intense primary ion beams on a hot target material coupled to an ion source (referred as Target Ion Source System (TISS)). The facility makes use of primary beams (from C to U) and allows to impinge on a carbon target [8]. A right combination of primary beam, target and the reaction allows delivering the desired radioactive isotopes. The produced radioactive isotopes are effused into an ion source (e.g. ECR ion source) through a cold transfer tube and become multi ionized. They are accelerated by an external voltage

applied to the ion source extraction. The extracted radioactive ions are then sepa-
rated and accelerated in the Cyclotron d'Ions de Moyenne Energie (CIME) (K =265)
[9].
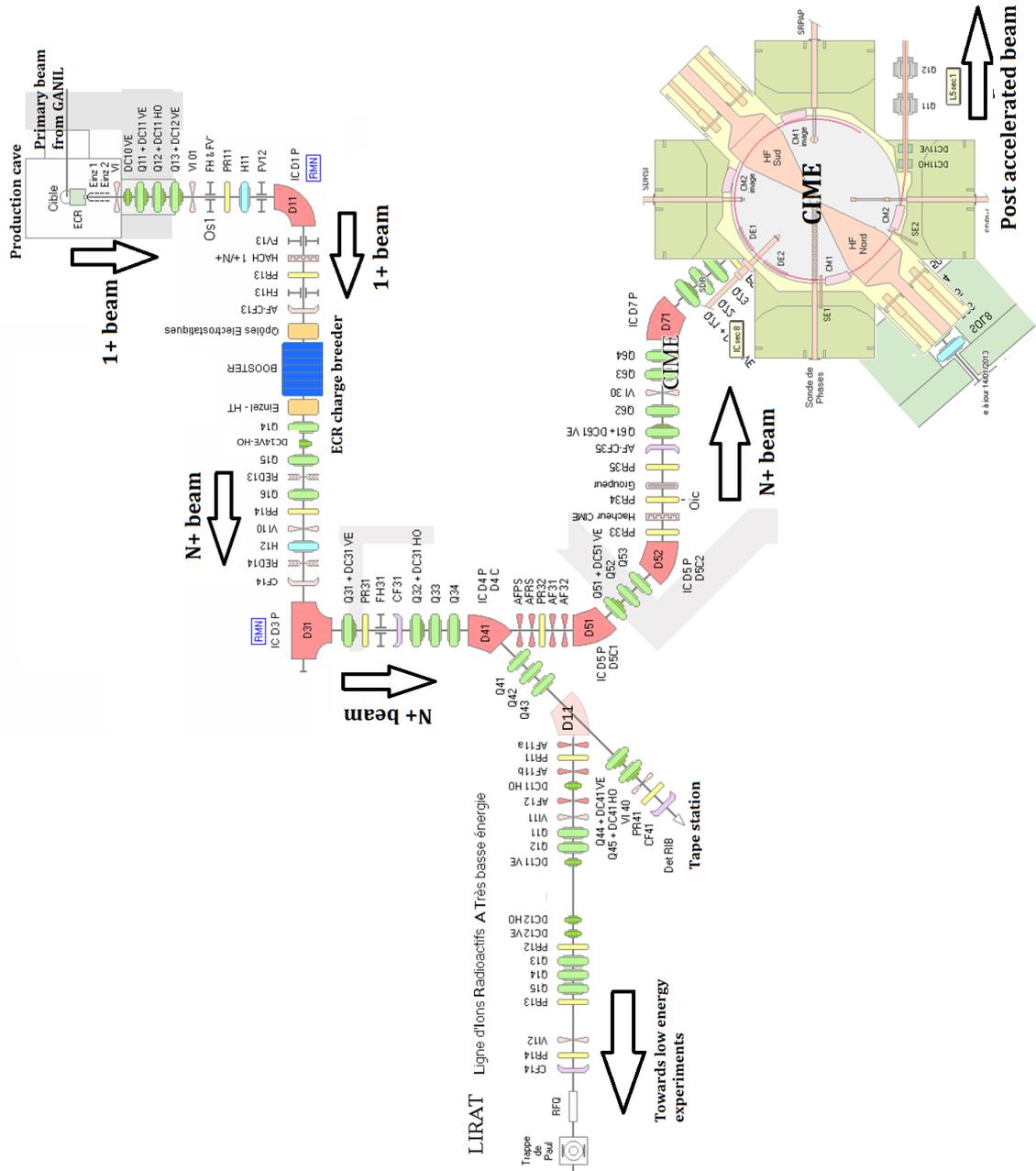
FIGURE 2.2: Layout of upgraded SPIRAL1 facility.

Since 2001, the facility has been delivering the radioactive ion beams of gaseous
elements at high intensity for the nuclear physics experiments [8]. In order to ex-
tend the research on exotic nuclei properties far from stability, an upgrade has been
undertaken at SPIRAL1 [2] to extend the range of post accelerated exotic beams as
well as to provide low energy (keV) radioactive beams to LIRAT and the future DE-
SIR (Désintégration, Excitation et Stockage d'Ions Radioactifs) experimental area.
A schematic of the upgraded SPIRAL1 facility is presented in figure 2.2. The pro-
duction cave was modified to accommodate new Target Ion Source System (TISS)

[2, 10] and also a ECR charge breeder in the Low Energy Beam Transport (LEBT) to increase the charge state of the radioactive ions from 1+ to N+ with the required injection characteristics of the post-accelerator (Cyclotron CIME). Following the upgrade, there is a possibility to produce stable and radioactive ion beams of gaseous, condensable and alkali earth elements using three kinds of ion sources [2], which are discussed in the section 2.2.

2.1 Charge breeding technique for post acceleration

The SPIRAL 1 upgrade project consisted in the implementation of 1+ / N+ method in order to permit the use of new TISSs for extending the range of condensable RIB elements for the nuclear physicists. In this context, a detailed study of charge breeding techniques was started within the European research and technical development program: EURISOL and EURONS [11]. These programs aimed at optimizing the existing charge breeding techniques and thereby designing the new generation of charge breeders in the view of unprecedented intensities expected for the next generation ISOL facilities [12]. In the following section, a short description of the three main charge breeding techniques is discussed.

Stripping technique

In this technique, the ion beam impinges on a foil, where they loose electrons due to the interaction with the matter and then ionized to higher charge states. The stripper can be a gaseous material [13] or a solid foil [14, 15]. This technique is routinely operated in a Tandem accelerators or superconducting LINAC. The only requirement is that the ion beam must be pre-accelerated up to 150 keV/u when using the solid foils and up to 25 keV/u in case of gaseous material. At GANIL, a carbon foil is used to strip ions between CSS 1 and CSS 2 cyclotrons [16]. The beam quality and the charge state distribution depend on the initial energy of the ion beam and the thickness of the foil. Several experiments were performed on various stripping materials [17, 18]. However, the main drawback of this technique is the pre-acceleration of ions in order to be efficient and the replacement of stripping foil which could add an additional cost [15, 19].

Electron Beam Ion Sources (EBIS) based charge breeder

The schematic figure 2.3 [20] shows the main elements of an EBIS [15]. This device mainly comprises of electron gun which produces an electron beam. EBIS consists of combination of a strong magnetic field created by a long solenoid (often a superconducting one) and an axial electrostatic potential generated by the electrodes to trap the ion beam. The electron beam interacts with the beam of ions and increases the charge state of the ions. In the final stage, the potential is lowered to extract the highly charged ions. This device is maintained under Ultra-High Vacuum (up to 10^{-11}). To achieve high charge breeding efficiencies, the electron beam should be in good alignment with axis of the magnetic field. This device requires a preparation stage where the single charged ion beam is cooled and bunched with a penning trap

[21] or a RFQ cooler buncher [22]. This technique allows a good mass separation of highly charged ions by maintaining low background level [23].
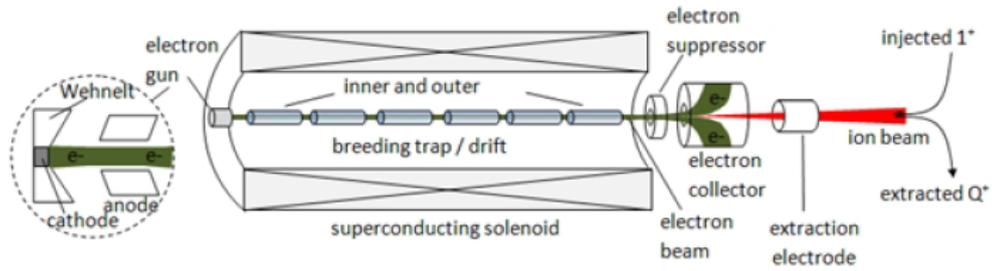
FIGURE 2.3: Schematic view of EBIS/T charge breeder

ECR-based charge breeder

The ECR ion source [24] is transformed in to charge breeder [15, 25] by modifying the injection part in order to accept the single charged ion beam as shown in the figure 2.4. The incoming 1+ ions are injected slowly into the charge breeder through a grounded tube. In this device, microwaves are used to ignite and sustain the plasma. The plasma electrons are confined inside the magnetic structure with a so-called *minimum-B configuration* created by the set of solenoids (axial confinement) and a hexapole (radial confinement). The cyclotron motion of the plasma electrons is excited resonantly by the RF and consequently gain energy and ionizes the rest gas by collisions with the atoms. An electrostatic potential is given to the plasma chamber to slow down the incident 1+ ions and extract the multi charged ions after the ionization. The injected ions are captured by the plasma ions and ionized to higher charge state by successive electron impact ionization.
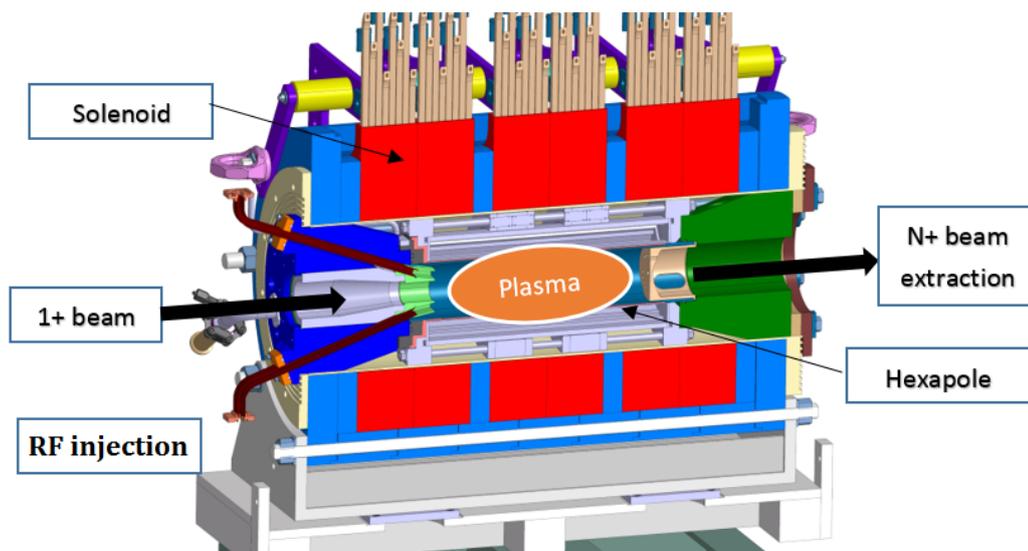
FIGURE 2.4: Schematic view of ECRIS based charge breeder

Among the two charge breeding techniques, EBIS has shown very good performance in terms of charge breeding efficiencies and times [22]. In case of ECR charge breeder, numerous tests of different chemical elements with different masses were studied and achieved promising results in terms of extracted high charge states. The status of research and development has promoted a few ISOL facilities to consider the ECR charge breeder as an injector for post-accelerator. Considering the advantage of the continuous mode of operation and resolving power of CIME [9, 26, 27] cyclotron, an ECRIS based charge breeder has been found suited for SPIRAL1 facility. In the framework of SPIRAL 1 upgrade [2, 10, 28], a PHOENIX type ECR charge breeder designed by LPSC [29] is already on-line and operational since 2016. The SPIRAL1 charge breeder (SP1 CB) has gone through several modifications [5] to improve its performance. The operational performance of the SP1 CB was validated at LPSC test bench [5] prior to its installation in the SPIRAL1 LEBT. The objective of this thesis is to validate the performance of this device in SPIRAL1 LEBT and thereby to study the fundamental processes involved in charge breeding.

2.2 Ion sources for stable and radioactive ion beam production

The different types of ion sources used in the upgraded SPIRAL1 production cave are explained in this section. Generally, an important parameter for an ion source to produce RIBs is the ionization efficiency. This parameter is variable depending on the type of ion source used and the selected chemical element that has to be ionized.

2.2.1 NANOGAN-III ECR ion source

The figure 2.5 shows the schematic view of NANOGAN-III plasma ion source [26, 30] coupled with the graphite target. This source was initially a 10 GHz ion source and later, it has been upgraded to 14 GHz. The magnetic field is provided by permanent magnets adapted for multi charged ion production. This source is mounted on a insulated support with a maximum extraction voltage of 34 kV. The electrons in the plasma are heated with a RF signal fed into the plasma chamber.

NANOGAN III has produced a number of stable and radioactive ion beams of gaseous elements (He, Ne, Kr, Ar, O, C and F) with total ionization efficiencies greater than 90% for different gases (Ar, Kr and Ne). The main drawback of NANOGAN III is due to the presence of cold transfer tube between the hot target and plasma cavity. It exhibits an advantage to make a chemical selection and also to eliminate the isobaric species that can condense on the tube before they enter into the plasma cavity. On the other hand, this becomes disadvantage for the production of condensable elements [10].

2.2.2 FEBIAD ion source

It has been suggested that the FEBIAD (Forced Electron Beam Induced Arc Discharge) ion source can be used to deliver a wide range of stable and radioactive
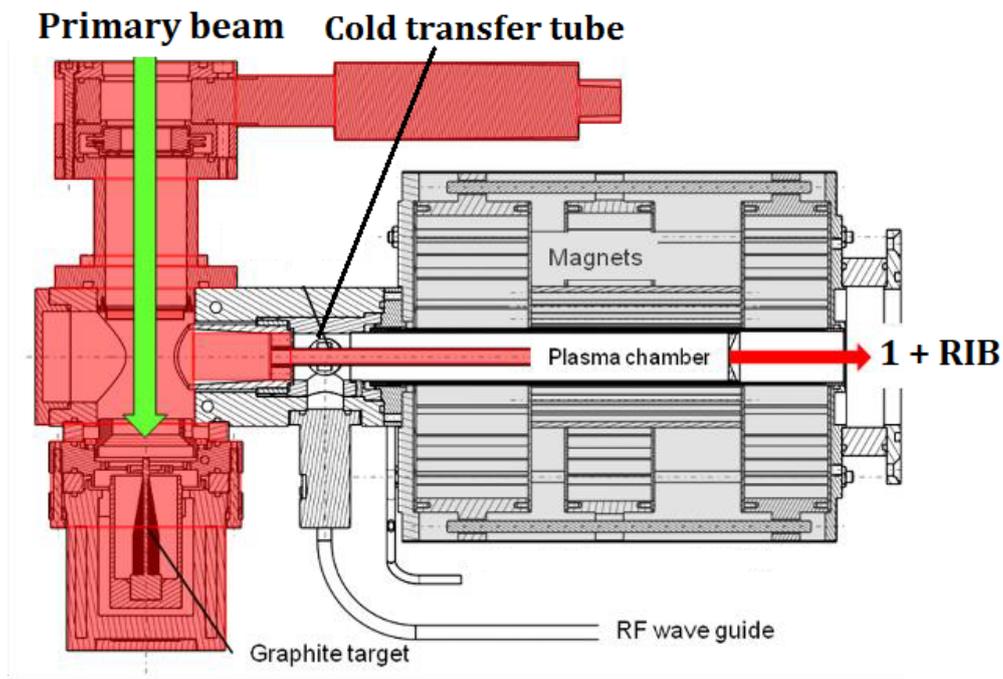
FIGURE 2.5: NANOGAN III ECR ion source coupled with the graphite target

condensable metallic elements. The radioactive isotopes from the target are effused to the anode via transfer tube and ionized in the anode cavity by an electron impact process[31, 32].
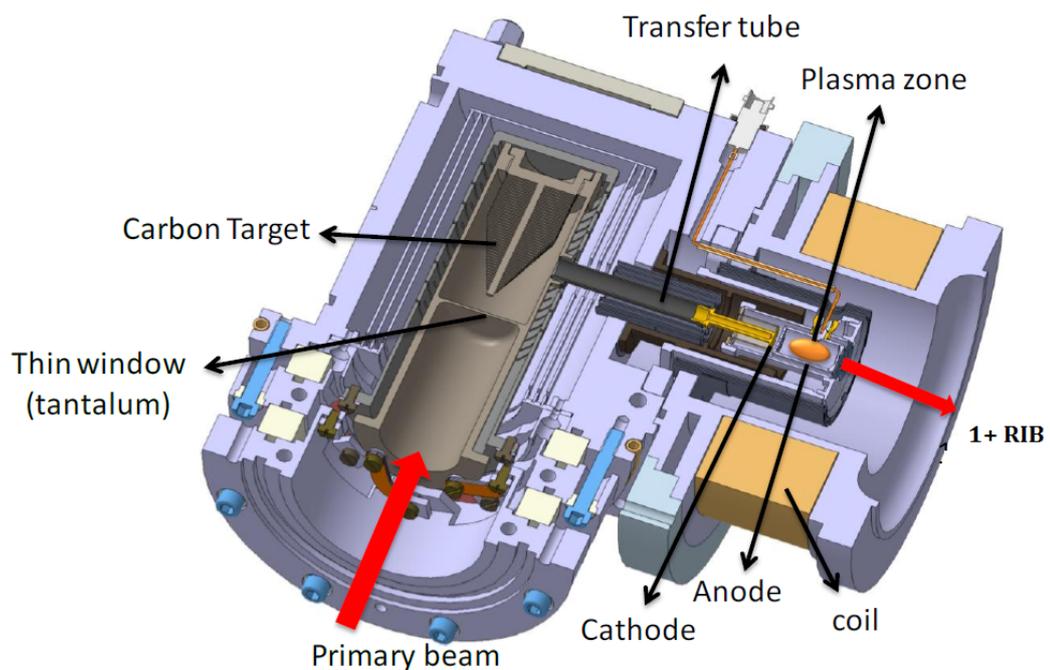
FIGURE 2.6: VADIS type FEBIAD ion source.

The figure 2.6 presents the FEBIAD ion source (the so called VADIS from ISOLDE) developed for SPIRAL1 facility at GANIL. This source works with a hot anode cavity which is placed after hot cathode in order to accelerate the ionizing electrons. A magnetic coil is placed around the ionization chamber in order to optimize the ionization process. The major advantage of this source is its small size that minimizes the delay time and allows an access to the wide range of condensable elements that has a shorter half life. Recently, this source has been installed in the production cave and a $^{38m}K/^{38}K$ radioactive ion beam has been successfully delivered to the physics experiment with the yields in the range of 2-4 $\times$ 10^6 pps at 9 MeV/A [33].

2.2.3 Thermionic ion source

This source was developed at GANIL in order to utilize during the commissioning of upgraded SPIRAL1 facility. The pellets from the Heat wave Labs [34] are installed in the source to produce singly-charged stable ion beams from alkali metals (K, Na, Li, Rb and Sr).
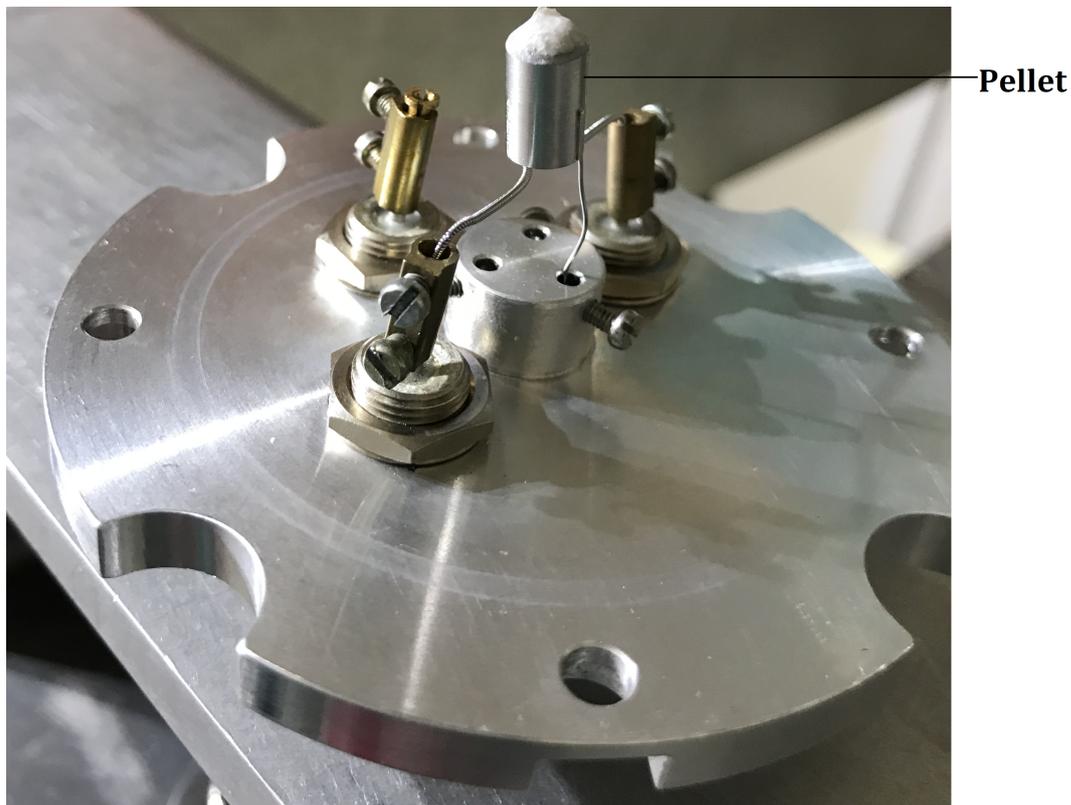
Pellet

FIGURE 2.7: Actual setup with a sodium pellet connected to the two terminals.

The figure 2.7 shows the pellet setup of the thermionic ion source. The sample in liquid form is deposited in the center of the pellet and dried usually in neutral atmosphere or in air. The doped sample in the center of the pellet is placed in the source and an electric current is passed through it. The pellet heats the sample to a high temperature in order to volatilize and ionize the element. Alkali elements with high ionization potential require high temperature. However, the evaporation rate

increases with increase in temperature and therefore decreases the sample lifetime. Unlike ionization potential, the work function is highly dependent on the properties of the sample (crystal structure, composition, grain size and texture). In fact, there are a few disadvantages of this source. The doped samples in the filament can behave erratically in the following cases: while changing the pellets during the measurements, the impurities in the sample could affect the ionization efficiency and the quality of doping. The source must be vented while changing the samples. During the measurements, this could take some time to get back the normal vacuum conditions. It has to be mentioned that the experimental activities presented in this thesis were performed with this source.
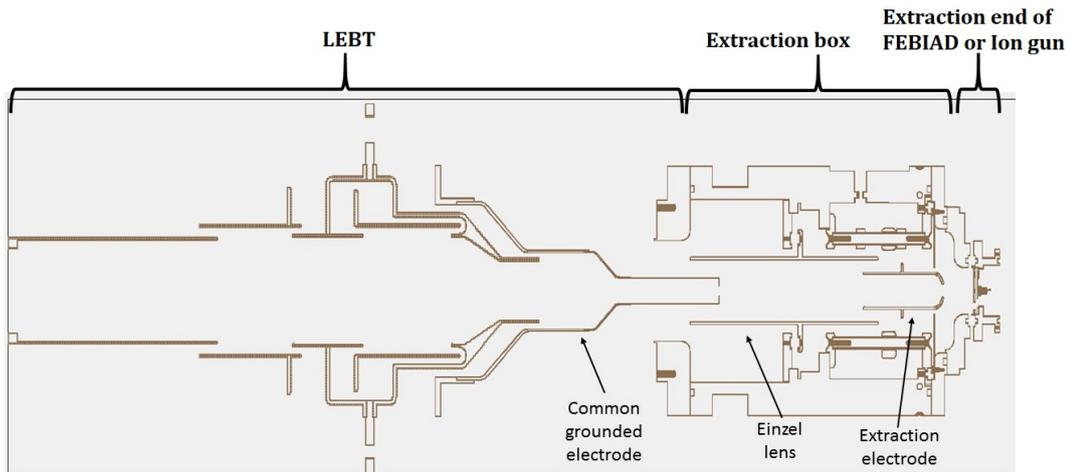
FIGURE 2.8: A cross section of the electrostatic extraction system connected between the extraction aperture of the TISS and the LEBT line.

The cross-section of the extraction box connected between the TISS and the low energy beam line is shown in the figure 2.8. Due to the compact size of the FEBIAD TISS and thermionic source, this extraction system has been designed to connect the extraction aperture of the FEBIAD or ion gun to the LEBT line. In case of NANOGAN III, the extraction box will be removed and the extraction aperture is directly connected to the LEBT line.

The extraction system consists of extraction electrode and einzel lens system. The puller is typically at the laboratory grounded potential. The potential difference between the ion source extraction and puller electrode provides the electric field for accelerating the charged particles forming an ion beam, whose kinetic energy is proportional to the voltage applied to the extraction electrode (KE = qV_0). The extraction voltage (V_0) applied to the ion sources is therefore set according to the required characteristics of the low energy beam line. The intensity of the extracted beam is defined in terms of the beam current I_{beam}, which in principle same as an electric current:

$$I_{beam} = \frac{qeN}{t} \tag{2.1}$$

where N is the number of ions, q is the extracted ion charge state and t the time. The energy profiles of 1+ beam from the FEBIAD and NANOGAN III sources are of high interest for the charge breeding performances. It has been mentioned that the energy acceptance of ECR charge breeders is typically from 5 to 10 eV FWHM for

condensable elements [10]. The energy dispersion of the FEBIAD and NANOGAN III sources has been measured [10] using a retarding field analyzing device developed by LPC Caen and found the value within the acceptance range measured with SP1 CB [5]. Since the charge breeding experiments presented in this thesis were performed with thermionic source, the energy dispersion (FWHM) has been measured with the retarding field analyzing device, which is estimated as ≈ 2 eV with the corresponding uncertainty on the order of $\pm\, 10\%$.

2.3 The concept of beam emittance

The quality of the beam is determined by the *beam emittance* and *brightness*. It can be understood as the product of beam size and the angle of propagation and thereby introducing an idea of the transportability of the beam. The importance of this concept comes from the Liouville's theorem [35]. Brightness relates the beam intensity to the emittance. In the accelerator community, the *normalized emittance* is particularly used when comparing different ion sources and accelerators that operate at different beam energies. These aspects will be discussed in more detail.

In the beam transport line, the ion beam travels through several ion optical elements. Let us consider a beam of particles moving in the same direction. The dynamic state of each individual particle, at any given instant of time, is defined by the three space coordinates (x, y, z) and three momentum coordinates (P_x, P_y, P_z). The six dimensional space spanned by the three spatial and momentum components are known as *phase space*:

$$f(x, y, z, p_x, p_y, p_z) \tag{2.2}$$

If z is the particle trajectory direction, then we can assume $p_z \gg p_x, p_y$. This is called *paraxial approximation*. While working with CW beams, the beam properties at given location z are of more interest than the longitudinal properties. Thus we limit the analysis to the transverse subspaces (x, p_x) and (y, p_y). Assuming the paraxial approximation, the transverse momenta can be replaced with the angles of the particle trajectories (x', y'):

$$x' = arctan\frac{p_x}{p_z} \approx \frac{p_x}{p_z} \qquad and \qquad y' = arctan\frac{p_y}{p_z} \approx \frac{p_y}{p_z} \tag{2.3}$$

Thus, the four dimensional distribution for transverse phase space can be expressed as

$$f(x, y, x', y') \tag{2.4}$$

Finally, the beam emittances (ϵ_x and ϵ_y) are determined based on the area occupied by the charged particles in the (x, x') and (y, y') phase space. In accelerators, some of the ion optical devices have an acceptance window within which they can operate. So, the size and shape of the beam envelope is a very important quality measure for ion beams. Smaller the emittance higher is the beam quality. Generally, the

emittance is expressed as phase space area (A) of the two dimensional projections divided by π, which can be written as:

$$\epsilon_x = \frac{A_{xx'}}{\pi} \qquad [\pi.mm.mrad] \tag{2.5}$$

This emittance is given in units of π.mm.mrad or π.m.rad. The one of the limitation of this approach is in the beam evaluation with strong distortion in phase space. The strongly distorted beam can have small emittance (small area), but cannot be matched to the acceptance of a few ion optics elements in the beam transport system. Therefore, there are several different approaches to amend this problem, which can be sorted out in two different cases [36, 37]. In the first case, the emittance is determined based on the area of an ellipse encompassing the phase space pattern. In this case, the ellipse is chosen as it observed to be the contours of 2D Gaussian distribution. The definition of the emittance is similar to equation 2.5, but the integration is performed over the area of an ellipse. With this definition, the true beam quality can be better evaluated. On the other hand, the drawback of this approach is the possibility of overestimation of the emittance (if the pattern exhibits strong distortions with low particle density or in the case of low intensity beam halos). These aspects are considered in the second case, where emittance is determined statistically. It is defined as the variance of the distribution of the particles $g(x, x')$ which form the ion beam and can be written as

$$\epsilon_{xrms} = \sqrt{\langle x^2 \rangle \langle x'^2 \rangle - \langle xx' \rangle^2} \qquad [\pi.mm.mrad] \tag{2.6}$$

with the expectation values

$$\langle x^2 \rangle = \frac{\sum x^2 g(x, x')}{\sum g(x, x')} \qquad \langle x'^2 \rangle = \frac{\sum x'^2 g(x, x')}{\sum g(x, x')} \qquad \langle xx' \rangle^2 = \frac{\sum xx' g(x, x')}{\sum g(x, x')} \tag{2.7}$$

where $g(x,x')$ is the Gaussian distribution of particles in phase space. The rms-emittance value is related with the contour of an ellipse in the phase space. The equation of ellipse in phase space (x, x') can be written as

$$\gamma x^2 + 2\alpha xx' + \beta x'^2 = \epsilon \tag{2.8}$$

and the constraint

$$\beta\gamma - \alpha^2 = 1 \tag{2.9}$$

where α, β and γ are known as Twiss parameters. The relation between the Twiss parameters and emittance important characteristic values [38] are shown in the figure 2.9.

The collective trends of particle movement at the given location z can be estimated using the orientation of the above given phase space pattern. This is demonstrated in the figure 2.10.
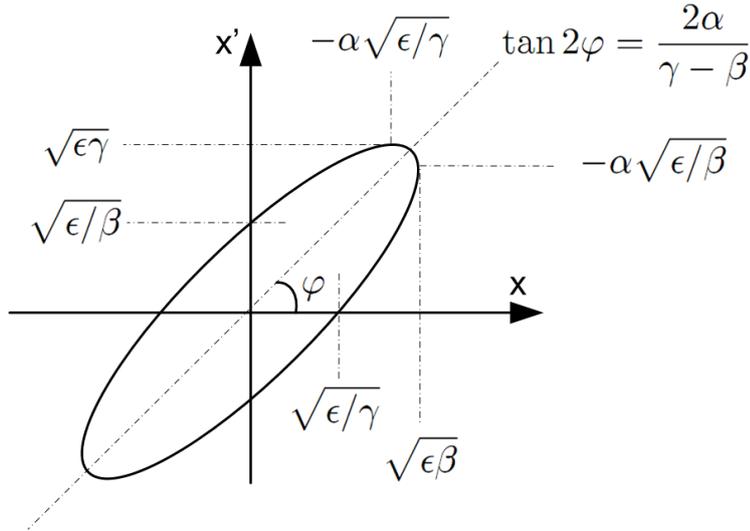
FIGURE 2.9: Phase space ellipse properties with Twiss properties
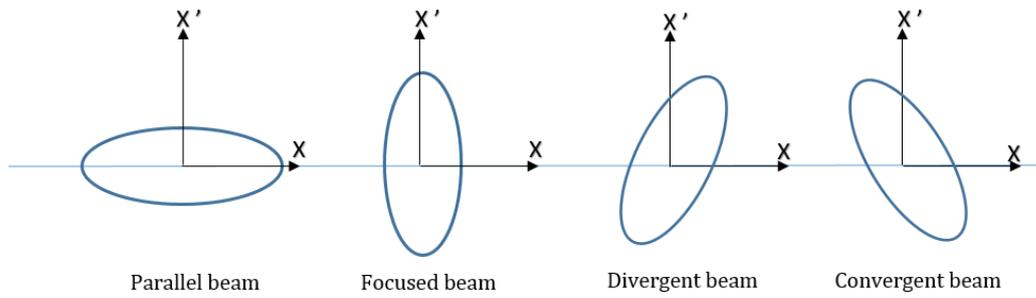
FIGURE 2.10: Orientation of transverse phase space ellipse. The axis coordinate x' represents the beam divergence angle expressed in *mrad* and x is transverse beam size in *mm*

Based on this orientation it can be determined whether the beam is *diverging* ($\alpha >$ 0) or *converging* ($\alpha < 0$). For $\alpha = 0$, the beam size has minimum (waist) or maximum (anti-waist). The Twiss parameters can also be defined statistically from the distribution $g(x,x')$ with the relations 2.8 and 2.9:

$$\alpha = -\frac{\langle xx' \rangle}{\epsilon} \qquad \beta = \frac{\langle x^2 \rangle}{\epsilon} \qquad \gamma = \frac{\langle x'^2 \rangle}{\epsilon} \qquad (2.10)$$

Following Lapostolle we define the effective rms-emittance as

$$\epsilon_{rms} = 4 \cdot \sqrt{\langle x^2 \rangle \langle x'^2 \rangle - \langle xx' \rangle^2} \qquad (2.11)$$

Because an ellipse with area 4 times the area of the rms emittance fully encompasses the Kapchinsky-Vladimirsky (KV) distribution. The so called 4-rms emittance is often used as the the quoted number instead of 1-rms emittance. The Gaussian distribution is infinite in size, the 1-rms ellipse contains 39% of the beam, the 4-rms ellipse contains 86% of the beam and the 6-rms ellipse contains 95% of the beam. Finally, a

new term called *normalized emittance* is introduced to compare emittances of beams with different energies (i.e. different extraction voltages). In fact, the beam emittance is altered at different ion beam energies. If an ion beam gains higher energy, the longitudinal momentum of the particles increase, while the transverse momentum remains unchanged. This leads to reduction in angles, as is seen from equation 2.3 and consequently reduction in emittance. Therefore, the normalized emittance can be written by multiplying the geometrical emittance with relativistic factors β and γ (different from Twiss parameters):

$$\epsilon_{norm} = \beta\gamma\epsilon \tag{2.12}$$

where the relativistic factors

$$\beta = \frac{v}{c} \qquad and \qquad \gamma = \sqrt{\frac{1}{1-\beta^2}} \tag{2.13}$$

According to the Liouville's theorem, the normalized emittance ϵ_{norm} is invariant for all energies as long as the beam transport is linear.

2.4   Low energy beam transport

In SPIRAL1 facility, the goal of the Low Energy Beam Transport (LEBT) is to transport the ion beam to the next acceleration section, which includes the CIME cyclotron (see figure 2.2) and transported to the experimental areas. The LEBT system consists of focusing elements and field free regions (drifts) between the ion Source and the CIME cyclotron. In order to achieve a high quality beam transport, a detailed understanding of the beam requirements at the end of the LEBT system and the beam characteristics at the beginning of the line are crucial. Generally, different beam transport configurations can be utilized to achieve the same beam characteristics. However, the LEBT system design always represents a compromise between the complexity, ease of operation, flexibility and cost.

It is very important to understand the two aspects of the charged particle dynamics in order to optimize the performance of the charged particle transport in the low energy beam line. The first one is the collective effects caused by the electric and magnetic fields generated by the beam itself and the second one is the single-particle dynamics in external electric and/or magnetic fields. Going into the details on the collective effects would go far beyond the scope of this thesis. Therefore, I will concentrate on the basics of the single-particle dynamics in external fields and the ion optical elements in the beam transport line.

2.4.1   Motion of charged particle in electromagnetic fields

Particle accelerators use arrays of external electromagnetic forces to guide and accelerate the ion beam. The dynamics under these fields can be explained using Lorentz equation that includes magnetic and electric fields. Consider a particle with an elementary charge q moving with velocity v under the influence of an electromagnetic

field. The moving particle is subjected to the Lorentz force **F** which is given as

$$\frac{dp}{dt} = F = q(E + v \times B) \tag{2.14}$$

with p the momentum of the charged particle, **E** is the electric field and **B** is the magnetic field. We can deduce the applied work by this force with the energy theorem to obtain:

$$\Delta W = \int F \cdot dr = \int q(E + v \times B) \cdot dr \tag{2.15}$$

$$= q \int E \cdot dr + q \int (v \times B) \cdot dr \tag{2.16}$$

It is clear that always (v × B) · dr = 0. As a result we reach the conclusion that the electric field is used to change the kinetic energy of a particle and the magnetic fields are used to guide and focus the beam particles. It is important to mention that the acceleration occurs along the direction of the electric field and the energy gained by the particle is independent of its speed.

2.4.2 Ion optical elements in SPIRAL1 LEBT

Generally, the beam lines at the accelerator facilities are not straight and they either follow several deviations or have to split in different sections. So, there are a set of common beam line optical elements such as einzel, dipole, steerer, quadrupole and hexapole lenses. A short introduction to each of these elements is given in the following.

Einzel lens

The device is equiped with three electrodes as shown in the figure 2.11. The geometry of einzel lens system is normally cylindrical symmetric.
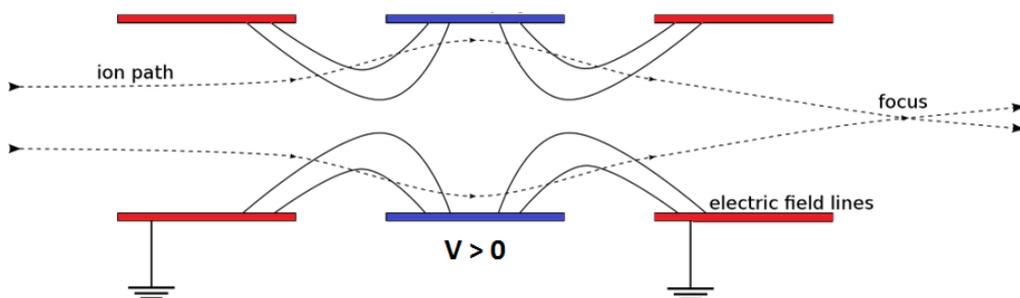
FIGURE 2.11: Principle of einzel lens. Reproduced from [39]

The first and last electrodes are maintained at same voltage V_0 and middle electrode

is held at different voltage V_e. The voltage difference between these electrodes define the focal length [40]. The relationship between these parameters is shown in the equation 2.17

$$\frac{1}{f_e} = \frac{V_e - V_0}{4LV_eV_0} \qquad (2.17)$$

Where L is the distance between electrodes. Due to voltage difference between the electrodes, a strong focusing of the ions is maintained without changing their kinetic energy. The voltage of the middle electrode can be higher or lower and its polarity is determined by the beam charge and the properties required after the einzel lens.

Magnetic dipole as a mass analyzers

At ISOL facilities, magnetic mass separators are crucial devices. They are based on the bending of the trajectory of ion in a magnetic field perpendicular to the direction of the ion motion. From equation 2.14, the force F perpendicular to the velocity of the ion, in the absence of electric field, becomes
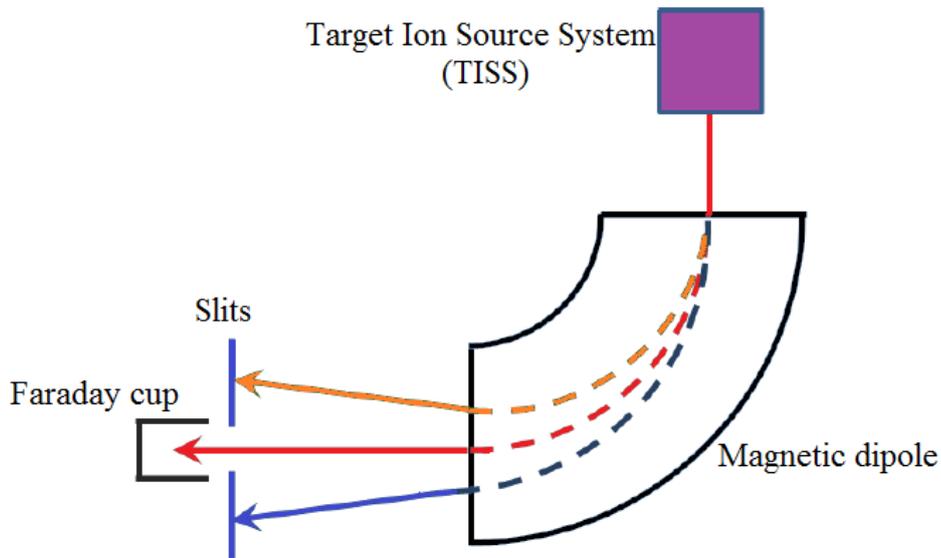
FIGURE 2.12: The principle of mass analyzer

$$F = evB \qquad (2.18)$$

The magnetic dipole is constructed from coil winding creating a constant magnetic field pointing in the transverse direction. Consider a beam of charged particles moving in the horizontal plane and bent onto a curved trajectory during its traversal through a magnetic dipole field as shown in the figure 2.12. The charged particles in the magnetic field follow circular trajectories with radius

$$\rho \approx \frac{mv_z}{Bq} \tag{2.19}$$

where B is the magnetic field strength inside the device, v is the particle velocity, m is the particle mass and q is the ion charge state. For different masses, the radius of the trajectory differs. The mechanical geometry of the separator and the quality of ion beam traversing through the device will finally determine the quality of the separation. In order to express this feature, the so-called *resolution R* [9] is used, which is defined as:

$$R = \frac{C_d}{4\Delta x} \tag{2.20}$$

Where C_d is the transverse dispersion coefficient (in meters) and Δx is the width of the ion beam. If the dispersion coefficients in angle and position are zero at the spectrometer object point, then C_d becomes 4ρ at the image point [9]. In LEBT line, the spectrometer installed in the 1+ line constitutes a maximal magnetic rigidity (Bρ = 0.22 T.m). By assuming the emittance of NANOGAN III ECRIS as 80π.mm.mrad (at 20 keV), with angular disperison of 26 mrad, Δx = 3 mm, the resolution of the spectrometer is 147.

Electrostatic and magnetic quadrupoles

Electrostatic and magnetic quadrupoles are often used as focusing elements in LEBT. In SPIRAL1 LEBT, the ion beam is focused and transported along the beam lines without losses by using electrostatic quadrupoles. These devices are equipped with four hyperbolic electrodes installed symmetrically around the beam axis. The electric field generated by these devices focuses the ion beam in one of the transverse planes whilst defocusing in the other one. The figure 2.13 shows the quadrupole electric field created using two pairs of hyperbolic electrodes of different polarities. The potential in such configuration is given by [41]:

$$V = \frac{x^2 - y^2}{a^2} V, \tag{2.21}$$

where x and y are the transverse directions along horizontal and vertical plane and a is the half aperture of the quadrupole. The electrostatic field created by the potentials is given by

$$\vec{E} = -\frac{2V}{a^2}x\hat{x} + \frac{2V}{a^2}y\hat{y}, \tag{2.22}$$

In some cases, the combination of quadrupole lenses which are called as doublets and triplets are used in LEBT. In the case of SPIRAL1 LEBT, a quadrupole triplet is used before the ECR charge breeder. The installed triplet consists of three quadrupole lenses arranged in series. The main purpose of the triplet is to focus the ion beam (minimizing the angular divergence of the beam), i.e. to transport the beam as parallel as possible towards the ECR charge breeder. During the optimization in LEBT, the
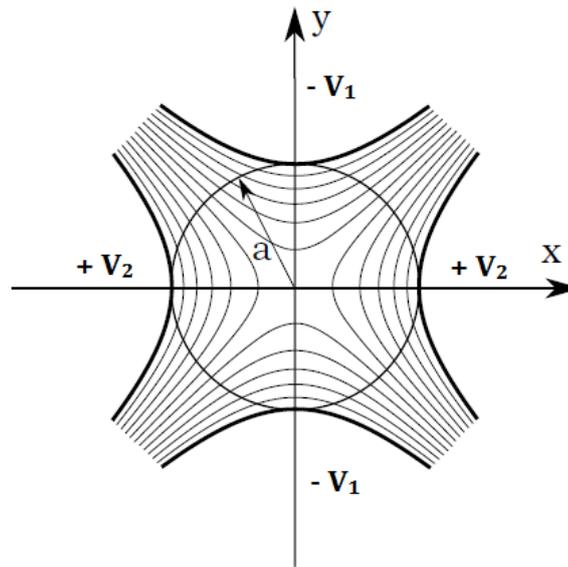
FIGURE 2.13: Electrostatic quadrupole with *a* being the distance from the optical axis to the electrode tip. The equipotential lines are drawn between positive and negative potentials.

last quadrupole of the triplet is operated as a steerer where the 4 electrodes are biased independently. This will not disturb the field distribution inside the quadrupoles which means that the alignment of the ion beam orbit can be adjusted independently.
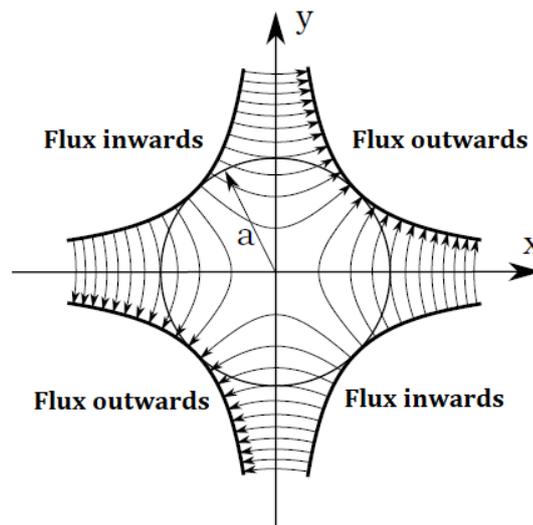
FIGURE 2.14: Magnetic quadrupole with *a* being the distance from the optical axis to the electrode tip. The field lines are drawn between the poles.

The magnetic quadrupole has a similar geometry to the electrostatic one. The magnet poles are made to be hyperbolic and arranged is such a way that opposite poles have magnetic flux towards the beam and the other two poles have flux outwards.

The orientation of the magnetic poles are assumed as shown in figure 2.14, then the magnetic filed in such system [41] is

$$\vec{B} = \frac{B_T}{a} y \hat{x} + \frac{B_T}{a} x \hat{y}, \tag{2.23}$$

where B_T is the density of the magnetic field at the pole tip. The charge particles (positive ions) transversing with a velocity v feel a $\vec{F}$:

$$\vec{F} = q B_T v \left(\frac{-x\hat{x} + y\hat{y}}{a} \right) \tag{2.24}$$

which is focusing in x-direction ad defocusing in y-direction. The main purpose is to try to transport the beam as parallel as possible. Therefore, using the combination of focusing and defocusing elements can improve the beam transport.

Fields with more than 4 poles are normally used to correct the distortions on the ion beam motion created by the non-ideal or quadrupole fields. In the case of SPIRAL1 LEBT, hexapole corrects the aberrations of field errors (x^2) and for octupoles (x^3).

2.5 Beam preparation for physics experiments

Following the SPIRAL1 upgrade, the LEBT line (see figure 2.2), incorporating the SP1 CB, is now available to operate in two operation modes: with the SP1 CB **ON** and with the SP1 CB **OFF**. The first operation mode is used to transport the extracted 1+ stable and/or radioactive ions, from the TISSs installed in the production cave, into the charge breeder for the subsequent formation and extraction of highly charged ions for the post-acceleration in CIME. The scheme of this mode is illustrated in the figure 2.15.
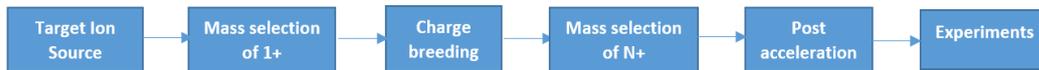
FIGURE 2.15: The scheme of the first operation mode.

The second operation mode is used to transport the extracted 1+ stable and/or radioactive ions from the TISS installed in the production cave directly to the low energy experimental areas (LIRAT and DESIR) or either sent towards a tape station for identification. The scheme of this mode is illustrated in the figure 2.16. The challenging part of this mode comes from the permanent installation of SP1 CB in the beam line, where a strong focusing of 1+ ions is required in order to transport them through the extraction system (plasma electrode of 6mm diameter and the einzel lens) of the SP1 CB.

The concepts introduced in this chapter give useful information to properly set the area of interest of this thesis. The concept of ion beam motion and the beam emittance is crucial to understand the topics discussed along this thesis work. Because of the high acceptance (in terms of intensity and injected beam emittance), the ECRIS

| Target Ion Source | → | Mass selection of 1+ | → | Transport through charge breeder | → | Low energy Experiments |

FIGURE 2.16: The scheme of the second operation mode.

based charge breeder (ECR-CB) was chosen for SPIRAL1. The fundamental physics processes and principle of ECRIS (ECR-CB) for the production of high charge states are discussed in the following chapter.

3 Fundamental aspects of plasma physics for the production of highly charged ions using ECRIS

3.1 Introduction

In this chapter, the physical processes for the production of highly charged ions in Electron Cyclotron Resonance Ion Source (ECRIS) and ECRIS based charge breeders (ECRIS-CB) are discussed. They were originally developed in 1970's by getting information from fusion research. In order to understand the performance of ECR ion source, several plasma processes has to be taken into consideration. Therefore, a review of the most important fundamental aspects of plasma physics will be disussed below.

3.2 Fundamentals aspects of plasma

Irving Langmuir described the word *plasma*, as a collection of ions, electrons and neutrals. Nowadays, Human made plasma is used in a large variety of applications like metal working, manufacturing electronic devices like semiconductors, fusion technology etc. In most of the existing ion sources, the extracted beam which consists of charged particles are created in plasma. Therefore, the properties of the plasma have an effect on the properties of the extracted beam.

3.2.1 Degree of ionization of an ECR plasma

The degree of ionization of plasma is the ratio between the number of positive ions and the total number of ions and neutrals. It is expressed by

$$\eta = \frac{n_i}{n_i + n_n} \tag{3.1}$$

Where n_i is the ion density and n_n is the neutral density. The degree of ionization for standard ion sources sustained in low-pressure discharges is typically 10^{-6} to 10^{-3}. But, if the discharge is assisted by an external magnetic field (in ECRIS plasmas), the degree of ionization can reach values of 10^{-1} or higher. The higher the ionization degree, the lower the pressure required to sustain the discharge.

3.2.2 Plasma temperatures (T_e, T_i)

In a plasma, the electrons and ions follow Maxwellian distribution (in first approximation), independent of each other, with their characteristic temperature T_e and T_i, respectively. The velocity distribution function f(v_e) of electrons is given by

$$f(v_e) = n_e \left(\frac{m_e}{2\pi k T_e} \right)^{3/2} \exp \left(- \frac{m_e v_e^2}{2k T_e} \right) \tag{3.2}$$

where v_e is the particle velocity components, n_e is the particle density, m_e is the mass of the particle, k is the Boltzmann constant, kT_e is the electron temperature. Likewise, the velocity distribution function of ions f(v_i) is given by

$$f(v_i) = n_i \left(\frac{m_i}{2\pi k T_i} \right)^{3/2} \exp \left(- \frac{m_i v_i^2}{2k T_i} \right) \tag{3.3}$$

By integrating the expressions 3.2 and 3.3, we find the average velocity of electron and ion as

$$\langle v_e \rangle = \sqrt{\frac{8kT}{\pi m_e}} \qquad \langle v_i \rangle = \sqrt{\frac{8kT}{\pi m_i}} \tag{3.4}$$

The mean kinetic energy of electron and ion as

$$E_e = \frac{3}{2} k T_e \qquad E_i = \frac{3}{2} k T_i \tag{3.5}$$

Table 3.1 and 3.2 shows the average velocity of electron and ion (A =1) calculated for selected electron and ion temperatures.

TABLE 3.1: The average velocity of electrons for selected electron temperatures

Electron temperature (kT_e)	$\langle v_e \rangle$
10 eV	2118726 m/s
1 keV	21187260 m/s
5 keV	47376154 m/s
10 keV	67000000 m/s

Because of their lower mass, the electrons are faster than the ions for a given temperature. Under typical ECR ion source plasma conditions, the electrons, different ion species and neutral particles interact with each other at different collision rates and therefore all the particles have their own unique velocity distributions. Typically, the velocities of each particle species are described by Maxwellian distributions and temperatures.

TABLE 3.2: The average velocity of ions (atomic mass = 1) for selected ion temperatures

Ion temperature (kT_i)	$\langle v_i \rangle$
0.1 eV	4964 m/s
0.5 eV	11101 m/s
1 eV	15700 m/s
5 eV	35106 m/s

3.3 Criteria for the definition of a plasma

Plasma can have internal charge distributions and their properties are governed by electromagnetic interactions. The criteria to define plasma are: the Debye length should be largely smaller than the size of plasma, the number of electrons inside the Debye sphere should be large, and the average electron- neutral collision frequency must be smaller than the plasma frequency.

3.3.1 Macroscopic neutrality

The positive and negative charged particles are created when a neutral gas is ionized and hence gives the condition of quasi-neutrality

$$\sum_i Q_i n_i - n_e = 0 \tag{3.6}$$

Where Q_i is the charge state of ion species, n_i is the density of ion species and n_e is the electron density. This means that the neutrality condition is fulfilled over macroscopic distances. Without macroscopic neutrality a plasma temperature of millions of degrees of Kelvin would be required in order to balance the electric potential and thermal potential energies [42].

3.3.2 Debye length

One of the most important physical parameter for the description of plasma is Debye length. If an electric field is created in plasma, charged particles quickly rearrange themselves in such a way as to effectively shield the electric field within in a specific distance. In other words, the charged particles try to counteract the effect of electric fields. Especially, electrons (due to their high mobility) respond faster to reduce the local electric fields. The response of these charged particles to counteract the effect of local electric fields is called Debye Shielding. Let us assume that an electrically conducting surface is immersed in plasma that is initially quasi-neutral. If a charged particle, that has a positive electric charge q, is introduced in plasma, the shielded potential created by the charge is commonly known as Debye potential:

$$\phi(r) = \frac{q}{4\pi\epsilon_0 d} \exp\left(-\frac{\sqrt{2}d}{\lambda_D}\right) \tag{3.7}$$

where ϵ_0 is the permittivity constant ($\approx$ 8.854.10-12 F/m), and d is the distance from the charge. The factor λ_D in the equation 3.7 is called the Debye length:

$$\lambda_D = \sqrt{\frac{\epsilon_0 kT}{n_e e^2}} \tag{3.8}$$

where k is the Boltzmann constant ($\approx$ 1.38 $\times$ 10^{-23} J/K), T_e is the electron temperature (Kelvin), n_e is the electron density and e is the elementary charge ($\approx$ 1.602$\times$ 10^{-19} C). For an example, the λ_D for electrons using typical values of ECR plasma (electron density $n_e = 10^{12}$ cm^{-3} and kT_e = 10 eV) is about 23.5 μm. To consider ionized gas as plasma, the characteristic dimension L of plasma must exceed the Debye length. This condition is the first plasma criterion

$$L \gg \lambda_D \tag{3.9}$$

Another parameter, which is related to the Debye length, is the number of particles N_D in a Debye sphere. The Debye length is derived by assuming a significant number of electrons inside the Debye sphere, whose number is given by [42]:

$$N_D = \frac{4}{3}\pi\lambda_D^3 n_e = \frac{4}{3}\pi \left(\frac{\epsilon_0 kT_e}{n_e^{1/3} e^2} \right)^{3/2} \tag{3.10}$$

In order to fulfil the collective behaviour of charged particles in plasma, the number of electrons in the sphere must be large. Thus, a second criterion for achieving plasma behaviour can be stated as

$$n_e \lambda_D \gg 1 \tag{3.11}$$

Therefore, it is necessary that the Debye length must be smaller than the size of plasma and much larger than the average distance between the electrons in the system.

3.3.3 Plasma frequency

In a plasma, an electric field is generated when it is disturbed by changing locally space charge neutrality. Because of the significant difference in masses between the electrons and ions, the mobility of electrons in plasma is relatively higher than ions and reacts quickly to the electric field. As a result, they oscillate about the ions due to the electric force between ions and electrons. The harmonic oscillation of electrons is given by

$$\omega_{pe} = \sqrt{\frac{e^2 n_e}{\epsilon_0 m_e}} \tag{3.12}$$

where e is the elementary charge, n_e is the electron density, ϵ_0 is the vacuum permittivity and m_e is the electron mass. The plasma electron frequency can be written as

$$f_{pe} = \frac{\omega_{pe}}{2\pi} \tag{3.13}$$

$$f_{pe} = 8.97\sqrt{n_e} \tag{3.14}$$

If we consider the electron density in a Helium plasma is $n_e = 10^{12}\ cm^{-3}$, the plasma frequency is ≈ 8.97 GHz. Similarly, the ions being massive also oscillate at a very low frequency which is given by

$$\omega_{pi} = \sqrt{\frac{q_i^2 n_i}{\epsilon_0 m_i}} \tag{3.15}$$

where q_i, n_i and m_i are respectively the ion charge, ion density and the mass of an ion. If we consider the electron and ion density in Helium plasma (q = 1) is $n_e = n_i = 10^{12}\ cm^{-3}$ (assuming quasi-neutrality), the plasma ion frequency is ≈ 105 MHz We can observe that the plasma electron frequency is in GHz range and plasma ion frequency is in MHz range. For propagation of an electromagnetic radiation in plasma, the plasma refractive index is given by

$$n = \left[1 - \frac{\omega_{pe}^2}{\omega_{rf}}\right]^{1/2} \tag{3.16}$$

Where ω_{rf} is the frequency of the electromagnetic radiation. An electromagnetic wave will propagate in plasma if only $\omega_{pe} < \omega_{rf}$. Beyond this frequency, the plasma becomes opaque. This frequency is known as cut-off frequency and the corresponding density is called cut-off density (n_e). For a 14.5 GHz SP1 ECR charge breeder, the cut-off density is $\approx 2.63 \times 10^{12}\ cm^{-3}$. In order to exhibit the collective behaviour of plasma, the electron and neutral collision frequency (ν_{en}) must be less than the plasma oscillation frequency (ν_{pe}), i.e.,

$$\nu_{pe} \gg \nu_{en} \tag{3.17}$$

If the above condition is not satisfied, then dynamics of the system is dominated by the motion of neutrals. This condition is fulfilled when the degree of ionization of the plasma increases.

3.4 Collisions in plasma

In this section, an important mechanism of collisions and physics processes, responsible for the charge breeding process in ECR plasma is presented. Electrons and ions experience the collision process while the mechanism for neutral – neutral and

charge - neutral collisions are different. In fully ionized plasma, charge particle experience the Coulomb force followed by the collisions. Collisions in plasma can be divided into weakly ionized and fully ionized plasmas. When the plasma is not dominated by the Coulomb collisions, i.e. $\nu_{ei} < \nu_{en}$, then it is said to be weakly ionized. The term fully ionized plasma is said when it is in a collisional regime, i.e. $\nu_{ei} > \nu_{en}$.

3.4.1 Collisions between charged particles and neutrals

The most dominant interactions are charged - neutrals and neutral-neutral collisions. If the collisions are elastic, the total kinetic energy of particle is conserved and drives them towards thermal equilibrium. If the collisions are inelastic, the processes drive the particles towards excitation or ionization. The collision frequency between charged particles and neutrals can be expressed as

$$\langle \nu_{ne} \rangle = n_n \sigma_{ne} \langle v_e \rangle \tag{3.18}$$

Where σ_{ne} is the collision cross-section between neutrals and charged particles (e.g. electrons), n_n is the neutral density and $\langle v_e \rangle$ is the average velocity of the charge particle. For a typical Helium plasma, the total cross section for electron-Helium atom collision processes is $\approx 5.5 \times 10^{-20}\ m^2$ (for T_e = 1.5 eV) [43]. Then the average collision frequency of a charged particle and neutrals gives 0.9 kHz.

3.4.2 Collisions between charge particles (e → i, e → e and i → i)

Because of the long range Coulomb force acting between the charged particles, the elastic scattering cross section is much higher. These long range distant collisions represents small angle deflections of single particle with many other particles such that the cumulative effect turns out to give a large angle scattering, which could be about 90°. To compare the electron-ion collision cross section to a charged-neutral cross section, a cross-section formula has been derived for the cumulative collision process [44], which is given by

$$\sigma_{ei} = \frac{q^2 e^4 \ln \Lambda}{4\pi \epsilon m_e^2 v^4} \tag{3.19}$$

The average electron-ion collision frequency can be approximated by assuming the Maxwell-Boltzmann distribution for the electrons:

$$\langle \nu_{ei} \rangle = \frac{1}{\tau_{ei}} \simeq \frac{\sqrt{2} n_i q^2 e^4 \ln \Lambda}{12\pi^{3/2} \epsilon_0^2 \sqrt{m_e} (KT_e)^{3/2}} \tag{3.20}$$

where n_i is the ion density, e is the elementary charge, m_e is the mass of electron, ϵ_0 is the permittivity of vacuum, T_e is the electron temperature, $\ln\Lambda$ is the Coulomb logarithm and the estimated value for laboratory plasmas is $\ln\Lambda \approx 10$ and q is the ion charge state. Along with the electron-ion collisions, the interactions between

electron-electron and ion-ion take place in plasma. The collision frequencies for these processes are approximated [44] as

$$\langle \nu_{ee} \rangle = \frac{1}{\tau_{ee}} \simeq \frac{\langle v_{ei} \rangle}{n_i q^2 / n_e} \tag{3.21}$$

$$\langle \nu_{ij} \rangle = \frac{1}{\tau_{ii}} \simeq \frac{n_i q^4 e^4 \ln \Lambda}{12 \pi^{3/2} \epsilon_0^2 \sqrt{M} T_i^{3/2}} \tag{3.22}$$

where, A_i is the mass number of the ion i for which the collision frequency is determined, while $\sum_j A_j$ are the masses of the ions species j making up the plasma. The term $\sum_q n_j^q q^2 \approx n_e q_{eff}$ is the given approximate plasma quasi neutrality. In ECR plasmas, the ion behaviour differs significantly from the electrons behaviour. Due to their heavier mass, they move slowly and experience many collisions with each other. The ion temperature in the equation 3.22 is in eV and electron density n_e in cm^{-3}. As an example, we consider a typical Oxygen plasma in a 14.5 GHz ECRIS SP1 charge breeder with T_i =1 eV, T_e = 1 keV and $n_e \approx n_i \approx 10^{11}$ cm^{-3}, mean plasma effective ion charge $q_{eff} \approx 5$, assuming $\ln\Lambda$ = 10; the average collision frequencies given in the equations 3.21, 3.20 and 3.22 can be estimated as

$$\langle v_{ee} \rangle \approx 92 \; Hz \quad \langle v_{ii} \rangle \approx 7.5 \; MHz \quad \langle v_{ei} \rangle \approx 2.3 \; KHz \tag{3.23}$$

From the numerical example, it is clear that the ion - ion collision frequencies are more frequent than other types of collisions. This is due to their strong dependence of the ion temperature. As the ion temperature increases, the collisions become less frequent. The collision frequency of 1 keV electrons is approximately 92 Hz while the collision frequency of 10 eV electrons calculated with similar plasma parameters is approximately 92 kHz. This explains that the electron-electron collision frequency strongly depends on the electron temperature (T_e). The collision rate increases with high electron densities and lower electron temperatures. The collision frequencies between electron-ion and ion-ion can be compared to the gyrofrequencies of ions and electrons in a typical ECR charge breeder ion source. For example, for a typical SP1 CB magnetic field range of 0.38-1.38 T and the Oxygen charge state of 5+, the range of ion gyrofrequency is estimated as 1.78 - 6.47 MHz. At the same time the range of electron gyrofrequency is estimated as 10.6 - 38.6 GHz. Since the ion-ion collision frequency of high charge state ions is higher than their gyrofrequencies, the high charge states cannot be considered to be magnetically confined and this is observed to be opposite for electrons.

During the elastic collisions between the electrons and ions, ions can gain energy from the electron population. In ECR plasmas, the ion temperature is estimated to be only a few electron volts. The electron-ion collisional equipartition rate can be derived assuming steady state conditions in ECR plasma [45] as

$$v_{ei,e \longrightarrow i} = \frac{1}{\tau_{ei,e \longrightarrow i}} \approx \frac{3.2 \times 10^{-9} \ln \Lambda}{T_e^{3/2}} \sum_i \frac{\sum_i n_i^q q^2}{A_i} \tag{3.24}$$
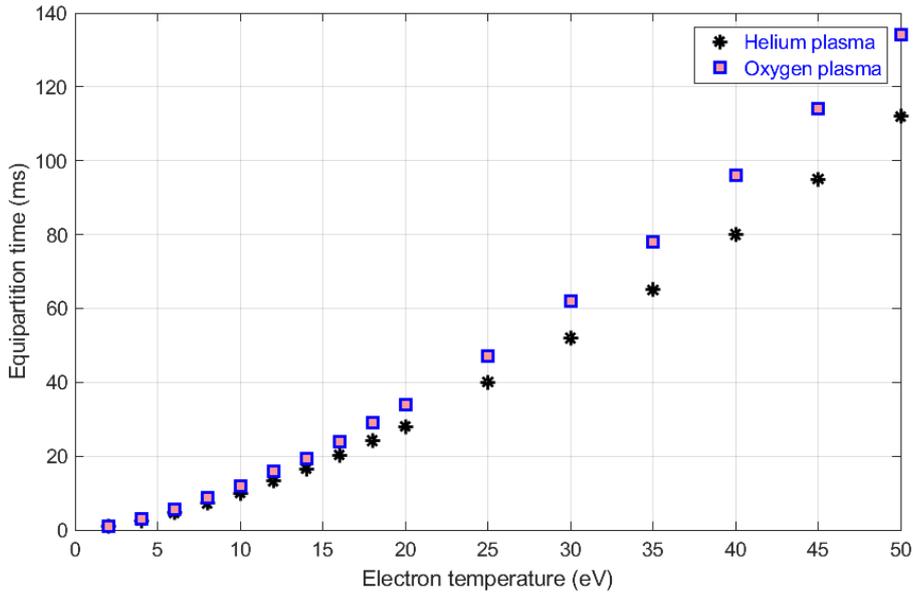
FIGURE 3.1: The energy equipartition time calculated for Helium and Oxygen plasmas according to the equation 3.24. Their effective charge states are 1.5 and 5 respectively.

In equation 3.24, it can be seen that the energy equipartition time and frequency depend on the electron temperatures. Figure 3.1 shows the equipartition times for Helium and Oxygen ions in pure plasmas with the cold electron component as a function of electron temperature. The calculation need a cold electron density ($n_{e,cold}$), which is assumed to be less than a order of magnitude of the cut-off density (i.e., $n_{e,cold} = 0.1 \times$ cut-off density). The mean plasma effective charge of Helium and Oxygen plasma are assumed as 1.5 and 5. For Helium and Oxygen plasmas, the equipartition time with warm electron population ($T_e \approx 1$ keV) are about 10 s and 12 s. Ions cannot reach these energies since the equipartition times (in order of s) are much longer than their confinement times in plasma (in order of ms). For the cold electron population ($T_{e,cold} \approx 10$ - 100 eV), the equipartition time is in the order of tens of milliseconds. It can be seen from the figure 3.1 that in a Helium or Oxygen plasmas the ions may gain energy greater than 20 eV, if they remain in the plasma for more than 55 ms. Due to the difference in masses, the equipartition times in the case of Oxygen plasma are bit longer.

3.5 Plasma sheath and potential

In ion sources, the plasma is enclosed by a vessel or chamber. The chamber wall is a sink for charged particles, causing electrons and ions to flow towards the wall. Their continuous flow towards the wall corresponds to electric currents with anti-parallel current densities. As the electrons exhibit much larger velocities than the ions due to their low mass, they preferentially leave the plasma and charge the plasma slightly positive. Thus, an electrostatic potential (*sheath potential ϕ_s*) develops between the plasma and the chamber wall, which repels the electrons and accelerates the ions.

The variation in potential near plasma wall is described in figure 3.2. The electrons that have high energy tail of the distribution function can escape and reach the wall [46].
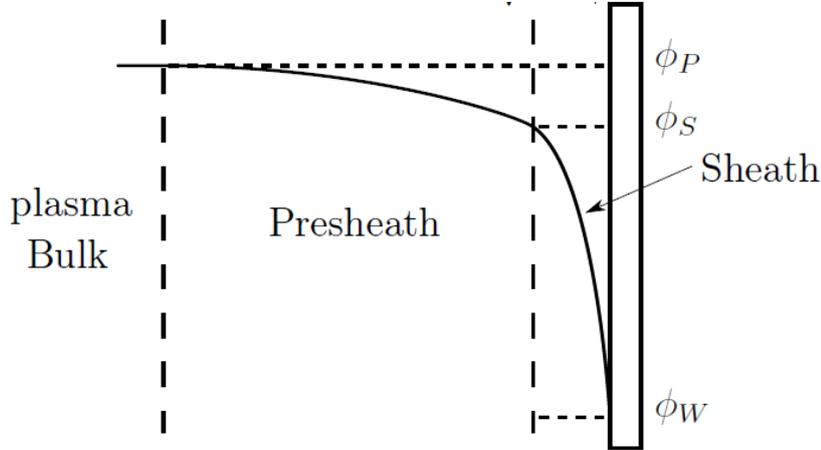
FIGURE 3.2: The electrostatic potential of a collisionless plasma near the chamber wall, defining sheath and presheath.

Let's analyze in level of detail the structure of the non-neutral layer near to the chamber wall in contact with plasma. To simplify our analysis, we make use of 1D model where the chamber wall is electrically isolated. Bohm has given a simple description of plasma sheath by introducing the sheath criterion, which sets the low velocity limit for the ions reaching to the sheath edge [47, 48]. Denoting the velocity of the test charge in plasma (v_i) having the electrostatic potential (ϕ), which is due to the distribution of charged particles surrounding it, and entering in the sheath by v_0, their energy conservation reads (always assuming a collisionless sheath)

$$\frac{m_i}{2}v_i^2 + e\phi = \frac{m_i}{2}v_0^2 \tag{3.25}$$

with electrostatic potential $\phi = 0$ V at sheath boundary. Here, m_i is the mass of ion species, n_i and n_e are the ion and electron densities in plasma. Inserting equation 3.25 into ion continuity equation ($n_i v_i = n_0 v_0$), the ion density becomes

$$n_i = n_0 \left(1 - \frac{2e\phi}{m_i v_0^2}\right)^{-1/2} \tag{3.26}$$

The distribution of electrons are assumed to be in thermal equilibrium at a temperature T_e and their density given by Maxwell Boltzmann distribution

$$n_e = n_0 \exp\left(-\frac{e\phi}{kT_e}\right) \tag{3.27}$$

Substituting the equations 3.27 and 3.26 into Poisson equation [42], the sheath potential is written as

$$\frac{d^2\phi}{dx^2} = -\frac{e}{\epsilon_0}(n_i - n_e) = \frac{e}{\epsilon_0}(n_e - n_i) = \frac{en_0}{\epsilon_0}\left[\exp\left(\frac{e\phi}{kT_e}\right) - \left(1 - \frac{2e\phi}{m_i v_0^2}\right)^{-\frac{1}{2}}\right] \quad (3.28)$$

where n_e and n_i are the densities of electrons and ions, v_0 is the initial velocity of ions arriving at the sheath and n_0 is the density in plasma. The equation 3.28 is only valid when it satisfies the *Bohm sheath criterion :*

$$v_0 \geq v_B = \sqrt{\frac{kT_e}{m_i}} \quad (3.29)$$

Where v_B is the Bohm velocity which uses the temperature of electrons and the ion mass. This relation gives minimum velocity of ions arriving at the sheath (*Bohm velocity v_B*). In a low pressure plasma with $KT_i \ll KT_e$, this velocity is much larger than the ion thermal velocity. For ions to gain this velocity there exist a pre-sheath in which the ions are accelerated by a potential drop of

$$\Delta\phi \geq \frac{kT_e}{m_i} \quad (3.30)$$

The plasma potential with respect to the sheath boundary is calculated from the acceleration to the Bohm velocity

$$\frac{m_i}{2}v_B{}^2 = e\phi_p \quad (3.31)$$

$$\phi_P = \frac{kT_e}{2e} \quad (3.32)$$

The potential variation of plasma close to the chamber wall is shown in the figure 3.2. The Bohm velocity and plasma density at sheath boundary defines the ion flux as

$$\Gamma_i = n_0 v_B \quad (3.33)$$

and the electron flux given by the average thermal electron speed modified by the Boltzmann relation with respect to the wall potential is given by

$$\Gamma_e = \frac{1}{4}n_0\langle v_e\rangle exp\left(-\frac{-e\phi_w}{kT_e}\right) \quad (3.34)$$

where

$$< v_e > = \left(\frac{8kT_e}{\pi m_e}\right)^{\frac{1}{2}} \quad (3.35)$$

is the average electron speed. For a chamber wall at zero potential, the ion and electron fluxes must be equal at the border between the pre-sheath and plasma sheath [49]. Finally, the plasma potential with respect to the chamber wall results as

$$\phi_p - \phi_w = \frac{kT_e}{2e}\left(1 + log\left(\frac{m_i}{2\pi m_e}\right)\right) \tag{3.36}$$

3.6 Atomic physics processes for production of high charge state ions in ECR plasma

In ECR plasma, the collisions include atomic physics processes such as ionization, charge exchange and recombination. Ionization takes place stepwise from one charge state to the next charge state; on the other hand the charge exchange and recombination compete with the ionization process to decrease the charge state. It is also possible to have a double ionization where two electrons to be ejected in an electron-ion collision. However, the stepwise process is much more probable. As the charge state of ion increases, the ionization potential for further ionization also increases. Therefore, sufficient density of high energy electrons is required for the production of highly charged ions. Long confinement time allows the ions to undergo multiple ionizing collisions with electrons, which improves the production of high charge state ions. Shirkov et al [50] has articulated certain desirable properties of ECR plasma to produce HCIs. A set of non-linear differential equation has been formulated taking into the account only the electron impact ionization and charge exchange. The equation describes the time evolution of ion densities of a certain charge state species i with charge state q reside inside an ECR plasma taking into account only the charge exchange and electron impact ionization:

$$\sum_{q=1}^{Z} \frac{dn_i^q}{dt} = n_e n_i^{q-1}\langle\sigma_{ion}^{q-1\longrightarrow q}v\rangle - n_e n_i^q\langle\sigma_{ion}^{q\longrightarrow q+1}v\rangle + n_0 n_i^{q+1}\langle\sigma_{cx}^{q+1\longrightarrow q}v\rangle -$$
$$n_0 n_i^q\langle\sigma_{cx}^{q\longrightarrow q-1}v\rangle - \frac{n_i^q}{\tau_i^q} \tag{3.37}$$

where σ and v is the corresponding cross sections and interaction velocities, n_i^{q-1} is the ion density of ions with charge state $q - 1$, n_i^q is the ion density of ions with charge state q, n_i^{q+1} ion density of ions with charge state $q + 1$, n_0 is the neutral density, $\langle\sigma_{ion}^{q-1\longrightarrow q}v\rangle$ is the ionization rate coefficient from charge state $q - 1$ to q, $\langle\sigma_{ion}^{q\longrightarrow q}v\rangle$ is the ionization rate coefficient from charge state q to $q + 1$, $\langle\sigma_{cx}^{q+1\longrightarrow q}v\rangle$ is the charge exchange coefficient from charge state $q + 1$ to q, $\langle\sigma_{cx}^{q\longrightarrow q-1}v\rangle$ is the charge exchange coefficient from charge state q to $q - 1$, τ_i^q is the confinement time of ions of charge state q and species i and Z is the number of electrons of the neutral atom. The last term relates to diffusion process for ion losses towards the plasma chamber walls and/or extracted from the ion source.

3.6.1 Electron impact ionization

According to the equation 3.37, the ion densities of high charge state ions depends on the ion confinement time, plasma densities and the rate of ionization cross sections. The process of single ionization by electron impact is generally expressed as

$$e^- + X^q \longrightarrow X^{(q+1)} + 2e^- \tag{3.38}$$

Among the empirical models [51] developed to estimate the electron impact ionization cross section $\sigma_{q-1,q}$, the empirical formula proposed by Lotz [52, 53] is widely used and can be written as

$$\sigma_{q-1,q} = \sum_{i=1}^{N} a_j n_j \frac{\ln(E/P_j)}{EP_j} \{1 - b_j[-C_j((E/P_j - 1)]\} \ and \ E \geq P_j \tag{3.39}$$

Where, a_j, b_j, c_j are the empirical constants, which depend on the ion species to be ionized. E_e is the energy of bombarding electrons, n_j is the number of equivalent electrons in j^{th} sub-shell and P_j is the binding energy of electrons in the jth sub-shell of the ion.
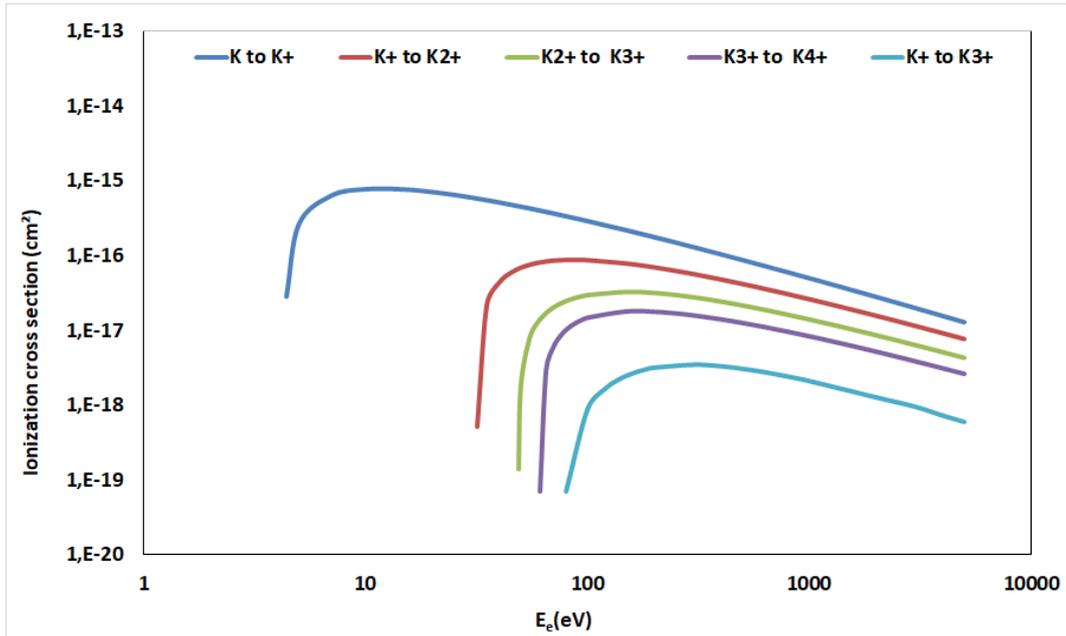
FIGURE 3.3: Ionization cross section of potassium atom from ground state to K^{4+} as a function of electron energy.

The ionization rate with respect to the energy of bombarding electrons is expressed by writing

$$v_{q-1 \to q}^{ion}(E_e) = \langle \sigma_q^{ion} v \rangle (E_e) n_e(E_e) \tag{3.40}$$

Where, n_e is the density of electrons and σ_q^{ion} is the cross section of ions with charge
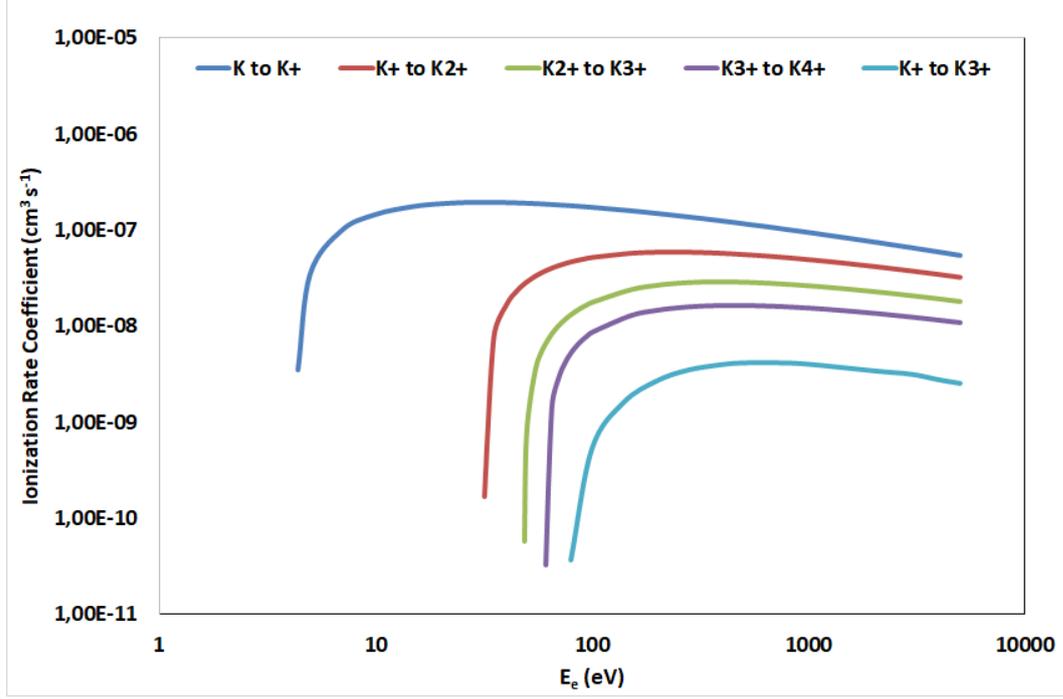
FIGURE 3.4: Ionization rate coefficients of potassium atom from ground state to K^{4+} as a function of electron energy.

state q. The above formula can be written if the electron temperature KT_e is a Maxwell-Boltzman distribution

$$v_{q-1 \to q}^{ion} = \int \sigma_{q-1 \to q}^{ion}(E_e) v(E_e) n_e \frac{2}{\sqrt{\pi}} \left(\frac{E_e^{1/2}}{KT_e^{3/2}} e^{-E_e/KT_e} \right) dE_e \qquad (3.41)$$

The equation 3.41 depends on low and high energies of the impact electron. The average ionization time taken during the transition from charge state q_1 to another charge state q_2 over the electrons distribution [24] is

$$\tau_{q_1 q_2} = [n_e S_{q_1 q_2}(T_e)]^{-1}$$
$$S_{q_1 q_2} = < \sigma_{q_1 q_2}(v_e) v_e > \qquad (3.42)$$

Using the equations 3.39 and 3.4, a rough calculation of the ionization cross section for potassium atom from ground state to K^{4+} as a function of electron energy and their ionization rate coefficients are presented in the figure 3.3 and 3.4. It is shown that the cross-section strongly depend on the ionization potential and incident electron energy. The cross-section rises when the electron kinetic energy is equal to the ionization potential of the electron to be removed and peaks at approximately 2-3 times the ionization potential. This relation generally holds for all highly charged ions. As the charge state of potassium increases from ground state to K^{4+}, the optimum bombarding energy increases by a factor of ten and the ionization cross section decreases approximately by two orders of magnitude. Finally, the cross section decreases while going over the optimum bombarding energy. These trends clearly

show that the warm electron population is mainly responsible for the ionization processes in the ECR plasma, and not the hot electrons population having energies up to hundreds of keVs. As can be seen from the figure 3.4, the ionization rate coefficient has an optimum electron energy, increasing with the desired ion charge q. However, one needs a plasma electron temperature that is optimum for the highest desired charge state q. This can be achieved with in a electron temperature of the order of five times the ionization potential. The electron impact ionization cross sections and ionization rate coefficients of Na (ground state to Na^{4+}) are calculated and presented in the appendix A.

3.6.2 Double ionization by electron impact

The double ionization of neutrals and ions by electron impact plays a prominent role in the atomic collision processes. The mechanism of double impact ionization can be explained as

$$e^- + A \longrightarrow e^- + A^{2+} + 2e^- \tag{3.43}$$

Generally, the multiple ionization takes place through different processes [54]: the simultaneous ionization of two outermost electrons (direct process), by ejecting two electrons from the atom, where the first one is removed by the incident electron and the second is ejected due to the interaction of the second electron with the other electrons of the atom and finally the last mechanism is due to the ionization or/and excitation of a single inner-shell electron by Auger decay. The semi-empirical formula for double ionization cross section is given as [54]:

$$\sigma_{++} = \frac{N_e(N_e - 1)}{4\pi r^2} \left(\frac{\sigma_0}{U_i^2} \right) \left(\frac{\sigma_0}{U_{ii}^2} \right) g \left(\frac{E_1}{U_i^2 + U_{ii}^2} \right) \tag{3.44}$$

where U_i is the first ionization potential, U_{ii} is the second ionization potential, E_1 is the incident energy of the impacting electron, N_e is the number of equivalent electrons in the shell, $\sigma_0 = 6.56 \times l0^{-14} \ eV^2 \ cm^2$. r is evaluated by the expression

$$R = rN_e^{\frac{1}{3}} \tag{3.45}$$

Where, R is the mean radius of the atom. The ionization energy needed at each step grows dramatically higher as the charge state increases. For example, the ionization energies for producing K^+ to K^{3+} are 4.34 eV, 31.7 eV and 45.8 eV respectively. As seen in figure 3.3, the ionization cross section decreases several orders of magnitude when compared with single ionization. Because of the electron energy distribution, the production of singly charged ions strongly dominates the multiple ion production. To produce multiply charged ions, the ion life time in the plasma has to be long enough, which can be achieved by suppressing the charge exchange reactions by maintaining low neutral pressure (i.e. operating the ion source in low vacuum).

3.6.3 Recombinations

The ion charge state in ECR plasma is reduced due to the recombination process between electron and ion. The three different recombination mechanisms are:

- **Charge exchange recombination**: The highly charged ion decreases their own charge state by colliding with neutrals or/and low charge species.
- **Radiative recombination**: In this mechanism, the electron after the collision is captured by ion and therefore, emitting a photon.
- **Dielectric recombination**: This mechanism comprises of three steps, where an electron excites an ion, then it is captured, and a photon is emitted.

Among the three mechanisms, the charge exchange recombination mechanism is more dominant in ECR ion sources. The following scheme shows the charge exchange mechanism and the estimated cross-section.

$$X^{q+} + Y \Rightarrow (XY)^{q+} \rightarrow X^{q-1} + Y^+ \tag{3.46}$$
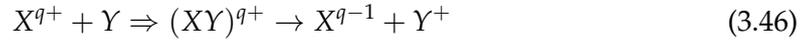
The charge exchange collision between the highly charged ion and neutral atom forms a metastable molecular ion and finally convert to lower charge state (q-1). The estimated cross section for charge exchange reaction is given by [55]

$$\sigma_{i,i-1} = A_k \cdot i^{\alpha k} \cdot I_{[eV]}^{\beta k} \quad and \quad k = 1, 2, 3, 4 \tag{3.47}$$

where $\sigma_{i,i-1}$ is in cm^2, i is the initial charge state, k denotes the number of electrons transferred in the process and I is the first ionization potential given in eV. αk, βk and A_k are the free fit parameters to the experimental data. With the aid of this equation, the total charge exchange cross sections are calculated for K^{i+} ions incident on He (Helium) and O_2 (Oxygen). The total charge exchange cross section is estimated by single electron transfer (k = 1), which is considered as a dominant process.

Comparing the figures 3.3 and 3.5, the single ionization and charge exchange cross sections are on the same order of magnitude for low charge-state ions while the charge exchange cross section is considerably larger than the electron impact ionization cross section for highly charged ions. This emphasizes the importance of low neutral density along with high electron density for the production of highly charged ions in ECRIS plasmas. The cross section of other two processes (dielectric and radiative recombination) is very low and therefore, they are not considered in this thesis.

3.7 Fundamentals of ECR based ion source

In ECR ion sources, the charged particles are confined by using external magnetic and electric forces to enhance the ion production. So, it is important to introduce and understand the particle dynamics under the influence of electric and magnetic fields.
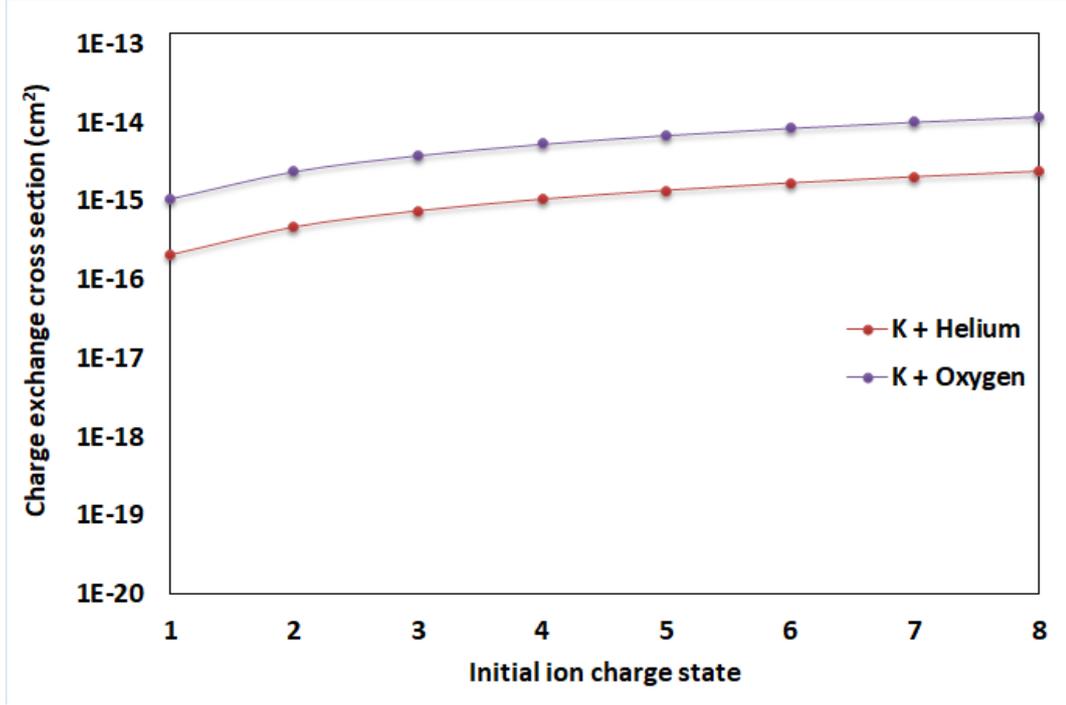
FIGURE 3.5: Charge exchange processes for Potassium charge states on Helium and Oxygen targets (k=1). k in the equation 3.47 denotes the number of electrons transferred during the charge exchange process.

3.7.1   Charged particle movement and cyclotron frequency

Let us consider a singly charged particle of mass (m) and charge (q) in a combination of a stationary force $\vec{F}$ and a stationary magnetic field with induction $\vec{B}$. The velocity of the particle is denoted by $\vec{v}$. The equation of motion in vector notation,

$$m\frac{dv}{dt} = q\vec{v} \times \vec{B} + \vec{F} \tag{3.48}$$

includes a set of three differential equations. The cross product term in the equation 3.48 represents component perpendicular to the magnetic field $\vec{B}$. Thus the equation of motion describes a constant acceleration parallel to $\vec{B}$ by the respective component of $\vec{F}$. Perpendicular to $\vec{B}$, we have a system of two coupled inhomogeneous equations 3.48

$$m\frac{dv_{\perp}}{dt} = q\vec{v}_{\perp} \times \vec{B} + \vec{F}_{\perp} \tag{3.49}$$

The homogenous part of the equation 3.49 is

$$m\frac{dv_{\perp}}{dt} = q\vec{v}_{\perp} \times \vec{B} \tag{3.50}$$

which describes the motion of charged particle under the influence of magnetic field. The motion is a gyration with a constant velocity in the plane perpendicular to $\vec{B}$, which is called cyclotron motion. Thus, the gyration of the particle occurs at constant speed $v_\perp$ at a Larmor radius

$$r = \frac{mv_\perp}{qB} \tag{3.51}$$

where, $v_\perp$ is the velocity of the particle in the plane perpendicular to $\vec{B}$. The respective angular frequency (cyclotron frequency) is given by

$$\omega = \frac{qB}{m} \tag{3.52}$$

where, the direction of rotation is determined by the sign of the charge state q. The inhomogeneous part of equation 3.49 in case of constant $\vec{v_\perp}$ is

$$-q\vec{v}_\perp \times \vec{B} = \vec{F}_\perp \tag{3.53}$$

and can be solved by taking its cross product with $\vec{B}$, i.e.

$$\vec{v}_\perp = \frac{\vec{F}_\perp \times \vec{B}}{qB^2} \equiv \vec{v}_{drift} \tag{3.54}$$

The drift velocity causes the particle to drift across the magnetic field from one line to another. The drift caused by a magnetic field gradient $\nabla \mathbf{B}$ is relevant for the purpose of ECR ion sources. The gradient causes charged particles gyrating in the field to move perpendicular to the magnetic field or towards regions of lower magnetic field. The gradient parallel to $\vec{B}$ the charged particles drift towards weaker magnetic field due to the conservation of the magnetic dipole moment of the gyrating particle.

3.7.2 Magnetic confinement

In ECR Ion Sources and ECR based charge breeders, the magnetic confinement is based on minimum-B magnetic field configuration formed in the plasma chamber where the ECR condition is fulfilled and provides magnetic confinement for the charged particles created through ionization process. This configuration is realized with a combination of axial magnetic field created by solenoids and radial magnetic field created by the hexapole or multipole field. The magnetic field strength in this configuration has a minimum in the center of the structure and increases from there in all directions. The solenoids are placed at the ends of plasma chamber producing axial mirror trap. The configuration generates the magnetic field equipotential surfaces inside the plasma chamber, creating a large Electron Cyclotron Resonance surface.

The axial and radial field profiles created by solenoid and hexapole in a GANIL GTS 14.5 GHz ECRIS are shown in figure 3.6. The axial mirror field is asymmetric with
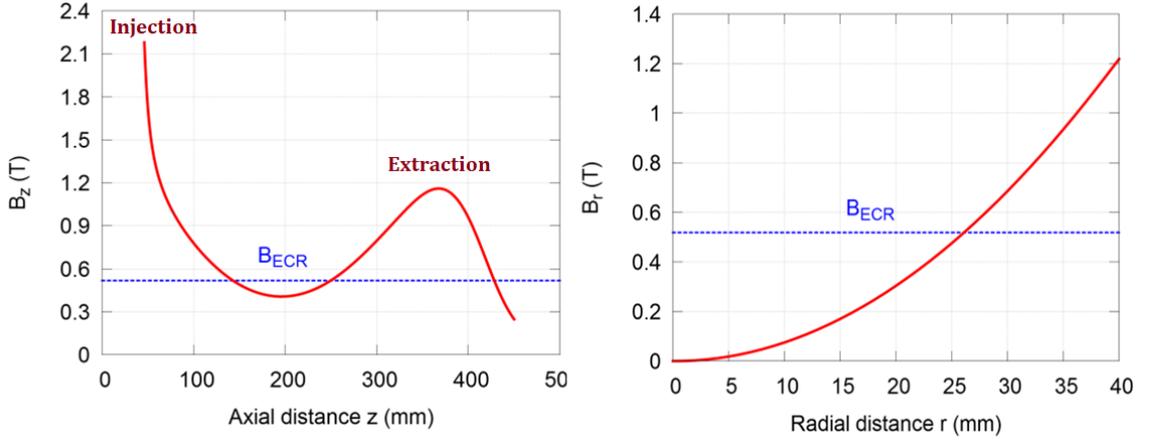
FIGURE 3.6: Magnetic field profile of a GTS 14.5 GHz ECRIS: Axial magnetic field created by solenoids from injection to extraction (left) and a radial field created by hexapole from the center of the plasma chamber towards a magnetic field pole (left). The blue dashed line indicates the location of resonances at 14.5 GHz

lower peak magnetic field at the extraction end of the plasma chamber, which favors the extracted ions through the extraction aperture and consequently enhances the extraction efficiency. For radial confinement of plasma in ECRIS, various multipole fields have been tested but hexapole is commonly used and offers a balance between the shape and size of an axial plasma flux [24] concentrated close to the axis of plasma chamber such that the ions are extracted easily through round extraction aperture.

In order to understand the principle of magnetic confinement, the magnetic moment of the charged particle need to be introduced. The charged particle during its gyromotion produces a circulating current which is given by

$$I = \frac{|q|\omega}{2\pi} \tag{3.55}$$

where, q is charge of the particle and ω is the angular frequency. The area inscribed by gyrating charged particle around the magnetic field $A = \pi r_L^2$ with Larmor radius r_L produces the magnetic moment which can be expressed as

$$\mu = I \cdot A = \frac{m v_\perp}{2B} = \frac{W_\perp}{B} \tag{3.56}$$

where, m is the mass of the particle, $v_\perp$ is the perpendicular velocity component with respect to the magnetic field and $W_\perp$ is the perpendicular kinetic energy of the particle with respect to the magnetic field. The magnetic moment during the particle motion is conserved if the spatial variation of the magnetic field inside the orbit of the particle is small. As the particle move towards the converging field, the magnetic flux enclosed by the particle orbit is conserved. Moreover, the total kinetic energy W_{tot} is conserved as the particle move towards the converging field which results in decreasing parallel velocity $v_\parallel$. The particle is reflected back when it reaches the

location where its parallel velocity component reaches zero and may travel back and forth, becoming trapped. This phenomenon is known as the magnetic mirror effect.

Despite of the confinement, the effectiveness of a magnetic confinement is distinguished by mirror ratio B_{max}/B_{min}, where B_{max} is the maximum magnetic field at the reflection point and B_{min} is the magnetic field minimum at Electron Cyclotron Resonance. This ratio determines whether the particle is confined in the magnetic mirror field. Let us consider a charged particle defined in a velocity space $(v_\perp, v_\parallel)$ having a pitch angle α_0. At the reflection point B_m $(v_\parallel = 0)$, where the pitch angle α_0 is $90°$, then

$$\sin \alpha_0 = \sqrt{\frac{B_{min}}{B_{max}}} = \frac{1}{\sqrt{R}} \tag{3.57}$$
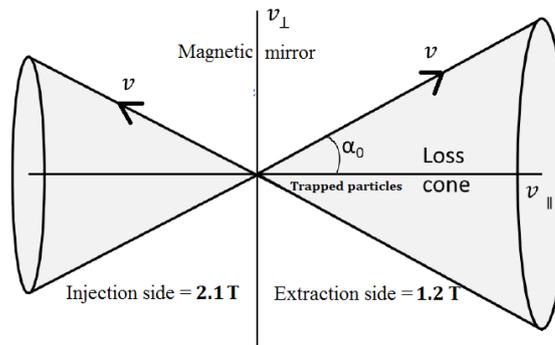
FIGURE 3.7: Loss cone with different magnetic field strengths. The angle of the loss cone is larger in the lower magnetic field (right-hand side of the figure, extraction of an ECRIS) than in the higher magnetic field (left-hand side of the figure, injection of an ECRIS).

where, R is the mirror ratio. The equation 3.57 defines a region in velocity space in the shape of cone called loss cone (see figure 3.7). The loss cone is independent of charge and mass of a particle. The ions and electrons are confined equally without collisions. The ions and electrons confinement is complicated in ECR plasma, since the magnetic confinement depends on ratio of Larmor frequency and collision frequency, which consequently depends on energy and position of the particles.

$$v_{ee,ei} \propto (kT_e)^{-3/2} \tag{3.58}$$

The mirror ratio given in 3.57, is usually used to decribe the magnetic mirror systems. In case of ECR ion sources, the B_{min} is usually replaced in the mirror ratio with B_{ECR}, because passing through the resonance has a strong influence on the electron perpendicular velocity, which determines the electron confinement. The confinement is better in higher mirror ratios and consequently the production of highly charged ions is increased. However, the mirror ratio should not be too high since the HCI have to escape from the mirror trap in order to be extracted from the ion source. Therefore, there should be careful optimization of the mirror ratio while operating the ECRIS for HCI production.

3.7.3 Diffusion of charged particle in magnetic field

In magnetized plasma, the collisions of charged particles play an important role. As illustrated in the figure 3.8, plasma becomes anisotropic under the influence of external magnetic field. The charged particles follow their helical orbits due to the long range coulomb collisions and transported through the perpendicular magnetic field by diffusion. There is a difference between transport, such as diffusion, along and across the magnetic field. The diffusion along the magnetic field resembles transport in non-magnetized plasma. Let us consider $D_{\|e}$ and $D_{\|i}$ be the electron and ion diffusion coefficients for this case. The respective formula for the charged particle mobility in non-magnetized plasma is given by

$$\frac{D_e}{D_i} = \sqrt{\frac{m_i}{m_e}} \tag{3.59}$$

which means electrons diffuse much faster than ions. Here m_i is the mass of the ion in ion-neutral collision system, m_e stands for mass of the electron in electron - neutral collision system.
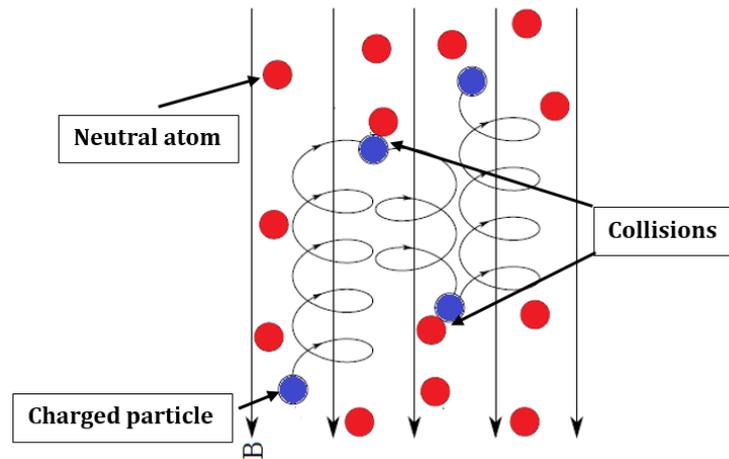
FIGURE 3.8: Diffusion of charged particle in a magnetized plasma. Reproduced from the reference [44]

To understand the diffusion across the magnetic field, we must consider the Brownian motion of electrons in magnetized plasma (see figure 3.8). The trajectories of neutrals will be straight between the collisions and change its trajectories by collisions. In the presence of external magnetic field, the free-moving charged particles spiral around the magnetic field lines. The situation shown in figure 3.8 happens when the cyclotron frequency of the spiralling particles is large compared to any collision frequency. Due to the collisions with neutrals, the particles jump from one field line to another, upon which its Larmor radius also changes and possibly the direction of its motion along the magnetic field.

Considering the situation in figure 3.8, the average distance travelled between the successive collisions across the magnetic field is the average cyclotron radius $<r_B>$

(comparing equation 3.51. Thus, we may estimate the diffusion coefficient for charged particle diffusing across the magnetic field by

$$D \approx v \langle r_{Be,i}^2 \rangle \approx \sqrt{m_{e,i}} \quad (3.60)$$

where, $r_{Be,i}$ is the particle Larmor radius and v is the collision frequency. Due to the large difference between masses, the diffusion of electrons in transverse magnetic field is slower due to its smaller Larmor radius. In case of parallel direction to the magnetic field, ions are diffused slowly due to their large mass. The particles of opposite charges diffuse together due to their interaction, which is described as "ambipolar diffusion" . It is expressed by diffusion constant D.

$$D_\perp \approx v_{ei} \langle r_{Le}^2 \rangle (1 + \frac{T_i}{T_e}) \quad (3.61)$$

Due to the helical trajectory of the particle, the average step size in the parallel direction is smaller but only by a small factor. Therefore, for $D_\parallel$, an order of magnitude estimate is valid. In the equation 3.61, where v_{ei} is the electron-ion collision frequency and the r_{Le} is the Larmor radius of electrons which is expressed as

$$\langle r_{Le}^2 \rangle = \langle \frac{m_e^2 v_\perp^2}{q^2 B^2} \rangle \propto T_e \quad (3.62)$$

In ECR ion source plasmas, the electrons generally exhibit much larger velocities than the ions due to their low mass. So, they preferentially leave the plasma and build-up a positive plasma potential with respect to the plasma chamber. Thus the plasma losses are ruled by ions across the magnetic field and electrons along the magnetic field lines.

3.7.4 Electron Cyclotron Resonance heating

In ECR based ion sources, the plasma electrons are heated by transferring the energy from RF waves through Electron Cyclotron Resonance in an external magnetic field. The electrons that are trapped in magnetic field follow helical paths along the field lines. The ECR-condition takes place when the cyclotron frequency matches the microwave frequency.

$$\omega_c = \omega_{RF} = \frac{eB}{m_e} \quad (3.63)$$

where, ω_{RF} is the microwave angular frequency, ω_c the cyclotron frequency, e the electron charge, B_{ECR} the magnetic field at the resonance and m_e the electron mass. At the resonance surface, the magnetic field B is given by

$$B_{ECR} = \frac{f_{RF}}{28} T \; and \; f_{RF} = \frac{\omega_{RF}}{2\pi} GHz \quad (3.64)$$

where, f_{RF} is the injected microwave frequency in gigahertz [24]. The study of ECR heating and electromagnetic wave propagation in ECR plasma is complicated due to combined phenomena. The electrons at the resonance zone gains or lose energy depending on the phases between their motion and RF field component perpendicular to the magnetic field. Electrons gain energy at the accelerating phases while passing through the resonance region multiple times. Therefore, the electrons undergo a stochastic ECR heating [56] and quickly reach keV energies that are sufficient to ionize atoms via successive electron impact ionization. Depending on the source parameters, the electron density in ECR plasma is estimated between 10^{11} and 10^{12} cm^{-3}. In addition, the external magnetic field gradient influences the energy transfer from microwave to electrons. Adjusting the field gradient at the resonance effectively increases or decreases the thickness of resonance surface and consequently varying the surface volume and effectiveness of energy transfer from microwaves to electrons.

It is well established that Electron Energy Distribution Function is non-Maxwellian and recently, it has been verified experimentally [57]. It has also been suggested that the ECR plasma never achieved a Maxwellian distribution due to hot electrons component with long equilibration times [45]. Based on the experimental investigations [58] and arguments [59], three different electron populations are assumed to be reside inside an ECRIS plasma and represented according to their energies: the cold electron component of EEDF are typically in a range of tens of electron volts [127]. They suffer frequent scattering collisions but cannot induce ionization from inner shell of atoms due to their insufficient energy. The warm electrons (few keV to tens of keV), which are experimentally observed [57] are responsible for the ionization processes exhibits sufficient collision frequency for the production of intense high charge state ions. Hot electrons are confined in the mirror and exhibits low cross-section, but still, they can create multiply charged ions.

As the ionization cross-section is inversely proportional to the electron temperatures, the ionization cross-section exhibits maximum at $E_e > 3W_i$ [56], where W_i is the binding energy of the electron to be removed, which is estimated between 5 eV to 1.5 keV. The production of highly charged ions increases with increase in microwave power up to the maximum point after which it decreases due to RF induced plasma losses [46, 61]. Better performance of ion source for high charge states can be achieved by stabilizing the plasma against RF induced plasma instabilities. The electron losses from the mirror trap are largely influenced by the plasma instabilities [46, 62]. Current research is going on in these two directions: the minimization of electron losses by plasma instabilities and enhancing the performance of ion source in terms of intensities and charge state distributions by introducing additional RF power. Such investigations would yield more information on the ion source tuning parameters.

3.7.5 Confinement of ions

In ECR plasma, ions are confined by electrostatic field and poorly confined by the magnetic field. Their gyromotion in the magnetic field is strongly disturbed by the collisions. Therefore, different expressions for the ion confinement times has been derived [45] by considering their collisionality and dimensions of the plasma (the

resonance zone volume). Since their collisionality rate is higher compared to electrons, the ion temperature is assumed to have same for all ions in the plasma regardless of their charge. In the following three ion confinement models will be discussed.
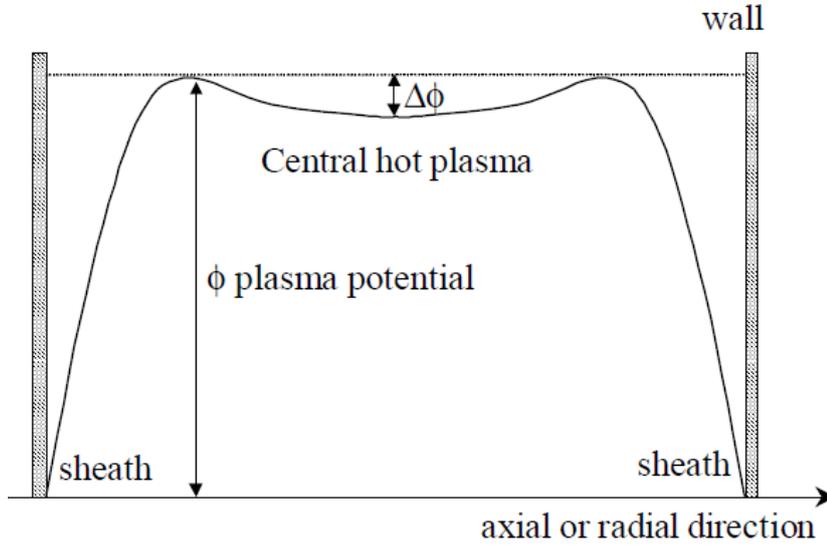
FIGURE 3.9: The supposed form of the plasma potential along the axis. Reproduced from the reference [63]

It has been suggested that the warm and hot electrons are well confined by the magnetic confinement system inside the ECR surface and the cold electron population that is responsible for the build up of plasma potential which is in order of 10 - 60 V [64]. In T. Ropponen et al [65], it has been indirectly detected that the electron density at the plasma center is slightly higher due to the trapped hot electron population. These hot electrons are collisionless and creates a potential dip $\Delta\phi$ [66, 67] in the center of the potential profile (see figure 3.9), where the depth of the well is estimated around or less than 1 V [59]. In fact, there is a disagreement on the formation of dip in the profile and it has never been directly measured in an ECR ion sources. The potential dip model leads to the resulting expression for ion confinement time [68]

$$\tau_q = R \frac{\sqrt{\pi}L}{v_T} \exp \frac{|qe\Delta\phi|}{kT_i} \tag{3.65}$$

where R is the mirror ratio, L is the half length of plasma and $v_T = \sqrt{KT_i/m_i}$ is the ion thermal velocity. In equation 3.65, it can be seen that the confinement improves at lower ion temperatures (kT_i).

Ambipolar diffusion model : an alternate expression is given for ion confinement time [45, 59] by considering that the diffusion of ions out of plasma due to the ambipolar electric field E created by the positive plasma potential. This ambipolar field leads to estimate the ion confinement time in axial direction, which is

$$\tau_q = 7.1 \times 10^{-20} L q \ln \Lambda \sqrt{A_i} \frac{n_e Z_{eff}}{T_i^{3/2} E} \tag{3.66}$$

where, A_i is the ion atomic mass number and q is the charge state of ion. The effective charge of plasma is $Z_{eff} n_e = \sum_q n_q\, q^2$. The radial losses are not taken into account in the equation 3.66 and only considers the diffusion towards injection and extraction ends of the ion source plasma chamber.

Random walk diffusion : if we consider a stochastic diffusion of ions towards the low plasma density region due to the collisions between themselves, then the random walk diffusion due to thermal motion gives a ion confinement time

$$\tau_q = 7.1 \times 10^{-20} L^2 q^2 \ln \Lambda \sqrt{A} \frac{n_e Z_{eff}}{T_i^{5/2}} \tag{3.67}$$
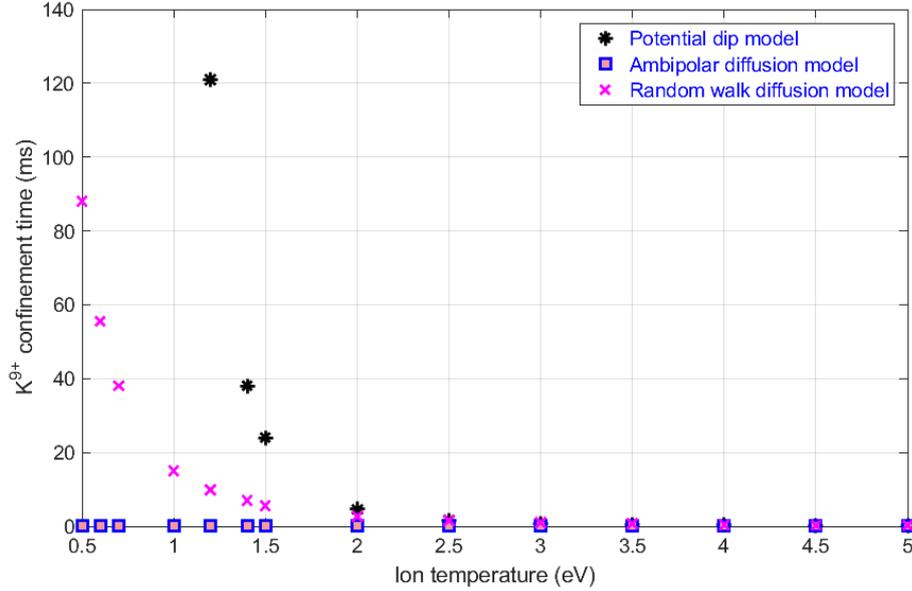
FIGURE 3.10: The confinement time of $^{39}K^{9+}$ ions as a function of the ion temperature calculated by using the equations 3.65, 3.66 and 3.67

The units for the individual parameters in the equations 3.66 and 3.67 are: τ_q in s; n_e in cm^{-3}; L in cm; T_i in eV; E in V/cm. The confinement times for $^{39}K^{9+}$ in Helium plasma can be calculated from the three different models discussed in this section. The parameters of SPIRAL1 14.5 GHz ECR charge breeder ion source were considered in the calculations: B_{inj}/B_{ECR} = 2.65, the effective plasma length is approximately 12 cm ($\pm$ 20% depending on the magnetic configuration), $E \approx 5$ V/cm, the plasma density (n_e), the average effective charge (Z_{eff}) and the potential dip are assumed as $\approx 2 \times 10^{11}$ cm^{-3} (@ 200W), 1.5 [69] and ≈ 1V [59]. The value of Coulomb logarithm (lnΛ) in the calculation is assumed as 10.

Figure 3.10 shows the confinement times calculated for $^{39}K^{9+}$ in Helium plasma as a

function of plasma ion temperature (kT_i). Looking at the trends of the different diffusion models, the confinement times calculated from the ambipolar diffusion model are significantly lower than the confinement times calculated from other two models. According to the measurement results presented in the reference [70], the charge breeding time (capture + confinement + extraction) of $^{39}K^{9+}$ is in the range of 35 ms. Therefore it seems that the ambipolar diffusion model results into too short confinement times with very low ion temperatures. The random walk diffusion model and the potential dip model lead to the correct order of magnitude for the confinement time when the ion temperature is between 0.7 and 1.4 eV.

3.8 ECRIS scaling laws

ECR ion sources are developed for the production highly charged ions with high intensities. In 1987 Geller *et al* proposed a set of semi-empirical scaling laws [24] in order to understand the performance of ECR ion source and to estimate the effects of different controllable parameters. The laws can be expressed as

$$
\begin{aligned}
n_e v_e \tau &\propto B^{3/2} \\
n_e v_e \tau &\propto \omega_{rf}^{7/2} \\
q_{peak} &\propto \ln B^{3/2} \\
q_{peak} &\propto \ln \omega_{rf}^{7/2} \\
q_{peak} &\propto P_{rf}^{7/2} \\
I_{peak} &\propto \omega_{rf}^2 m_{ion}^{-1}
\end{aligned}
\tag{3.68}
$$

In the semi-empirical scaling laws 3.68, v_e is the speed of electrons, τ is the confinement time of ions, B is the average magnetic field, ω_{RF} is the microwave frequency, q_{peak} is the charge state that produces the maximum beam current and I_{peak} is the ion beam current of charge state q_{peak}. These laws point out that the performance of ECR ion source strongly depend on magnetic field and microwave frequency. The electron confinement can be improved by increasing the magnetic field, which also increases the density of plasma. Consequently, the charge state distribution shifts to higher charge states. Comprehensive experiments [71] have been performed to understand the significance of minimum-B field structure on the performance of ECR ion source. Based on the results from the experiments, the optimum fields should have the following characteristics:

$$
\frac{B_{inj}}{B_{ECR}} \geq 4, \quad \frac{B_{ext}}{B_{ECR}} \geq 2, \quad \frac{B_{rad}}{B_{ECR}} \geq 2, \quad \frac{B_{min}}{B_{ECR}} \approx 0.8, \quad \frac{B_{ext}}{B_{rad}} \approx 0.9
\tag{3.69}
$$

where, B_{inj} and B_{ext} are the axial field maxima at injection and extraction, B_{rad} is the maximum radial field, B_{ecr} is the resonance field and B_{min} is the minimum field. The extraction efficiency can be enhanced by maintaining low mirror ratio at the extraction in order to favour the particle losses towards the plasma electrode.

In this chapter, the aspects of the physics and technology of ECR ion sources that are relevant for the work described in this thesis are briefly outlined. The collision rates

and the confinement models discussed in this chapter are furthermore used in the analysis of the results from the simulations. In the following chapter, the technical aspects of SP1 CB and its installation in the LEBT will be discussed.

4 Charge breeding technique using SPIRAL1 14.5 GHz ECR charge breeder ion source

The technique to increase the ion charge state (stable and radioactive ions) of injected 1+ ions is referred as charge breeding. This technique is employed in a device called charge breeder which accepts the singly charged ion beams with a low kinetic energy of some tens of keV (stable and radioactive ion beams). The injected 1+ ions are slowed down, trapped and ionized to higher charged states q with the required characteristics of the post accelerator (such as A/q, intensity and emittance). The charge bred ions are either delivered to low energy experimental areas, which require charge bred ions (energy in tens of keV) or post accelerated to high energies (up to 25 MeV/u) in order to deliver the beam to the nuclear physics experiments. As described in chapter 1, an ECR based charge breeder ion source has been chosen for the SPIRAL1 facility. This device is based on a Phoenix ECRIS developed at LPSC laboratory [29, 72, 73] and built by Pantechnik company [74]. In early 90's, the team of R. Geller performed the first experiments of charge breeding technique using an ECR ion source (MINIMAFIOS) [75, 3]. The results from the experiments opened the way to improve its ability to obtain high charge states with high efficiencies and short charge breeding times. The labs that are operating the ECR charge breeders are the following: LPSC [76, 77], GANIL/SPIRAL1 [5, 78, 79], SPES [80] and Texas A&M [81]. The summary of charge breeding performances obtained from the above mentioned facilities is presented in the article [82].

In the framework of SPIRAL1 upgrade, the 14.5 GHz SP1 ECR charge breeder (CB) is installed between the RIBs production cave and the post accelerator as shown in the figure 4.1. Based on the conclusion of the EMILIE collaboration studies [4], the SP1 CB has gone through several modifications [5] to improve its performance. Prior to its installation in the SPIRAL1 low energy beam transport line, the operational performance of the SP1 CB was validated at LPSC test bench [5]. As described in the chapter 1, the main objective of this thesis is the commissioning of this device in SPIRAL1 LEBT and to study the charge breeding processes for the production of highly charged stable and radioactive ion beams. The study of charge breeding technique plays an important role for optimizing the high energy exotic beams for the post nuclear physics experiments. Thus, it is important to operate the charge breeder efficiently. Its performance is evaluated by various criteria:

- The **charge breeding time** which represents the characteristic time required for the mono-charged ions to be captured and multi ionized to the desired charge state. Usually, physics experiments are performed with the RIBs having a short half life (order of second or less). Therefore, this parameter has to be shorter than the characteristic decay times of RIBS.
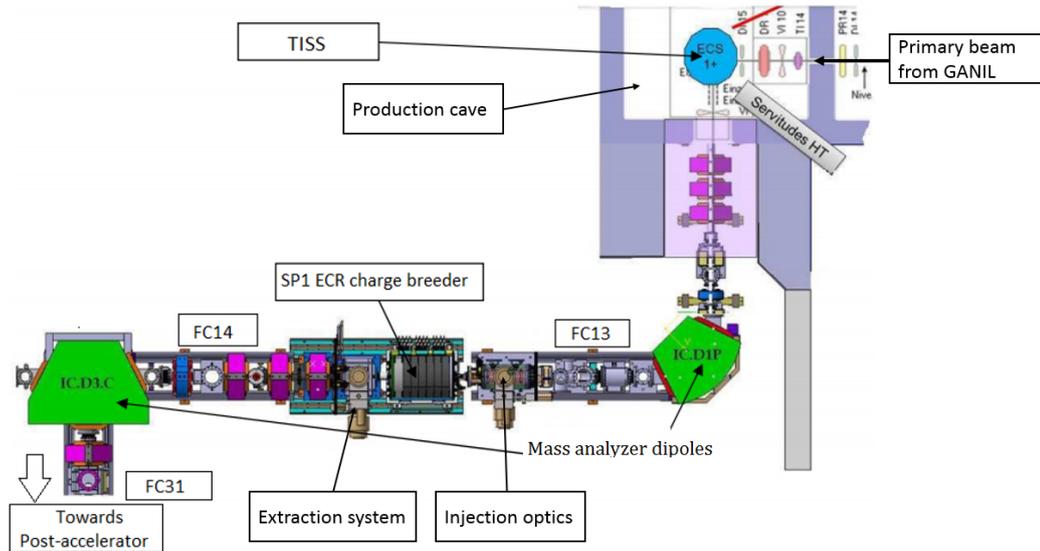
FIGURE 4.1: Layout of SPIRAL1 LEBT. The installation of SP1 14.5 GHz ECR charge breeder between injection and extraction optics.

- The **charge breeding efficiency** for a given charge state should be as high as possible. It is defined as the ratio between extracted multi-charged ion current (I_{N+}) to the mono-charged ion current (I_{1+}). This parameter is an important for RIBs, as their production yield during the charge breeding could be very low (10^4-10^6 pps).

- The extracted charge states from the charge breeder should be as high as possible. In other words, the **A/q** value should be low in order to match the acceptance of the post accelerator. With higher charge states, higher energies are available (in a cyclotrons, the final energy of the extracted beam is proportional to the square of the charge).

- The **acceptance** of the charge breeder should correspond to the range of masses, intensity and also the emittance of the injected 1+ beam.

- The **contamination** in the charge breeder should be limited for an efficient charge breeding of RIB and to tune it.

- The **emittance of the extracted charge bred beam** should be low in order to minimize the further losses along the LEBT up to CIME cyclotron.

Before discussing the experimental activities performed with SP1 CB, this chapter will give a description of this device in terms of technical aspects and its installation in LEBT and then, a brief description of the beam capture process in ECR plasma is discussed. This chapter will conclude by describing the simulation tools used to understand the ion transport in a SP1 CB and fundamental processes involved in ECR charge breeder plasma.

4.1 About SPIRAL1 ECR charge breeder

The 3D cross-section of SPIRAL1 ECR charge breeder connected between injection and extraction systems is shown in the figure 4.2.
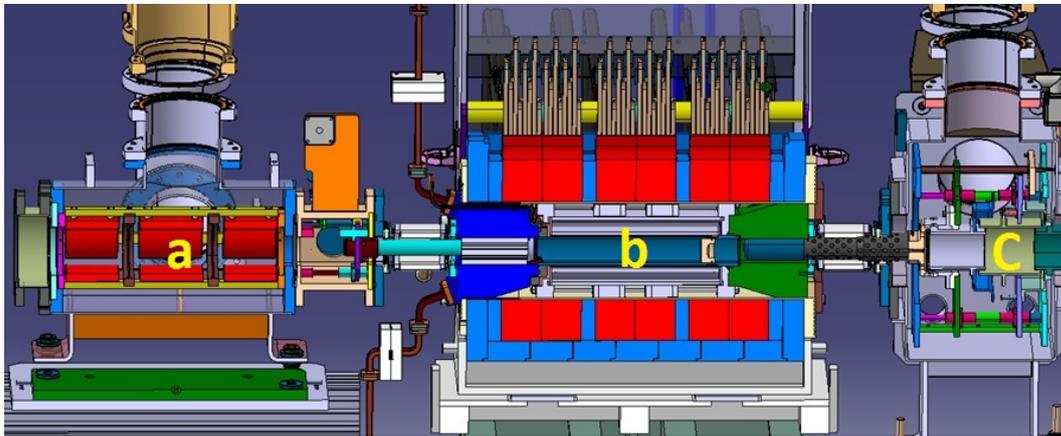
FIGURE 4.2: The 3D cross-section of SP1 ECR Charge Breeder (SP1 CB) (b) connected between electrostatic quadrupole triplet (a) and extraction einzel system (c).

It consists of pure aluminium plasma chamber surrounded by a permanent magnet hexapole. It is important to highlight a few key parameters which are needed for the production of high charge state ions: the injection optics system, the magnetic field, the operating frequency, residual gas pressure and the extraction optics system. These parameters are described in the following subsections. The configuration of SP1 CB allow the injection of 14.5 GHz microwaves through the rectangular wave guides and buffer gas through a controlled gas inlet. There is an additional RF port, which can be used to launch 8- 18 GHz waves in the plasma chamber. A cylindrical RF blocker, made up of a soft iron is installed at the injection to boost the magnetic field. The 1+ ion beam is injected through an injection aperture (ϕ = 28 mm) and the charge bred beam is extracted through a small round aperture ($\phi \approx$ 6 mm). It has been suggested that the emittance of the extracted charge bred beam should be low in order to minimize the ion losses downstream the charge breeder. Thus, the diameter of the extraction aperture is chosen according to the required emittance of the extracted beam. The $\sim$ 1.3 liter plasma chamber made of aluminium is placed beneath the hexapole. The important limiting characteristic of ECR charge breeders is the contamination which often deteriorates the performance. Several techniques have been employed to minimize the contamination and a few attempts are currently ongoing and demonstrated significant reductions in the background contamination level [83, 84].

4.1.1 The injection optics system

Figure 4.3 shows the injection system, which consists of a three set of electrostatic (ES) quadrupoles to focus and steer the beam towards the injection side of the SP1 CB. A close look of the electrostatic quadrupole triplet is shown in the figure 4.3.

The electrodes are installed symmetrically around the beam axis. For the first two quadrupoles, different polarities are given to the vertical and horizontal electrodes to focus the ion beam in transverse plane while defocusing in the other one. The third quadrupole is used as a combined focusing and steering of the 1+ beam towards the beam line axis. A proper focusing and alignment of the 1+ beam is necessary to avoid the losses near injection.
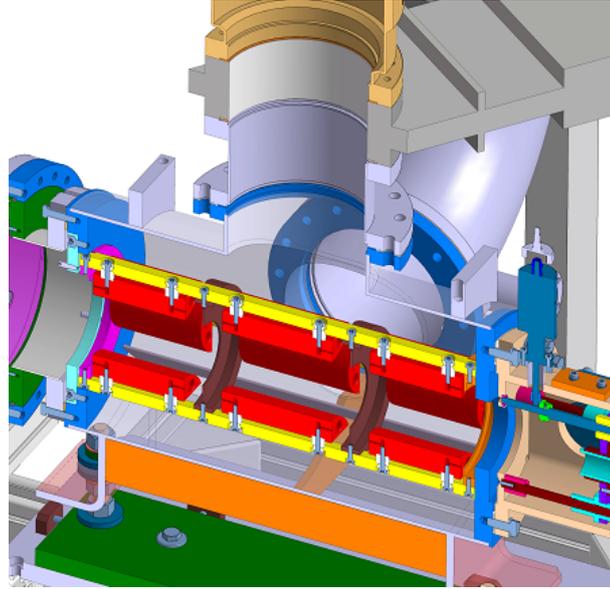
FIGURE 4.3: The 3D cross-section of electrostatic quadrupole triplet.

4.1.2 Deceleration tube

The focused 1+ ion beam from the electrostatic (ES) triplet enter the charge breeder plasma region through a aluminium tube called as "deceleration (grounded) tube". It has an inner diameter of 24 mm over 240 mm length. The 3D cross-section of the deceleration tube is shown in the figure 4.4.

The focused 1+ ion beam is decelerated due to the decelerating electric field and injected slowly into the plasma chamber. The tube has been installed on a movable platform and its optimum position has been found between 5 to 21 mm upstream the injection plug of the charge breeder. In T.Lamy et al [85], charge breeding experiments were performed by replacing the deceleration tube with a new large diameter electrode and obtained high efficiency yields.

4.1.3 The axial and radial magnetic field profile

The **"Minimum-B"** magnetic field structure is created by the three solenoid coils (axial field) and hexapole (radial field) magnet enclosed in an iron yoke. In this configuration, the magnetic field is minimum at the center of the plasma chamber and increases towards injection and extraction ends of the SP1 CB. Each solenoid coil consists of two water-cooled coil wrapped around a metallic core. The magnetic
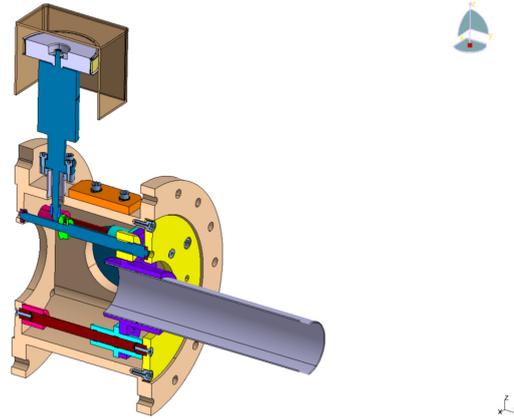
FIGURE 4.4: The 3D cross-section of the movable deceleration (grounded) tube.

field is produced when an electric current is passed through it.

Movable soft iron rings
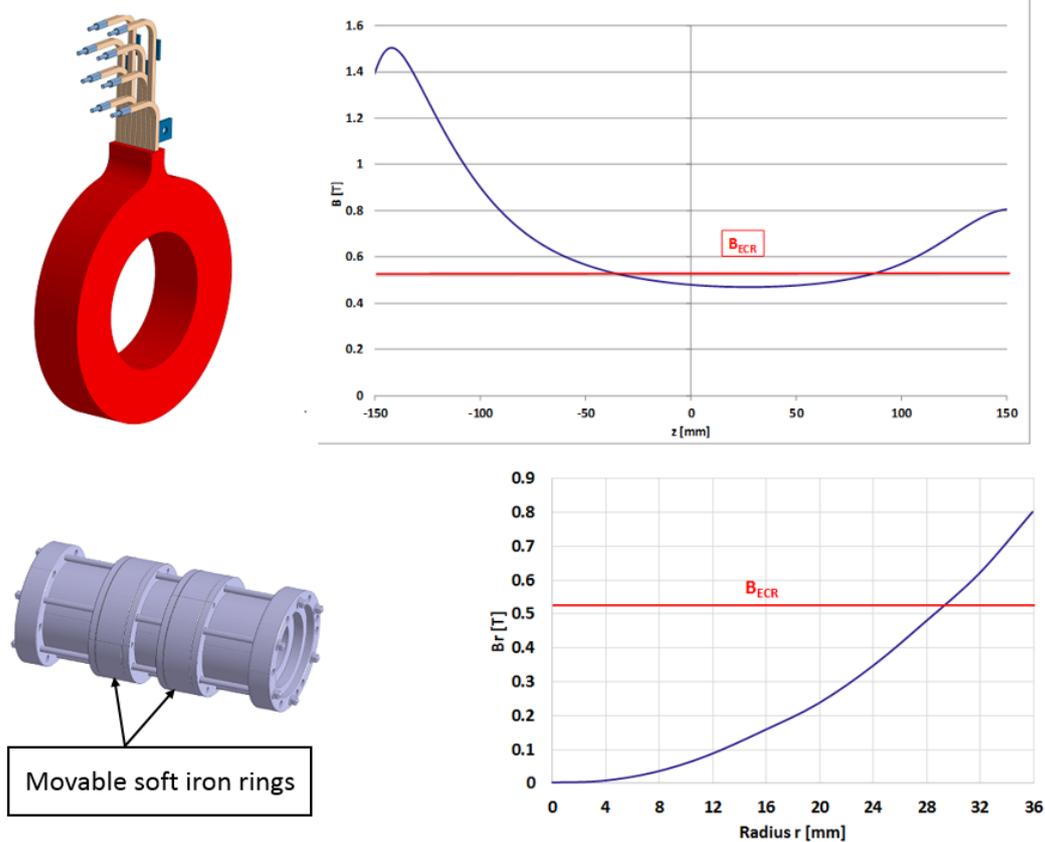
FIGURE 4.5: The axial and radial field profiles generated by the solenoid coils and hexapole magnet. The magnetic field at the injection, center and extraction of the SP1 CB is 1.49 T, 0.45 T and 0.8 T, respectively. The magnetic field corresponding to the ECR resonance (B_{ECR}) at 14.5 GHz is 0.519 T and it is indicated with a red line.

For example, the currents given to the solenoids at the injection, center and at the

extraction is 1200A/350A/700A, then the axial magnetic field profile is generated, as shown in figure 4.5. It is believed that the plasma is actually confined between the two maxima of the B-field. The plot of radial field is expressed as a function of the plasma chamber radius is shown in figure 4.5. The maximum field at the plasma chamber wall is ≈ 0.8 T.
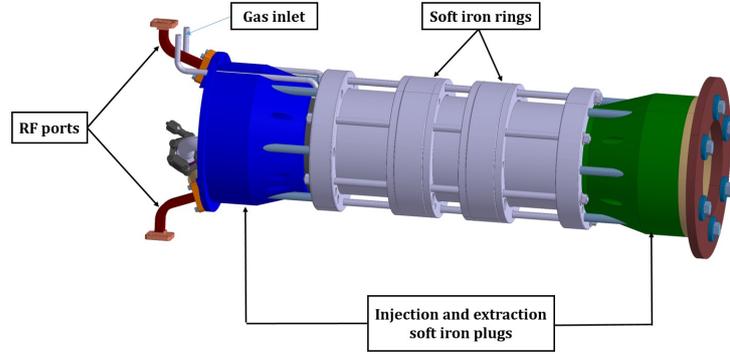
FIGURE 4.6: The central core of SP1 CB between injection and extraction soft iron plugs.

The figure 4.6 shows the central core of the SP1 CB connected between injection and extraction soft iron plugs. It also includes two movable soft iron rings around the central core to optimize the axial magnetic field gradient. The plasma chamber and the plasma electrode are enclosed by the hexapole, which is not shown in the figure 4.6. The hexapole is constructed as a closed Halbach structure [86]. During the operation, the central core, including the extraction electrode, is maintained at high voltage.

4.1.4 The operating frequency and pressure

To sustain the plasma inside the SP1 CB, there are two rectangular RF ports (shown in red color) near the injection side of the SP1 CB, as shown in figure 4.6. These ports allow the possibility to use two microwave injection frequencies. At present, only the primary port is being used to ignite and sustain the plasma in the 14.5 GHz band (up to 2 kW). The secondary port can be used to inject the microwaves between 8-18 GHz. To protect the amplifier from the reflected power coming from the charge breeder, the microwave signal is fed through a circulator. The effective power given to the plasma is measured by the two directional couplers, which will allow to measure the injected power P_{RF} and the reflected power P_r.

The support gas is injected into the plasma chamber through a gas inlet. Usually, Helium or Oxygen is used as a support gas. It has been observed experimentally that Helium is superior, in comparison to Oxygen, for optimizing the charge breeding efficiencies of ions up to mass number A < 40 (approximtely) [5]. In the case of heavier masses (such as Rb and Cs), Oxygen is preferred for the optimization of the high charge state extraction currents. The incident microwave power required to ignite the plasma depends on the nature of the support gas. For charge breeding, heavy gases are usually avoided to limit the contaminated peaks which are imposed on the desired charge state. The effect of different buffer gas on the charge states of potassium has been studied experimentally [70]. The charge state distribution of
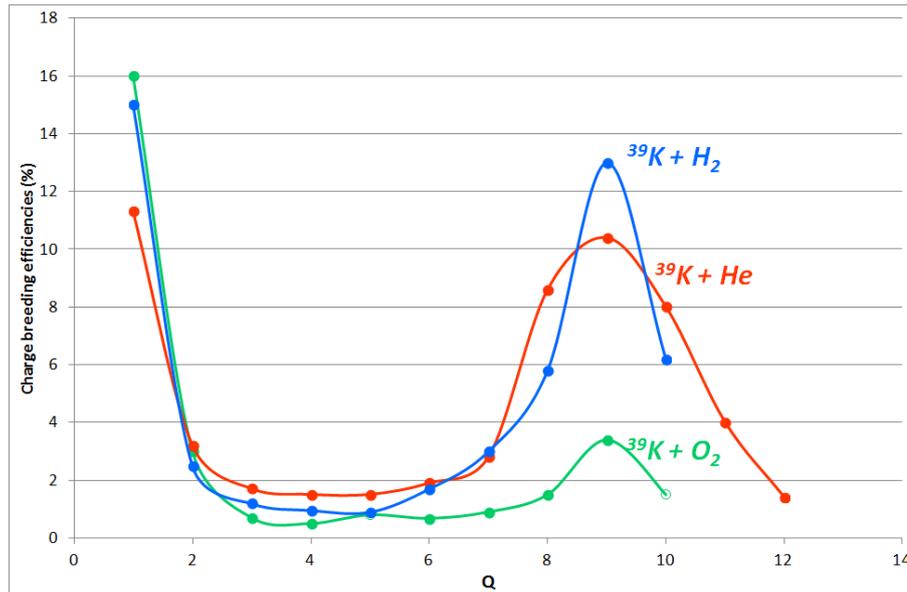
FIGURE 4.7: The effect of different buffer gas (O_2, He and H_2) on charge state distribution of ^{39}K [70].

potassium as a function of charge breeding efficiency is exhibited in the figure 4.7. The charge state distribution becomes narrow and exhibits high charge breeding efficiencies with the hydrogen plasma. The charge state distribution becomes wide and low charge breeding efficiencies are recorded while increase in the mass of the support gas. These trends are seen with potassium case but it may vary for other elements with different masses. In addition to this, the residual gas pressure is found to be a critical parameter for the improvement of charge breeding efficiency. In L. Maunoury et al [70], the effect of residual gas pressure on charge breeding efficiency has been studied. It has been demonstrated that the performance of the source increases at very low pressures (around 10^{-8} mbar). At present, the SPIRAL1 charge breeder is operated $\approx 3 \times 10^{-8}$ mbar regime with plasma and $\approx 1 \times 10^{-8}$ mbar without plasma.

4.1.5   The extraction system

The single gap extraction system consists of a puller electrode coupled with an electrosatic einzel lens as shown in the figure 4.8. The extracted beam from the charge breeder should have a low emittance to avoid further ion losses. This system is designed to control the extracted 1+/N+ ions. A positive potential is applied to the plasma chamber wall and the plasma electrode to extract the charge bred ions. The ion beam is formed in the gap between the plasma electrode and puller (grounded) electrode. The electric field created by the potential difference between these two electrodes accelerates the ion beam from the SP1 CB. The ion beam is focused by an einzel lens, which consists of three cylindrical symmetric electrodes. The device can deliver the beams with A/q values between 3 and 9 with an energy spread of (1-10)*q eV. Considering the variability of the expected A/q's and to match the injection energy of the CIME cyclotron, different extraction voltages are applied to the SP1 CB.

Plasma electrode   **Puller (grounded) electrode**   **Einzel lens**
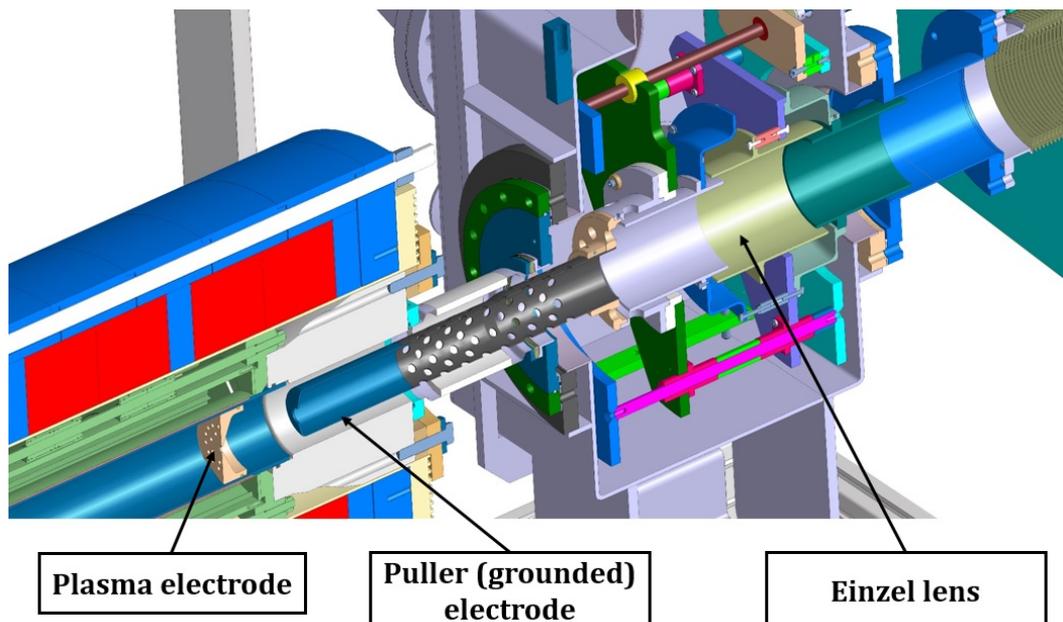
FIGURE 4.8: The 3D cross-section of an SP1 CB single gap extraction system: It includes a movable puller electrode and electrostatic einzel system.

4.2   SP1 CB installation in LEBT

The installation of SP1 CB in LEBT is described by figure 4.9. The production cave is equipped with TISS, which is able to produce stable and radioactive mono charged or multi charged ion beams. Different TISS used at SPIRAL1 production cave is discussed briefly in chapter 1. At present, the SP1 CB is being characterized with stable ion beams of different isotopes from the TISS.

FC13

FC14

FC31

Chopper

Magnetic mass analyzer (D1)   Injection optics   SP1 charge breeder (SP1 CB)   Extraction optics   N+ line Quadrupoles   Magnetic mass analyzer (D3)

FIGURE 4.9: The layout of SP1 charge breeder line from 1+ mass analyzer (D1) to Faraday cup 31 (FC31).

A mass analyzer dipole (a 90° focusing dipole D1) is used to select the desired 1+ ions. After the 1+ selection, the beam is properly focused by optimizing the electrostatic quadrupoles arranged in series along the beam line. Vertical and horizontal slits are used to define the emittance of 1+ beam and the beam profiles are monitored using profilers. It is very important to monitor the beam characteristics in order to determine its influence on the performances of the SP1 CB. The 1+ beam towards the entrance of the SP1 CB is checked by measuring the current on the Faraday cup (FC13) and then, it is slowly (at very low energy (few eV)) injected into the SP1 CB through an electrostatic quadrupole triplet and a deceleration (grounded) tube. The ES triplet focuses and aligns the 1+ beam towards the beam line axis and the tube decelerates the 1+ ions and allows them to interact with ECR plasma. After their capture with ECR plasma ions, they are charge bred to high charge states through step-wise ionization and extracted from the SP1 CB. The extracted beam is properly focused and the desired A/q ratio is selected by a 90° mass analyzer dipole (D3). The beam current of the selected high charge state is measured at Faraday cup FC31. The SP1 CB can be used as solenoid lens for transporting the singly charged RIBs to the tape station or to the LPCTrap device [87]. In future, a high resolution spectrometer will be developed at CENBG [88], which will be installed for removal of contaminants from the low energy RIBs before its use for the nuclear physics experiments at DESIR experimental area. The advantage of the SP1 CB is the high acceptance of 1+ beam (up to 50π .mm.mrad).
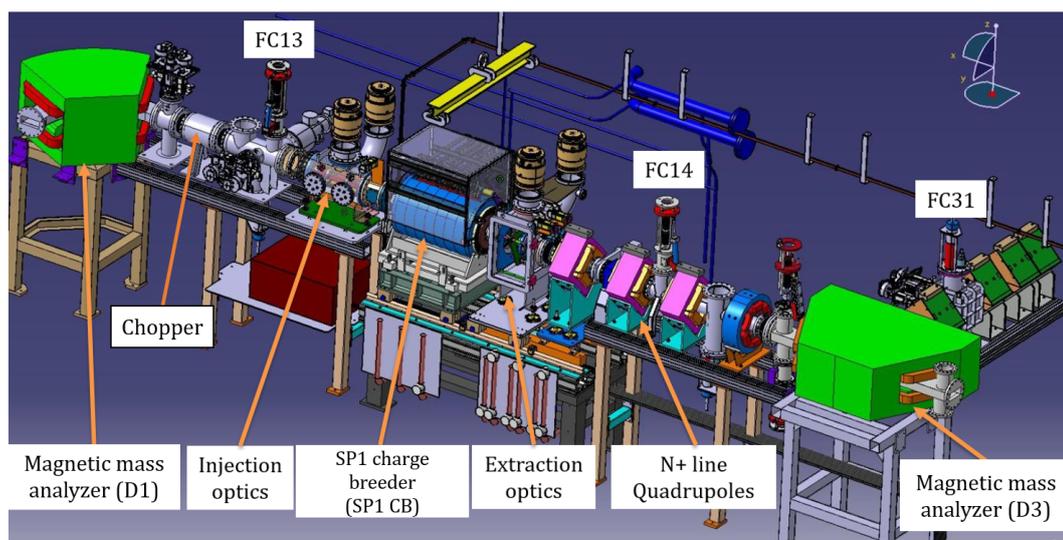
4.3   1+ to N+ technique

Before going into the details, it is necessary to discuss the calculation of charge breeding efficiency by properly regulating the voltages between the 1+ source and SP1 charge breeder. Figure 4.10 explains the scheme of potential distribution between the 1+ source and the SP1 CB. In SPIRAL1, a common power supply platform is being used to provide high voltages to the TISS (V_{1+}) and SP1 CB (V_{CB}). During the charge breeding, the high voltages applied to the two ion sources are equal (V_{1+} = V_{CB}). Due to the presence of plasma in SP1 CB, the 1+ ions should have a sufficient kinetic energy to overcome the positive potential barrier created by the plasma (V_P). Their energy can be controlled by an additional voltage supply to the 1+ source called ∆V. By properly regulating this parameter, the 1+ ions can be injected slowly into the SP1 CB plasma chamber. On the other hand, the voltage applied to SP1 CB is always fixed in order to maintain constant $B\rho$ downstream the charge breeder.

The 1+ to N+ efficiency depends on the injection efficiency, the 1+ ion capture efficiency, the ionization efficiency, the extraction efficiency and the transport efficiency downstream the charge breeder. The capture process plays a main role determining the global charge breeding efficiency η_g, which is traditionally defined as

$$\eta_g = \frac{\sum(I_q/q)}{I_{1+}} \tag{4.1}$$

In addition to the global efficiency, the charge breeding efficiency of a given charge state q is defined as the ratio between the number of ions extracted to the number of ions injected. This is expressed in terms of beam currents as
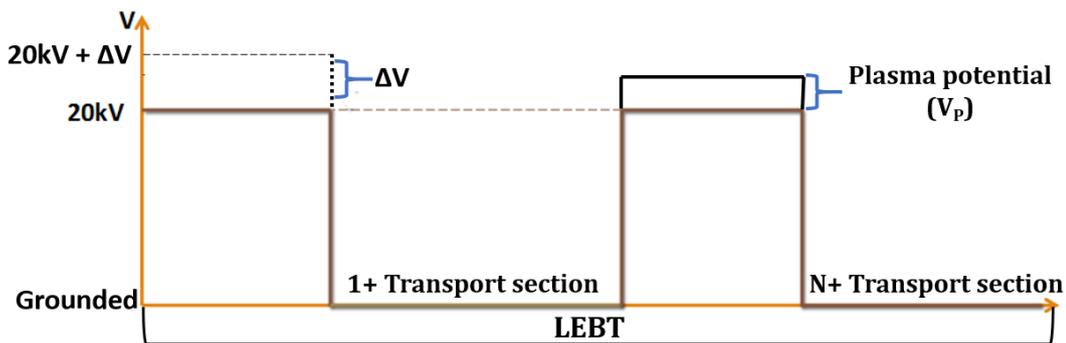
FIGURE 4.10: The potential distribution for 1+ source and SP1 charge breeder.

$$\eta_q = \frac{I_q/q}{I_{1+}} \qquad (4.2)$$

where I_q and I_{1+} are the extracted and injected beam currents.

4.3.1 1+ beam slowing down process in ECR plasma

The single charged ions entering the charge breeder are first slowed down by the decelerating electric field, and then they encounter multiple interactions with ECR plasma ions and electrons. Each collision of incident 1+ ion with a plasma ion or electron yields a small-angle deviation, but the cumulative effect is to give a large-angle scattering of 90° [89]. In early 1950's, Chandrasekhar has proposed the theory of long range interactions by studying the stellar dynamics [90, 91]. Later, Spitzer has applied the formalism to the Coulomb scattering of charged particles in plasma [92]. In this concept, he promoted that in strongly ionized plasma (ECR plasmas) the cumulative deflection due to small-angle, long-range scattering with plasma charges is larger than single two-body large angle scattering. These collective small-angle scatterings result in a 90° collisions. After a few of 90° collisions, the incident ions can be slowed down and thermalized (trapped) in the plasma.

In order to utilize the beam slowing down concept, a few suppositions are necessary for the model to be valid. Let us consider the injected test particles as **a** and the plasma particles as **b**:

- The injected particles **a** do not interact each other. In other words, the injected ion intensity should be a fraction of the buffer gas ions inside the plasma.

- The injected ions **a** interacts only with plasma particles **b** via 90° long range cumulative collisions.

- The plasma particles **b** have a maxwellian velocity distribution.

- The mean free path between 90° collisions is smaller than the actual size of plasma.

The two kinds of 90° plasma collisions are proposed in the Spitzer collision theory: the interaction of injected test particle **a** with a plasma ion and interaction of injected test particle **a** with a plasma electron. Considering the mean free paths between these interactions, one finds the ion (a)- ion (b) collision mean free path can become smaller than the size of the ECR plasma [93]. Therefore, the ion-ion interactions are responsible for ion slowing down process inside an ECR plasma. This process has been studied by Delcroix and Bers [94] and formulated a slowing down coefficient (in m/s^2) in ion-ion collision between incident ions **a** and plasma species **b** as

$$\frac{\langle \Delta v_{a'\parallel} \rangle}{\Delta t} = -\frac{n_b}{2\pi\epsilon_0^2} \left[\frac{Z_a Z_b e^2}{m_a \langle v_b \rangle} \right]^2 \left(1 + \frac{m_a}{m_b} \right) R(u_{ab}) \ln \Lambda \tag{4.3}$$

In the above formula n, Z, m and w are the plasma densities, charge states, masses and velocities of the a and b particles, respectively. The most probable speed of the Maxwelllian background plasma ions $\langle v_b \rangle = \sqrt{\frac{2kT_i}{m_i}}$. The equation 4.3 is valid for the ion velocity component parallel to the beam propagation. The parameter $R(u_{ab})$ depends on the ratio of the velocities of **a** and **b** particles and defined as

$$R(u_{ab}) = \frac{2}{\pi^{\frac{1}{2}}} \frac{1}{u^2} \int_0^u x^2 \exp^{-x^2} dx \tag{4.4}$$

with $u_{ab} = \frac{v_{a'\parallel}}{\langle v_b \rangle}$. The parameter $R(u_{ab})$ exhibits maximum when the ratio between the longitudinal component of incident ion velocity $\langle v_{a,\parallel} \rangle$, and the most probable speed of the plasma ions $\langle v_b \rangle$ becomes unity. In other words, the optimum of the slowing down occurs if the incident 1+ particles a enters into the b plasma ions, with a velocity approximately equal to the average velocity of the plasma ions b. The optimum injection energy for the best slowing down [69] can be written as

$$E_a = \frac{m_a}{m_b} (kT_i) \tag{4.5}$$

If we assume the temperature of Helium plasma ions is about 0.5 eV [69], the optimum slowing down for Na ions is ≈ 3 eV. Based on the beam slowing down theory, the adjustment of ΔV is crucial for the thermalization of 1+ beam inside the charge breeder plasma. If the velocity of the injected particle is high, they may hit the plasma chamber wall or escape from the plasma without being trapped. This case is different with noble gas ions because they can impinge on the plasma chamber wall, neutralize and can be recycled into the plasma. So, they can be charge bred even at higher injection energies (typically some tens of eV). As an example, Figure 4.11 shows the charge breeding efficiency as a function of incident 1+ ion beam energy (ΔV) for gaseous and metallic alkali ions. It can be seen that the ΔV curves are narrow in the case of condensable elements and wide in the case of gaseous elements.

Normally, SP1 CB is operated in CW mode, meaning that the ion injection is continuous. However, this device can also be operated in a pulsed mode where the injected ion beam is pulsed with an electrostatic deflector. The pulsing rate is driven by a TTL signal (a square signal) generated by a signal generator and the extracted N+ pulse is measured at the Faraday cup. In this way, the charge breeding time (capture
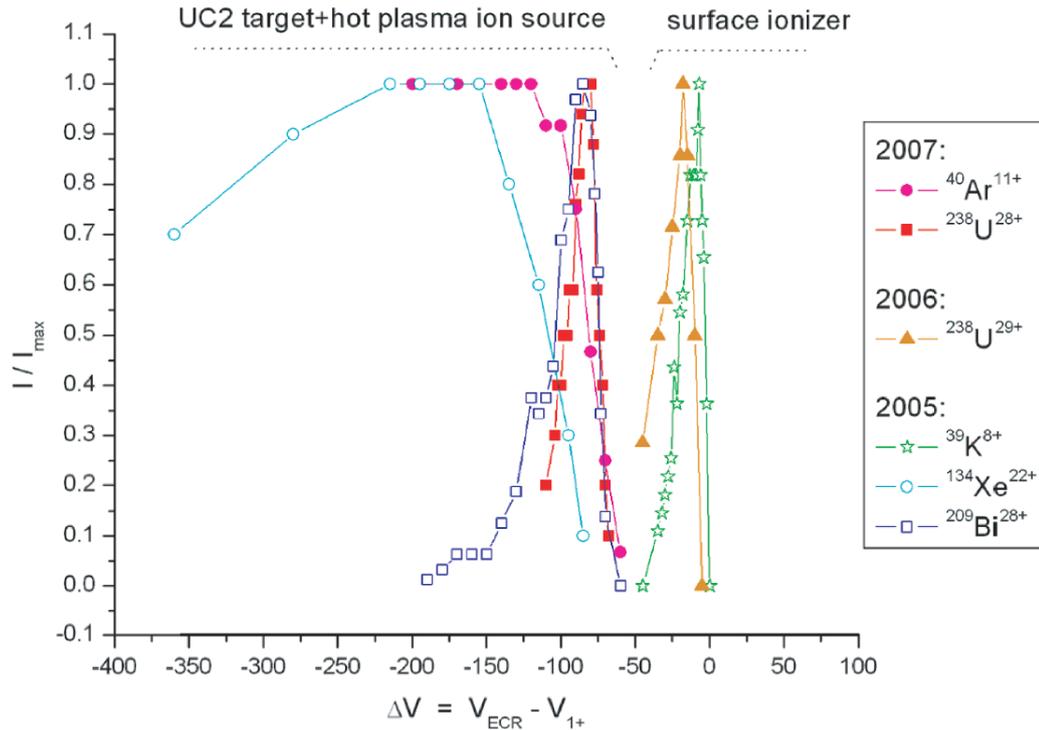
FIGURE 4.11: Normalized beam intensities as function of the potential difference between the 1+ source and the Phoenix ECR charge breeder. Reproduced from [12].

+ confinement + extraction) of a selected charge bred ions can be determined. This method also allows discriminating the extracted N+ beam current from the stable background currents which may have a similar A/q.

4.4   Possible modes to use SP1 charge breeder

Apart from 1+ / N+ technique, the SP1 CB at SPIRAL1 facility can be operated in different possible modes [79] to deliver the ion beams to the physicists as shown in figure 4.12.

In the first (a) and second (b) mode, the stable and radioactive ion beam (1+ or N+) from the TISS is transported through the SP1 CB. The high voltage of the CB and RF amplifier are switched off and only the magnetic field is used to guide the ion beam through 6 mm extraction aperture. In this mode, it is very important to maintain maximum transmission efficiency. Therefore, the ion optical elements in 1+/N+ beam line and the magnetic field of the SP1 CB are optimized before actually delivering the beams to the experimental areas. In the third mode (c), a high voltage of the SP1 CB and the RF amplifier are switched on, which means that the device is ready to charge bred the incident 1+ ion beam. The extracted stable and radioactive ion beams are transported towards CIME cyclotron and finally post accelerated to the experimental areas. In the fourth mode, the SP1 CB is operated as an injector. Since the ion source is operated using an ECRIS principle, the buffer gas is used to sustain the plasma and the element to be ionized needs to be introduced into the
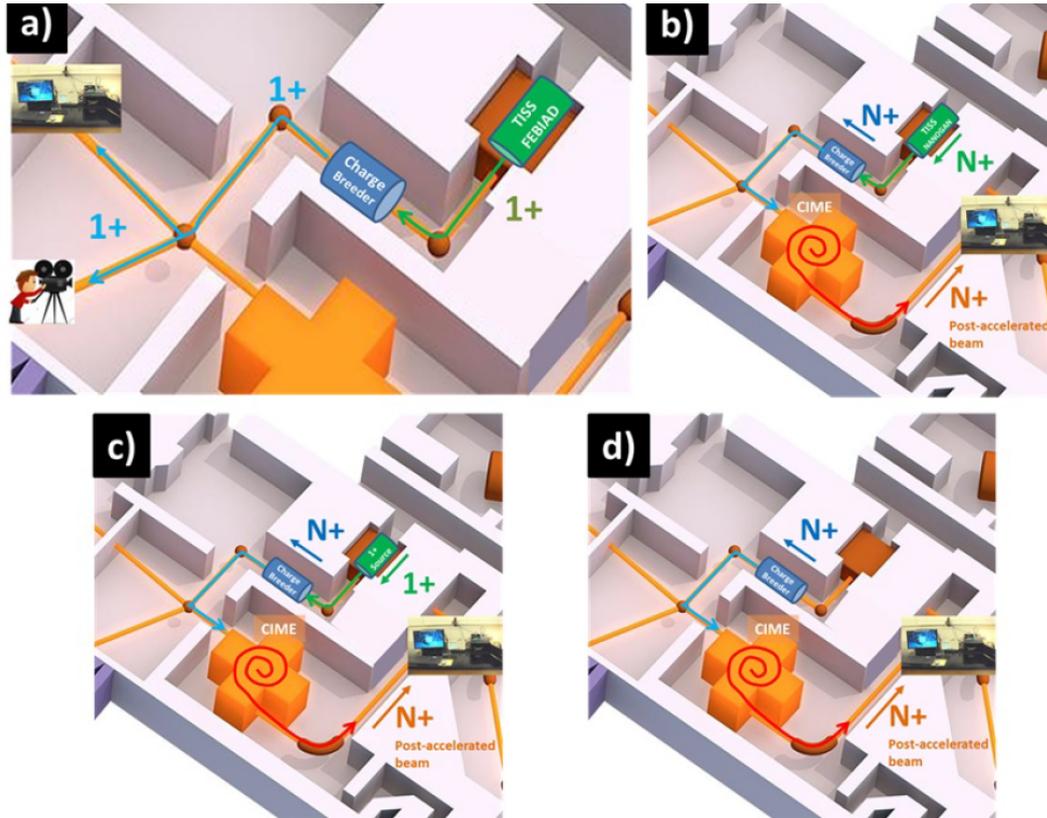
FIGURE 4.12: Operation of SP1 CB with different modes: a) 1+ shooting through, b) N+ shooting through, c)1+/N+ mode, d) SP1 CB as an injector [79]

plasma volume to undergo ionization and subsequent extraction. The desired extracted charge bred ions are selected by their A/q ratio and injected into the CIME cyclotron and finally, post accelerated them towards the experimental areas.

4.5 On-going R&D with SP1 Charge Breeder

4.5.1 Charge breeding efficiency improvement for light elements

Currently, investigations are being carried out to improve the charge breeding efficiency of light elements. In J. Angot et al [77], the high charge breeding efficiencies were obtained by improving the magnetic field at the injection of LPSC charge breeder. Similar modifications were implemented at the injection of SP1 CB, which improved the injection magnetic field from 1.38 T to 1.45 T. The modifications and the charge breeding efficiency experiments performed with this configuration are presented in the Ref. [33]

4.5.2 Two-frequency heating

This technique is initially implemented on the AECR (advanced ECR) ion source at Lawrence Berkeley National Laboratory by employing two power sources simultaneously heating the plasma electrons. This technique was employed by using a fixed frequency amplifier (klystron) as primary power source (14 GHz) and a variable frequency generator like Travelling Wave Tube Amplifier (TWTA) as a secondary power source (10 GHz). The operational performance of the source has been improved in terms of plasma stability, high charge states intensity and charge state distribution towards high charge states [95]. Several explanations have been proposed for the investigation of two frequency heating [46]. At Argonne National Laboratory, the effectiveness of two frequency heating has been studied with CARIBU ECR charge breeder [84, 96, 97]. The results from these experiments has shown a great improvement in achieving stable beam during operation, charge breeding efficiency and charge state distribution towards high charge states. Similar technique is being implemented with SP1 CB by injecting the TWTA as a secondary power source. Experiments to study the charge breeding efficiency as a function of two frequency heating will be studied in the beginning of 2020. This will open a new door for the ECR charge breeder community to investigate the effectiveness of this mechanism on the internal plasma parameters (such as electron and ion temperatures), confinement times, plasma kinetic instabilities etc.

4.5.3 1+ Beam as a diagnostic tool

In O. Tarvainen et al [98], it has been demonstrated that the 1+ beam can be applied as a probe for diagnostics of the ECRIS plasma parameters. This novel method allows one to estimate the mean free path, the lower limits of ion-ion collision frequencies and electron densities in the ECR charge breeder plasmas. Also, the interaction of 1+ ion beam in an ECR plasma has been numerically studied [99] by implementing a formalism based on the Langevin equation [100]. The observed experimental changes were reproduced by propagating the 1+ ions through background ECR plasma model. Coming back to the work presented in this thesis, the injected ion beam dynamics of the 1+ → N+ process has been investigated based on the concepts presented in the above experimental and numerical studies. The physical mechanisms behind the 1+ → N+ process has been studied by a full six-dimensional (6D) phase space Monte Carlo charge-breeding simulation code (MCBC) [101, 102], developed by Far-Tech, Inc [103]. The simulation code models Coulomb collisions of the injected 1+ ion beam in an ECR plasma and atomic processes which includes ionization and charge exchange. Several experimental studies were performed with SP1 CB and gathered data for the MCBC simulations. Before going in to the investigations of these experimental and simulation studies, detailed information on the beam capture theory in MCBC code is presented in the following section.

4.6 Description of ion transport and charge breeding simulation tools

4.6.1 SIMION

SIMION 8.1 is a ion optics code which is widely used to simulate the charged particles under the influence of electric and magnetic fields [104]. The code provides a graphical use interface (*ion optics workbench*) to create and modify the electrostatic and magnetic potential arrays (PA). In PA's, the array of points are organized into 3D cubic grids. Each array point have a potential and can be classified as an *electrode* or *non-electrode*. The group of electrode points create an electrode. Normally, PA's can be created either in SIMION or through the geometry files (.gem format) written by the user. Also, this code has an option to convert the CAD files (.STL format) into PA's. The created PA's can be utilized as a planar (2D and 3D arrays) and cylindrical symmetries (2D arrays).

The array points in the workbench volume are automatically scaled to 1mm/grid unit. The potential at any point within the electrode can be calculated by solving the Laplace equation. The Laplace equation constrains all the potential fields to a zero volume density assumption (no space charge). For example, the equation is satisfied when the potential of any point is approximated as the average of its four nearest neighbour points. Once the equation is solved, SIMION can scale the potentials for different voltages applied to the respective electrodes. This is called as *fast adjusting*. To fly the particles through these electrodes, the particle initial conditions are defined either by uploading a particle definition file (.ION format) or using an option "*define particles*". In this work, the ions are initiated by uploading an input file, containing the beam characteristics, which are externally calculated using TraceWin [105]. With the acquired beam properties (particle position and velocities), they can be flown in the workbench and their trajectories are calculated by using a fourth order Runge-Kutta method.

Moreover, SIMION provides a very important feature called *workbench program* written by the user in the scripting language *Lua*. It provides an access to record the ion parameters at various stages during the ion flight. The user can also control the electrode voltages, redefine the particle parameters at various stages and perform many other tasks. In this work, this feature is used to calculate the ion losses at different locations during the transport, to obtain beam characteristics at the preferred locations and finally to calculate and export the 3D electric field for the charge breeding simulations. These features are discussed in the following chapter.

4.6.2 Monte Carlo charge breeding code (MCBC)

The full 3D3V Monte Carlo charge breeding code has been developed by an American based company "*FAR-TECH, Inc.*" in collaboration with ion source group from Argonne National Laboratory (ANL). The developed code investigates the interaction and capture of 1+ beam by an ECR plasma [101, 102]. MCBC tracks the trajectories of injected 1+ ions under the influence of electric and magnetic fields in an ECR plasma, models the Coulomb collisions and atomic physics processes (electron impact ionization and charge exchange recombination) until the ions are captured or

lost. As a case study, MCBC simulations were carried out on the ANL-ECR charge breeding experimental results [102] and compared the simulation results with the experimental data. MCBC has accurately predicted the peak of highly charged state in the charge state distribution. In accordance with our request, the MCBC code has been upgraded with a few features: the code can give the extracted particle positions, velocities and energies in a separate output file and also allows the user to define the diameter of the plasma electrode.

MCBC beam capture modeling

This section gives a detailed introduction about modelling of beam capture dynamics in MCBC. In an ECR charge breeder, the charge breeding works effectively when the injected ions are decelerated and captured in the plasma. The longer they stay in ECR plasma the higher the chance for them to become highly charged. As the injected ions propagate through ECR plasma, they collide with plasma electrons and ions. Now, let us focus on how the beam slowing down is modelled in MCBC.

When the injected test particles enter the plasma, they are first slowed down and diffused in velocity space due to multiple interactions with the particles in the background plasma. In the model, the density of injected ions is assumed to be much smaller than that of background plasma ions (i.e., no interaction between injected ions). The beam dynamics between two successive collisions observe the following equation of motion [101]:

$$m_a \frac{d\vec{v}}{dt} = q_a \vec{E}(\vec{r}) + q_a \vec{v} \times \vec{B}(\vec{r}) + Coulomb\ collision \tag{4.6}$$

where m_a are q_a are the mass and charge of the injected test particle (a), $\vec{r}$ is the position vector, $\vec{v}$ is the velocity vector, $\vec{E}$ = -$\nabla \phi$ is the electric field and $\vec{B}$ is the external magnetic field. The equations are solved by fourth order Runge-Kutta method. In MCBC, the formulations given by Tribnikov [106], summarized in NRL formulatory [107] and also in [44, 108], are used to treat the effect of Coulomb collisions on the injected test particle (a) of mass m_a and charge Z_a propagating with a velocity (v_a) through a Maxwellian background plasma particles b of mass m_b and charge Z_b. In these formulations, the rates for the slowing down (ν_s), perpendicular diffusion ($\nu_\perp$) and parallel diffusion ($\nu_\parallel$) resulting from the collisions of a test particle (a) on a Maxwellian background plasma particles (a) are given as

$$\frac{dm_a v_a}{dt} = -\nu_s^{a/b} m_a \vec{v_a} \qquad \longrightarrow \qquad beam\ slowing\ down$$

$$\frac{d}{dt}(\vec{v_a} - \langle \vec{v_a} \rangle)_\perp^2 = \nu_\perp^{a/b} \vec{v_a}^2 \qquad \longrightarrow \qquad transverse\ diffusion \tag{4.7}$$

$$\frac{d}{dt}(\vec{v_a} - \langle \vec{v_a} \rangle)_\parallel^2 = \nu_\parallel^{a/b} \vec{v_a}^2 \qquad \longrightarrow \qquad Parallel\ diffusion$$

in which $\vec{v_a}$ is the average velocity of the test particle, $(\vec{v_a} - \langle \vec{v_a} \rangle)_\perp^2$ and $(\vec{v_a} - \langle \vec{v_a} \rangle)_\parallel^2$ indicate the diffusion spread of the test particle velocity in directions perpendicular,

parallel to its direction of motion. The relevant scattering rates are given as

$$\nu_s^{a/b} = \left(1 + \frac{m_a}{m_b}\right)\psi(x)\nu_0^{a/b}$$

$$\nu_\perp^{a/b} = 2\left[\left(1 - \frac{1}{2x}\right)\psi(x) + \psi'(x)\right]\nu_0^{a/b} \tag{4.8}$$

$$\nu_\parallel^{a/b} = \left[\frac{\psi(x)}{x}\right]\nu_0^{a/b}$$

The parameter $\psi(x)$, originated from the work on stellar collisions [90, 91], is conveniently written in terms of Maxwell integral:

$$\psi(x) \equiv \frac{2}{\pi}\int_0^x dt\sqrt{t}e^{-t}, \tag{4.9}$$

which has the properties

$$\psi' \equiv \frac{d\psi}{dx} = 2\sqrt{\frac{x}{\pi}}e^{-x}, \qquad \psi + \psi' = erf(\sqrt{x}) \tag{4.10}$$

in which $x \equiv x^{a/b} = \frac{m_b v_a^2}{2kT_b}$. m_b and kT_b are the mass and temperature of background plasma particles. Due to the difference in the mass, the beam slowing down due to the Coulomb collisions with plasma electrons is orders of magnitude smaller than slowing down due to collisions with ions. Therefore, the slowing down mechanism due to plasma electrons in MCBC is neglected. The function $\psi(x)$ shows a maximum ($x = 1$) when the test particle velocity is equal to the most probable thermal speed of background plasma ion. The term $\nu_0^{a/b}$ refers to the fundamental Coulomb collision frequency [109] for all the processes in the equation 4.8 is written as:

$$\nu_0^{a/b} = \frac{4\pi Z_a Z_b n_b \ln \Lambda_{ab}}{\{4\pi\epsilon_0\}^2 m_a^2 v_a^3} \tag{4.11}$$

The notations in the above equation are: m_a and m_b are the masses of the test particles (a) and plasma particles (b), kT_i is the plasma ion temperature, n_b is the plasma density, $\ln \Lambda_{ab}$ is the Coulomb algorithm and Z_a and Z_b are the charge states of the test particle (a) and plasma particles (b), respectively.

Monte Carlo Coulomb collision operator

The equations 4.7 and 4.8 provides a complete and useful description of the evolution of the test particles (a) suffering Coulomb collisions with background plasma ions. Applying these equations, Boozer [110, 111] has derived a convenient long range Coulomb collision formula for Monte Carlo simulations of beam slowing and scattering. In the collision operator, the collisions are represented in two separate operations: the first is the change in injected ion velocity vector without changing its magnitude, and the second is change in energy as a consequence of beam slowing down and energy diffusion. The pitch angle scattering operator relates the old (previous time step) velocity (v_{old}) of the injected ion and the new (after a time step

τ) velocity (v_{new}) as

$$v_{new} = \left(1 - \nu_\perp \frac{\tau}{2}\right) v_{old}\hat{v} + \sqrt{\left(1 - \frac{1}{4}\nu_\perp\tau\right)\nu_\perp\frac{\tau}{2}}(\pm\hat{\varphi} \pm \hat{\theta}v_{old}) \tag{4.12}$$

In the above formulation, $\hat{v} \equiv v_{old}/|v_{old}|$, $\hat{\varphi}$ and $\hat{\theta}$ are the orthonormal vectors in velocity space, $\nu_\perp$ is the ion-ion collision frequency perpendicular to beam direction. Each $\pm$ refers to the random choice in either direction on each time step τ with equal probability of each sign. The equation 4.12 only changes the direction of ion velocity while conserving the ion energy. The second operator which change the magnitude by collisional drag is given as

$$E_n = E_o - \frac{2\nu_s^{a/b}\tau}{1 + m_b/m_a}\left[E_o - \left(\frac{3}{2} + \frac{d\ln\nu_s^{a/b}}{d\ln E_o}\right)T_i\right] \pm 2\sqrt{\frac{T_i E_o \nu_s^{a/b}\tau}{1 + m_b/m_a}} \tag{4.13}$$

with $E \equiv \frac{1}{2}mv_b^2$ the kinetic energy. The notations in the above equations are conventional; v, E_o, m_i, and m_b are, respectively, the 1+ ion beam velocity, old (previous time step) ion energy, mass of plasma ion and mass of injected ion. The first term in the equation 4.13 describes the ion beam slowing down, the second term describes the diffusion of the injected beam energy and the $\pm$ sign refers to a random choice in either direction on each time step τ with equal probability of each sign. It is to be noted that the mass dependence in the equation 4.13, which is not appeared in Boozer's formula, was added to accept the different masses of injected 1+ ion beams and the plasma ions [101]. Finally, the full time step τ for Coulomb collisions first chooses a new direction for the ion velocity using the Monte Carlo angular scattering operator and then chooses a new magnitude for the velocity with the energy scattering operator.

Modeling of atomic physics processes in MCBC

In addition to the Coulomb collisions, the collisions due to atomic physics process such as electron impact ionization and charge exchange and recombination are included in MCBC. The formulations given by Lotz and M*ü*ller were used to model the step-wise electron impact ionization and charge exchange recombination. The ionization rates are calculated from these cross sections. MCBC assumes the collisions as a discrete and thus are treated in probabilistic way by using a rejection technique. The probability of a 1+ ion beam collision with other particles in the ECR plasma during a time interval of Δt is given by

$$P_m = 1 - \exp(-\nu_{total}\Delta t) \tag{4.14}$$

where the total collision frequency ν_{total} summed over all types of collisions as

$$\nu_{total} \approx n_n\sigma_{ion}v + n_n\sigma_{cx}v + n_n\sigma_{rec}v \equiv \nu_{ion} + \nu_{cx} + \nu rec \tag{4.15}$$

The notations in the equation 4.15 are: σ_{ion} the ionization cross section, σ_{cx} the charge exchange cross section, σ_{rec} the recombination cross section, n_n neutral density and v the relative velocity of two colliding particles. The next step determines which scattering process occurs. This is implemented by lining up the relative cross sections from 0 to 1, i.e. 0, $n_n\sigma_{ion}v/v_{total}$, $(n_n\sigma_{ion}v+n_n\sigma_{cx}v)/v_{total}$,.....,1. Then, the simulation uses a uniform random number to choose the type of collisions. The size of each time step in the Coulomb collision operator is chosen to be small compared to the shortest time scale for changes in the ion beam trajectory. In MCBC, three time scales are considered. The first time scale is a combination of short range collisions times and the cyclotron period, which is expressed as

$$\tau_1 = \frac{1}{\nu_{ion} + \nu_{cx} + \nu_{rec} + \frac{\omega_b}{2\pi}} \tag{4.16}$$

where the times are for ionization, charge exchange, recombination and ion cyclotron frequency. The size of the time step is chosen to be shorter compared to the above mentioned time scales for the changes in the trajectory. The second and third are time for the injected test particles to slow down due to Coulomb collisions and perpendicular velocity diffusion time. These time scales are determined from the equations 4.8.

MCBC simulation procedure and output

MCBC considers the simulation domain extending from the entry of ECRIS plasma chamber to the plasma electrode. The general input parameters for MCBC are specified in a separate input file where the beam properties and ECR device parameters are defined. The first step of the simulation procedure is to model ECR plasma by creating the simplified 3D ECR plasma parameters profiles (plasma density, electron temperature, ion temperature and average effective charge of ECR plasma). The 3D magnetic and electric fields are also included in the simulation domain. The simulation follows the trajectories of the test particles, entering the ECR plasma column, until they are slowed down to the background plasma ion speed (captured), hit far end of the device, lost to the radial wall or reflected back towards the injection aperture. The fraction of particles that are back streamed (f_{back}), lost to the walls (f_{lost}), reach the plasma electrode (f_{Exit}) and captured while propagating through an ECR plasma (f_{trap}) are given by

$$f_{Lost} = \frac{N_{Lost}}{N_a} \qquad f_{Exit} = \frac{N_{Exit}}{N_a} \qquad f_{Back} = \frac{N_{Back}}{N_a} \qquad f_{Trap} = \frac{N_{Trap}}{N_a} \tag{4.17}$$

where, N_a is the number of particles injected into the simulation and N_{back}, N_{lost} and N_{capt} are the number of particles that are back streamed, lost to the walls and number of particles captured in the ECR plasma, respectively.

Figure 4.13 presents the sample print out at the end of the simulation run. On the first line, the number of injected ions (*Nion*), moving time of the last ion (*Time*) and the number of steps traced for the last ion (*Itime*) are displayed. The second and third lines display the percentages of ions that are lost to the wall (*lost*), ions that are at the extraction end (*Exit*), come back to the injection end (*Back*), ions that are captured in

```
-------------------------------------------------------------
  Nion =    2000,   Time = 0.145E-03    I_time=       123

  Lost = 13.20%,   Exit = 13.10%,   Back =   0.00%
  Trap = 73.15%,   Move =  0.00%,    Neu =   0.55%
  1+ = 33.55%,     2+ = 34.40%,     3+ =   4.95%
  4+ =  0.15%,     5+ =  0.00%,     6+ =   0.00%

-------------------------------------------------------------
```

FIGURE 4.13: Summary display on the screen at the end of the charge breeding simulation.

the plasma (*Trap*), ions that are still moving in the plasma when the maximum time step is reached (*Move*) and ions that are neutralized (*Neu*). The last two lines display the percentage of the ions in these charge states when they are captured (1+....N+). The efficiency of the extracted charge bred ion can be calculated as

$$\eta_{cb} = \frac{number\ of\ charge\ bred\ ions}{number\ of\ injected\ particles} = \frac{N_n/n}{N_i} \tag{4.18}$$

where N_n is the number of charge bred ions of charge state n and N_i is the number of ions injected into the model. MCBC generates the output files which consist of the profile of captured test ions and diagnostics data. In the following chapter, a brief description of the experimental and numerical simulation studies performed with SP1 CB during the commissioning of upgraded SPIRAL1 facility is given. The 1+ beam transport and the physical mechanisms involved in charge breeding process are briefly investigated using the simulation tools introduced in this chapter.

5 Experimental and numerical studies with SP1 ECR charge breeder

The main goal of this work is described in this chapter: the commissioning of SP1 CB in Low Energy Beam Transport (LEBT) line associated with numerical simulations to understand the ion transport in LEBT and to study the ECR plasma by introducing the 1+ ion beam as a probe. In 2017, the commissioning phase was initiated to validate the SP1 CB performance. The work will focus on stable alkali metal (A < 40), which represents typical masses of the targeted RIBs. Measurements with stable ions allow fine tuning of the injection optics and optimal ΔV. The optimization of injection optics and ion source parameters with the stable beams constitutes the starting conditions to perform the measurements with radioactive ions (A < 40).

5.1   Investigations on SP1 CB axial magnetic field

5.1.1   Validation of SP1 CB axial magnetic field

After the installation of SP1 CB in LEBT, the commissioning phase has been initiated by performing the measurements to study the SP1 CB axial magnetic field. The goal of this measurement is to verify the magnetic field generated by the three solenoid coils in SP1 CB and to validate a numerical model of the SP1 CB magnetic system. The numerical model is used to produce realistic 3D magnetic field maps for the ion transport and charge breeding simulations.

The magnetic field measurements were performed with a F. W. Bell Inc. Model 615 Gaussmeter. The photo of the measurement setup is shown in figure 5.1. A cylindrical shaped triaxial probe with 8 mm diameter was connected to the Gaussmeter. A mu-metal [112] (black color), shown in the figure 5.1 (left), was used to shield the probe tip to achieve zero field during the time of calibration. The probe tip was initially introduced from the extraction side of the SP1 CB and moved towards the injection plug. When the probe tip is in contact with the injection iron plug, the closest B_z value is measured 1.5 mm from the plug surface. This is very close to the location of the center of the injection solenoid coil and thus gives a good approximation of maximum B_z seen by the plasma. The B_z measurements were performed by varying the injection, center and extraction coils currents. The coil power supplies can provide highest coil current values (1200 A at the injection, 500 A at the center and 1200 A at the extraction).
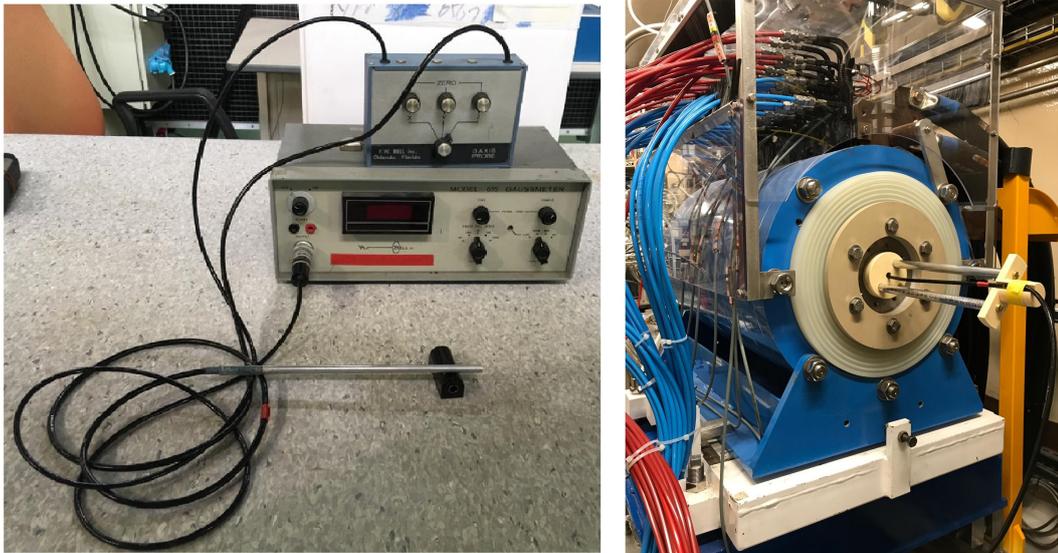
FIGURE 5.1: Axial magnetic field measurement setup (left). Insertion of a probe into the SP1 CB from the extraction side (right).

Comparison of the experimental values with a numerical model

The SP1 CB magnetic system has been built using Radia [113]. Radia is a package, which can interface with Wolfram Mathematica [114], for fast and accurate 3D magnetostatic computations. The geometry of the magnetic model is shown in the figure 5.2.
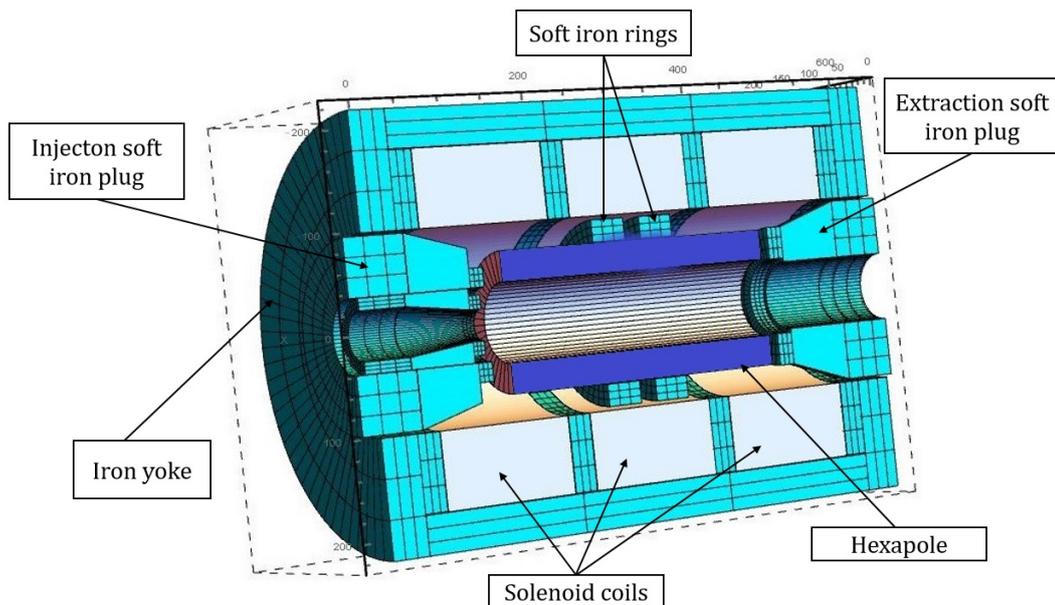
FIGURE 5.2: SP1 CB magnetic model built using Radia.

The model includes all of the magnetically relevant parts of SP1 CB, i.e., the soft

iron parts (green), the hexapole (blue) and the coils (light grey). The dimensions of the model are gathered from the existing drawings of the SP1 CB. In the numerical model, a nonlinear isotropic magnetic material has been used to represent the iron parts. The measured axial magnetic field case was calculated with the model, and the results are presented in figure 5.3 with the corresponding experimental data. The corresponding uncertainty in the readings is estimated to be less than 1%.
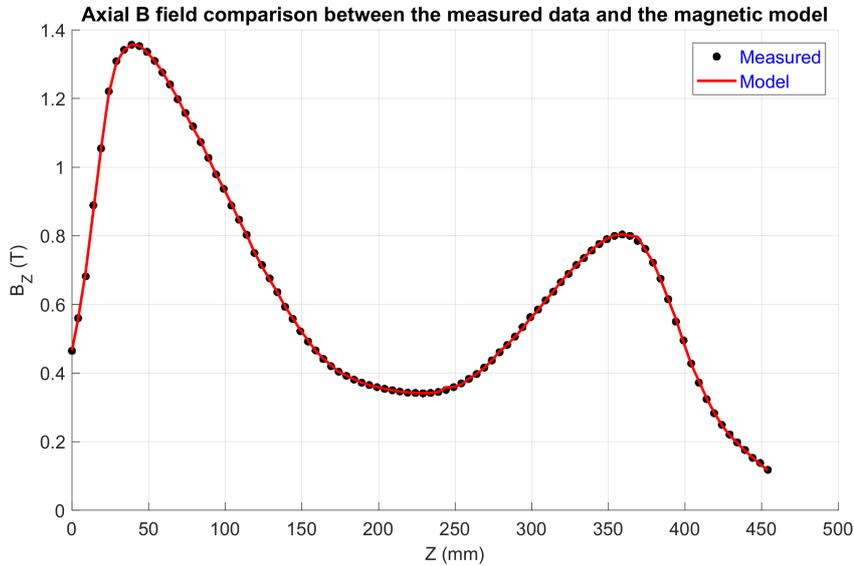

FIGURE 5.3: Measured axial magnetic field profile compared to the values given by the numerical model of the SP1 CB magnetic system. The coil currents used in measurements are 1200 A (inj)/250 A (center)/700 A (ext).

As is seen from the figure 5.3, the numerical model of the SP1 CB magnetic system is able to recreate the measured axial field results. The model benchmarks well with the measured data and as such can be considered as a valid input for the SP1 CB numerical simulation studies.

5.1.2 Modification of axial magnetic field gradient

In ECR ion source based charge breeders, the "Minimum-B" configuration is essential to form a closed resonance surface in the plasma chamber where the ECR condition is fulfilled. In SP1 CB, this configuration is created by three independent solenoid (axial field) and hexapole (radial field) magnets enclosed in an iron yoke.

The axial magnetic field gradient at the resonance can be adjusted by the two movable soft iron rings around the hexapole as shown in the figure 5.4. The magnetic field calculations were performed using the numerical model of SP1 CB magnetic system, to study the axial magnetic field profile by adjusting the iron rings to different positions. The B_z profiles for different rings positions are shown in the figure 5.5.

The B_z profiles shows significant variations in the size of ECR zone in axial direction. The effect of these variations was investigated by performing charge breeding
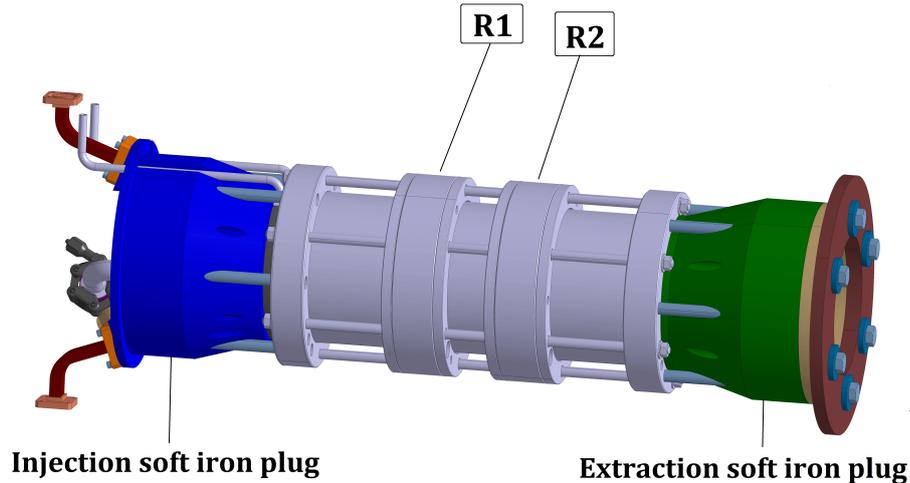
FIGURE 5.4: The two soft iron rings (R1 and R2) around the hexapole.
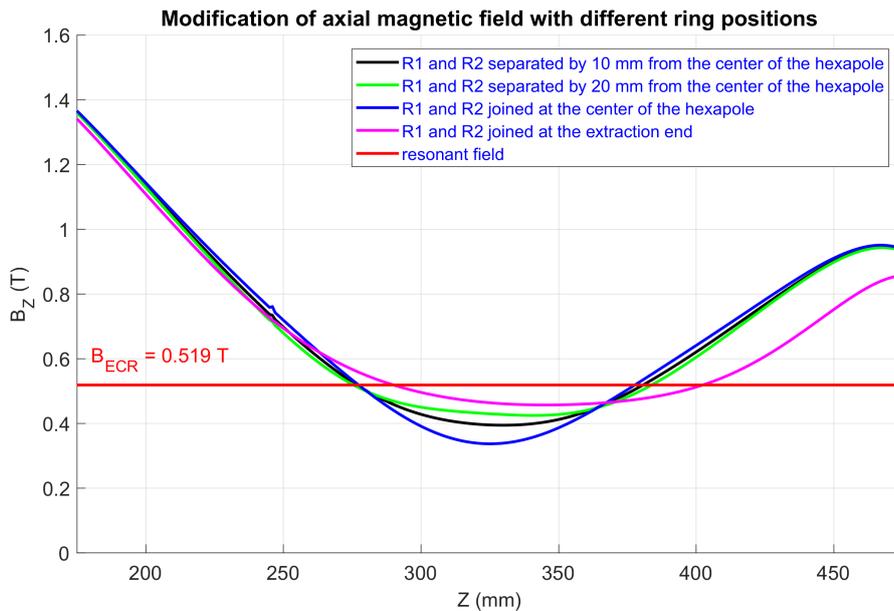
FIGURE 5.5: Axial B fields with different positions of the two soft iron rings. a) rings separated by 10 mm from the center (Black) b) rings separated by 20 mm from the center (green) c) two rings touched at center (blue) d) two rings at the extraction of CB (magenta). Center refers to the center of plasma chamber (320 mm).

efficiency measurements with K^+ beam. At the beginning of the measurements, the two soft iron rings (R1 and R2) were pushed towards the extraction end of the SP1 CB. This configuration is currently being used in LPSC PHOENIX charge breeder [115, 116] and found maximum charge breeding efficiencies for Sodium beams. The device has been optimized to extract K^{9+} with an efficiency of 7.44%. Later, the rings were axially pushed to different positions around the hexapole. The best charge

breeding efficiency has been found when the rings R1 and R2 were separated by 10 mm from the middle of the hexapole. The charge breeding efficiencies on $^{39}K^{9+}$ with different positions of two soft iron rings are shown in the table 5.1.

TABLE 5.1: $^{39}K^{9+}$ Efficiency measured at different rings positions. Center is referred as center of plasma chamber (320 mm)

Rings position	$^{39}K^{9+}$ *efficiency*
R1 and R2 at extraction	7.44 %
R1 and R2 centered	10.08 %
R1 and R2 separated by 20mm from center	10.88%
R1 and R2 separated by10mm from center	11.6%

As a result, this configuration has increased the charge breeding efficiency by a factor of ≈ 1.6. Therefore, this configuration has been maintained for further charge breeding measurements. The associated relative uncertainties are estimated in the following sub-section.

5.2 Experimental activities with SP1 ECR charge breeder

In the following, the transmission and charge breeding efficiencies are estimated during the optimization of SP1 CB. During the experiments, the extracted 1+ and N+ ion currents from the thermionic gun and the SP1 CB are subjected to significant uncertainty. This is may be due to the degradation of the pellet installed in the ion gun and also the SP1 CB operating conditions, which may cause the extracted N+ currents unstable. Therefore, the relative uncertainties associated to the charge breeding efficiencies are estimated. In this work, the SP1 CB has been operated in two different modes: shooting through mode (SP1 CB switched OFF) and charge breeding mode (SP1 CB switched ON). In the first mode, the 1+ ions from the thermionic gun were directly transported through the SP1 CB extraction system and the transmission efficiencies are calculated using the relation:

$$\begin{cases} \epsilon_{transmission} = \dfrac{I_{out}}{I_{injected}} \\[2ex] \dfrac{\Delta\epsilon_{transmission}}{\epsilon_{transmission}} = \sqrt{\left(\dfrac{\sigma_{I_{out}}}{I_{extracted}}\right)^2 + \left(\dfrac{\sigma_{I_{out}}}{I_{injected}}\right)^2} \end{cases} \quad (5.1)$$

where, $\sigma_{I_{out}}$ is the absolute error in the 1+ current coming out from the SP1 CB and $\sigma_{I_{injected}}$ is the absolute error in the 1+ current injected into the SP1 CB. In the second mode, the 1+ ions are extracted from the ion gun and injected in to SP1 CB, where the charge state is increased to q. The extracted q+ current is measured after the mass separation. In this case, the charge breeding efficiencies are calculated as

$$\begin{cases} \epsilon_{charge\ breeding} = \dfrac{1}{q}\dfrac{I_{q+}^{with\ 1+} - I_{q+}^{without\ 1+}}{I_{1+}} \\[2ex] \dfrac{\Delta\epsilon_{charge\ breeding}}{\epsilon_{charge\ breeding}} = \sqrt{\dfrac{\sigma_{I_{1+}}^2}{I_{1+}^2} + \dfrac{(\sigma_{I_{q+}^{with\ 1+}}^2 + \sigma_{I_{n+}^{without\ 1+}}^2)}{(I_{q+}^{with\ 1+} - I_{q+}^{without\ 1+})^2}} \end{cases} \quad (5.2)$$

where, $\sigma^2_{I^{with\ 1+}_{q+}}$ is the absolute error on the q+ current extracted (with 1+ injection) from the SP1 CB and $\sigma^2_{I^{without\ 1+}_{q+}}$ is the absolute uncertainty in the q+ current extracted (without 1+ injection) from the SP1 CB. During the experiment, the intensity of 1+ ions was around 450 - 500 nA with an absolute error of $\pm$ 10 nA. In the case of shooting through mode, it was observed that the relative uncertainty is about $\sim$ 3 %. In the case of charge breeding mode, the relative uncertainty is about $\sim$ 5% on low charge states (1+, 2+ and 3+) and about $\sim$ 10% on the high charge states (7+, 8+ and 9+). During the experiments, it was observed that the high charge states are more sensitive to the variations of ion source parameters. The estimated uncertainties should be considered for the charge breeding efficiency results presented in this thesis.

5.2.1   Transmission of ^{23}Na$^+$ and ^{39}K$^+$

After the validation of the magnetic field configuration, the SP1 CB was set to optimize for high charge breeding efficiency. Figure 5.6 describes the scheme of the experimental setup for the optimization of SP1 CB and also for the charge breeding efficiency measurements. The thermionic ion gun, developed at GANIL, has been installed at the production cave in the SPIRAL1 facility to produce the 1+ beams of alkali elements (using the pellets from HeatWave labs [34]). The experiments were performed with Helium (He) as buffer gas in SP1 CB, which is observed to be the best support gas for optimizing the charge breeding efficiencies of high charge states of K and Na [70].

Before initiating the optimization of SP1 CB, the Na^+ beam with typical intensity of 500 nA was extracted from the ion gun and transported through the SP1 CB with an emittance of 50 π.mm.mrad. The SP1 CB was switched to shooting through mode (without high voltage and RF power), where the coil currents were properly adjusted to maximize the transport of 1+ beam through the 6mm plasma electrode aperture. The ion optics elements in the 1+ and N+ line were optimized to achieve maximum intensity up to the Faraday cup (FC_{13}), installed upstream the SP1 CB and up to the Faraday cup (FC_{31}), installed downstream the SP1 CB. During this procedure, the ion optics elements in the 1+ and n+ line were initially defined from TraceWin [105] code and finely optimized. This work was carried out in collaboration with a instrumentation specialist from Institut Pluridisciplinaire Hubert CURIEN (IPHC) of Strasbourg. Finally, the transmission efficiency of 78% on Na^+ was recorded at the Faraday cup (FC_{31}). Later, a 450 nA K^+ beam has been transported in 1+ and N+ line with the emittance of 50 π.mm.mrad. The ion optics elements for this test were scaled from the parameters used in Na^+ transmission. As a result, the transmission efficiency of 80% was recorded on K^+. Therefore, the decision was made to use the 1+ line ion optics parameters as a reference parameters for the future experiments. The corresponding uncertainty is calculated and presented in the section 5.2.
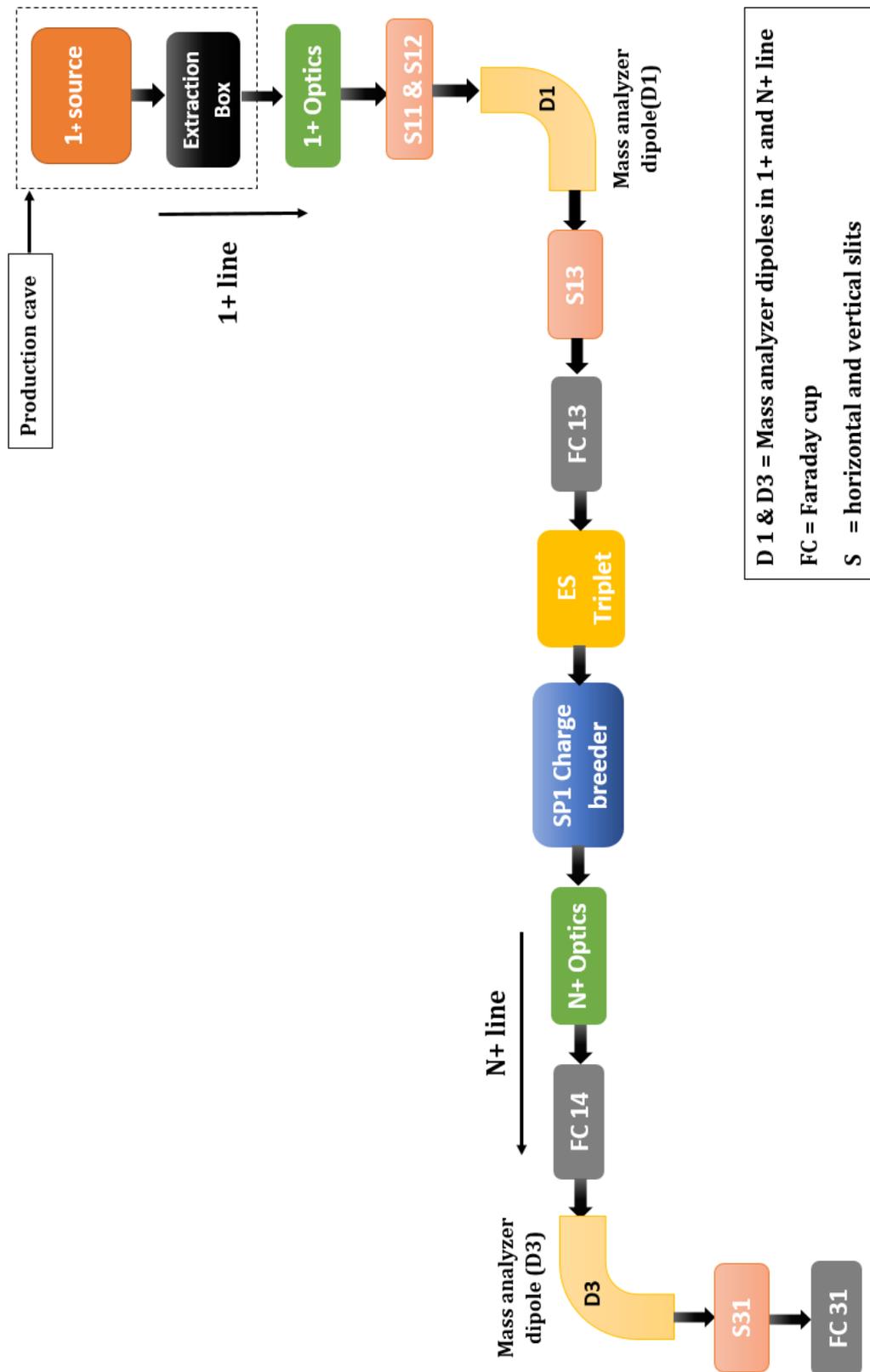
FIGURE 5.6: Scheme of the experimental setup for the optimization of charge breeding efficiency experiments using SP1 CB.

5.2.2   Optimization of SP1 ECR charge breeder

Effect of Injection optics on charge breeding efficiency

The charge breeding efficiency can be improved by optimizing the ion optics of 1+ ion injection. In July 2018, experiments were performed to improve the performance of the SP1 CB by optimizing the injection optics. Due to the limited access to the 1+ source and the SP1 CB, the optimizations were performed only with ^{23}Na$^+$ beam at an extraction voltage V_{1+} = +(20 kV + ΔV). The 1+ ions are selected by a 90° mass analyzer dipole (D1) and steered through a set of slits where the emittance (4σ) is defined as 50π.mm.mrad (non-normalized). The beam is focused again by an electrostatic quadrupole triplet and injected into SP1 CB with an intensity of 500 nA. The high voltage applied to the SP1 CB (V_{CB}) is 20 kV. The V_{1+} is regulated through ΔV with respect to V_{CB} in order to optimize 1+ injection. The charge bred ions are extracted through extraction system and the required charge state is selected by the 90° mass analyzer dipole in the N+ line. Finally, the charge breeding efficiency is calculated using the equation 5.2.
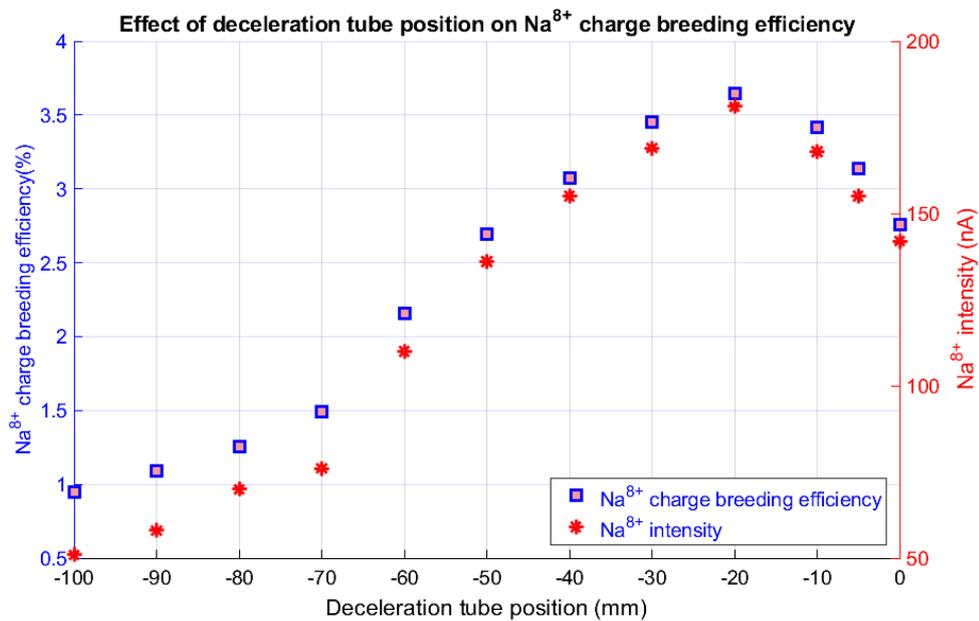
FIGURE 5.7: Effect of deceleration tube position on Na^{8+} charge breeding efficiency.

Initially, the SP1 CB has been optimized to achieve maximum charge breeding efficiency for Na^{8+}. Before optimizing the position of deceleration tube, the charge breeding efficiency of 2.6% was calculated. The tube has been moved to either end of its travel (i.e. all the way towards the plasma chamber (position 0 mm in figure 5.7) or all the way out (position 100 mm in figure 5.7). For each position, the Na^{8+} charge breeding efficiencies and intensities were recorded. The optimum position was found when the deceleration tube is located in such a way, that it ends 21 mm upstream from the SP1 CB injection plug. In a previous test performed with the SP1 CB at the LPSC 1+/n+ test setup the deceleration tube position had marginal effect

for the charge breeding efficiency [70]. This test setup featured different injection optics scheme [70] compared to the GANIL installation (numerous optic parameters in 1+ beam line), which can affect the injection efficiency and consequently, the charge breeding efficiency.

FIGURE 5.8: Effect of injected beam emittance on Na^{8+} charge breeding efficiency.

After the optimization of deceleration tube, the charge breeding efficiency reached 3.6% on Na^{8+}. Maintaining the optimum position of the tube, the effect of 1+ beam emittance on charge breeding efficiency was investigated. The 1+ beam emittance was varied from 5π.mm.mrad to 80π.mm.mrad. During the measurements, the intensities of Na^+ and Na^{8+} were recorded at the Faraday cup (FC_{13}) placed before the injection optics of SP1 CB and Faraday cup (FC_{31}) placed in N+ line after the 90° mass analyzer dipole (D3). The Na^{8+} charge breeding efficiency has been calculated using the equation 5.2. Figure 5.8 presents th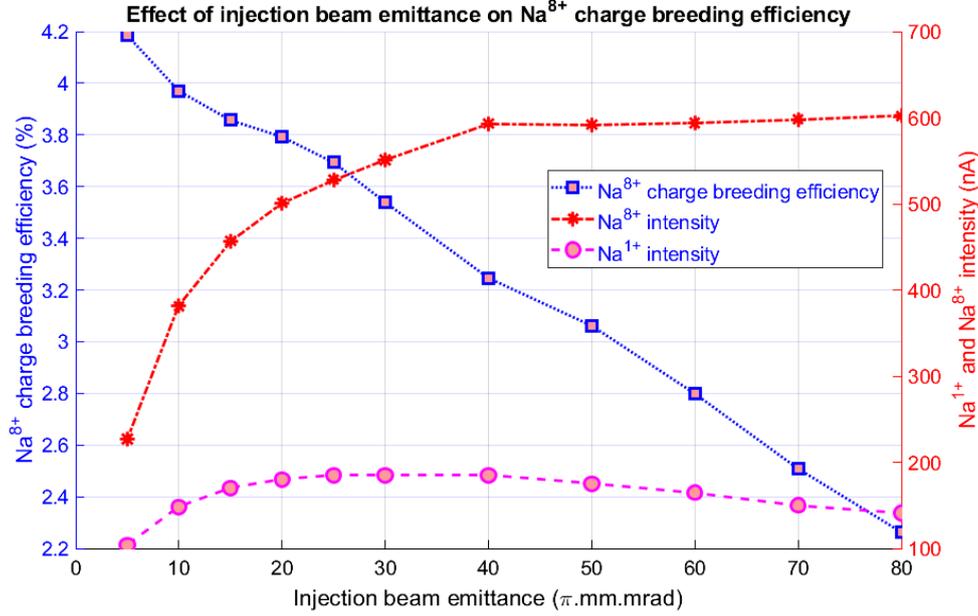e Na^{8+} charge breeding efficiency and 1+ / 8+ intensities as a function of injected 1+ beam emittance. At low emittance ($< 40\ \pi$.mm.mrad), the 1+ beam is collimated by the set of slits, which represents a significant decrease in 1+ beam current. At the same time, the N+ current shows a significant decrease at low emittance. At higher emittance ($> 50\ \pi$.mm.mrad), a small decrease in Na^{8+} beam currents has been observed. It suggests that perhaps increased 1+ ion losses near the injection region influence negatively the injection efficiency. From these measurements, it can be concluded that the LEBT acceptance in the injected beam emittance is in the range of 50 π.mm.mrad. On the other hand, the charge breeding efficiency exhibits a steady linear increase with decrease in 1+ beam emittance. These trends reveal the significance of 1+ beam emittance on injection efficiency and consequently, the charge breeding efficiency. The influence of this parameter will be investigated in the charge breeding simulations.

TABLE 5.2: Typical optimum parameters used obtained from the charge breeding efficiency measurements

Parameters	$Na + Helium$	$K + Helium$	$K + Oxygen$
1+ source potential (V)	20006.5	15007.5	15006.5
Injection triplet potentials (kV)	$\pm$ (1.15/0.7/0.25)	$\pm$ (1.3/1.7/0.35)	$\pm$ (1.3/1.7/0.35)
SP1 CB potential (V)	20000	15000	15000
B-field in T (inj/min/ext)	1.38/0.39/0.94	1.38/0.41/0.88	1.38/0.4/0.88
Extraction Einzel potentials (kV)	11.5	10.4	10.4
1+ intensity (nA)	500	450	460
Optimum ΔV (V)	6.5	7.5	6.5
RF power (W)	470	207	209
Pressures without plasma (mbar)	2.9×10^{-8} (1+) 6.8×10^{-8} (N+)	2.7×10^{-8} (1+) 6.5×10^{-8} (N+)	3.4×10^{-8} (1+) 5.2×10^{-8} (N+)
Pressures with plasma (mbar)	4.9×10^{-8} (1+) 7.5×10^{-8} (N+)	4.7×10^{-8} (1+) 7.2×10^{-8} (N+)	4.2×10^{-8} (1+) 6.5×10^{-8} (N+)

### 5.2.3   Charge breeding of ^{23}Na and ^{39}K

Following the optimization of SP1 CB, charge breeding efficiency experiments were performed, starting from the end of July 2018 to September 2018, to collect the data for charge breeding simulations. Low mass species (A < 40) were chosen for the experiments to understand their capture with different buffer gas species. The chosen combinations are the following: a) Sodium + Helium as a support gas, b) Potassium + Helium as a support gas and c) Potassium + Oxygen as a support gas. Due to unfavourable gas mixing conditions, it was decided not to perform charge breeding measurements with Sodium while using Oxygen as a support gas. Since the Sodium pellet was already installed in the ion gun, the charge breeding measurements were initiated with Sodium (Helium as support gas).

Around 500 nA of Na^+ was extracted from the ion gun and injected into the SP 1 CB with an emittance of 50 π.mm.mrad. By properly regulating the ΔV, the charge breeding efficiencies were calculated. In the similar fashion, the charge breeding efficiencies were measured for other two cases (K with He and O_2), In these cases, the 1+ intensities were around 450 nA. In addition, the ΔV curves were also recorded for low and high charge states of Na and K. The optimum charge breeding parameters and charge breeding efficiency results for all the cases are presented in the table 5.2 and 5.3. The ΔV curves are recorded with the parameters mentioned in 5.2. It should be noted that the mass analyzer dipole (D1) in 1+ line was tuned for each ΔV (for ΔV curves) in order to maintain the alignment of 1+ beam.

Figure 5.9 shows the comparison of Na^+ and Na^{2+} ΔV curves with the one recorded for high charge states (Na^{8+}). The ΔV curves for other two cases are shown in appendix B. The charge breeding efficiency of singly charged ions rapidly increases

TABLE 5.3: Charge breeding efficiency results obtained from the three experimental cases

$Na + He(\Delta V = 6.5V)$		$K + He(\Delta V = 7.5V)$		$K + O_2(\Delta V = 6.5V)$	
Na^+	3.1%	K^+	2.5%	K^+	6.4%
Na^{2+}	0.9%	K^{2+}	1.35%	K^{2+}	1.28%
Na^{7+}	3.17%	K^{3+}	0.36%	K^{3+}	0.28%
Na^{8+}	3.63%	K^{9+}	6.53%	K^{9+}	1.0%
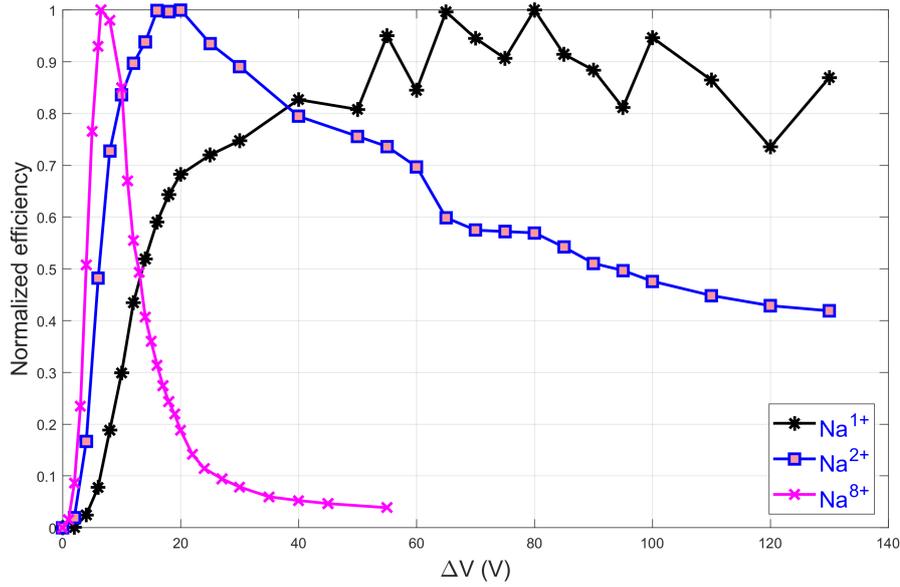
FIGURE 5.9: ΔV curves acquired from the charge breeding of Na.

up to $\Delta V = 40$ V and starts to exhibit periodic variations at higher ΔV. At the same time, the trends of 2+ curves is more or less up to $\Delta V = 20$ V and decreases gradually with increasing ΔV. The trends of high charge state ions (Na^{8+} or K^{9+}) are completely different, where the efficiency is too low after $\Delta V = 30$ V. Moreover, the typical optimum ΔV value for high charge states of Na and K is between 6 and 8 V. Experimental studies [116] have demonstrated that the trends of 1+ ΔV curves represents a fraction of uncaptured incident 1+ beam propagating through the charge breeder ECR plasma, and the 2+ ΔV curves is considered to represent in-flight ionization by electron impact and/or 1+ ions captured and ionized to 2+. On the other hand, the ΔV curves of high charge states (8+ and 9+) represents the ion population that has been captured by the background plasma ions and ionized by consecutive electron impacts. In this work, the discussed hypothesis will be deeply investigated by performing numerical simulations.

5.2.4   Charge breeding time investigations

In chapter 3, it has been mentioned that the charge breeding time (τ_{CB}) is one of the key parameter that describes the performance of the ECR charge breeder. It represents the characteristic time required for the injected 1+ ions to be ionized to the high charge state q^+. This time is typically expressed either in milliseconds or in milliseconds per charge state (ms/q), and should be short to avoid radioactive decay losses during the charge breeding process in the case of RIB production. The CB time is measured when the extracted high charge state ions reaches 90% of its final saturation current. This is a traditional method widely accepted in the ECR charge breeder community to measure the charge breeding time [76].
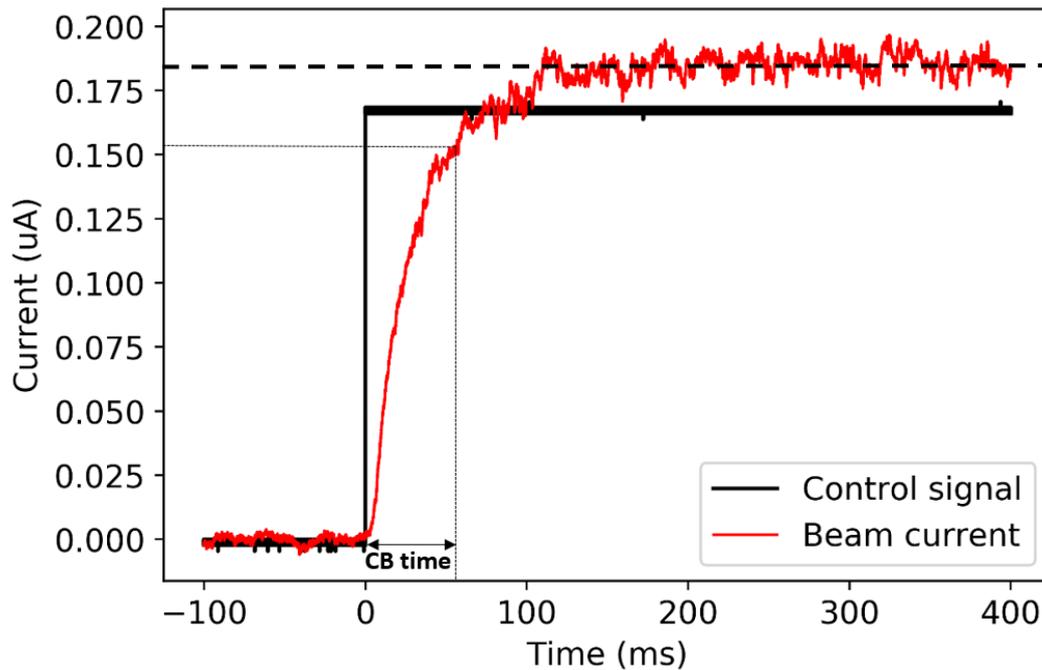

FIGURE 5.10: Charge breeding time measurement principle. The Black line is TTL signal from the function generator and the response of the extracted ions corresponds to the red line.

The rising edge of the 1+ ion beam is generated by pulsing the 1+ beam using a chopper installed upstream the SP1 CB and finally the rise of the extracted q^+ signal is measured. In the above example, the charge breeding time of K^{9+} is measured as 63 ms. The charge breeding performances obtained at different facilities are reported in Ref. [70, 117]. It was found that the source parameters (such as microwave frequency, RF power, support gas and the strength of the magnetic field) strongly influence the charge breeding time [70]. This is demonstrated by considering an example: the SP1 charge breeder was optimized to K^{9+} using Hydrogen and Helium as buffer gas. The charge breeding efficiencies are found to be 13% (Hydrogen) and 11.7% (Helium) and the charge breeding times are reported as 35.1 ms and 117 ms [70]. The source parameters (B-field, drain current, 1+ beam intensity, operating pressures and RF power) are maintained similar in two cases. In order to understand the physics involved in these variations, intensive investigations are required.

In December 2018, the experiments were carried out in collaboration with the ion

source team from JYFL accelerator laboratory. The goal of these experiments was to estimate the charge breeding time and the confinement times (residence time) from the beam current transients in SP1 CB and finally to verify the results obtained from a conventional ECRIS [118], where sputtering was used for sample injection. At JYFL, these times were studied as a function of the different source operational parameters. Therefore, similar approach has been followed during the experiments with SP1 CB. Each source parameter (such as microwave heating power, the B_{min}/B_{ECR}-ratio, the intensity of 1+ injected ion beam and the 1+ injection energy (ΔV)) has been varied independently and their effects were studied by observing the trends of the charge breeding efficiency (ϵ_{CB}) and time (τ_{CB}). In the following, the charge breeding times obtained from the experiments are reported. For each figure, lines are drawn to guide the eye. The confinement times will be reported in M. Marttinen et al [119].

Measurement setup

Figure 5.11 shows a flow chart of the measurement setup. A thermionic ion gun was used to extract the K^+ beam. The extracted beam passes through the 90° mass analyzer dipole (D1), where the 1+ beam is selected.
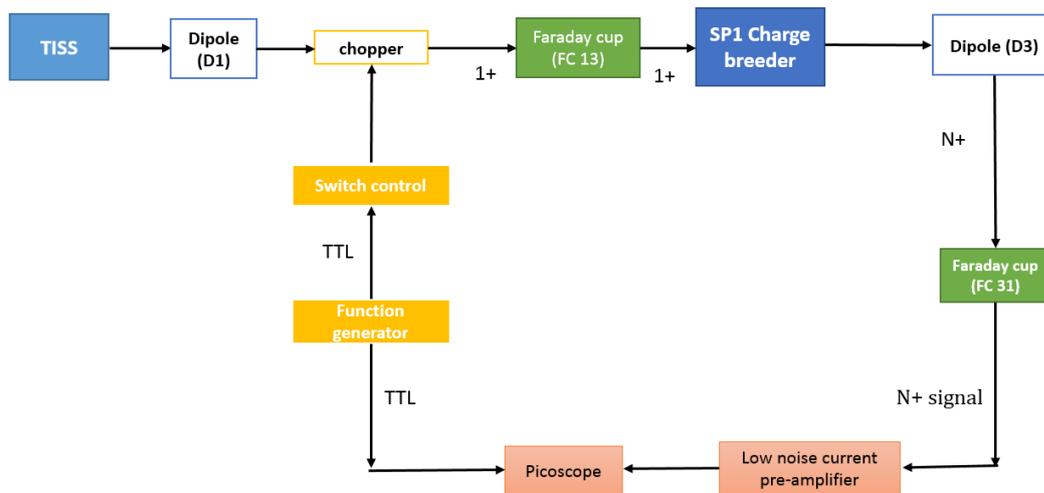
FIGURE 5.11: Flowchart of the experimental setup.

The selected 1+ beam was then transported through the chopper, which is a pulsing system that consists of two horizontal plates. One plate is connected to a switching system, which is driven by a slow control command and the other plate is grounded. The selected beam is then focused by electrostatic triplet and injected into the SP1 CB, where it is trapped and ionized to higher charge state. The extracted beam was m/q-analyzed at the 90° mass analyzer dipole (D3) and the desired high charge state ions were collected at the Faraday Cup (FC 31). Because of low extracted currents (typically in nA scale), the current was first sent through a SRS Model SR570 Low-Noise Current Preamplifier. Finally, the current was measured at the digital oscilloscope. Because of the noise, the currents were averaged over 32 samples.

The SP1 CB was optimized to achieve maximum charge breeding efficiency on K^{9+}. The measurements were performed by using Helium as buffer gas. The extraction

voltage of 1+ source and the SP1 CB was set to 20 kV. The magnetic field strength at the injection, minimum and extraction are 1.38 T, 0.41 T and 0.88 T, respectively. The incident microwave power is 253 W and the reflected power is about 6 W. The plasma chamber gas pressure was approximately 2.3×10^{-8} mbar - 3.5×10^{-8} mbar. The RF power and the buffer gas injection were optimized carefully to maintain the drain current around 0.9 - 1.1 mA. The potential given to the extraction system was kept at 12.7 kV. With the optimum parameters, an efficiency of 4.9 % was recorded on K^{9+}. This value is identical to the one obtained during the continuous injection of 1+ ion beam. The ΔV value throughout the measurements was approximately 5.3 V. During each parameter sweep, the cycle time was varied between 0.909 - 1.667 s to suppress 50 Hz oscillation. This time was sufficient for the extracted ion current to saturate and also to decay completely.
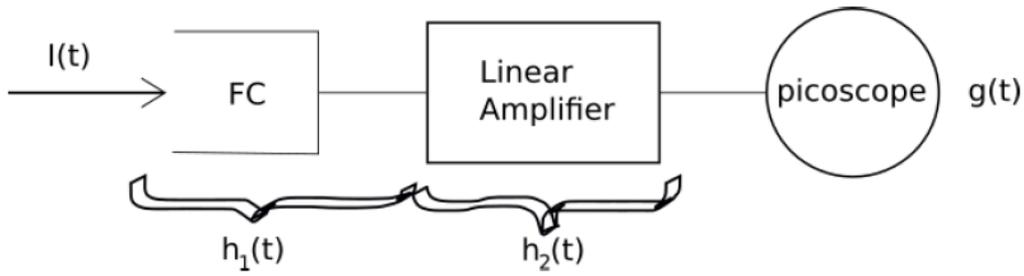

FIGURE 5.12: Schematic illustration of the signal progression through the setup. *I(t)* is the extracted, physical ion current, h_1(t) and h_2(t) the impulse responses of the FC 31 and the amplifier respectively, and *g(t)* is the picoscope readout.

The setup and the signal progression through the system is illustrated in the figure 5.12. The current produced by the extracted high charge state ions at the Faraday Cup (FC 31) is propagated through two coupled systems: one being the SRS-SR570 linear amplifier and other being the system from the FC 31 to the amplifier. The final signal measured at the oscilloscope readout is a convolution of actual and physical current with the impulse response of the coupled systems. This must be deconvolved from the measured signal in order to obtain the true physical times. The physical rising edge of the current has been considered as *I(t) = I (1 - $e^{-t/\tau_{rise}}$)*. The effects of the measurement setup has been eliminated from the rising edge of the current (refer appendix C for a detailed solution) and hence, the oscilloscope readout will be

$$g(t) = I(1 - e^{-t/\tau_{rise}}) - I\frac{\tau_{rise}}{\tau_2 - \tau_{rise}}(e^{-t/\tau_2} - e^{-t/\tau_{rise}}) \tag{5.3}$$

which has been fitted to the data in order to obtain the charge breeding time (rise time τ_{rise}). In the above equation, τ_2 is the response time of the amplifier.

Error estimation

As mentioned earlier, the parameter sweeps were performed with respect to the RF power, B_{min}/B_{ECR} ratio, injection energy of 1+ ion beam (ΔV) and the intensity of

incident ion beam. The SP1 CB parameters were first set to default optimum operational conditions and thereafter each parameter has been independently varied. The transient of the extracted ion current was measured for low charge states (K^{1+} and K^{2+}), medium charge state (K^{4+}) and high charge state (K^{9+}). After each parameter variation, the SP1 CB was reset to the default condition and the next parameter sweep was initialized.

Due to the dependency of the SP1 CB operating conditions (contamination, fluctuations in pressures etc), the extracted ion currents were observed to be unstable during the experiment. Thus, the measured charge breeding efficiencies and charge breeding times are subjected to significant uncertainty. In the case of charge breeding efficiencies, the error analysis is already performed and reported in the section 5.2. In the case of charge breeding times, the error analysis is performed by averaging the charge breeding times of the each charge state obtained from all the parameter sweep experiments at default optimum ion source operating conditions.

TABLE 5.4: Standard deviations and relative uncertainties of the average charge breeding times obtained for the Potassium ions from the parameter sweep experiment at the default setting of 253 W microwave heating power, ΔV of 5.3 V, $B_{min}/B_{ECR} \approx 0.81$ and Helium pressure set to produce a drain current of 0.9-1 mA.

Ion charge states	Average CB time (ms)	Standard deviation (ms)	Relative uncertainty (%)
1+	0.67	0.033	4.9
2+	0.41	0.064	16
4+	4	0.86	21
9+	65.75	8.06	12.25

Table 5.4 presents the average time constants, acquired at same ion source operating conditions from all the parameter sweep experiments, their standard deviations and relative uncertainties. The significant uncertainty to the average value of the response time ranges from ∼5% to ∼21%. There is no clear tendency to the uncertainty with respect to the ion charge state. But, the estimated uncertainty is observed to be higher for medium and high charge states due to the dominated background current.

Influence of minimum-B field

The influence of minimum-B field on the Potassium charge breeding process was investigated by varying the B_{min}/B_{ECR} ratio from 0.68 to 0.88 (center coil current was varied from 250 A to 400 A with 25 A steps), with all other source parameters kept constant. The charge breeding times of the four charge states (1+, 2+, 4+ and 9+) and their efficiencies were recorded and shown in the figure 5.13 and 5.14. During the sweep, the plasma was observed to be unstable when the B_{min}/B_{ECR} ratio exceeds 0.86 or lies within 0.72 [120]. When the ratio is increased from 0.68 to 0.87, the gradient of the magnetic field decreases and consequently, the ECR surface becomes broader. It can be seen in the figure 5.13 that the response time of 1+ ions increases
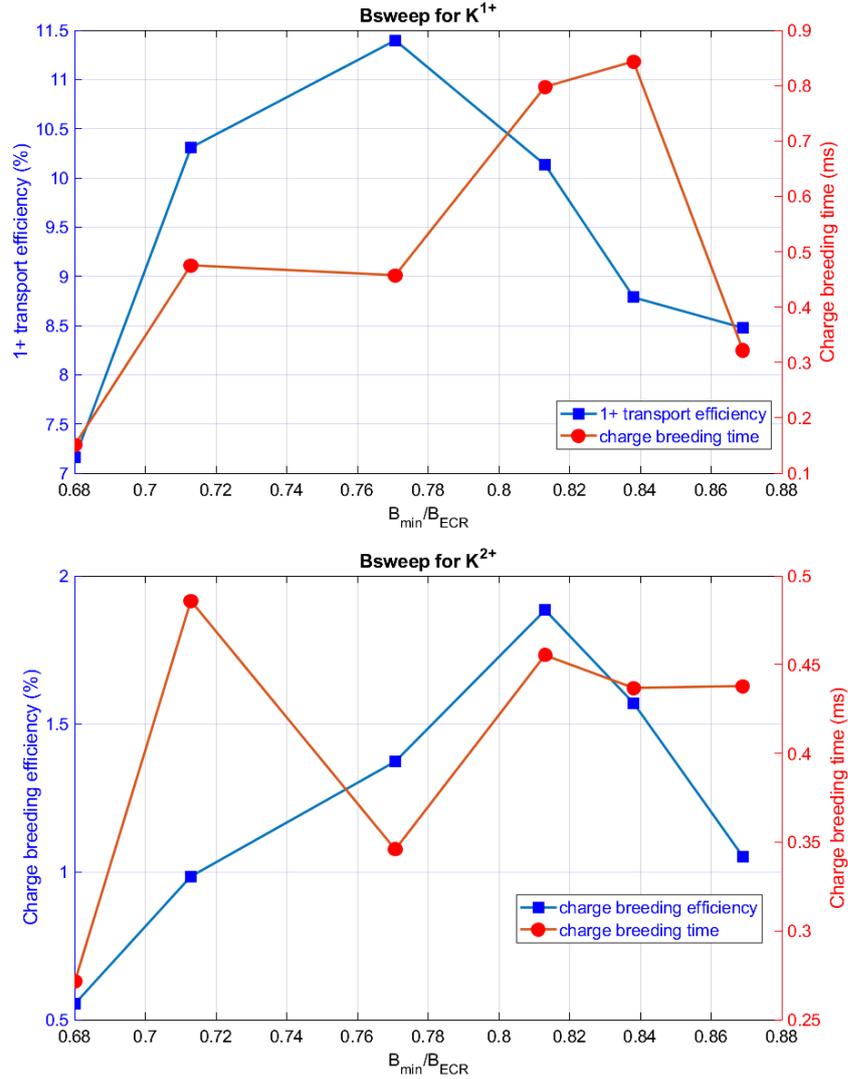
FIGURE 5.13: The charge breeding time and charge breeding efficiencies for the low charge states of ^{39}K as a function of SP1 CB B_{min}/B_{ECR} ratio.

with increase in B_{min}/B_{ECR} ratio. The best configuration is observed to be at 0.77, where the efficiency is high and the value of the response time is very short compared to 4+ and 9+ charge states. This implies that they are poorly confined in the ECR plasma. In the case of 2+ charge state, the optimum point was shifted towards the higher B_{min}/B_{ECR} ratio = 0.81. In the case of 4+ and 9+ (see fig 5.14), the charge breeding efficiency increases as the value of B_{min}/B_{ECR} ratio is increased, until the plasma becomes unstable (> 0.86). The extracted intensity of 4+ and 9+ simultaneously peaks at 0.811. At the same time, the charge breeding time measured on these charge states are shorter at B_{min}/B_{ECR} ratio = 0.811. This value corresponds well with the optimum mirror field ratio ($B_{min}/B_{ECR} \approx 0.8$) [46], that favors the ion confinement, and hence, enhancing the production of highly charged ions. In the case of low charge state (1+), the behavior is observed to be different when compared with high charge states. Finally, it can said that the configuration (B_{min}/B_{ECR} at 0.811 or the center coil current at 350 A) is beneficial for a short lived isotopes.
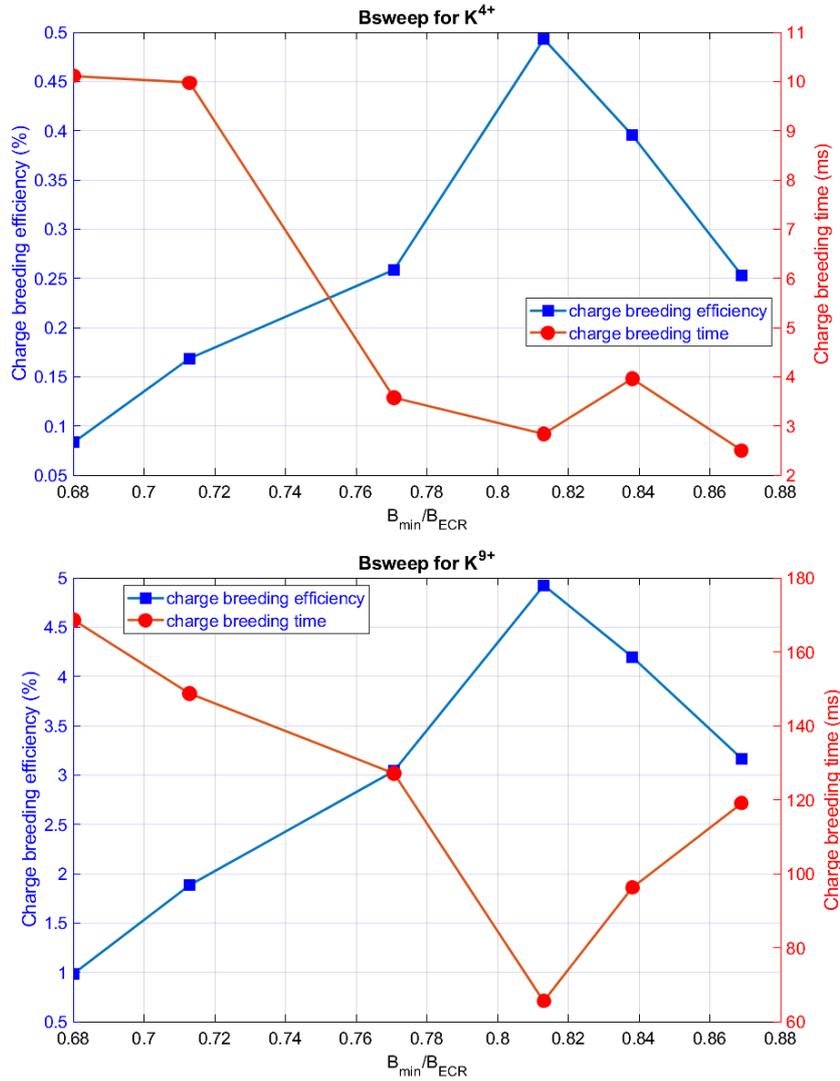
FIGURE 5.14: The charge breeding time and charge breeding efficiencies for the low and high charge states of ^{39}K as a function of SP1 CB B_{min}/B_{ECR} ratio.

Influence of microwave power

Figure 5.15 shows the charge breeding efficiency and charge breeding time for low and high charge states of ^{39}K for different microwave powers. The data for 2+ charge state was not measured during this sweep. The efficiency of 1+ is higher at 200 W than at 375 W and the response time of 1+ increase with increase in RF power. In recent simulations, this behaviour has been studied by successfully reproducing the experimental trends and efficiencies [69] at different microwave power levels (470 W and 200 W). In case of Helium plasma, the plasma densities were estimated as 4 $\times 10^{11}$ cm^{-3} for 470 W and 2×10^{11} cm^{-3} for 200 W. At higher electron densities, the simulation revealed high capture efficiency and low 1+ transport efficiency. This behaviour was quite opposite at lower electron densities. This study is clearly evident in the case of high charge states. The charge breeding efficiency is higher at higher microwave power ($\approx$ 260 W) and at the same time, the CB time is shorter (4+ and

(A)

(B)
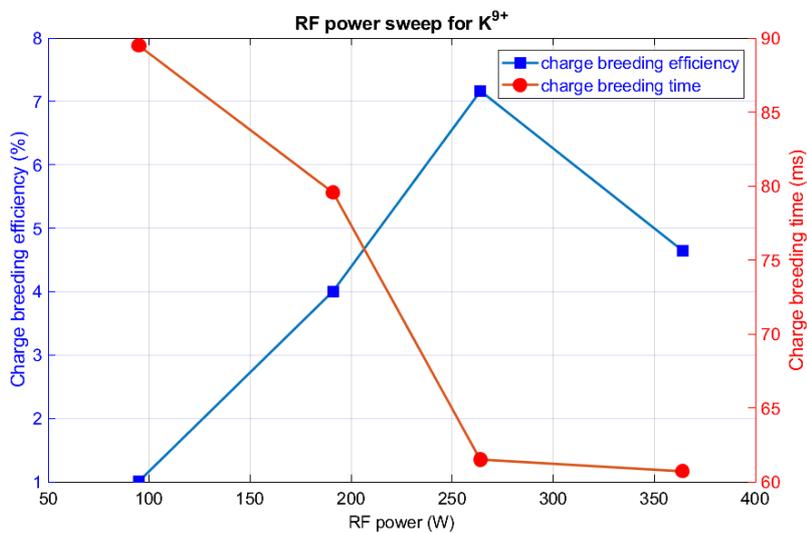
(C)
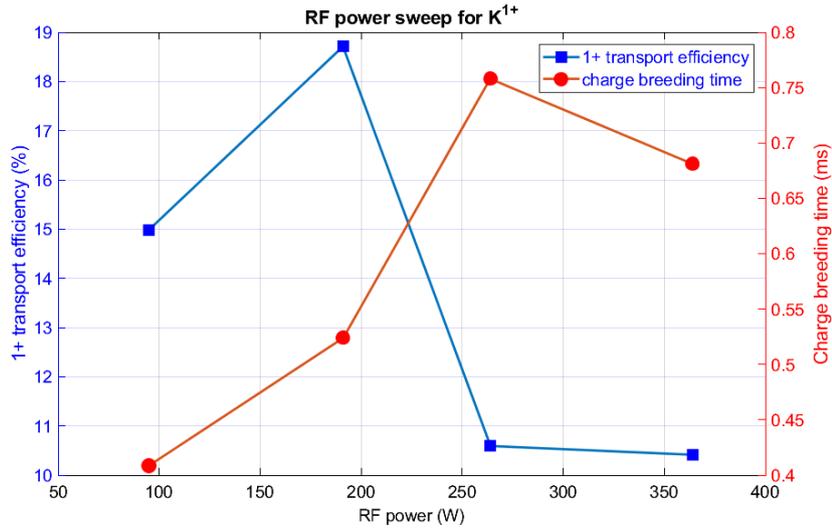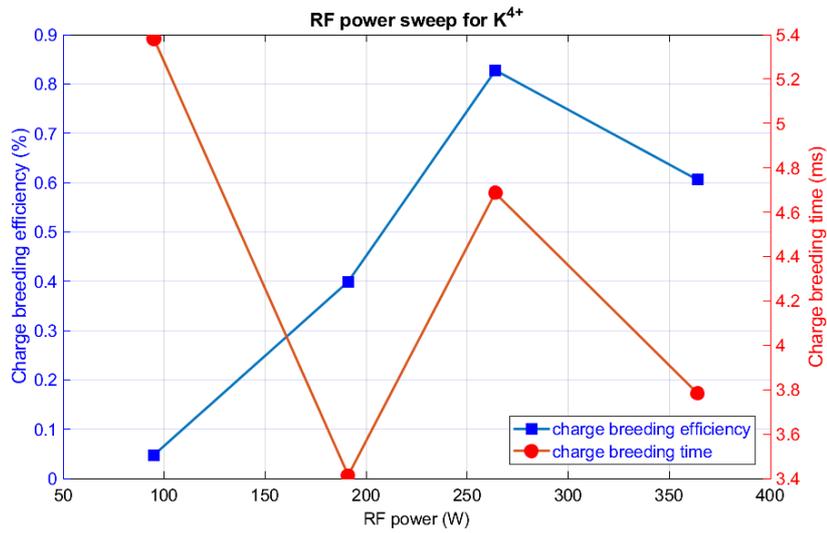
FIGURE 5.15: The charge breeding time and charge breeding efficiencies of low and high charge states of ^{39}K as a function of incident microwave power.

FIGURE 5.16: The charge breeding time and charge breeding efficiencies of low and high charge states of ^{39}K as a function of incident 1+ beam energy (ΔV).

9+). The plasma was unstable at powers higher than 300 W and thus, observed a drop in charge breeding efficiency and also in charge breeding time.
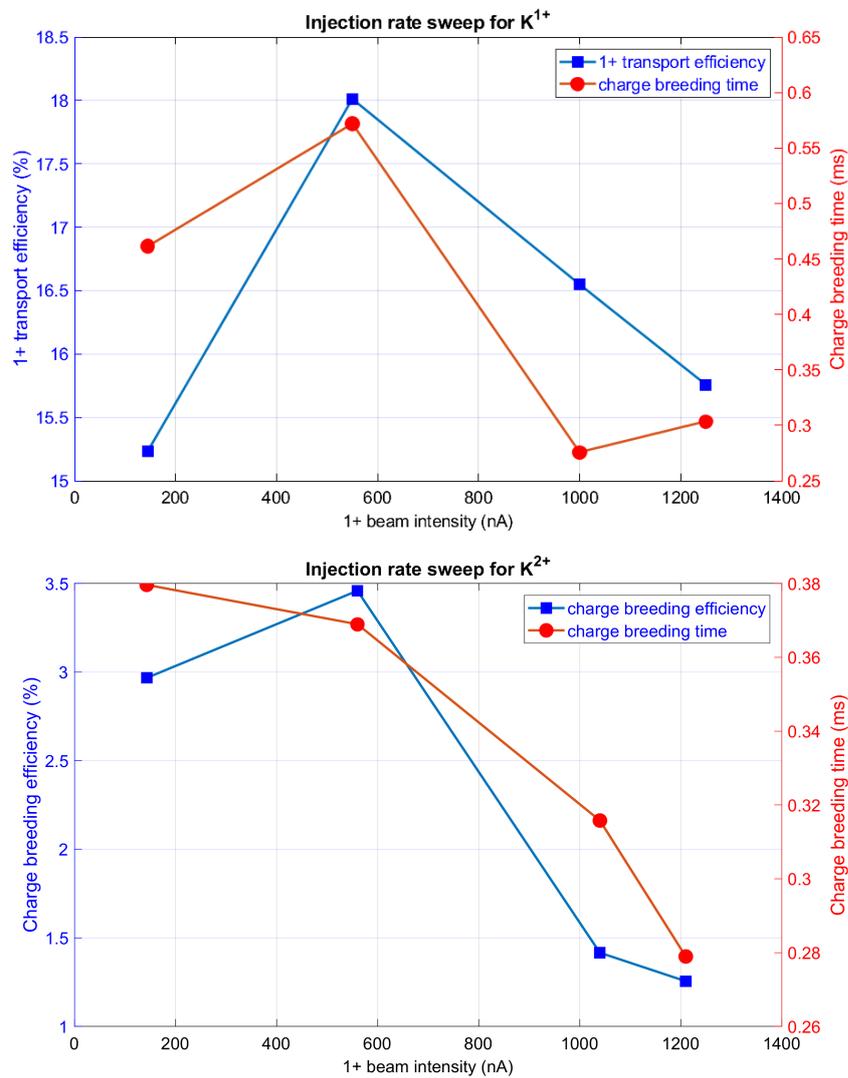
FIGURE 5.17: The charge breeding times and charge breeding efficiencies of low charge states of ^{39}K as a function of 1+ beam intensity.

Influence of 1+ beam injection energy (ΔV)

In this study, the injection energy of 1+ beam into the plasma core was varied from 0 to 10 eV. The data for 2+ charge state was not measured during this sweep. Before performing the sweeps, the SP1 CB was optimized to achieve maximum charge breeding efficiency on K^{9+}, which is around 6.5 %. The ΔV was set to 5.3 V. Then, the value of ΔV was varied from 0 to 10 eV for each charge state and the charge breeding efficiencies and times were recorded. The results from this sweep are shown in the figure 5.16. The efficiency of the high charge states reach their maxima at approximately 5.3 eV and the charge breeding time is observed to be much shorter at this value. At higher injection energies (>10 eV), the charge breeding time decreases
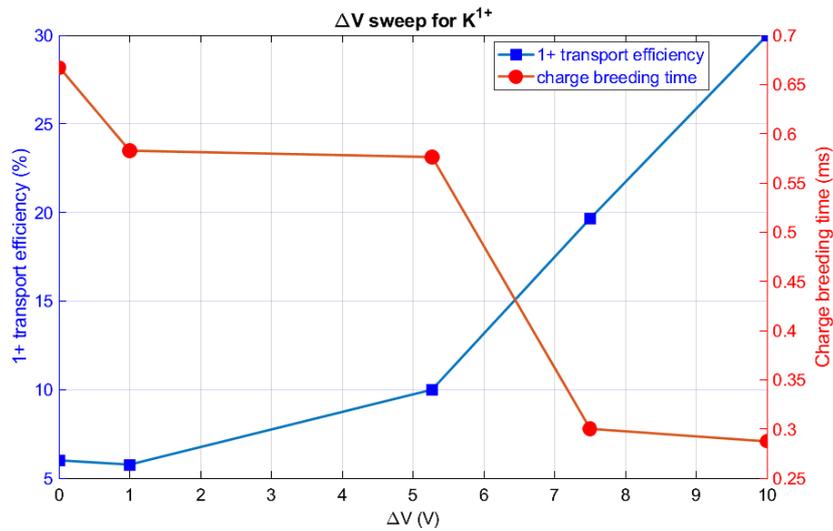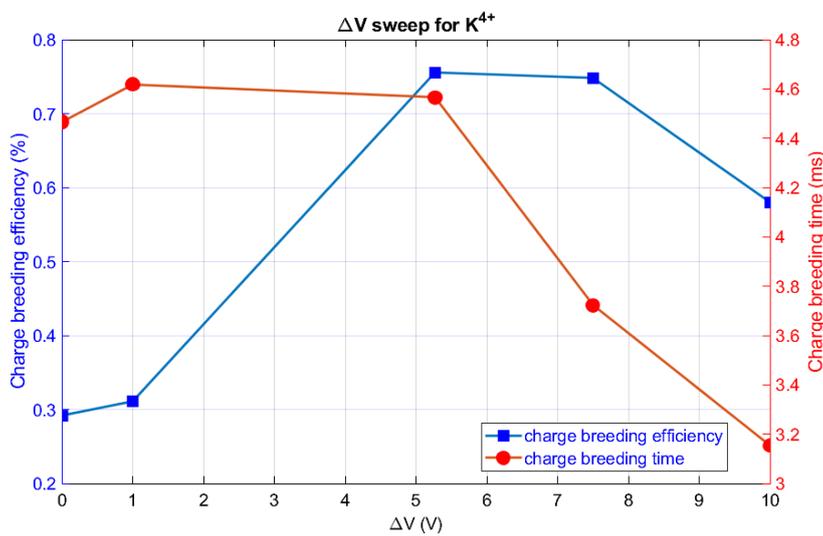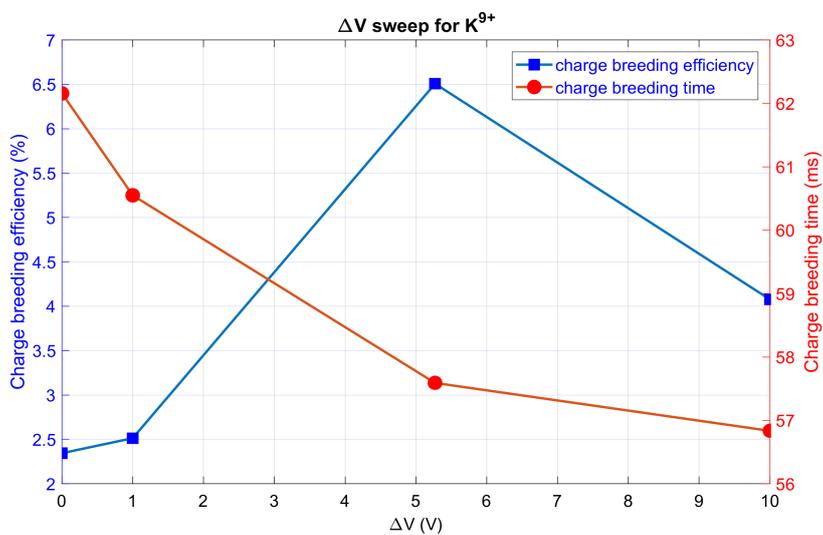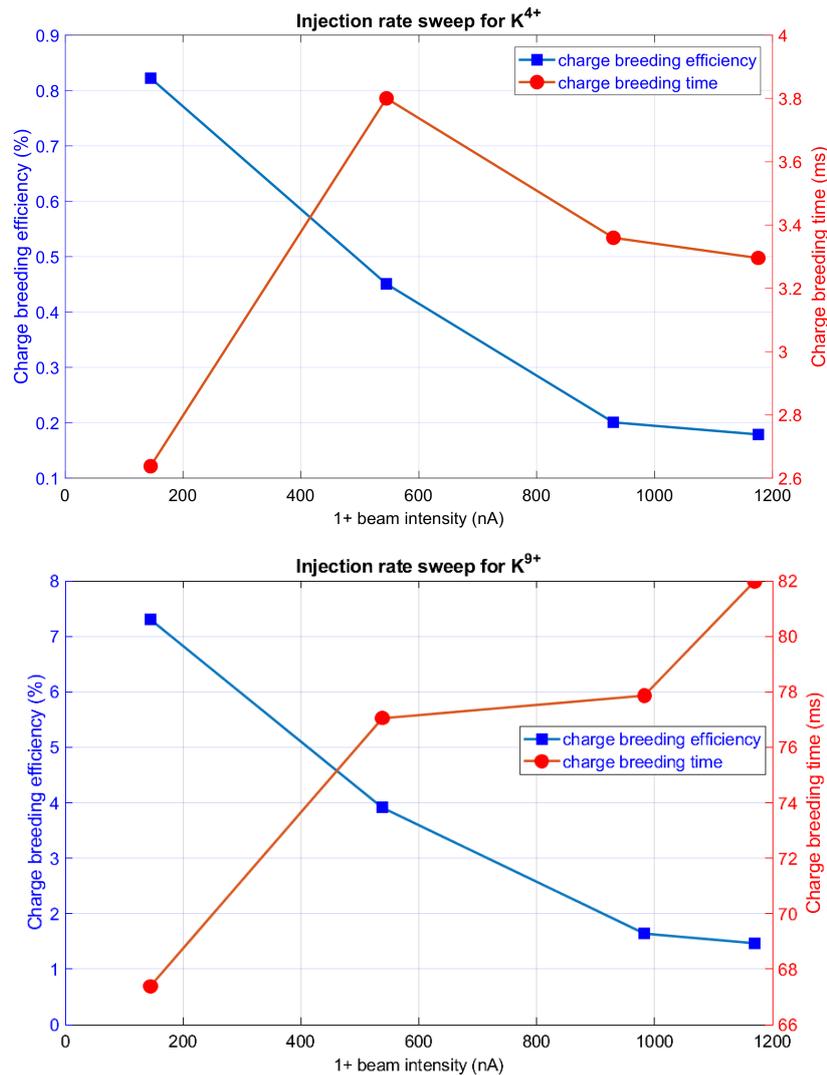
FIGURE 5.18: The charge breeding times and charge breeding efficiencies of high charge states of ^{39}K as a function of 1+ beam intensity.

with decrease in efficiency, which implies that the 1+ ions are not sufficiently slowed down in ECR plasma. As a result, the extracted 1+ ion population is high and the high charge states population is low. At optimum injection energies, the 1+ ion are captured and then ionized by electron impact, thus the charge breeding times are drastically longer. As a result, the efficiency of high charge states is high and at the same time the 1+ reach the only moderate values.

Influence of 1+ beam intensity

The intensity of 1+ ion beam was varied from 150 nA to 1.2 μA. The charge breeding efficiency and time were recorded for the low and high charge states of Potassium and shown in figure 5.17 and 5.18. The response time and the transport efficiency of 1+ were observed to be optimum at 580 nA of 1+ intensity. When the source was tuned to high charge states, the optimum values were at low 1+ intensity ($\sim$ 180

nA). It has to be mentioned that the SP1 CB was initially optimized to K^{9+} by injecting K^{1+} with an intensity of 570 nA. During the sweep, the current given to the K pellet was varied keeping the SP1 CB parameters constant. It can be seen that the charge breeding efficiency is constant at low intensity, while at high intensity there is a drop (2+, 4+ and 9+). The opposite holds for the charge breeding times (4+ and 9+). Similar trends were also observed in the experiments performed with 14.5 GHz PHOENIX ECR charge breeder at LPSC test bench [70]. The influence of this parameter has become an open question to the ECR community. Intensive investigations are still required to understand the physics processes involved in this kind of behaviour.

TABLE 5.5: Optimum charge breeding parameters for K^{9+}.

Ion charge state	B_{min}/B_{ECR}	$RF power$	$Intensity\ of\ K^+$	ΔV
K^{9+}	0.81	270 W	200 nA	5.3 V

The experimental investigations on K charge states provided an overview of best source tuning parameters that improve the charge breeding efficiency and minimize the charge breeding time. The optimum parameters are summarized in the table 5.5. In future, experimental investigations will be carried out on different masses of 1+ ion beam and the buffer gas species. In addition to that, the effect of double frequency heating and the frequency tuning will be investigated, whose consequences on the charge breeding performances are still controversial.

5.3   Numerical simulation studies with SP1 charge breeder

Numerical simulations were performed to investigate the ion losses during the transport of 1+ beam through the SP1 CB and to understand the physical mechanisms involved in the charge breeding process. These cases correspond with the situations where SP1 CB is operated in shooting through mode i.e. switched OFF (no high voltage and plasma) and charge breeding mode i.e. switched ON (high voltage and plasma). These two cases can be investigated by using two different simulation tools (SIMION and MCBC), which are discussed in chapter 4.

5.3.1   Ion transport simulations using SIMION

In section 5.2.1, the transmission efficiencies of 80% and 78% on $^{39}K^+$ and $^{23}Na^+$ were recorded at CF_{31}. It was not clear whether the ion losses are in the injection & extraction optics or inside the SP1 CB. For this reason, it was decided to perform ion transport simulations using SIMION. The motivation of this simulation is to reproduce the transmission efficiencies of Na^+ and K^+ and to investigate the ion losses during the transmission. In order to reproduce the experimental results, realistic starting conditions (beam properties) are needed. During the experiments, the transversal emittance of 50π.mm.mrad (non-normalized) was used for the transmission of 10 keV $^{39}K^+$ beam and 15 keV $^{23}Na^+$ beam. The optics parameters from the two cases were used in the TraceWin simulation to calculate the beam envelopes along the LEBT.

D2: position where the beam properties are recorded
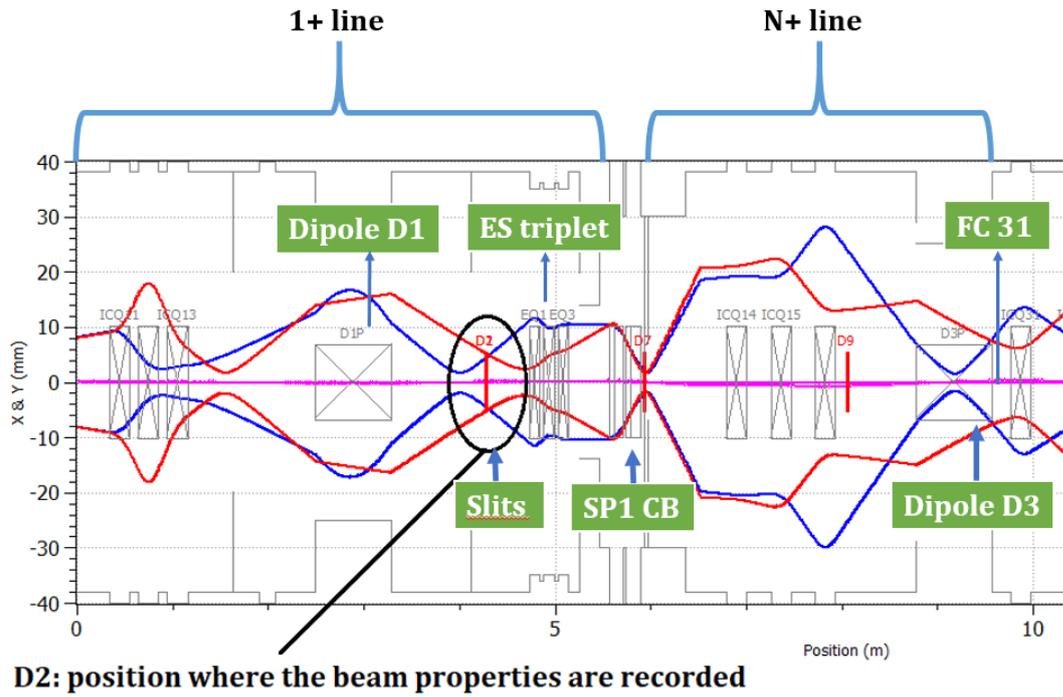
FIGURE 5.19: The calculated envelopes for the entire LEBT line. D2 is the slits position where the transverse beam properties are recorded.

TABLE 5.6: Beam properties recorded at D2 position where the emittance of 1+ beam is defined by the slits (S13).

Beam properties	20 keV $^{23}Na^+$	15 keV $^{39}K^+$
α	-1.438	-1.079
β (mm/mrad)	0.482	0.3616
ϵ_{rms} (π.mm.mrad) [norm]	0.0148	0.0177

Figure 5.19 shows the beam envelope for 20 keV ^{23}Na$^+$ beam. The beam properties were recorded for 50π.mm.mrad emittance and presented in the table 5.6. At the same time, the beam envelope for 15 keV K^+ beam were calculated by applying the experimental ion optical parameters. The recorded properties are shown in table 5.6.

The position D2 in the figure 5.19 refers to the position of slits (S13) where the emittance of the 1+ beam is defined. Using the properties shown in the table 5.6, the particle positions, angles and velocities were generated with a program written in Matlab. The particles created with program should satisfy the following phase space relations in order to be a part of the beam.

$$\gamma x^2 + 2\alpha x x' + \beta x'^2 \leq \epsilon \tag{5.4}$$
$$\gamma y^2 + 2\alpha y y' + \beta y'^2 \leq \epsilon \tag{5.5}$$

and the constraint

$$\beta\gamma - \alpha^2 = 1 \tag{5.6}$$

where, ϵ is the transverse emittance, x , y are the position coordinates and $x^{'}$, $y^{'}$ are the angles of propagation. At the same time, the geometry of the LEBT from the beam slits position to the extraction system of the SP1 CB was implemented in SIMION, as shown in the figure 5.20.
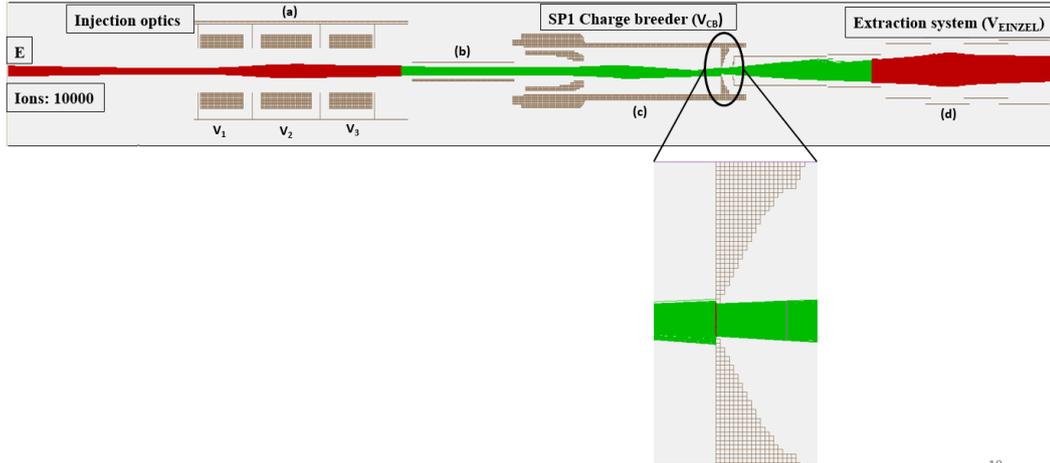
FIGURE 5.20: The geometry of electrostatic quadrupole triplet (a), deceleration tube (b), SP1 CB (c) and extraction einzel lens (d) used in the ion transport simulation. At the point E, 10000 Na^+ ions are initiated with the energy of 20 keV and simulated through SP1 CB. The total ions extracted from charge breeder are counted after the extraction system.

The geometry includes the injection optics (electrostatic quadrupole triplet, deceleration tube), SP1 CB and the extraction system of SP1 CB. The 3D magnetic field of SP1 CB was calculated by applying the coil currents to the SP1 CB magnetic system created using Radia. The electric field is calculated in SIMION by applying potentials (experimental values) to the geometry electrodes. The ion losses are monitored in the simulation by recording the particle count before and after the injection optics, charge breeder and extraction system. The transmission efficiency and beam losses are calculated from this information. Similar procedure has been followed for the transmission of K^+ ions. The final transmission efficiencies from the simulation are compared with the experimental results in the table 5.7.

TABLE 5.7: Comparison of transmission efficiencies obtained from simulation and experiment

Ion	Experimental results	Simulated results
Na^+	78 %	79 %
K^+	80 %	82 %

Final transmission efficiencies from the simulation show good agreement with the experimental results. From the observations, 100% transmission has been achieved up to the entrance of CB. In both cases, the simulation shows that up to 15% of ions

in the plasma chamber are lost at the plasma electrode and up to 5% of the ions extracted from SP1 CB are lost in the extraction system. It has been observed that when the ions enter into the region of rapidly varying B-field (from injection to extraction), their orbit eventually encircle the z-axis. Finally, 15% of ion losses is due to their defocusing behaviour near the plasma electrode. These losses can be minimized by properly adjusting the center coil (B_{min}) and the extraction coil (B_{ext}) keeping B_{inj} at its maximum (1190 A).

5.3.2 The study of 1+ ion transport in a simplified equipotential distribution of an ECR plasma

Before going into the details on the charge breeding simulations, a numerical simulation was performed to study the 1+ ion transport through a potential map that reflects the presence of ECR plasma. The 1+ ion transport is studied by decreasing the charge breeder potential up to few tens of volts.

Simulation description

In this simulation, the geometry of SP1 CB was modified by including cylindrically symmetric surfaces for representing the plasma potential (V_P), ECR zone (V_{ECR} = V_P) and potential dip (V_{dip}) inside the ECR zone. These thin surfaces are presented in figure 5.21. Fixed potentials are given to these surfaces to approximate the potential distribution in plasma volume. The plasma is considered to be contained within the two maxima of the magnetic field, thus the contour of plasma potential is considered as to have similar geometry of the plasma wall chamber with an extension, in the injection zone, towards the deceleration tube. The ECR zone is located at minimum-B structure formed by the three solenoids. It has been argued [45, 24] that a potential dip should be formed inside the ECR zone, so the potential dip is implemented inside the ECR zone, as shown in figure 5.21.
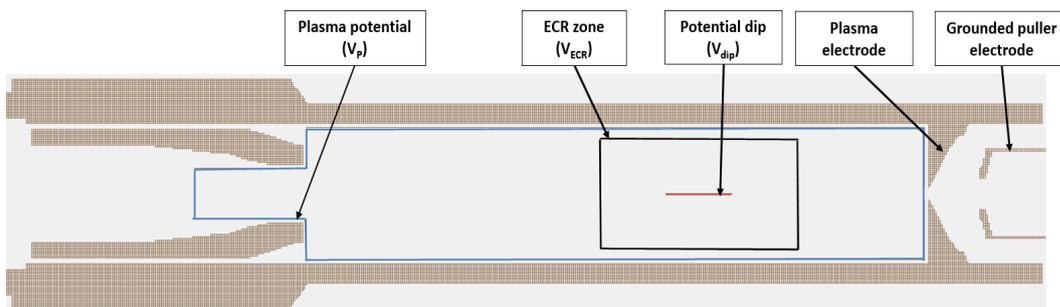
FIGURE 5.21: The geometry of ECR charge breeder with the ECR plasma potential features.

In order to consider the deceleration of 1+ ions, the plasma potential (V_P), extended up to the border of the ECR zone (V_{ECR}), is higher than the potential of the charge breeder (V_{cb}). The potential dip is always considered as $V_{dip} = V_{ECR}$ - 1 V. In this case study, Na^+ ions were initiated at the characterization point E with an energy E = eV_{1+} = 20 keV and transported through the potential distribution in CB plasma

volume. The plasma potential of +10 V with respect to charge breeder potential (V_{cb} < V_P) has been chosen in order to reproduce the ΔV curves. However, based on experimental optimum ΔV results we know that the plasma potential in reality is lower, most likely below 6.5 V. But in order to simulate the trends, this discrepancy should not be critical. With the above discussed scheme, the 1+ ions enter the plasma boundary with an energy E_{inj} = e(V_P - ΔV). The efficiency for each ΔV is finally calculated at the end of extraction system as the ratio between extracted and injected particles.

In addition to Na^+, also Na^{2+} ions were simulated through the model. As the model does not include collisions or other interactions between the ions, the Na^+ ions are randomly converted into Na^{2+} after entering the plasma sheath. A dedicated Lua program was written in SIMION, which randomly converts the 1+ ions to 2+ along the plasma chamber without changing their velocities (momentum) and without taking into account the cross section (1+ $\rightarrow$ 2+) . The ΔV plots for Na^+ and Na^{2+} are calculated and presented in the figure 5.22 and 5.23.
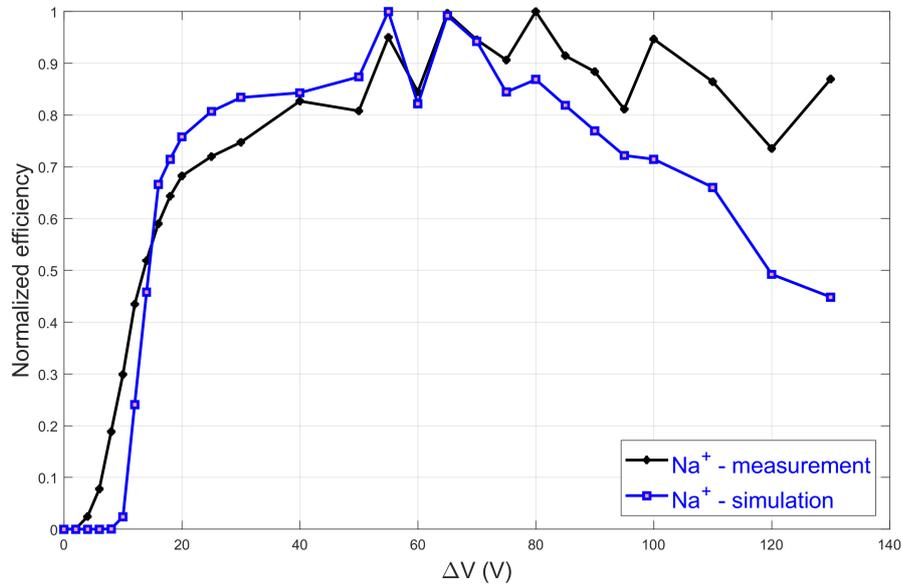
FIGURE 5.22: Normalized transmission efficiency of Na^+ as a function of ΔV. The measured and simulated Na^+ ΔV curves are normalized from 28% and 24%, respectively.

Results and discussion

As is seen in figure 5.22, the efficiency in experimental curve starts to incline at lower ΔV, whereas the efficiency in the simulated curve is observed after 10V of ΔV. This discrepancy may be due to the absence of Coulomb collisions and other interaction processes. Moreover, at low ΔV, most of the ions are reflected back to the deceleration tube due to positive plasma potential (e.g. 85% of ions with ΔV between 9–10 eV). When ΔV is at 55 eV, the maximum transmission of the Na^+ is obtained, and the ion losses at the entrance of plasma chamber is decreased to 15%. The location of
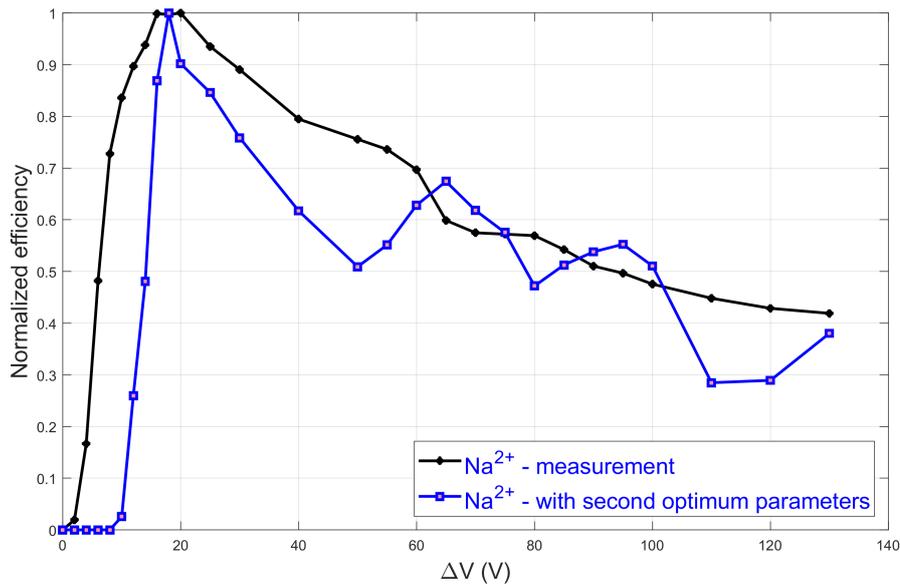
FIGURE 5.23: Normalized efficiency of Na^{2+} as a function of ΔV. The measured and simulated Na^{2+} ΔV curves are normalized from 0.9% and 21%, respectively.

maxima is quite in agreement with the experimental curves. In the simulation, periodic variation of the efficiency as a function of ΔV was observed with values higher than 50V. These variations observed in the simulations revealed that the 1+ beam traversing through the plasma chamber exhibits a periodic focusing/defocusing behavior due to the magnetic field, and consequently the phase of this motion at the extraction aperture influences the transmission. As this motion is ion energy dependent, varying ΔV influences the phase at the extraction aperture and therefore the transmission. As similar variations are present in measured data, it suggests that similar effect takes place in reality. In case of Na^{2+}, the simulation significantly overestimates the transmission efficiency (21%) compared to the measured value (0.9%). This is most likely due to the rough random conversion of 1+ to 2+ implemented in the simulations. The trend of ΔV curve at low beam energies is quite similar with the experimental data but shifted by 10 eV, whereas the trend in the higher beam energies are far from reality.

Finally, the results from the SIMION simulations showed good agreement regarding the rough simulations with the general trends observed in experiments. The discrepancy at low ΔV revealed the role of Coulomb collisions in the charge breeding process, leading to a necessary detailed analysis using a charge breeding simulation tool discussed in the following section.

5.3.3 The numerical study of 1+ ion beam - ECR plasma interaction

In the previous section, the 1+ ion is injected into the SP1 CB to understand its behaviour under the influence of potential distribution that reflects the presence of ECR plasma. Now, the 1+ ion beam interaction with ECR plasma will be studied by a full six-dimensional (6D) phase space Monte Carlo charge breeding code [101, 102]

developed by the Far-tech, Inc. The code has been developed to model the capture process and charge breeding of 1+ ions in an ECR plasma under the influence of external electric and magnetic fields. The background plasma has been modelled by considering the plasma profiles (plasma density, ion temperature, electron temperature and plasma potential). This code allows recording the ion trajectories, extracted particles characteristics (particles positions and velocity distributions), shows the evolution of captured particles for selected initial ion beam energies and calculates the efficiencies of the extracted ions for the given injection beam energies.

The theory of beam capture dynamics implemented in the model is discussed in the previous chapter. Before going into the details on the simulation strategy, it is important to discuss about a few limitations of the MCBC code: i) In the code, the simple ionization (also in-flight) and charge exchange cross section are included. No other ionization processes (double ionization, radiative and dielectric recombination) are included due to unobtainable cross section data for every element. ii) The code assumes a uniform distribution of neutral temperatures and also neutral density in the plasma domain. The code does not allow the user for further modifications (property of Far-Tech). iii) During the Coulomb collisions, the incident 1+ beam should collide with every ion charge state of the background plasma. This problem was simplified in MCBC by letting the 1+ ions to collide with one effective plasma ion which has effective charge $Z_{eff} = \sum_i I_i q_i / \sum_i I_i$, where I_i is the intensity of the plasma species which are in charge state q_i. iv) The 1+ ions are injected into the model at a time (t = 0). Therefore, the 1+ ions injected into the SP1 CB cannot reach the charge equilibrium to extract high charge states.

Considering the limitations of the MCBC code, the charge breeding efficiencies obtained from the MCBC can be different regarding the experimental efficiencies. Therefore, the charge breeding efficiency outputs (ΔV curves) from the code are compared with experimental results by reproducing their relative trends. For this reason, the experimental and simulated ΔV curves are normalized to make the comparison easier. The simulations were performed by varying each source parameter (electron density, ion density, ion temperature, plasma potential and electron temperature) independently with respect to the injected beam energy. By performing the parameter variations, it would be relevant to study the interaction of 1+ ions in ECR plasma and extract useful information like the percentage of 1+ ions captured in ECR plasma and percentage of 1+ ions lost in the simulation domain.

Initially, the proposal was to perform the simulations to reproduce the trends of ΔV curves of high charge state ions. Considering the limitations of the code and the typical charge breeding time (from few to hundreds of milliseconds) of highly charged ions, the simulation cannot reproduce the high charge states. Therefore, our attention was focused on the low charge states (1+ and also on 2+). From the dedicated charge breeding experiments, the ΔV curves were recorded for low charge states (1+ and 2+) and high charge states (8+) (see figure 5.9). Comparing the trends of ΔV curves, the low charge states (1+ and may be 2+) extracted from the charge breeder were found to be weakly interacting with the ECR plasma [99]. This was confirmed by measuring and comparing charge breeding time of 1+ ions with and without plasma and found to be in the order of 500 μs, which is appropriate to perform the simulations. So, the integration time for the simulations was set to 500 μs, which can possibly allow to reproduce the trends of the 1+ experimental curves.

It has to be mentioned that the charge breeding experiments were performed with

the 1+ beam intensities about 450-500 nA. In the studied intensity range, the perturbation caused by the 1+ beam injection on the SP1 CB plasma was relatively small. From the mass spectrum obtained during the experiments, the effective charge $\langle Z_{eff} \rangle$ of Helium and Oxygen plasma was calculated for the three experimental cases and presented in the table 5.8.

TABLE 5.8: Comparison of plasma effective charge $\langle Z_{eff} \rangle$ with and without 1+ injection.

	$Na + He$ $\langle Z_{eff} \rangle$	$K + He$ $\langle Z_{eff} \rangle$	$K + O_2$ $\langle Z_{eff} \rangle$
with 1+ injection	1.45	1.29	4.02
without 1+ injection	1.58	1.38	4.15

The values of $\langle Z_{eff} \rangle$ in the table 5.8 were calculated without taking into the account the impurities in the mass spectrum. The 1+ beam perturbation exhibited a small drop of intensity of multi-charged ions and a slight increase in the intensity of mono-charged ions.

Simulation domain

The physical boundaries of the SP1 CB simulation domain (SP1 CB plasma chamber), extending from the maximum of the injection of SP1 CB (z = 0 m) to the extraction aperture (z = 0.328 m), is shown in the figure 5.24. The SP1 CB plasma chamber is a cylinder with a radius $r = 0.036$ m. In the plasma domain, the minimum-B configuration is created by the three solenoid coils and a permanent magnet hexapole.
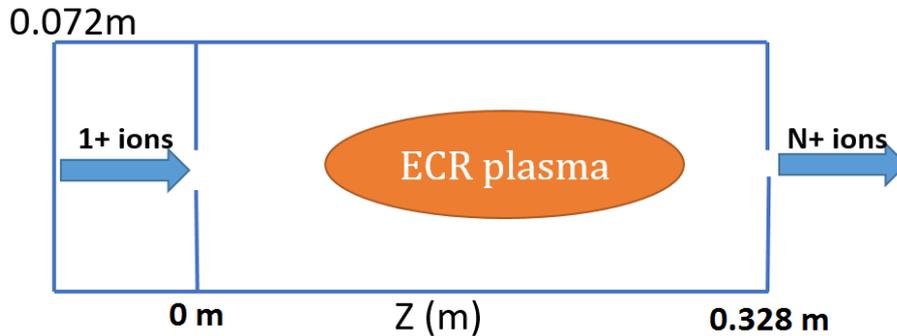
FIGURE 5.24: MCBC simulation domain (z = 0 m to 0.328 m) with respect to the plasma chamber dimensions.

In order to reproduce the experimental trends, realistic beam starting conditions are needed for the MCBC simulation, which can be obtained by the following approach, as shown in the figure 5.25: the 1+ ions are first simulated in SIMION code, where the 1+ ions are transported from the slits position up to the entrance of SP1 CB plasma chamber (including the magnetic fringe field). The starting conditions (particle positions and velocities) are recorded and given as an input for MCBC. Following the charge breeding simulation, the MCBC records the properties of ions, arriving at the plasma electrode, in a separate output file. This output file is given as an input for
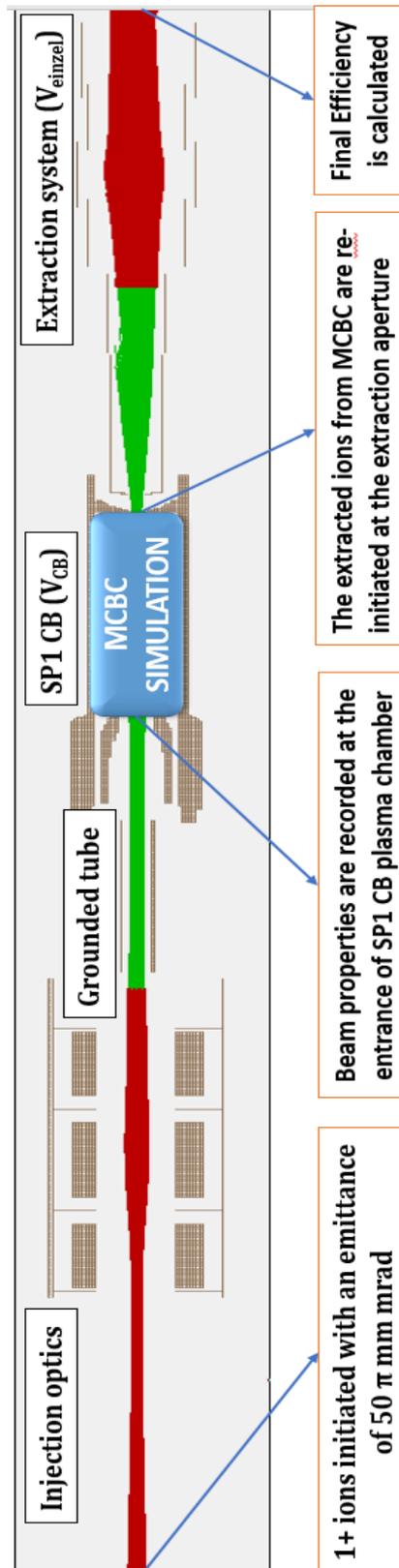
FIGURE 5.25: The simulation approach implemented to perform the charge breeding simulations.

SIMION geometry in order to simulate the extracted ions from the plasma electrode of the SP1 CB. Finally, the efficiency is calculated after the geometry of the extraction system of SP1 CB. This method is repeated for each injection energy of 1+ beam.

Input parameters and modeling of background ECR plasma

The input parameters for MCBC are defined in a separate input file. It includes the computational parameters, SP1 CB device parameters, plasma parameters, beam parameters and finally the parameters which are used to save or record the ion trajectories, ion extraction profiles and charge state distributions. In these set of parameters, only the injection beam energy parameter is modified for each run. In MCBC, the 3D background plasma parameters, magnetic field and electric field are read from ASCII files. If the user would like to perform simulations with homogeneous plasma, then the plasma parameters in the input file are used.

TABLE 5.9: Initial Helium plasma parameters

plasma parameters	values
Number of ions injected	50000 Na^+ ions
Buffer gas	^{4}He
Ion temperature	0.5 eV
Electron temperature	1 keV (plasmoid)
	5 eV (halo)
Electron density	4×10^{11} cm^{-3} (plasmoid)
	4×10^{10} cm^{-3} (halo)
Effective charge	1.58
Neutral density	0.46×10^8 cm^{-3}

In MCBC, a simplified ECR plasma model has been implemented by assuming the plasma into two zones: B $\leq B_{ECR}$ with a density n_e (plasmoid) and B $\geq B_{ECR}$ with a density n_e*10^{-1} (halo). This plasma model scheme has been proposed in a few articles [121, 122] and implemented in the charge breeding simulations [99, 123]. Among the three experimental cases, the first case (injection of Na^+ beam into Helium plasma) was chosen to demonstrate the method and finally, to extract the set of plasma parameters (plasma density, ion temperature , electron temperature and plasma potential). The Helium plasma parameters are acquired from the previous charge breeding simulation studies [99, 98, 123] and presented in the table 5.9. The effective charge $\langle Z_{eff} \rangle$ of Helium plasma is considered as 1.58, calculated from mass spectrum (see table 5.8). The neutral density in the three experimental cases are calculated and presented in the appendix D. Figure 5.26 shows the Helium plasma profiles generated according to the above mentioned axial magnetic field conditions. The injection & extraction optics potentials used in the Sodium case are given in the table 5.2. The ion density is calculated as

$$n_i = n_e / \langle Z_{eff} \rangle \tag{5.7}$$
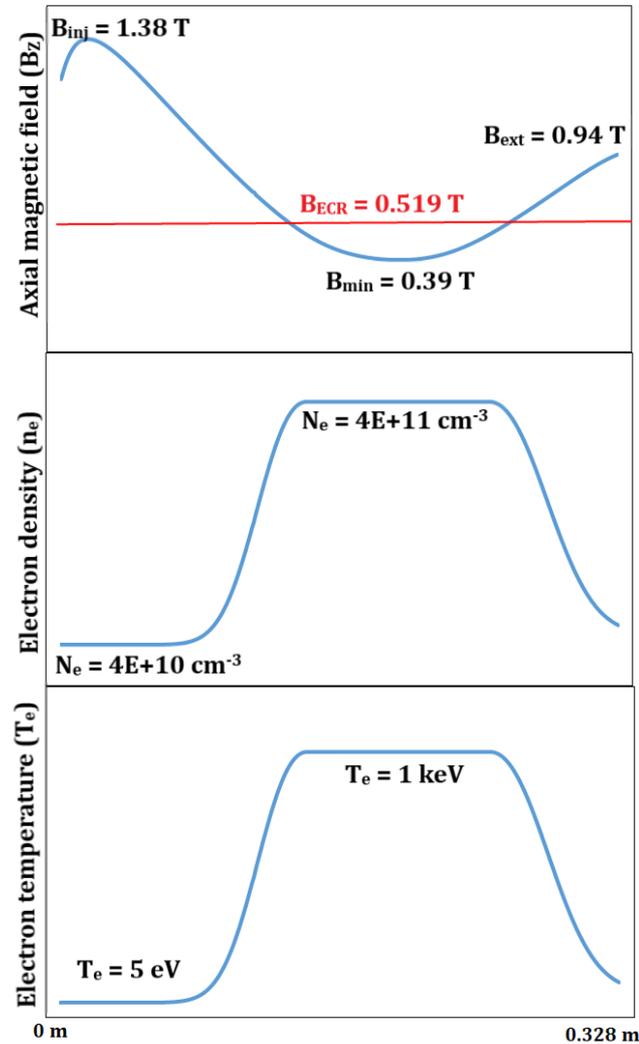
FIGURE 5.26: Background Helium plasma and axial magnetic field profiles.

where, $\langle Z_{eff} \rangle$ is the effective charge of Helium plasma.

The deceleration of incoming 1+ ions in the model is considered by calculating the 3D electric field from SIMION geometry, as shown in figure 5.27. The contour of plasma potential (V_P) in the figure is considered as to have similar geometry of the charge breeder plasma chamber wall (V_{cb}). The distance between the chamber wall and sheath is 1 mm. To take into account the deceleration of 1+ ions due to the positive plasma potential, the plasma potential (V_P) is considered higher than charge breeder potential (V_{cb}). The voltages applied to these electrodes are always fixed throughout the simulations. The ECR zone (V_{ECR}), approximated as cylindrically symmetric ellipsoid surface, is located at minimum-B structure formed by the axial and radial magnetic field.

As described in chapter 2, the confinement of highly charged ions is improved by the presence of a potential dip in the ECR surface. It has been suggested that a negative dip is formed due to the collision-less hot electron component in the ECR plasma [66]. To approximate a potential dip in the plasma model, a fixed voltage is given to
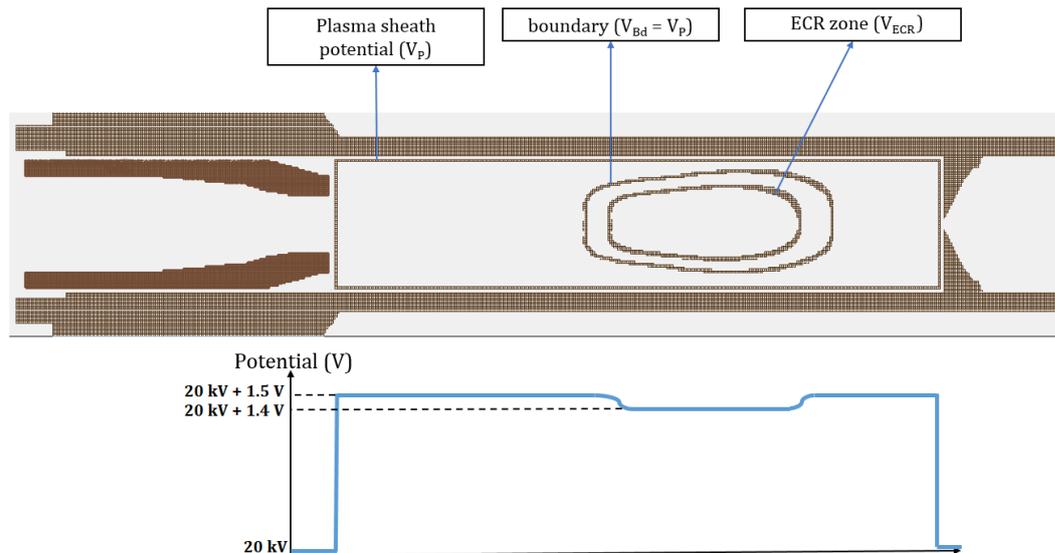
FIGURE 5.27: The modified SP1 CB SIMON geometry with ECR plasma potential features (top figure). The assumed plasma potential distribution for the charge breeding simulations (bottom figure).
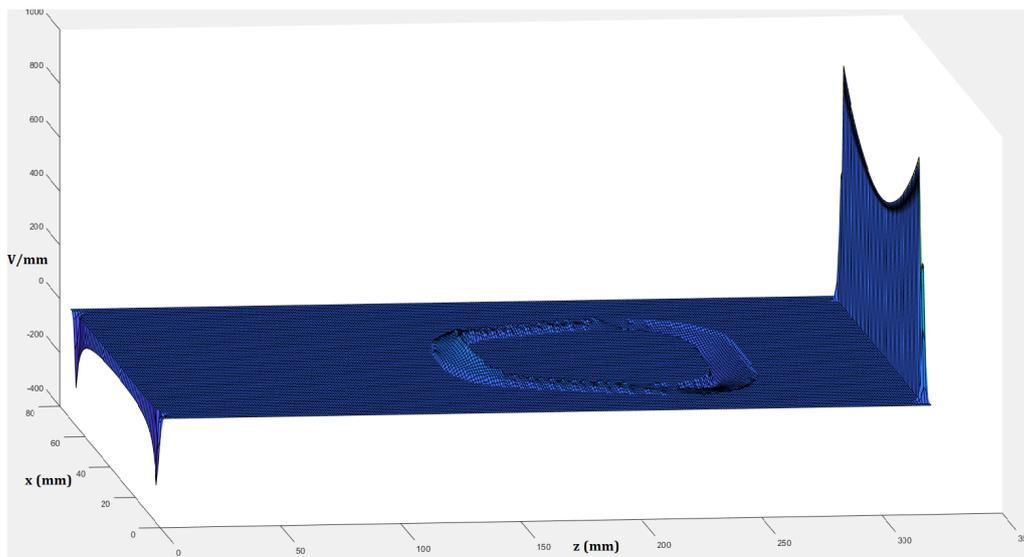
FIGURE 5.28: The electric field map (V/mm) related to the above given potential in the plane y = 0.

the ECR surface and considered to be always less than the plasma sheath potential ($V_{ECR} < V_P$). For an example, the plasma potential is considered as 1.5 V and the dip is assumed as 0.1 V. The potential distribution is shown in the figure 5.27. After applying the potentials to the geometry, SIMION generates the three components of the electric field (E_x, E_y, E_z) file. The electric field (on the plane y = 0) generated by applying 1.5 V to the plasma sheath and 0.1 V to the ECR zone is shown in the figure 5.28.

With the above discussed scheme, the 1+ ions enter the plasma boundary with an energy $E_{inj} = e(\Delta V - V_P)$. When they reach the ECR zone, they are first accelerated

and then decelerated inside the zone. This allows the 1 + ions to spend some time inside the ECR volume. Outside the ECR volume, ions are accelerated towards the chamber walls or towards the plasma electrode. The eΔV (additional energy (eV) given to the 1+ ions) is varied from 0 to 130 eV and the final efficiency is calculated after the extraction system of SP1 CB as shown in the figure 5.25. Finally, the ΔV curves are plotted as a function of final efficiency and the additional energy given to the 1+ ions (ΔV). The drawback of this assumption is that the plasma is assumed as a fixed equipotential surface without considering the potential drop near the device boundary (presheath effect) and the assumption of ion confinement (potential dip) without considering the plasma particles dynamics in the electromagnetic fields.

Simulation of beam capture

In the first set of simulation, 50000 Na^+ ions were initiated from beam slits position and transported through the injection optics and the deceleration tube. 100% transmission has been recorded up to the entrance of SP1 CB plasma chamber. The energy spread of the thermionic gun is ≈ 2 eV (measured by retarding field analyzer device), which is very small and therefore, neglected in the simulations. With the acquired beam properties, the 1+ ions are re-initiated in MCBC at z = 0 m with an integration time of 500 μs. The simulation was performed in 5×10^5 time steps with a time step fraction of 0.001 μs. For every injected beam energy, the percentage of particle that are lost and captured ions are calculated.

The parameters used in the first set of simulations are presented in the table 5.9. Charge breeding simulations were performed in two steps: In the first step, each plasma parameter was varied independently and the ΔV curves obtained from each sweep were compared with the Na^+ experimental curve. The *pearson's χ^2 test* [124] has been applied to find the closeness between the simulated ΔV curve and experimental one. The test gives the χ^2 value for each parameter used during the sweep. The parameter, which has a minimum χ^2 value, was chosen as an optimum plasma parameter. In the second step, the obtained optimum parameters were again varied independently and the final optimum plasma parameters from the χ^2 test were used to reproduce the experimental ΔV curve.

The simulations were initiated with the set of reference parameters. Several simulations were performed to find a good value for the plasma potential and the potential dip. Finally, the value was adjusted to 1.5 V for the plasma potential and 0.5 V for the potential dip, which was observed to best reproduce the shape of the experimental ΔV curve, as shown in the figure 5.29. The shape of the curve at lower injection energies (< 30 eV) is very similar to the experimental ones and exhibits the periodic variations after 40 eV, as observed in the SIMION simulations (see figure 5.22). Table 5.10 shows the particle percentages (captured and lost) and the percentage of 1+ ions extracted through extraction aperture for several injection beam energies. The particle losses constitutes four sub- columns: The percentage of ions reflected back to the injection side (**Back**), ions lost to the radial wall (**Wall**) and the ions arrived at the extraction end (**Ext**) are shown in the first three sub columns. The last sub-column is the total losses in the simulation domain (**Total**). Finally, the number of 1+ ions extracted through the plasma electrode is calculated and shown in the last column. It can be observed from the table 5.10 that the optimum capture is seen at the eΔV of 8 eV, which is bit higher to the value found during the experiments (ΔV = 6.5 V).
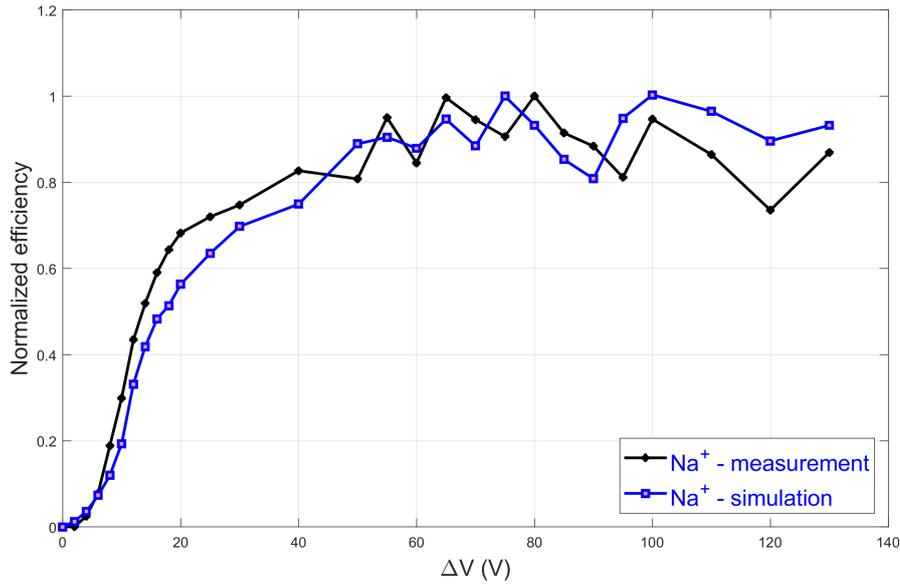
FIGURE 5.29: The comparison of $Na^+ \Delta V$ curves obtained by using the reference parameters in the simulation and experiment.

Following the observations, it can be said that the estimated plasma parameters (reference values) are almost close to the experimental ones. It is also shown in the table 5.10 that the fraction of 1+ ions, for the injection energies (> 50 eV), reach the plasma electrode without being captured or lost towards the wall. The ion losses near the wall and the plasma electrode were observed to be more dominant after 15 eV.

TABLE 5.10: Summary of the charge breeding simulation results obtained with the reference parameters.

$e\Delta V$ (eV)	Total capture (%)	Losses(%) Back	Wall	Ext	Total	$1 + ions$ extracted
2	6.32	92.66	0.86	0.16	93.68	50
4	14.33	83.13	2.28	0.26	85.67	110
6	25.04	69.84	4.24	0.88	74.96	250
8	**27.26**	**65.92**	**5.54**	**1.28**	**72.74**	**520**
10	26.88	64.3	6.6	2.22	73.12	970
15	11.48	40.05	17.48	30.99	88.52	1900
20	6.55	30.74	23.42	39.29	93.45	2670
25	2.86	23.24	26.74	47.16	97.14	3660
50	0.02	1.36	32.56	66.06	99.98	9660
100	0	0	30.96	69.04	100	12500
130	0	0	29.82	70.18	100	11340

In the first step, I considered to vary the different values of electron density starting

from 1×10^{12} (near to cut-off density $\approx 2.63 \times 10^{12} \ cm^{-3}$ (for 14.5 GHz) to 8×10^{10} cm^{-3}. At the same time, the ion density has been calculated, using the equation 5.7, for each electron density value. The ΔV curves obtained from this sweep are compared with the experimental ones, and presented in the figure 5.30.

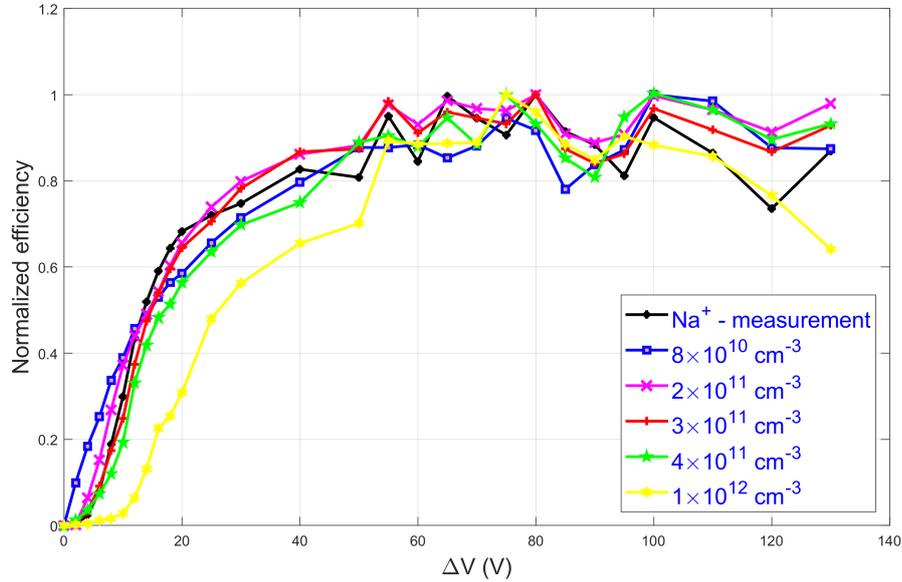FIGURE 5.30: The comparison of $Na^+ \Delta V$ experimental curve with the simulated $Na^+ \Delta V$ curves acquired for each electron density.

At higher electron densities ($1 \times 10^{12} \ cm^{-3}$), the total capture increases but the shape of the ΔV curve is not similar to the experimental ones. At lower densities, the trends of 1+ curve can be reproduced but with low captured fractions. It can be observed that the simulation with the electron density of $3 \times 10^{11} \ cm^{-3}$ match the shape of curve at the lower injection energies. The trends at higher injection energies are also reproduced but with a small discrepancy. Anyway, the χ^2 test has been applied to the curves and the minimum χ^2 value was found for the electron density of 3×10^{11} cm^{-3}, with an error bar of $\pm 1 \times 10^{11} \ cm^{-3}$ (refer appendix E). It was also observed that a few percent of simulated ions still present in the simulation domain after 500 μs.

After the electron density sweep, the influence of ion temperature (kT_i) was investigated by varying from 0.1 eV to 3 eV. Due to the strong dependence of ion temperature, the ion-ion collisions are more frequent than the other collision frequencies in ECR plasma. As the ion temperature increases, the collisions becomes less frequent ($\nu_{ii} \propto kT_i^{-3/2}$). Therefore, a great influence of this parameter on the 1+ capture was expected. For each ion temperature, the ΔV curve is obtained and compared with the experimental curve and presented in the figure 5.31. As expected, the parameter has shown a great influence in the capture region. When the temperature was set to 0.1 eV, the 1+ ions successfully entering the potential barrier are captured in the plasma and not extracted at the end of the simulation even at the injection energy of 10 eV. Moreover, the shape of the curve was observed to be far from experimental one. As the ion temperature increases up to 1 eV, the simulated curves at lower injection energies starts moving towards the experimental curve. In the higher ion
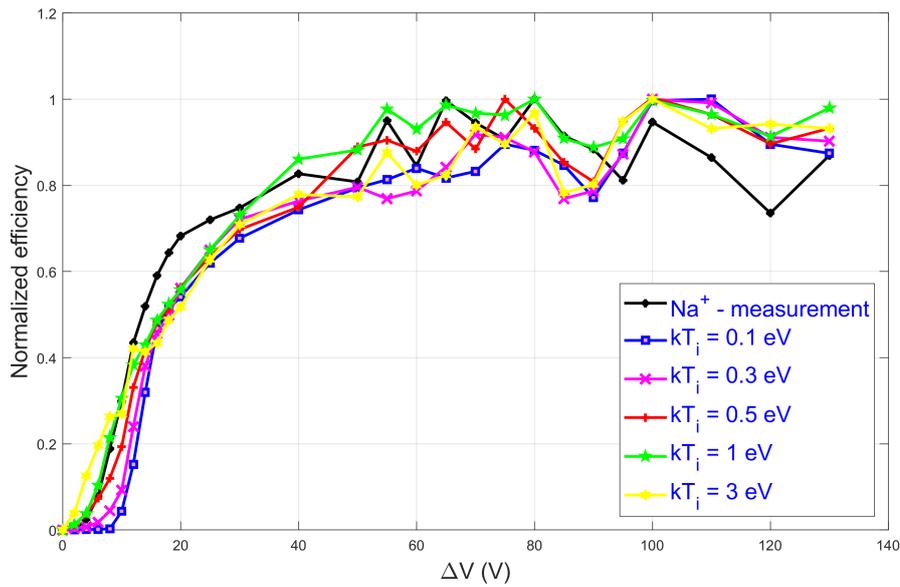
FIGURE 5.31: The comparison of $Na^+\Delta V$ experimental curve with the simulated $Na^+\Delta V$ curves acquired for each ion temperature.
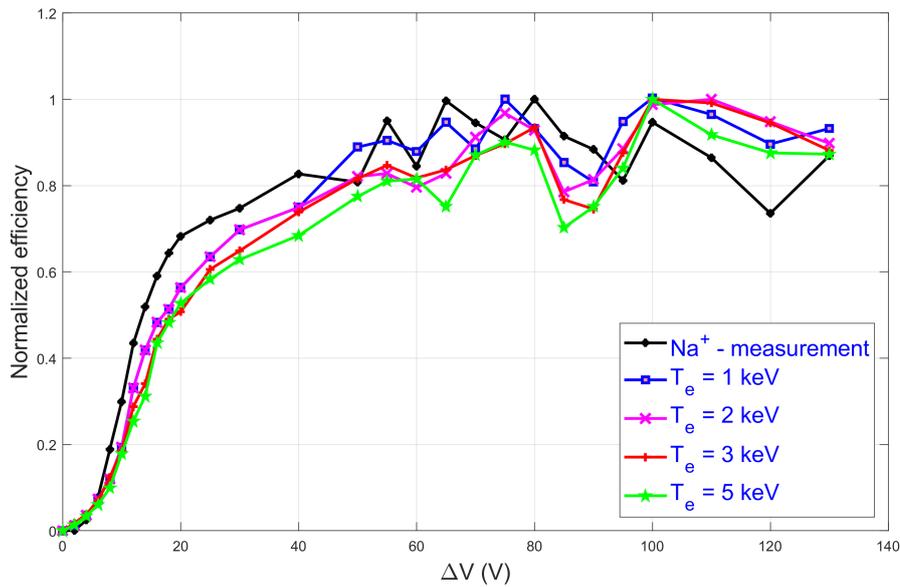
FIGURE 5.32: The comparison of $Na^+\Delta V$ experimental curve with the simulated $Na^+\Delta V$ curves acquired for each electron temperature.

temperatures (> 1 eV), the confinement is very poor due to low collision frequencies with the plasma ions and exhibits different trends at lower and higher injection energies. The χ^2 value has been calculated for each case and the minimum value was found when the ion temperature was set to 1 eV with an error bar of $\pm$ 0.5 eV (refer appendix E).

Following the variation of ion temperature, the electron temperatures were varied by

TABLE 5.11: The total capture at different electron temperatures.

Electron temperature KT_e (keV)	Total capture (%)
1	27.26
2	27.00
3	26.98
5	26.68

assuming warm electrons component (T_e) in the core (1 keV, 2 keV, 3 keV and 5 keV). The results obtained with these temperatures are compared with the experimental results and presented in the figure 5.32. While increasing the electron temperature (> 1 keV), simulations revealed no significant change in the shape of simulated curves at lower injection energies and different trends at higher injection energies. The capture efficiencies for the four electron temperatures corresponding to the eΔV of 8 eV are shown in the table 5.11.

TABLE 5.12: Calculated ionization times inside the plasmoid for Sodium charge states from 0 to 3+ considering different electron temperatures.

Ionization	$\tau_{ionization}$ (μs) 1 keV	$\tau_{ionization}$ (μs) 2 keV	$\tau_{ionization}$ (μs) 3 keV	$\tau_{ionization}$ (μs) 5 keV
$0 \rightarrow 1+$	37.1	46.4	53.2	63.6
$1+ \rightarrow 2+$	116	133	147	169
$2+ \rightarrow 3+$	207	232	253	288
$3+ \rightarrow 4+$	362	394	425	477

It can be seen that the total capture are quite similar for different electron temperatures. The χ^2 value has shown the electron temperature of 1 keV as an optimum with an error bar of $\pm$ 0.5 keV (refer appendix E). The negligible influence observed during the variation of this parameter can be explained by considering the ionization potentials of the corresponding ions, which are very small and thus, the four electron temperatures used in the simulation roughly lead to the similar ionization times, as shown in the table 5.12. Also, the ionization times for the first four charge states are shorter than the time span of the simulation (500μs). The ionization times are calculated using the relation [24, 125]:

$$\tau_{z_1 z_2} = \frac{1}{[n_e \sigma_{z_1 z_2}(v_e) v_e]} \tag{5.8}$$

The table 5.13 shows the comparison of optimum parameters obtained from the first step and the reference values used in the beginning of the simulation. Figure 5.33 shows the comparison of simulated and the experimental Na^+ ΔV curve. The simulated curve using first optimum parameters is very close to the experimental one.

TABLE 5.13: The comparison of optimum simulation parameters from the first step with the reference parameters used in the beginning of the simulations.

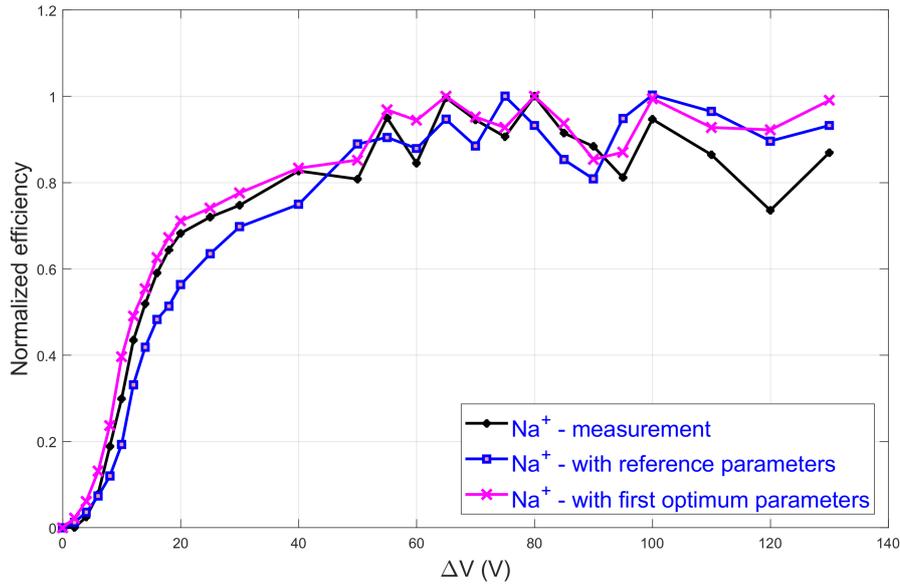| parameters	reference values	First optimum values
Plasma potential & dip	1.5 V and 0.5 V	1.5 V and 0.5 V
Ion temperature	0.5 eV	1 ± 0.5 eV
Electron temperature (plasmoid)	1 keV	1 ± 0.5 keV
Electron density (plasmoid)	$4 \times 10^{11}\ cm^{-3}$	$3 \pm 1 \times 10^{11}\ cm^{-3}$

FIGURE 5.33: The comparison of $Na^{+} \Delta V$ experimental curve with the simulated $Na^{+} \Delta V$ curves acquired using the optimum parameters and the reference parameters.

In the second step, the optimum parameters obtained from the first step are further optimized to find the correct parameters that can reproduce the experimental Na^{+} ΔV curve. The ion temperature was varied from 0.5 eV to 1.5 eV and the minimum χ^2 value was found in the range of 0.9 - 1.1 eV (refer appendix E). The electron temperature was varied from 500 eV to 2 keV and the minimum χ^2 value was found in the range of 1 - 2 keV . The electron density was varied in a small range i.e. from $2 \times 10^{11}\ cm^{-3}$ to $4 \times 10^{11}\ cm^{-3}$ and the minimum χ^2 value was found in the range of 3.3 - $3.7 \times 10^{11}\ cm^{-3}$. Considering the mean value in the estimated range of optimum values, the simulated ΔV curve was calculated and compared with the experimental curve. Figure 5.34 shows the final curve obtained from the model which is in very good agreement with the experimental Na^{+} ΔV curve.

The summary of charge breeding results obtained using the final optimum parameters is shown in the table 5.14. The optimum $e\Delta V$ is now (7.5 eV) which is still higher than the optimum ΔV found during the experiment (ΔV = 6.5 V). It can be seen that the total capture is reduced by a factor of 1.7 when compared with results obtained using the reference parameters (see table 5.10). The difference between the reference

FIGURE 5.34: The comparison of $Na^+ \Delta V$ experimental curve with the simulated $Na^+ \Delta V$ curves acquired using the optimum parameters from the first and second step.

TABLE 5.14: Summary of the charge breeding results obtained with the final optimum parameters.

$e\Delta V$	Total	Losses (%)				$1 + ions$
(eV)	capture (%)	Back	Wall	Ext	Total	extracted
2	3.86	91.94	2.94	1.26	96.14	170
4	10.62	81.84	3.52	4.02	89.38	530
6	15.15	69.37	9.32	6.16	84.85	1640
7.5	**16.44**	**63.36**	**10.74**	**9.46**	**83.56**	**2080**
8	15.12	60.88	13.26	10.74	84.88	2265
10	12.82	56	14.58	16.6	90.18	3440
15	6.06	41.28	21.86	30.8	93.94	8350
20	2.92	29.64	23.88	43.56	97.08	10260
25	1.26	23.02	26.76	48.96	98.74	11080
50	0	0	35.40	64.60	100	12000
100	0	0	38.36	61.64	100	14870
130	0	0	37.80	62.20	100	13890

parameters and the final optimum parameters is the electron density (from 4×10^{11} $cm^{-3} \rightarrow 3.5 \times 10^{11}$ cm^{-3}) and the ion temperature (from 0.5 eV $\rightarrow$ 1 eV), which exhibited a great influence on the total capture. Moreover, the particle losses near the wall and extraction end are significantly higher which explains that the fraction of
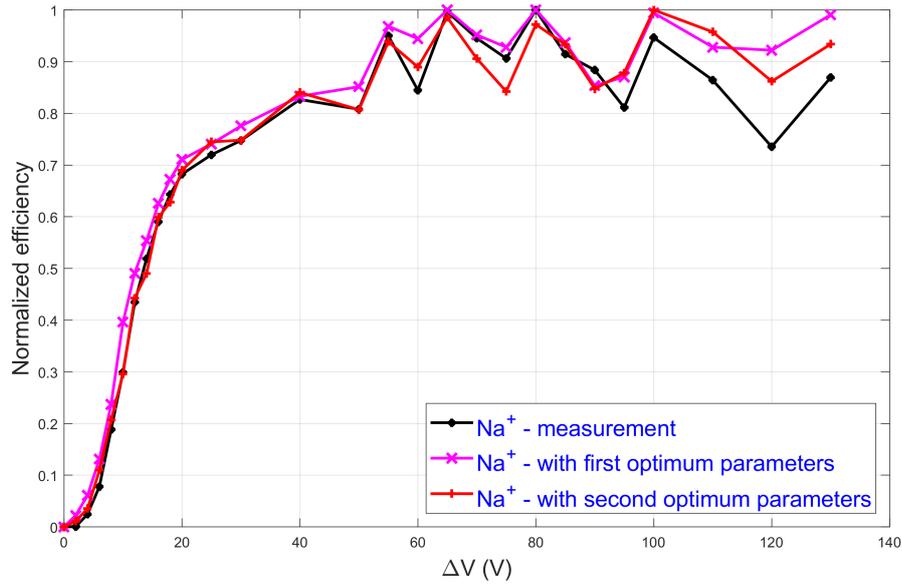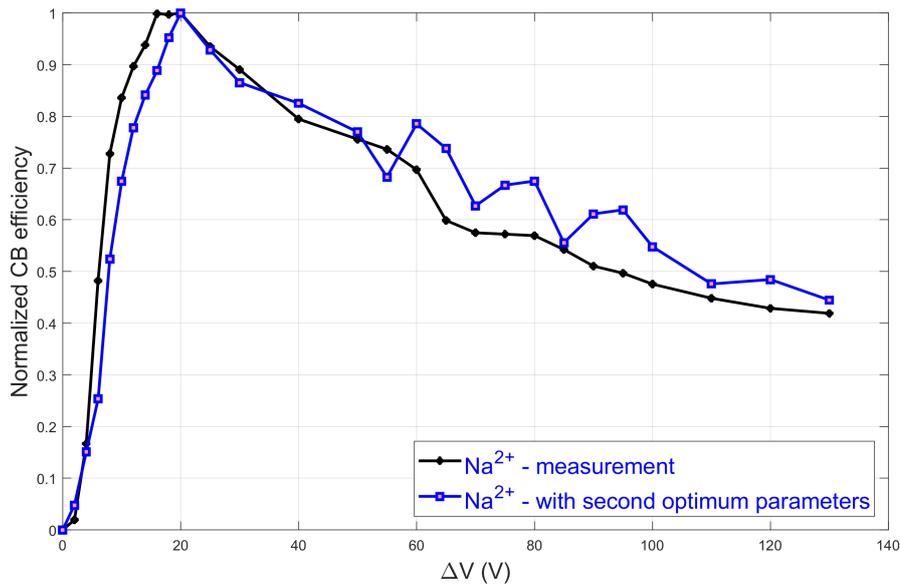
FIGURE 5.35: The comparison of $Na^{2+}\Delta V$ experimental curve with the simulated $Na^{2+}\Delta V$ curves acquired using the optimum parameters from the second step.

ions is not being slowed down sufficiently in the plasma. The amount of ions lost towards the injection is almost similar in the both cases.

Using the similar set of parameters, an attempt has been made to reproduce the experimental trends of Na^{2+} ΔV curve by increasing the simulation integration time from 500 μs to 700 μs. This modification was done keeping in the mind the charge breeding time of 2+ charge states, which is assumed to be around 700 μs. This value has been verified with the charge breeding time of K^{2+} (in Helium plasma) measured at the optimum SP1 CB operating conditions and found to be around 600 μs $\pm$ 16% (see section 5.2.4). The charge breeding times for other two cases (Na+ He and K + O_2) were not measured but, it was assumed to be in the similar range for Na^{2+} (in Helium plasma) and K^{2+} (in Oxygen plasma). Moreover, the ionization times (1+ $\rightarrow$ 2+) shown for the four electron temperatures, in the table 5.11, are shorter than the simulation integration time (500 μs). Figure 5.35 shows the comparison of Na^{2+} ΔV curve obtained from the simulation with the experimental Na^{2+} ΔV curve. At lower injection energies, the comparison shows a better agreement with the experimental curve. The periodic variations in the higher injection energies are observed and exhibited deviations from the experimental curve (largely in the case of K^{2+} in Helium plasma).

Interaction of K^+ ion beam with Helium and Oxygen plasma: Following the numerical analysis of Na^+ interaction in Helium plasma, the simulations of the K^+ capture in Helium and Oxygen plasma were performed by applying the above presented approach. The input parameters including the magnetic field configuration and potentials given to the electrostatic triplet for the two cases (K + He and K + O_2) are gathered from the table 5.2.

50000 K^+ ions were initiated in SIMION with an energy of 15 keV and transported

TABLE 5.15: Reference parameters used in the beginning of the simulations

parameters	$K + He$	$K + O_2$
Number of ions injected	50000 K^+ ions	50000 K^+ ions
Plasma potential and dip	1 V and 0.5 V	1 V and 0.5 V
Ion temperature	0.5 eV	1 eV
Electron temperature	1 keV (plasmoid) 5 eV (halo)	1 keV (plasmoid) 5 eV (halo)
Electron density	4×10^{11} cm^{-3} (plasmoid) 4×10^{10} cm^{-3} (halo)	4×10^{11} cm^{-3} (plasmoid) 4×10^{10} cm^{-3} (halo)
Effective charge	1.38	4.28
Neutral density	0.46×10^8 cm^{-3}	1.48×10^8 cm^{-3}

TABLE 5.16: Final optimum parameters obtained in the second step

parameters	$K + He$	$K + O_2$
eΔV	8.5 eV	8.5 eV
Plasma potential and dip	1 V and 0.6 V	1 V and 0.6 V
Ion temperature	0.7 - 0.8 eV	1.5 - 2.5 eV
Electron temperature (plasmoid)	1 - 2 keV	2 - 3 keV
Electron density (plasmoid)	1.5 - 2.5 $\times 10^{11}$ cm^{-3}	1.0 - 2.0 $\times 10^{11}$ cm^{-3}
Effective charge	1.38	4.15
Neutral density	0.46×10^8 cm^{-3}	1.48×10^8 cm^{-3}

through the electrostatic triplet with an emittance of 50 π.mm.mrad. The beam properties near the entrance of the SP1 CB plasma chamber were calculated and given as starting conditions for MCBC. In the two cases, the simulation integration time has been increased to 700 μs in order to reproduce the 1+ and also 2+ ΔV curves. Table 5.15 shows the set of plasma parameters which are called as 'reference parameters' used in the first step of simulations.

Each plasma parameter was varied independently and the optimum parameters are obtained in the first step. The χ^2 plots for each parameter sweep are presented in the appendix E. Each optimum parameter was varied again to find the correct plasma parameters that can reproduce the experimental trends. The final optimum parameters are shown in the table 5.16. Figure 5.36 and 5.37 shows the normalized simulated and experimental K^+ efficiency as a function of the incident ion energy obtained using the final optimum Helium and Oxygen plasma parameters. The simulated 1+ and 2+ CB efficiency trends, increasing with the incident ion energy, are in good agreement with the experimentally observed trends at lower injection energies and has shown apparent discrepancies in the higher injection energies (mainly in the case of K^{2+} in Helium plasma). Table 5.17 shows the comparison of the total estimated capture obtained from the three experimental cases for different eΔV. The
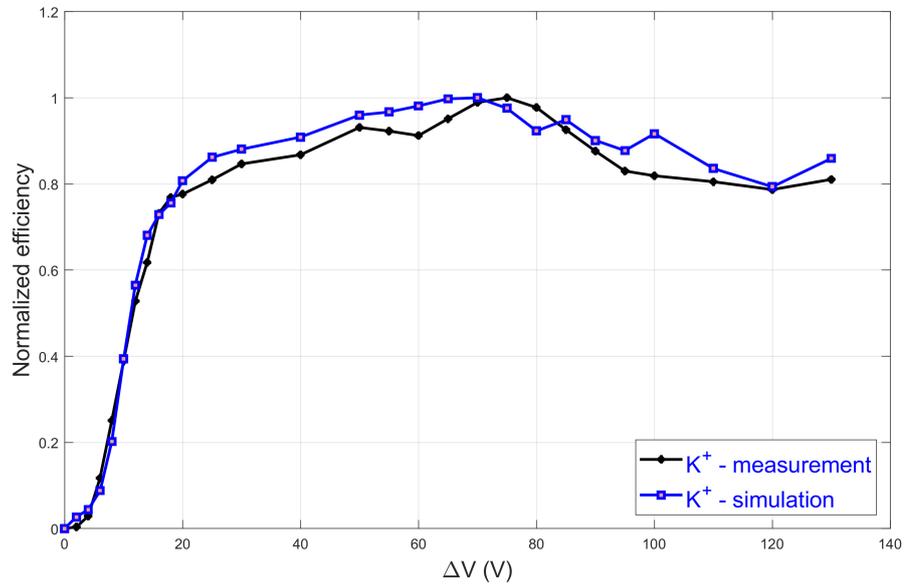
(A)
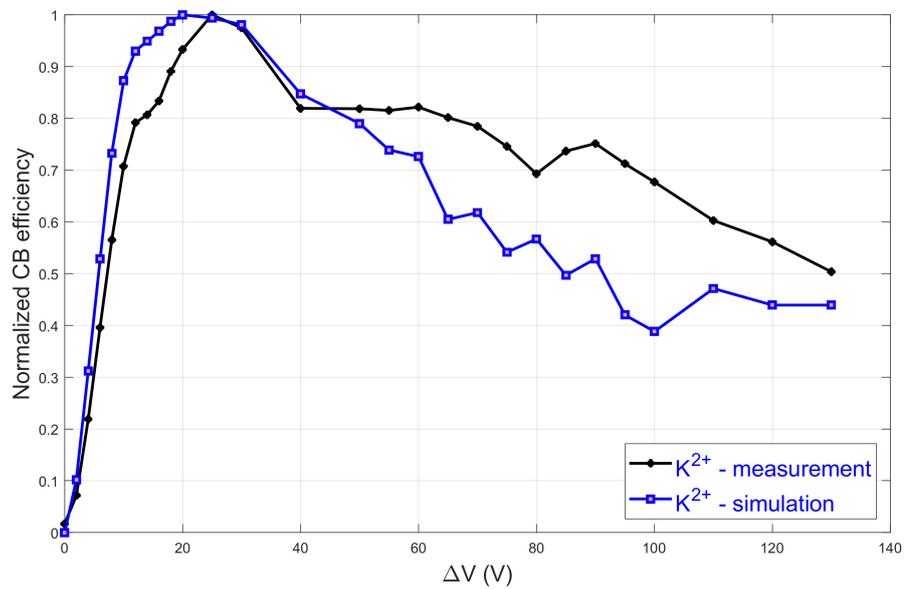
(B)

FIGURE 5.36: (A) Comparison of simulated and experimental K^{1+} and K^{2+} ΔV curves obtained from Helium plasma. A plasma density of 2×10^{11} cm^{-3} (for 207 W microwave power) and ion temperature of 0.75 eV were used in the simulation.
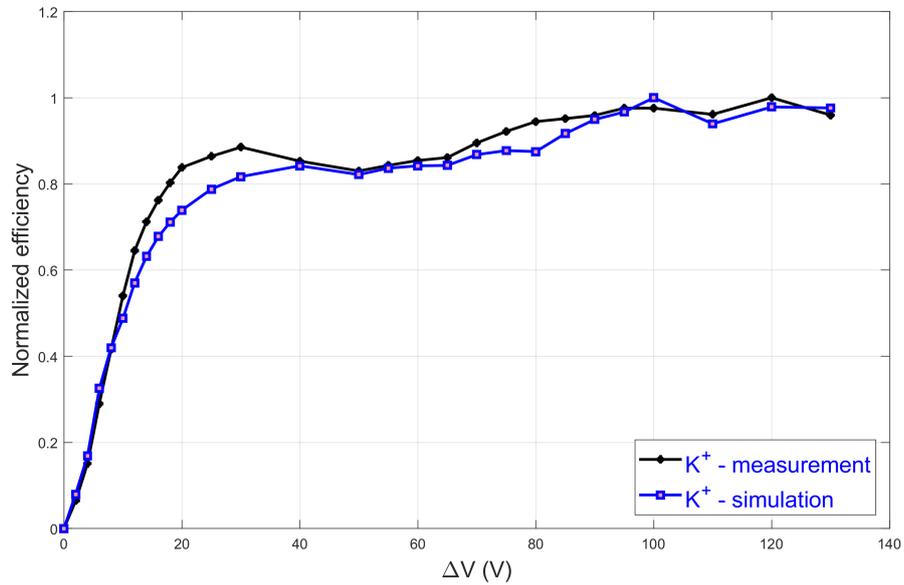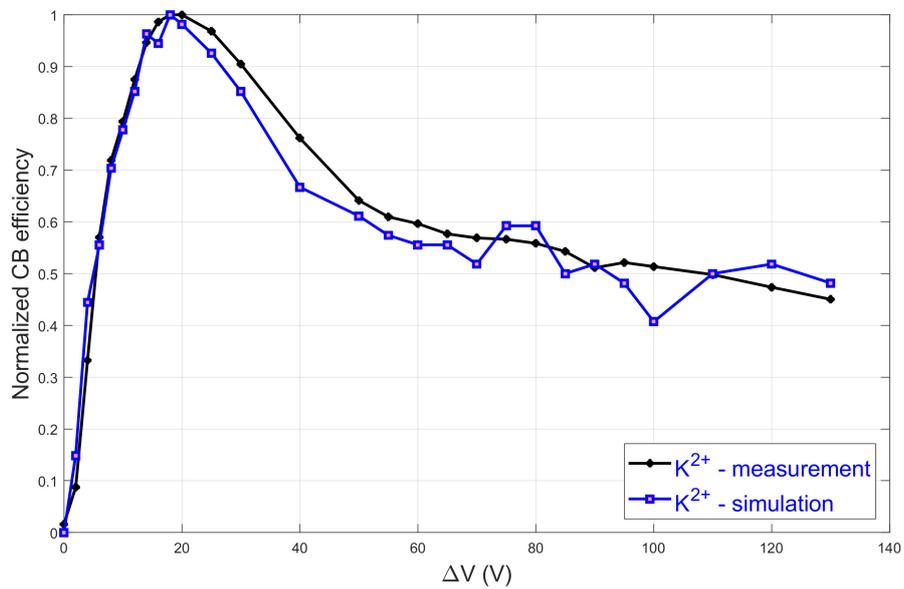
(A)

(B)

FIGURE 5.37: (A) Comparison of simulated and experimental K^{1+} and K^{2+} ΔV curves obtained from Oxygen plasma. A plasma density of 1.5×10^{11} cm^{-3} (for 209 W microwave power) and ion temperature of 2 eV was used in the simulation.

TABLE 5.17: Summary of the total capture efficiencies obtained with the final optimum parameters.

$e\Delta V$ (eV)	Total capture (%) Na+ He	Total capture (%) K + He	Total capture (%) $K + O_2$
2	3.86	4.96	2.4
4	10.62	11.98	4.78
6	15.15	18.22	5.94
7.5	**16.44**	23.44	6.26
8.5	14.44	**24.52**	**7.26**
10	12.82	23.28	6.64
15	6.06	12.06	2.42
20	2.92	4.58	1.02

optimum eΔV found in the three cases are highlighted in the table 5.17. The maximum capture efficiencies of Na and K in Helium plasma at different microwave powers (470 W and 200 W) are approximately 16% and 25%, respectively. While the corresponding value for K^+ ions in an Oxygen plasma is approximately 7%.

Discussions and summary

As described above, it was possible to find a set of plasma parameters that showed a very good agreement with the experimental trends. In the three simulation cases, the periodic variations exhibited in 1+ ΔV curves at higher injection energies are in good agreement with the variations seen in the experimental ΔV curves (especially with Na^+). It has to be reminded that the trends of 2+ ΔV curves are reproduced using the set of optimum plasma parameters found in the successful reproduction of experimental 1+ ΔV curves. The only parameter that was modified is the time span of the simulation (changed from 500 μs $\rightarrow$ 700 μs). The periodic variations in 2+ simulated ΔV curves at higher injection energies (> 50 eV) are bit deviated from the experimental one (largely deviated in the case of K^{2+} in Helium plasma). These deviations were also observed in simulated 1+ ΔV curves but very small when compared with simulated 2+ ΔV curves. This is may be due to the simplified background plasma model implemented in the simulations (see figure 5.26), where the standard deviation (σ) of the exponential function is considered as 0.179. The plasma density and temperatures profiles presented in the model are too simple compared to the plasma profiles reported in Ref. [126].

For the sake of clearness, the input parameters given to the MCBC and the plasma parameters obtained from the MCBC are gathered and presented in the table 5.18. The highlighted part in the table 5.18 is the data obtained from the charge breeding simulations. Now it is interesting to analyze more in detail the influence of each input parameter and the plasma parameter on the final capture efficiencies given by MCBC at optimum injection energies. Looking at the table 5.18, it can be seen that the RF power and injection optics are different in the case of Na (Helium as buffer

TABLE 5.18: Summary of input parameters and final optimum plasma parameters for the three experimental and simulated cases.

Parameters	$Na + He$	$K + He$	$K + O_2$
1+ source potential (V)	20006.5	15007.5	15006.5
SP1 CB potential (V)	20000	15000	150000
Injection triplet potentials (kV)	$\pm (1.15/0.7/0.25)$	$\pm (1.3/1.7/0.35)$	$\pm (1.3/1.7/0.35)$
power (W)	470	209	207
B-field in T (inj/min/ext)	1.4/0.39/0.94	1.4/0.41/0.88	1.4/0.4/0.88
Effective charge	1.58	1.38	4.18
ΔV_{exp} (V)	6.5	7.5	6.5
Beam radius (mm)	**4.9**	**4.25**	**4.25**
beam divergence (mrad)	**17.83**	**17.29**	**17.29**
Ion temperature (eV)	**0.9 - 1.1**	**0.7 - 0.8**	**1.5 - 2.5**
Electron density cm^{-3}	$\mathbf{3.3 - 3.7 \times 10^{11}}$	$\mathbf{1.5 - 2.5 \times 10^{11}}$	$\mathbf{1.0 - 2.0 \times 10^{11}}$
Electron temperature (keV)	**1 - 2**	**1 - 2**	**2 - 3**
Plasma potential (V)	**1.5**	**1**	**1**
potential dip (V)	**0.5**	**0.6**	**0.6**
$\mathbf{e\Delta V_{simulation}}$ $\mathbf{(eV)}$	**7.5**	**8.5**	**8.5**
$\mathbf{E_{inj} = e(\Delta V - V_P)}$ $\mathbf{(eV)}$	**6**	**7.5**	**7.5**
Total capture (%)	**16.44**	**24.52**	**7.26**

gas) and same in the case of K (Helium and Oxygen as buffer gas).

Influence of 1+ beam emittance on capture : Many simulations were performed to understand the influence of 1+ beam emittance on the capture dynamics. One of the experimental cases (e.g. Na+ He) was considered to investigate the influence of injected beam emittance (beam radius and divergence) on the beam capture dynamics. The simulations were carried out with the similar approach presented in the figure 5.25. The 1+ ions are initiated in SIMION with the beam properties (radius and angular divergence) given in the table 5.18. These properties correspond to $50.\pi$.mm.mrad emittance. The beam properties for each emittance value were obtained by scaling the beam properties of 50π.mm.mrad emittance. The final optimum plasma parameters obtained from the first experimental case (Na+ He) were used in the numerical study. For each emittance value, the total capture and the particle losses were recorded at an optimum ΔV of 7.5 eV.
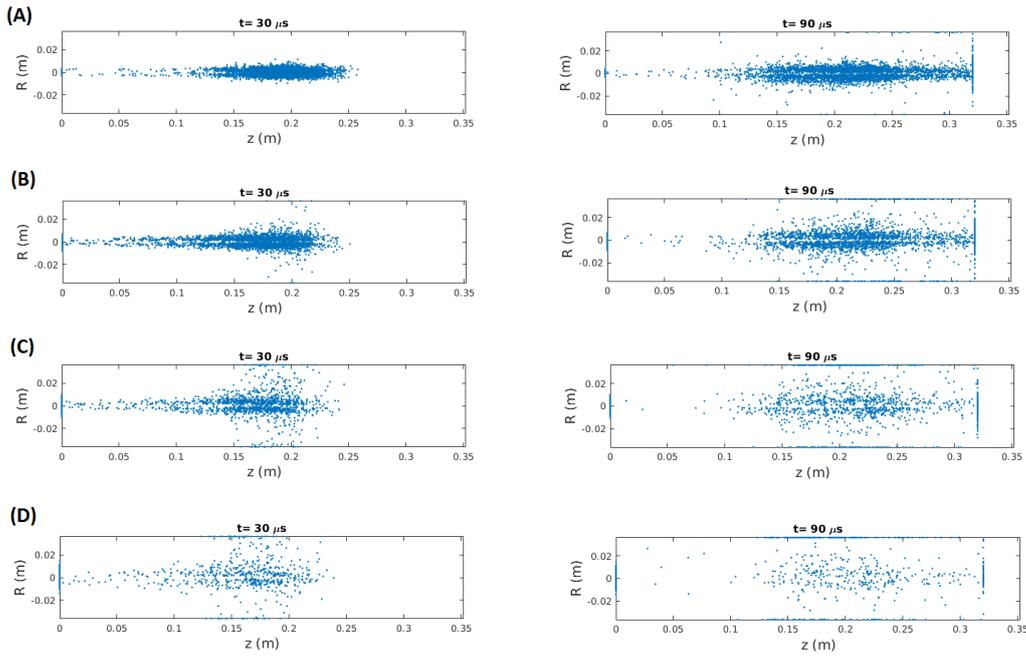
FIGURE 5.38: Snapshots of the captured ions 30 μs (left figures) and 90μs (right figures) after the Na^+ ions enter the device at z = 0.127 m (0 m in the figure). (A) Injected 1+ beam emittance of 10 π.mm.mrad (B) Injected 1+ beam emittance of 30 π.mm.mrad (C) Injected 1+ beam emittance of 50 π.mm.mrad (D) Injected 1+ beam emittance of 80 π.mm.mrad.

TABLE 5.19: Summary of the total beam capture and losses for several values of 1+ beam emittance.

Emittance	Total	Losses (%)				ϵ_{1+}
($\pi.mm.mrad$)	capture (%)	Back	Wall	exit	Total	(%)
80	3.08	80.08	15.48	1.36	96.92	0.8
70	7.32	75.5	14.38	2.8	92.68	1.06
60	12.1	69.24	12.58	6.08	87.9	2.06
50	16.44	61.46	10.64	11.46	83.56	4.16
40	22.56	54.54	7.64	15.26	77.44	6.46
30	27.04	43.48	6.88	22.6	72.96	10.94
20	29.8	35.88	4.28	30.04	70.2	14.24
10	37.04	24.18	4.02	39.76	67.96	20.53

Figure 5.38 shows the snap shots of injected ions at 30 μs and 90 μs and the summary of total capture and losses are shown in the table 5.19. At smaller emittance (10 π.mm.mrad), it can be seen that up to 30% of 1+ ions are trapped inside the ECR volume (plasmoid), while a fraction of ions are in halo region or lost to the wall and most of them are lost towards the plasma electrode. At higher injection emittance (80 π.mm.mrad), majority of ions are lost near the injection and the total capture is
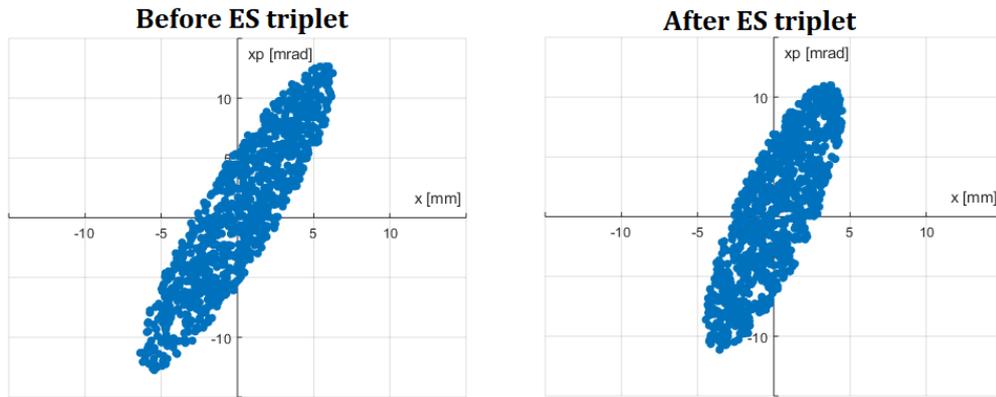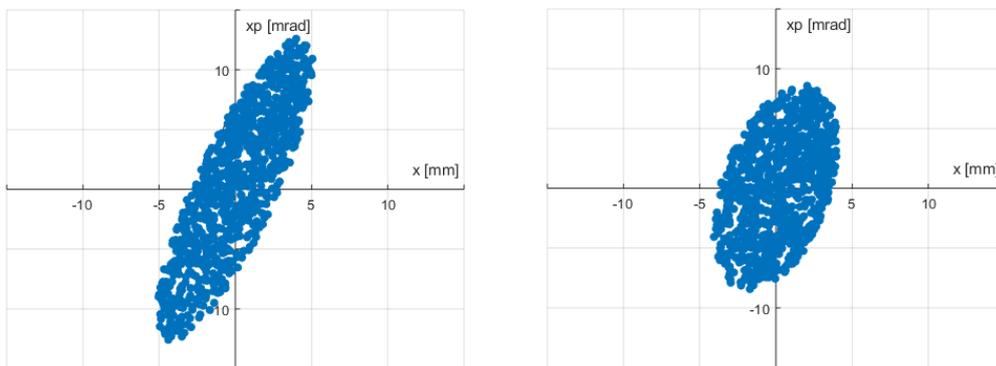
(A) Na$^+$ beam (@ 20 keV)

Before ES triplet

After ES triplet

(B) K$^+$ beam (@ 15 keV)

FIGURE 5.39: Simulated transverse beam properties before and after the electrostatic triplet for 20 keV Na^+ beam (Figure A) and 15 keV K^+ beam (Figure B). The simulation was performed with 5000 ions.

on the order of 3%. The simulation clearly shows that the 1+ beam emittance (radius and divergence) should be as small as possible to achieve high capture efficiency and consequently, high charge breeding efficiency. As a similar trend is observed in measured data (see figure 5.8), it suggests that similar effect takes place in reality. In charge breeding simulations, it has to be reminded that the experimental ΔV curves are reproduced using a 50 π.mm.mrad Na^+ and K^+ beam and achieved a total capture of 16 % and 24% with Helium as buffer gas. The beam characteristics for the the two cases are quite similar at the slit position (S13). After propagating through the injection optics (ES triplet and deceleration tube), the beam characteristics found to be different. Figure 5.39 shows the simulated transverse beam properties before and after the injection electrostatic triplet. After passing through the ES triplet, the K^+ beam (@ 15 keV) is observed to be focused than the Na^+ beam (@ 20 keV). This due to the difference in beam properties obtained at the slit position and also the potentials given to the electrostatic triplet.

Influence of plasma density and ion temperature : Charge breeding simulations revealed different Helium and Oxygen plasma densities at different microwave power, as shown in the table 5.18. The obtained plasma densities are an order of magnitude lower in comparison to the critical density of $n_{e,critical} \approx 2.6 \times 10^{12}$ cm^{-3} for 14.5 GHz microwaves. The Helium plasma density is higher for 470 W of microwave power

than at 200 W. In the three simulation cases the plasma density was varied up to the critical density value. From the figure 5.30, it can be seen that the 1+ transport efficiency is higher at lower plasma densities and the opposite holds for the higher plasma densities. At the same time, the total capture is improved at high densities than at lower densities. The estimated Oxygen plasma density at 200 W of microwave power is in good agreement with the estimates reported in the publication [98]. The estimated Helium plasma densities at 470 W and 200 W of RF power are close to the estimates reported in [69]. To find out the plausible explanation for the difference in total capture, the obtained plasma parameters (plasma density, plasma ion temperature and effective charge) are used to investigate the collision rates between the incident 1+ ions and background plasma ions and mean free paths of the cumulative long range ion-ion collision. The ion-ion collision frequency scales with the electron density and plasma ion temperature ($\nu_{ii} \propto n_e/(kT_i^{-3/2})$). The ion temperatures obtained from the simulations of three experimental cases are as follows: 0.7 - 0.8 eV (K in Helium plasma @ 200 W), 0.9 - 1.1 eV (Na in Helium plasma @ 470 W) and 1.5 - 2.5 eV (K in Oxygen plasma @200 W). The estimated ion temperature in Oxygen plasma at 200 W of microwave power is close to the estimates reported in [45]. The data obtained from the simulations can be used for estimating the mean free path of long range ion - ion collisions of the 1+ ions (λ_{ii}^{1+}), using the equation [98]:

$$\lambda_{ii}^{1+} = -\frac{L}{\frac{L}{\lambda_{1+}} + \ln\left(\frac{I_{plasma}}{I_{vacuum}}\right)} \tag{5.9}$$

where L is the effective plasma length, λ_{1+} is the mean free path of in-flight electron impact ionization, I_{plasma} is the 1+ ions transported through the SP1 CB plasma at optimum ΔV and I_{vacuum} is the 1+ ions transported without SP1 CB plasma. The effective plasma length is approximately 120 mm ($\pm$ 10% depending on the magnetic field configuration applied in the three cases). The electron impact ionization cross sections are calculated from the Lotz fromula [52]. The corresponding 1+ ions collision frequency can be calculated from the estimated mean free path by

$$\nu_{ii}^{1+} = \frac{v_a}{\lambda_{ii}^{1+}} \tag{5.10}$$

where, v_a is the velocity of incident 1+ ions at an optimum injection energy (E_{inj}). Using the above equations, the upper limit of 1+ ions mean free paths and the lower limits of the ion-ion collisions frequencies for Na^{1+} and K^{1+} in Helium and Oxygen plasma at different microwave power levels are shown in the table 5.20. From the table 5.20, it can be seen that the ion-ion collision frequency of Na^{1+} is bit higher compared to the K^{1+} ions in Helium plasma. In addition to that, the estimated ion-ion collision mean free paths of Na^{1+} and K^{1+} ions are almost in the similar range. However, the total capture is still higher for K^{1+} ions compared to Na^{1+} ions. On the other hand, the experimental results also revealed higher efficiencies in the case of K compared to Na in Helium plasma (see table 5.2). Finally, this implies that the difference in total capture efficiencies between the Na and K ions is mainly due to the proper focusing of K^{1+} beam than Na^{1+} beam.

In the case of K^{1+} ions in Helium and Oxygen plasma, the calculated mean free path of ion-ion collisions are approximately 30% longer for K^{1+} in Oxygen plasma

TABLE 5.20: Estimated ion-ion collision frequencies (lower limit) and the 1+ mean free path (upper limit) for Na^{1+} and K^{1+} ions, and the corresponding Helium and Oxygen plasma densities at different microwave powers. The value of Coulomb algorithm is assumed as 10.

	$Na + He$	$K + He$	$K + O_2$
power (W)	470	209	207
n_e (cm^{-3})	3.5×10^{11}	2.0×10^{11}	1.5×10^{11}
$E_{inj} = e(\Delta V_{exp} - V_P)$ (eV)	5.5	6.5	5.5
ν_{ii}^{1+} (KHz)	182	163	109
λ_{ii}^{1+} (mm)	37.08	34.63	47.52
Total capture (%)	16.44	24.52	7.26

compared to K^{1+} ions in Helium plasma. At the same time, the estimated ion-ion collision frequencies are higher for K^{1+} in Helium plasma compared to K^{1+} ions in Oxygen plasma. The differences in the collision rates can be seen in the experimental results, where the fraction of incident K^{1+} ions propagating through the Oxygen plasma is approximately 6.5%, while the K^{1+} ions propagating through the Helium plasma is around 2.5% at equivalent microwave powers. Finally, the good agreement between the experimental and simulated trends indicates that the difference in total capture between K^{1+} ions in Oxygen and Helium plasma is due to the difference in the collision rates.

In the charge breeding community, it is widely accepted that the optimum capture is achieved when the ratio of longitudinal component of the injected 1+ ion velocity (v_a) to the thermal velocity of the plasma ions (v_b) is 1 [94]. Corresponding to the above said condition ($v_a = v_b$), the optimum injection energy of the 1+ ions, for the best slowing down, can be estimated [69] as

$$E_{inj,D\&C} = \frac{m_a}{m_b} kT_i \tag{5.11}$$

Where, m_a is the mass of the injected ions, m_b is the mass of the background plasma ions and kT_i is the plasma ion temperature. According to the ion temperatures obtained from the charge breeding simulation, the Na^+ and K^+ ions are injected into Helium and Oxygen plasma at the optimum injection energy ($E_{inj,D\&C}$) of about 5.17 - 6.32 eV (Na+ He), 6.8 - 7.8 eV (K + He) and 2.43 - 6.09 eV (K + O_2), respectively. The experimental ΔV values for the three cases are found to be 6.5 V, 7.5 V and 6.5V. Excluding the plasma potential (only up to few eV for the three cases), then the optimum injection energy of the 1+ ions ($E_{inj,exp}$) falls within the estimated optimum injection energy range ($E_{inj,D\&C}$). In the presented simulations, the optimum ΔV values for the three cases are around 7.5 eV, 8.5 eV and 8.5 eV. Excluding the plasma potential, then optimum injection energies $E_{inj} = e(\Delta V - V_P)$ are in the estimated optimum injection energy range ($E_{inj,D\&C}$). The recent simulations showed that an additional energy is required to allow the 1+ ions to penetrate deep inside the ECR volume [99]. This kind of behaviour was not observed in the MCBC simulations. Moreover, the plasma potential was found to be very low for the three cases (up to few volts). This is may be due to the grounded injection tube positioned close to the

SP1 CB plasma chamber. With this kind of configuration, the decelerating field created by the grounded tube might push the cold electrons towards the dense plasma region, resulting to low potential near the entrance of the SP1 CB.

TABLE 5.21: Ion confinement times calculated for three confinement models using the plasma parameters obtained from the charge breeding simulations.

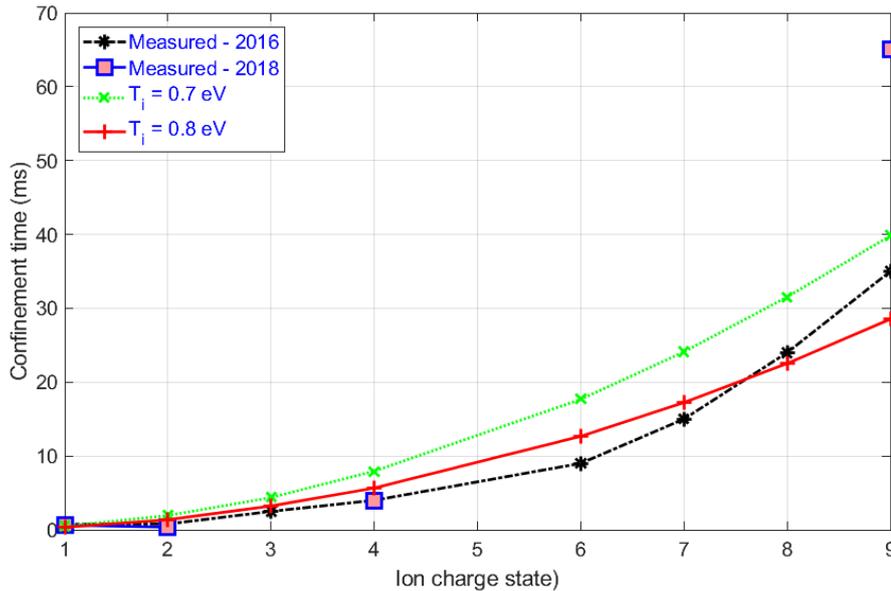| Parameters	Na+ He Na^{8+}	$K + He$ K^{9+}	K + O_2 K^{9+}
RF power	470 W	**207 W**	209 W
Ion temperature	0.9 - 1.1 eV	**0.7 — 0.8 eV**	1.5 - 2.5 eV
potential dip	0.5 V	**0.6 V**	0.6V
n_e	3.5×10^{11} cm^{-3}	**2.0×10^{11} cm^{-3}**	1.5×10^{11} cm^{-3}
Random walk model	29.40 - 17.80 ms	**39.8 — 28.5 ms**	12.0 - 3.28 ms
General dip model	16.02 - 5.49 ms	**196 — 70 ms**	4.38 - 0.80 ms
Ambipolar model	0.055 - 0.04 ms	**0.051 — 0.042 ms**	0.032 - 0.015 ms

FIGURE 5.40: The comparison of measured charge breeding times of K charge states with the confinement times calculated using random walk diffusion model.

Comparison of charge breeding times (confinement times): In chapter 2, three different ion confinement models are discussed: potential dip model, random walk diffusion model and the ambipolar diffusion model. The ion confinement times from the three models are calculated by substituting the plasma parameters obtained from
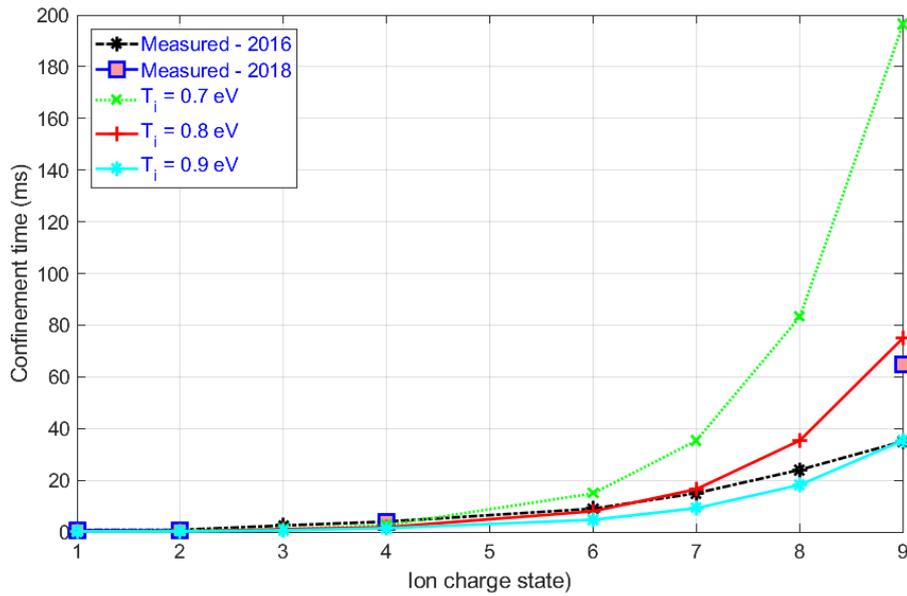
FIGURE 5.41: The comparison of measured charge breeding times of K charge states with the confinement times calculated using potential dip model.

the charge breeding simulations and presented in the table 5.21. The following values typical of the SP1 CB were used in the calculations: $\ln\Lambda = 10$, R = 2.658, $L = 12$ cm and E = 5 V/cm. In the same table, the highlighted experimental case (K + He) can be compared with the charge breeding time results reported in Ref. [70]. Except the RF power (350 W), the SP1 CB tuning parameters and the configurations are almost similar in both cases. With this configuration, the charge breeding times (capture + confinement + transport) of K charge states in Helium plasma were measured. Comparing these results with the confinement times calculated from three different models in the table 5.21, the random walk diffusion model leads to the correct order of magnitude. Figure 5.40 shows the comparison of measured charge breeding times of K charge states with the confinement times calculated using random walk diffusion model. It can be seen that the measured charge breeding times (K^{1+} to K^{9+}) are not far from the calculated confinement times. The confinement times calculated from the (axial) ambipolar diffusion model are too short than confinement times calculated from the other models. Therefore, the confinement times calculated from the ambipolar diffusion model is not shown in the figures.

On the other hand, the ion confinement times determined from the potential dip model depends exponentially on $|q\Delta\Phi|/kT_i$. Therefore, a small increase of $\Delta\Phi$ causes the confinement times to significantly exceed the confinement times determined from the experiment. It can be seen in the Figure 5.41, where the measured charge breeding times of K charge states [70] are compared with the confinement times calculated using potential dip model. From the charge breeding simulations, the value of potential dip is 0.6 V (see table 5.21). It can be seen that for the potential dip model results into too long confinement times when the ion temperatures is 0.7 eV. Except for the high charge states (8+ and 9+), the dip model leads to correct order of magnitude when the ion temperature is 0.8 eV. However, if the ion temperature is assumed as 0.9 eV, then the dip model leads to the correct order of magnitude for

the confinement times of all charge states measured in Helium plasma.

In this work, the charge breeding time of K charge states (1+, 2+ ,4+ and 9+) were measured. Except the RF power (270 W), the SP1 CB tuning parameters and the magnetic field configuration are similar compared to the experimental case (K + He) highlighted in the table 5.21. The charge breeding times measured for K in this thesis are compared with the calculated confinement times and presented in the same figure 5.40. Except for the K^{9+}, it can be seen that the measured charge breeding times are not so far from the calculated confinement times. On the other hand, the confinement times calculated using potential dip model leads to the correct order of magnitude for the charge breeding times measured for K charge states in Helium plasma (see figure 5.41 - 2018 measurements). Finally, the comparisons made above suggest that the random walk model and also the potential dip model must be taken into account to predict the ion confinement times ($\tau_{confinement} = \alpha \cdot \tau_{random\ walk} + \beta \cdot \tau_{potential\ dip}$). However, this supposition should be confirmed with further experimental investigations on the ion confinement times.

6 Conclusions and perspectives

The experimental work presented in this thesis focuses on the performance of SP1 CB in SPIRAL1 LEBT. After the installation of SP1 CB, the commissioning phase has been initiated with the optimization of SP1 CB. The optimizations were performed with stable alkali ions which represent the typical masses of the targeted RIBs. The presented results provide a general view of parameters (position of deceleration tube, axial magnetic field and the 1+ beam emittance) influencing the performance of SP1 CB.

The optimization of axial magnetic field gradient shows that the charge breeding efficiency is strongly influenced by the variation of the two soft iron ring positions around the permanent magnet hexapole. Significant variations are observed in the size of ECR volume in axial and radial direction. The effect of the injection optics and 1+ emittance on the charge breeding efficiency has been studied. It has been deduced from the observations that the charge breeding efficiency improves when the emittance of 1+ beam is smaller and the position of deceleration tube is close to the entrance of SP1 CB.

Furthermore, the charge breeding times of K charge states (1+,2+,4+ and 9+) were estimated by pulsing the injected K^{1+} beam. The influence of SP1 CB parameters (minimum-B field strength, microwave heating power, the intensity of incident 1+ beam and the ΔV) on charge breeding times of K charge states has been analyzed to extract the best set of experimental parameters. The results from these investigations showed the optimum SP1 CB tuning parameters ($B_{min}/B_{ECR} \approx 0.81$, RF power ≈ 270 W, 1+ beam intensity ≈ 200 nA) that can minimize the value of charge breeding time and enhance the charge breeding efficiency of the high charge states of K. This finding has important consequences for RIBs production, where the availability of the beam requires the radioactive ion to be ionized to a high charge state in a length of time which is short compared to its half life.

In addition to the experimental work, two sets of simulations were performed to understand the 1+ ion transport through the SP1 CB and to study the ECR plasma by injecting the 1+ beam as a probe. The first aspect has been investigated by performing ion trajectory simulations using SIMION 3D. In these simulations, the 1+ beam was transported through the geometry electrodes of electrostatic triplet, SP1 CB and the extraction system. During the transport, the 1+ ion losses were monitored throughout the simulation domain. The initial beam conditions for the ion transport simulations were obtained from the TraceWin simulations, which calculate the beam envelopes and record the beam properties (twiss parameters and emittance) at the desired locations in LEBT. For all the simulation studies presented in this thesis, the initial beam conditions are recorded at the slits position, where the emittance is defined by the horizontal and vertical slits in the 1+ line. The results from the ion transport simulations were benchmarked by comparing with the ion transport results obtained from the experiments. The simulations show that up to

15% of 1+ ions are in fact lost in the SP1 CB plasma chamber and up to 5% of 1+ ions are lost in the SP1 CB extraction system. The ion losses were observed due to the defocusing of the 1+ beam near the plasma electrode, which can be minimized by adjusting the center (B_{min}) and extraction coils (B_{ext}).

The second aspect has been investigated by performing numerical simulations, where 1+ injected beam has been introduced as a probe to reproduce the trends of low charge states (1+ and 2+) experimental results (charge breeding efficiency versus ΔV curves) and to estimate a set of plasma parameters. Initially, a simplified (crude) plasma model (without collisions) has been implemented in SIMION 3D to understand the transport of 1+ beam through the potential map created by the model. The result from the simulation exhibited periodic variation of the efficiency as a function of ΔV. The observed variations in the simulations revealed that the 1+ beam traversing through the plasma chamber exhibits a periodic focusing/defocusing behaviour due to the magnetic field of the SP1 CB. Finally, the simulation results showed good agreement with the experiments and also revealed the role of Coulomb collisions in the charge breeding process leading to a necessary detailed analysis using a full six-dimensional (6D) phase space Monte-Carlo Charge Breeding code (MCBC), developed by Far-Tech, Inc.

The MCBC code models the injected 1+ beam slowing down in ECR plasma due to Coulomb collisions and the atomic processes which include the electron impact ionization and charge exchange. Three experimental cases were considered for the simulation: interaction of Na^{1+} with a Helium plasma, interaction of K^{1+} with a Helium plasma and interaction of K^{1+} with an Oxygen plasma. In chapter 5, the limitations of the MCBC code were discussed. Considering those limitations, the charge breeding efficiency outputs (ΔV curves) from MCBC were compared with the low charge states experimental results (1+ and 2+) by reproducing their relative trends. The background ECR plasma has been modelled using a simplified plasma model scheme ($B \leq B_{ECR}$ (plasmoid) and $B \geq B_{ECR}$ (halo)). The input parameters mainly required for simulation are the following:

- Realistic beam starting conditions (beam properties)

- Injected beam energy

- Plasma density (electron and ion)

- Background plasma ion temperature

- Background plasma electron temperature

- Plasma potential and potential dip

Except the initial realistic beam starting conditions, each parameter listed above has been varied independently to reproduce the experimental trends of 1+ and 2+. The Pearson's χ^2 technique has been implemented to find the optimum parameters during the parameter variations. The implemented simple potential dip model has shown a minor effect on the experimental trends. With the precise combination of input plasma parameters, the experimental trends were nicely reproduced. The plasma parameters from each simulation case are summarized in the table 6.1.

The plasma parameters obtained from the three simulation cases are in good agreement with the results described in [45, 69, 98]. MCBC simulations revealed that a

TABLE 6.1: Optimum plasma parameters obtained from the charge breeding simulations.

Parameters	$Na + He$	$K + He$	$K + O_2$
ΔV_{sim} (eV)	7.5	8.5	8.5
Electron density (cm^{-3})	$3.3 - 3.7 \times 10^{11}$	$1.5 - 2.5 \times 10^{11}$	$1 - 2 \times 10^{11}$
Ion temperature (eV)	0.9 -1.1	0.7 - 0.8	1.5 - 2.5
Electron temperature (keV)	1 - 2	1 - 2	2 - 3
Plasma potential (V)	1.5	1	1
Potential dip (V)	0.5	0.6	0.6
Total capture (%)	16.44	24.52	7.26

special combination of plasma density and ion temperature is required to allow a direct matching of the simulations to the experimental data. This explains that due to the specific settings of SP1 CB magnetic field, size of the plasma chamber and RF power, ECR plasma configure itself at relatively low density and ion temperature, being the latter as the most critical parameter. On the other side, the simulation results identified that the emittance of injected 1+ ions mainly influence the injection efficiency and consequently, the capture efficiency. Based on these results, it can be said that the charge breeding performances can be improved by improving the 1+ beam quality. Finally, with the strategy followed so far in the charge breeding simulations, the MCBC can be used to estimate the above mentioned plasma parameters from the charge breeding experiments.

In this perspective, the good agreement between the simulations and the experiments encouraged us to extend the charge breeding simulations to heavier mass (Rb and Cs) in Helium and Oxygen plasma. In the experimental results reported in [5], the evolution of charge state distributions (CSD) of K in Hydrogen, Helium and Oxygen plasma are compared and observed a real increase of charge breeding efficiency of high charge states when the SP1 CB was optimized with Hydrogen plasma. An additional study should be performed to understand this behavior by investigating the interaction of different masses of 1+ beam (K, Na, Rb and Cs) with Hydrogen plasma using the charge breeding simulations. The complete set of plasma parameters from these simulations will allow studying the capture process and provides a goal for an R&D on the parameters (ion temperature and plasma density) that mainly influence the performance of SP1 CB.

In the same publication, the ΔV curves of different alkali elements (Rb, Na and K) exhibited a constant ΔV (around 7 V) in different plasma species (Helium, Oxygen and Hydrogen). According to the theory proposed by Delcroix & Bers [94], the optimum injection energy, for the best slowing down, depends on the ratio of the mass of injected 1+ ions and mass of the background plasma ions, and also the temperature of the plasma ions. MCBC simulations also found the similar optimum injection energies (between 5.5 to 6.5 eV) in the three cases (see table 6.1) and observed that the temperature of background plasma ions adjusting itself to reach these optimum injection energies. To understand this behaviour, intensive experimental investigations have to be envisaged, especially with regards to the ion temperature measurements [127] which will be carried out by ion source group from JYFL with LPSC ECR charge breeder. These measurements will be performed on one of the experimental cases presented in this thesis work. This will allow comparing the ion temperatures estimated from the charge breeding simulations with ion temperatures derived from measurements, which can provide an important benchmarking of simulation results,

model assumptions encoded in the MCBC simulations and finally, would allow to study the correlation between the optimum injection energy of 1+ beam and the temperature of background plasma ions.

The charge breeding time experiments carried out in this thesis work motivated us to perform further investigations with different masses of 1+ ion beam injected into different buffer gas species. Furthermore, the parameter variations will be performed on the operating pressures, intensities of 1+ beam (pA - μA scale) and magnetic field gradient etc. This study provides an overview of best source tuning parameters that enhance the charge breeding efficiency and minimize the value of the charge breeding time. At the same time, MCBC simulations will be performed on the experimental cases and the set of plasma parameters will be deduced with the strategy presented in this thesis. The complete set of source tuning parameters and ECR plasma parameters allows studying the properties of ECR plasma applied to the charge breeder.

A Electron impact ionization cross sections and ionization rate coefficients of Na
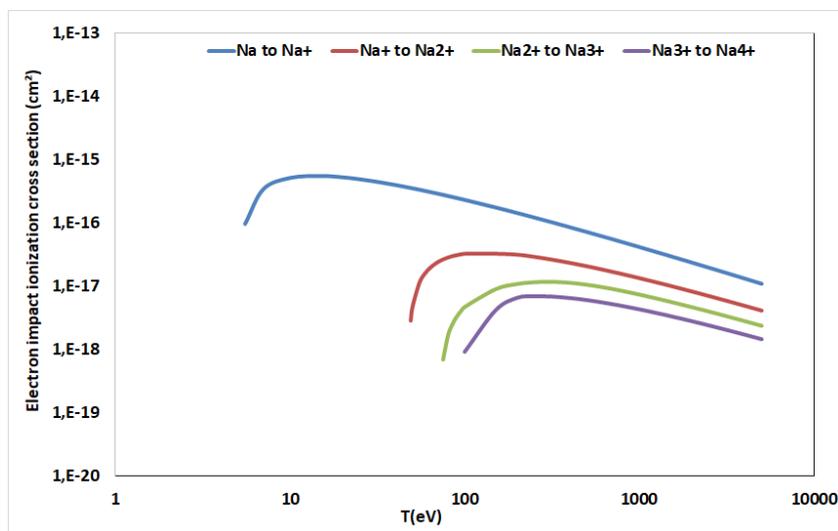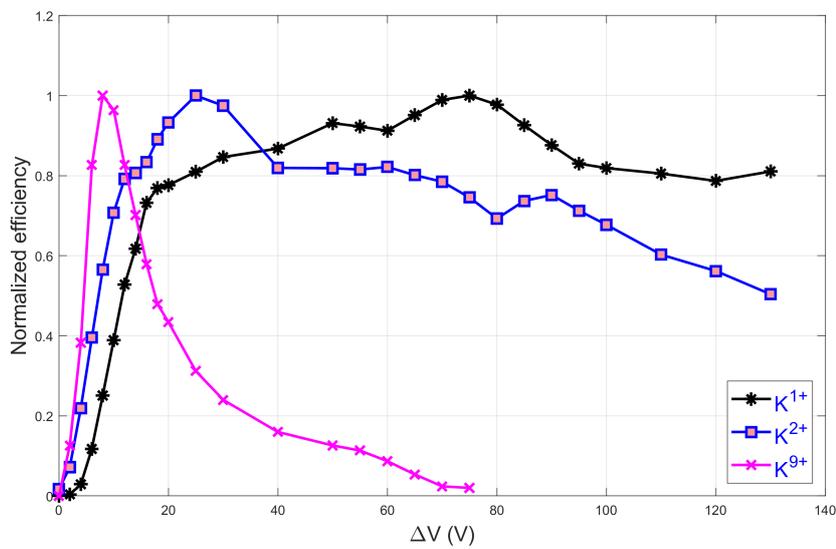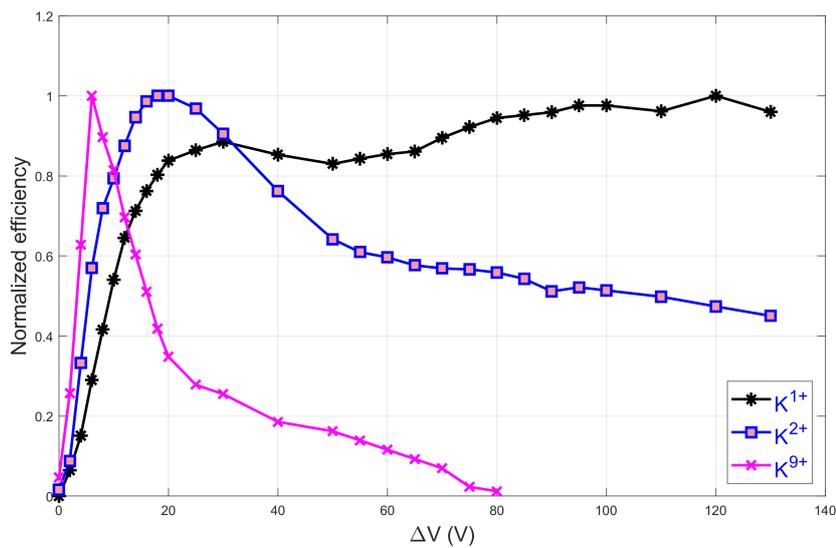

(A)
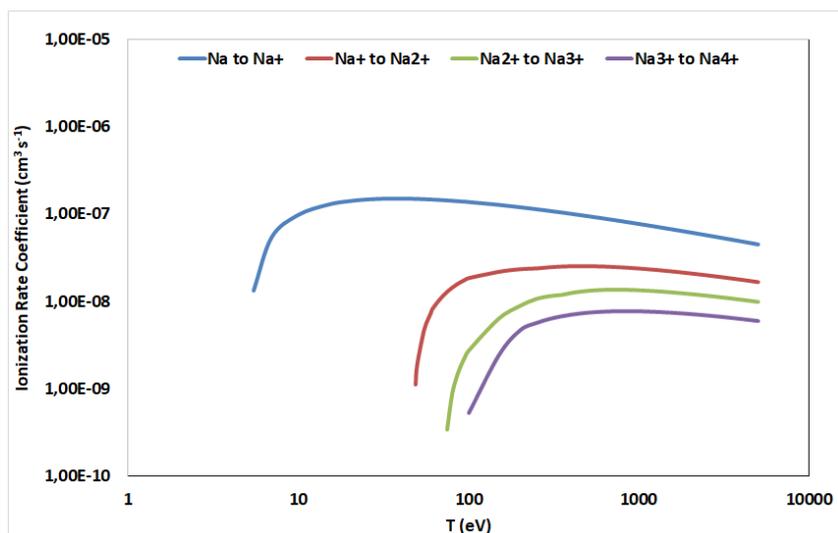
(B)

FIGURE A.1: Electron impact ionization cross sections (A) and ionization rate coefficients (B) of Na from ground state to Na^{4+} as a function of electron energy.

B ΔV curves of K in Helium and Oxygen plasma

(A)

(B)

FIGURE B.1: ΔV curves acquired from the charge breeding of K in Helium (A) and Oxygen (B) plasma.

C Response time of coupled systems

Problem

The current produced by the extracted ion flux arriving at the Faraday cup (FC) must propagate through — in effect — two coupled systems: One being the linear amplifier SRS–SR570, and the other one the system from the FC to the amplifier. Therefore, the signal measured as the picoscope readout is a convolution of the actual, physical current with the impulse responses of the coupled systems, and it must be deconvolved from the picoscope readout. The problem is obvious from figure C.1, where an order of magnitude change in the decay constant can be observed between mid-coil currents 250 A and 275 A. These data points correspond to amplifications of 10 nA/V and 20 nA/V respectively. This shows, that the amplification factor has significant effect on the response time of the measurement setup, and that this effect needs to be deconvolved from the measured signal in order to obtain the true, physical time constant.
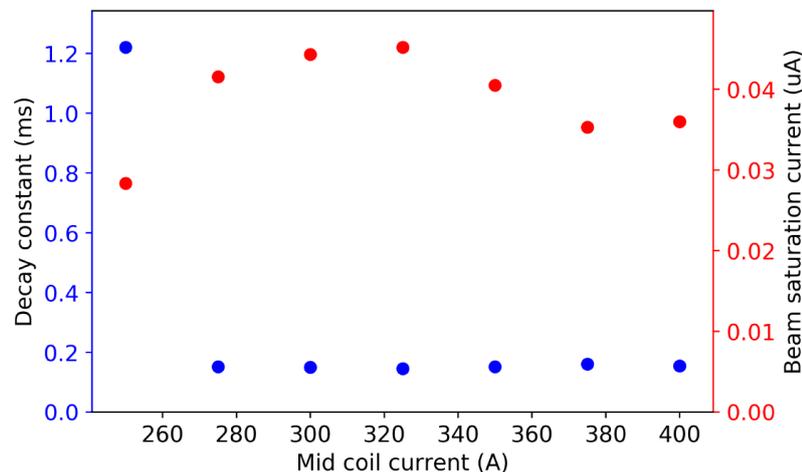

FIGURE C.1: Time constants of the decaying edge of the extracted K^{1+} current. Note the drastic, discrete change in time constant between 250 A and 275 A, where the amplification was changed from 10 nA/V to 20 nA/V.

The setup and the signal progression through it is illustrated in figure C.2. The physical ion current $I(t)$ causes a signal, which propagates through the FC along coaxial cable to the amplifier — where it is modified by their impulse responses $h_1(t)$ and $h_2(t)$ — and is read out at the picoscope as the readout signal $g(t)$. The signal $g(t)$ is

thus produced by the effects of the ion current, convolved with the response of the measurement setup. To find out the properties of the current $I(t)$, the effects of the setup have to be eliminated from the signal.
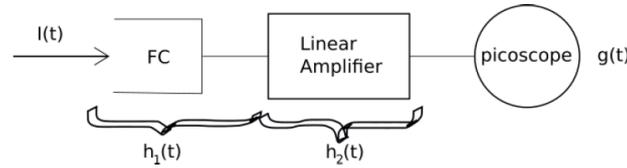

FIGURE C.2: Schematic illustration of the signal progression through the setup. $I(t)$ is the extracted, physical ion current, $h_1(t)$ and $h_2(t)$ the impulse responses of the FC and the amplifier respectively, and $g(t)$ is the picoscope readout.

Solution

The system from the FC to the amplifier has a time constant proportional to the product of its resistance and capacitance, $\tau_1 = RC$. The impulse response of the linear amplifier was measured as a function of its sensitivity[1]. The impulse response for an RC-system[2] is

$$h_i(t) = \frac{1}{\tau_i}e^{-t/\tau_i}, \tag{C.1}$$

where τ_i is the response time: τ_1 is the response time of the FC-switch box-cable system, and τ_2 is the response time of the amplifier. Note that the units of impulse response are by definition $[h] = 1\,/\text{s}$.[3] Given a physical current $I(t)$ of the form

$$I(t) = Ie^{-t/\tau}, \tag{C.2}$$

as derived from the balance equation, with I corresponding to the saturation current. The picoscope readout $g(t)$ is the convolution of $I(t)$ with the impulse response of the coupled system:

$$g(t) = I(t) * [h_1(t) * h_2(t)] \tag{C.3}$$

The convolution operation is defined as

$$I(t) * h(t) \equiv \int_{-\infty}^{\infty} I(t-u)h(u)\mathrm{d}u = \int_0^t I(t-u)h(u)\mathrm{d}u, \tag{C.4}$$

where the integration limits can be truncated for signals beginning at $t = 0$ and

---

[1] In the range 1 nA/V — 1 uA/V. Beyond 1 uA/V the response time is negligible.

[2] Source is Wikipedia. Can be calculated from the transfer function of the RC-circuit.

[3] The values for τ_2 have been determined experimentally, and the input impedances corresponding to different amplifications are listed in the device manual.

terminating at a later time t. The convolution (C.3) is solvable. First, to determine the system total response we solve the convolution

$$
\begin{aligned}
h_1(t) * h_2(t) &= \int_0^t \frac{1}{\tau_1} e^{-(t-u)/\tau_1} \frac{1}{\tau_2} e^{-u/\tau_2} \mathrm{d}u \\
&= \frac{1}{\tau_2 - \tau_1} \left(e^{-t/\tau_2} - e^{-t/\tau_1} \right) \\
&\equiv h(t)
\end{aligned}
\tag{C.5}
$$

and then take its convolution with the current $I(t)$ to get

$$
\begin{aligned}
g(t) &= \int_0^t I e^{-(t-u)/\tau} \frac{1}{\tau_2 - \tau_1} \left(e^{-t/\tau_2} - e^{-t/\tau_1} \right) \mathrm{d}u \\
&= \frac{I}{\tau_2 - \tau_1} \left[\frac{\tau_2 \tau}{\tau_2 - \tau} \left(e^{-t/\tau_2} - e^{-t/\tau} \right) - \frac{\tau_1 \tau}{\tau_1 - \tau} \left(e^{-t/\tau_1} - e^{-t/\tau} \right) \right]
\end{aligned}
\tag{C.6}
$$

Therefore, by making fits to the collected data according to equation (C.6) will yield the desired time constant τ as a fitting parameter, while isolating the contribution from the setup, which has been measured. It can also be seen from the equation, that for small values of τ_1 and τ_2 — i.e. comparatively fast system response times — it follows that $g(t) \to I(t)$, and the picoscope readout corresponds to the actual ion current.

If h1 and h2 have the same time constant

In this case, the convolution becomes

$$
\begin{aligned}
h(t) &= h_1(t) * h_2(t) \\
&= \int_0^t \frac{1}{\tau} e^{-(t-u)/\tau} \frac{1}{\tau} e^{-u/\tau} \mathrm{d}u \\
&= \frac{1}{\tau^2} e^{-t/\tau} \int_0^t e^{u/\tau - u/\tau} \mathrm{d}u \\
&= \frac{1}{\tau^2} e^{-t/\tau} \int_0^t 1 \mathrm{d}u \\
&= \frac{t}{\tau^2} e^{-t/\tau}.
\end{aligned}
\tag{C.7}
$$

RC system and amplifier response times

The response time of the amplifier, τ_2, was determined by inputting a square pulse from the picoscope, and investigating the rise- and decay times of the signal output by the amplifier. The resulting time constants of the impulse response are shown as a function of the amplifier sensitivity in figure C.3. It can be seen, that the amplifier response time is significant for fast, low intensity signals, because the impulse response occurs in the timescale of milliseconds.

Note here, that the response time of the amplifier at 10 nA/V is essentially the same
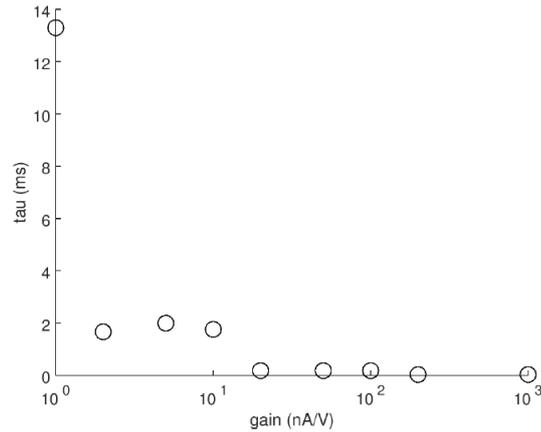
FIGURE C.3: Time constant of the impulse response of the amplifier.
gain = sensitivity!

TABLE C.1: Input impedance of the SRS SR570 -amplifier for different sensitivies.

Sensitivity (nA/V)	Input impedance
10^6	$1\,\Omega$
10^5	$1\,\Omega$
10^4	$100\,\Omega$
10^3	$100\,\Omega$
10^2	$10\,\mathrm{k}\Omega$
10^1	$10\,\mathrm{k}\Omega$
10^0	$1\,\mathrm{M}\Omega$
10^{-1}	$1\,\mathrm{M}\Omega$
10^{-2}	$1\,\mathrm{M}\Omega$
10^{-3}	$1\,\mathrm{M}\Omega$

as the decay constant of the measured K^{1+} current in figure C.1 at 250 A — which was measured at that particular amplification. The relevant input impedances of the amplifier are found in the device manual, and are listed in table C.1. For sensitivities above 10^3 nA/V the contribution from the amplifier may safely be ignored — the time constant of the response is less than 0.03 ms for a sensitivity of 10^3 nA/V.

The determination of τ_1 requires some trickery. Because the response time of the measurement setup in its totality was not measured on-site, it is difficult to combine the response of the FC-side of the setup (τ_1) with the amplifier side of the setup (τ_2). The easiest method is to assume the K^{1+} decay to be prompt — i.e. $\tau^{1+} = 0$. This is justified, because the vast majority of the K^{1+} current measured at the FC is composed of fly-through ions, with a negligible minority component resulting from trapped and recombined ions. In this case, $I^{1+}(t) = u(t)$, i.e. the step function. To calculate the decaying transient we must define the step function as

$$u(t) = \begin{cases} -I & t \in [0, T] \\ 0 & \text{else,} \end{cases} \tag{C.8}$$

where T is large compared with the response time. When the convolution of $u(t)$ is

now taken with the setup impulse response, and shifted by I, it yields the picoscope readout to be

$$
\begin{aligned}
g(t) &= u(t) * h(t) + I \\
&= \int_0^{t<T} (-I) \frac{1}{\tau_2 - \tau_1} \left(e^{-t/\tau_2} - e^{-t/\tau_1} \right) \mathrm{d}u + I \\
&= I \frac{\tau_2 e^{-t/\tau_2} - \tau_1 e^{-t/\tau_1}}{\tau_2 - \tau_1},
\end{aligned}
\tag{C.9}
$$

which starts from I at $t = 0$ and decays to 0 for t which are large compared to τ_1 and τ_2; OK. Equation (C.9) describes the picoscope readout for K^{1+} current. The values of τ_2 are known from measurement, and τ_1 can thus be obtained from a fit to the K^{1+} decaying transient according to the above equation. If τ_1 is small compared to τ_2 — as is expected — it follows that $g(t) \to I e^{-t/\tau_2}$, and the amplifier response determines the response of the system.

Determination of response times from experiment

By making fits to K^{1+} decay data according to equation (C.9), it was found that τ_1 is on the order of μs. It is thus negligible compared to the amplifier response time. In this case, the signal convolution in the measurement setup occurs according to

$$
\begin{aligned}
g(t) &= I(t) * h_2(t) \\
&= \int_0^t I e^{-(t-u)/\tau} \frac{1}{\tau_2} e^{-u/\tau_2} \mathrm{d}u \\
&= I \frac{\tau}{\tau_2 - \tau} \left(e^{-t/\tau_2} - e^{-t/\tau} \right),
\end{aligned}
\tag{C.10}
$$

where τ_2 is a function of the amplification used in the measurement, and is assumed to be no less than 0.3 ms when the sensitivity is more than 1 μA/V. The current $I(t)$ according to equation (C.2) was used. All measurements on the potassium currents were carried out in the sensitivity range of 1 nA/V $-$ 0.1 μA/V.

Rise time determination

In case of the rising edge of the current, the physical current is of the form

$$
I(t) = I(1 - e^{-t/\tau_{\mathrm{rise}}})
\tag{C.11}
$$

and hence, the picoscope readout will be

$$g(t) = I(t) * h_2(t)$$

$$= \int_0^t I(t-u)h_2(u)\mathrm{d}u$$

$$= \int_0^t I\left(1 - e^{-(t-u)/\tau_{\mathrm{rise}}}\right)\frac{1}{\tau_2}e^{-u/\tau_2}\mathrm{d}u \tag{C.12}$$

$$= \frac{I}{\tau_2}\left[\int_0^t e^{-u/\tau_2}\mathrm{d}u - e^{-t/\tau_{\mathrm{rise}}}\int_0^t e^{-u\left(\frac{1}{\tau_2} - \frac{1}{\tau_{\mathrm{rise}}}\right)}\right]$$

$$= I\left(1 - e^{-t/\tau_2}\right) - I\frac{\tau_{\mathrm{rise}}}{\tau_2 - \tau_{\mathrm{rise}}}\left(e^{-t/\tau_2} - e^{-t/\tau_{\mathrm{rise}}}\right),$$

which can be fitted to data in order to obtain the rise time constant τ_{rise}.

D Calculation of Helium and Oxygen neutral density

At 20° of air, we can calculate

$$1 \ mbar \ l/s = 4.3 \times 10^{-3} \ Kg/h$$

$$= \frac{4.3 \times 10^{-3} \times 1000}{3600} \ g/s \qquad \text{(D.1)}$$

$$1 \ mbar = 1.192 \times 10^{-3} g/l$$

We know that 1 litre = 1 cubic decimeter = $10^{-3} \ m^3$, then

$$1 \ mbar = 1.192 \ g/m^3$$

$$\qquad \text{(D.2)}$$

$$10^{-7} \ mbar = 1.192 \times 10^{-7} g/m^3$$

The molar mass of air is 28.96 g/mol, where 1 mole = 6.022×10^{23} particles. Using these values, the neutral density of air at 10^{-7} mbar pressure can be calculated as

$$10^{-7} \ mbar = \frac{6.022 \times 10^{23} \times 1.192 \times 10^{-7}}{28.96} \qquad \text{(D.3)}$$

$$\boxed{10^{-7} \ mbar = 2.47 \times 10^{15} \ particles/m^3} \qquad \text{(D.4)}$$

Finally, the density of Helium and Oxygen are calculated by considering the residual pressures. As an example, Let us consider the first experimental case (Na+ He). The operating pressures (with and without plasma) were recorded and presented in table 5.2. The mean values of the pressures with and without plasma has been calculated and presented in table D.1.

TABLE D.1: The calculated mean values of the operating pressures with and without ECR plasma.

	$Na + He$	$K + He$	$K + O_2$
with plasma (mbar)	4.9×10^{-8}	4.6×10^{-8}	4.3×10^{-8}
without plasma (mbar)	6.2×10^{-8}	5.9×10^{-8}	5.35×10^{-8}
Difference (mbar)	1.3×10^{-8}	1.3×10^{-8}	1.05×10^{-8}

The Helium density at a pressure of 1.3×10^{-8} mbar can be calculated as:

$$1 \times 10^{-7} \; mbar = 2.47 \times 10^{15} \; particles/m^3$$

$$1.3 \times 10^{-8} \; mbar = Helium \; density \; (\boldsymbol{x})$$

(D.5)

Finally,

$$\boxed{Helium \; density \; at \; 1.3 \times 10^{-8} \; mbar = 3.21 \times 10^{14} \; particles/m^3}$$
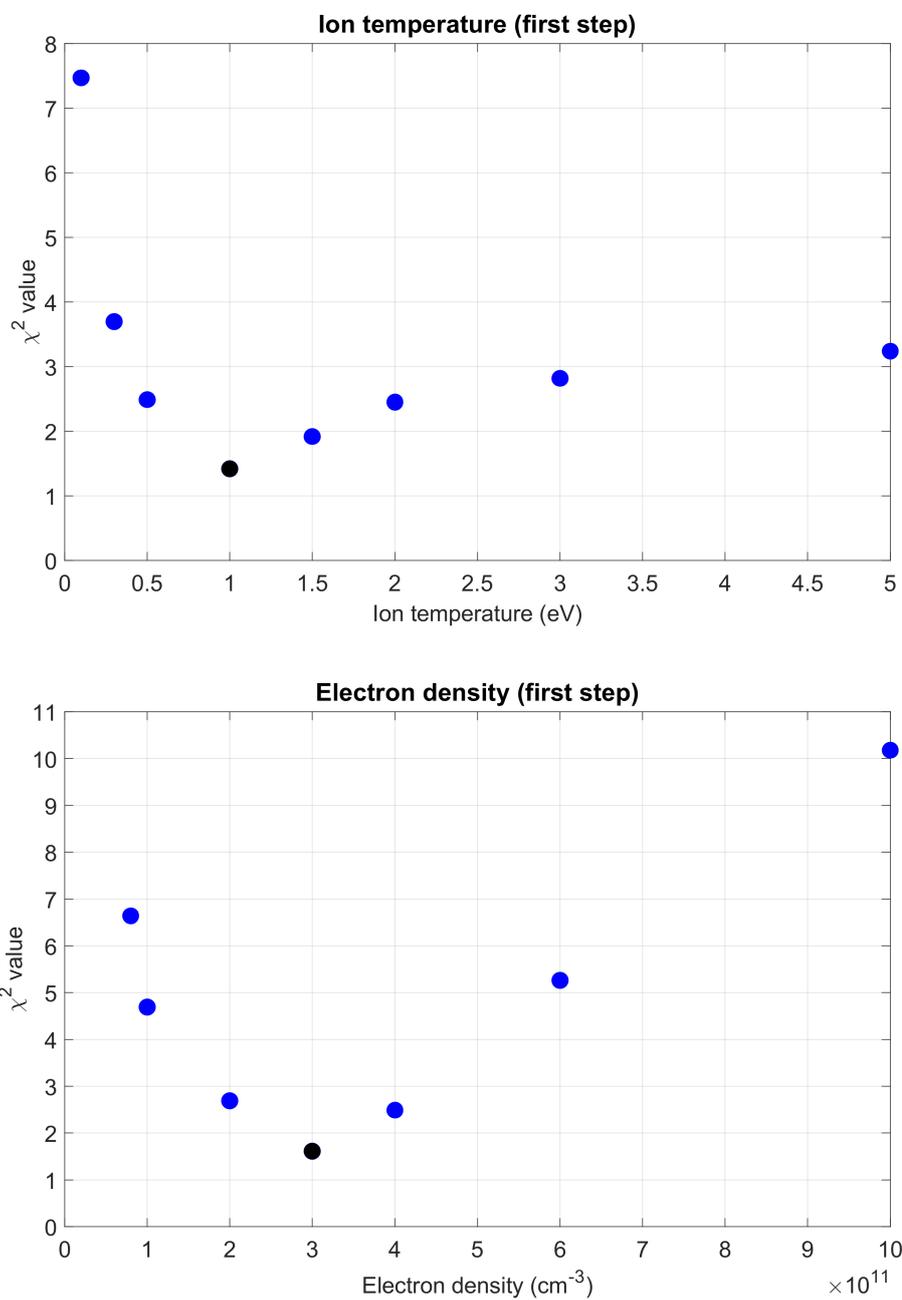
(D.6)

In the similar way, neutral densities are calculated for other two cases (K + He and K + O_2) as:

$$\boxed{Helium \; density \; at \; 1.3 \times 10^{-8} \; mbar = 3.21 \times 10^{14} \; particles/m^3}$$

(D.7)

$$\boxed{Oxygen \; (O_2) \; density \; at \; 1.05 \times 10^{-8} \; mbar = 2.59 \times 10^{14} \; particles/m^3}$$

(D.8)

E Calculation of χ^2 from three simulation cases

Na + He (χ^2 calculation in first step)

Ion temperature (first step)
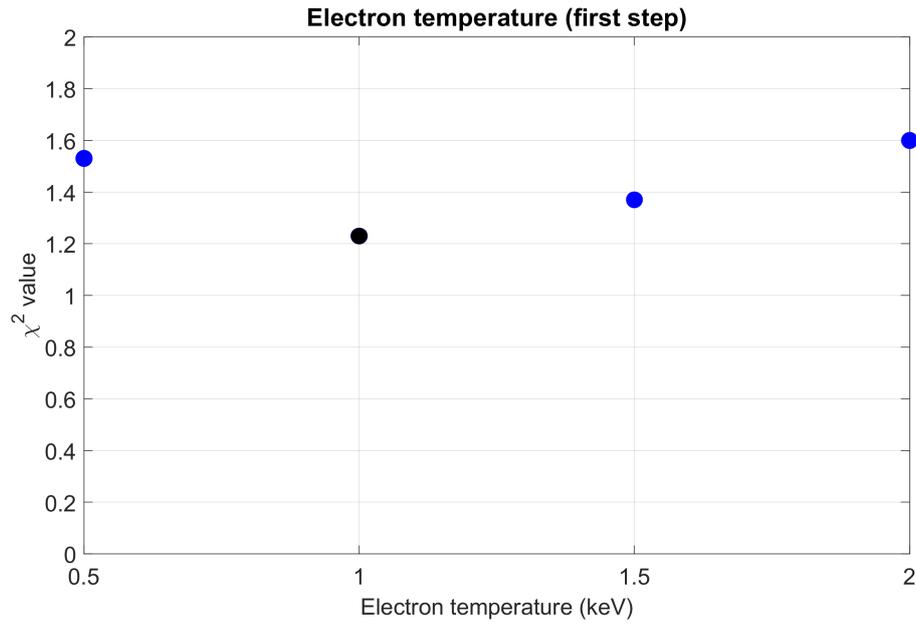

Electron density (first step)

FIGURE E.1: The χ^2 plots calculated in the first step. The minimum χ^2 value in each plot is considered as an optimum value of each plasma parameter. The minimum χ^2 value found in each parameter sweep is marked in black color.

Na + He (χ^2 calculation in second step)

Electron density (second step)

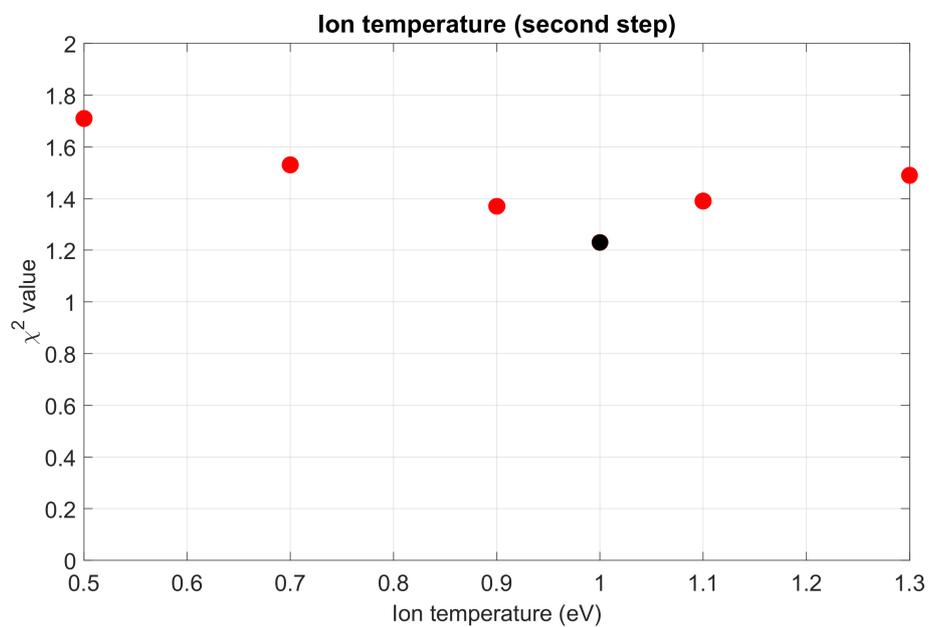**Electron temperature (second step)**

FIGURE E.2: The χ^2 plots calculated in the second step. The minimum χ^2 value in each plot is considered as an optimum value of each plasma parameter. The minimum χ^2 value found in each parameter sweep is marked in black color.
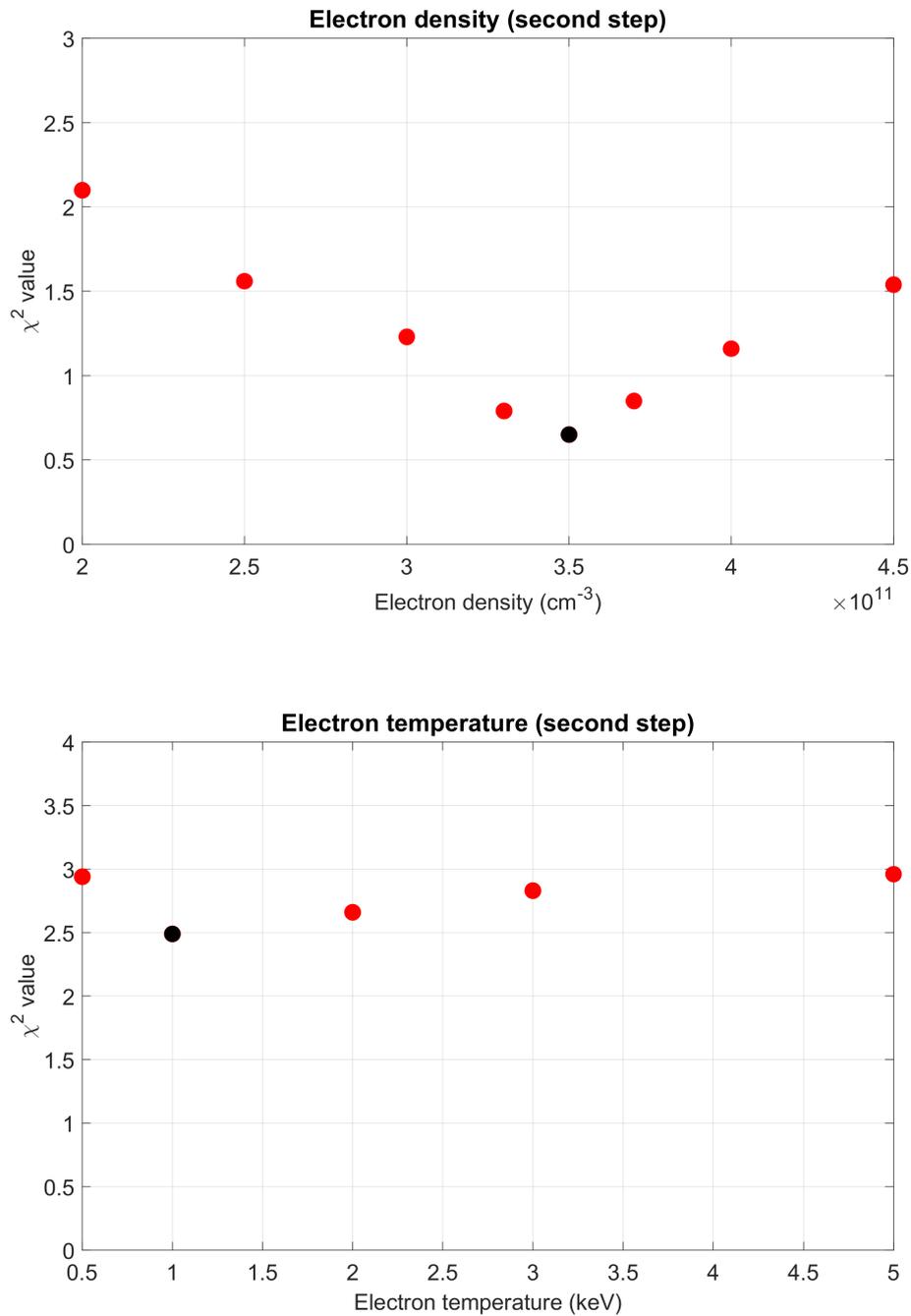
K + He (χ^2 calculation in first step)

(C)

FIGURE E.3: The χ^2 plots calculated in the first step. The minimum χ^2 value in each plot is considered as an optimum value of each plasma parameter. The minimum χ^2 value found in each parameter sweep is marked in black color.
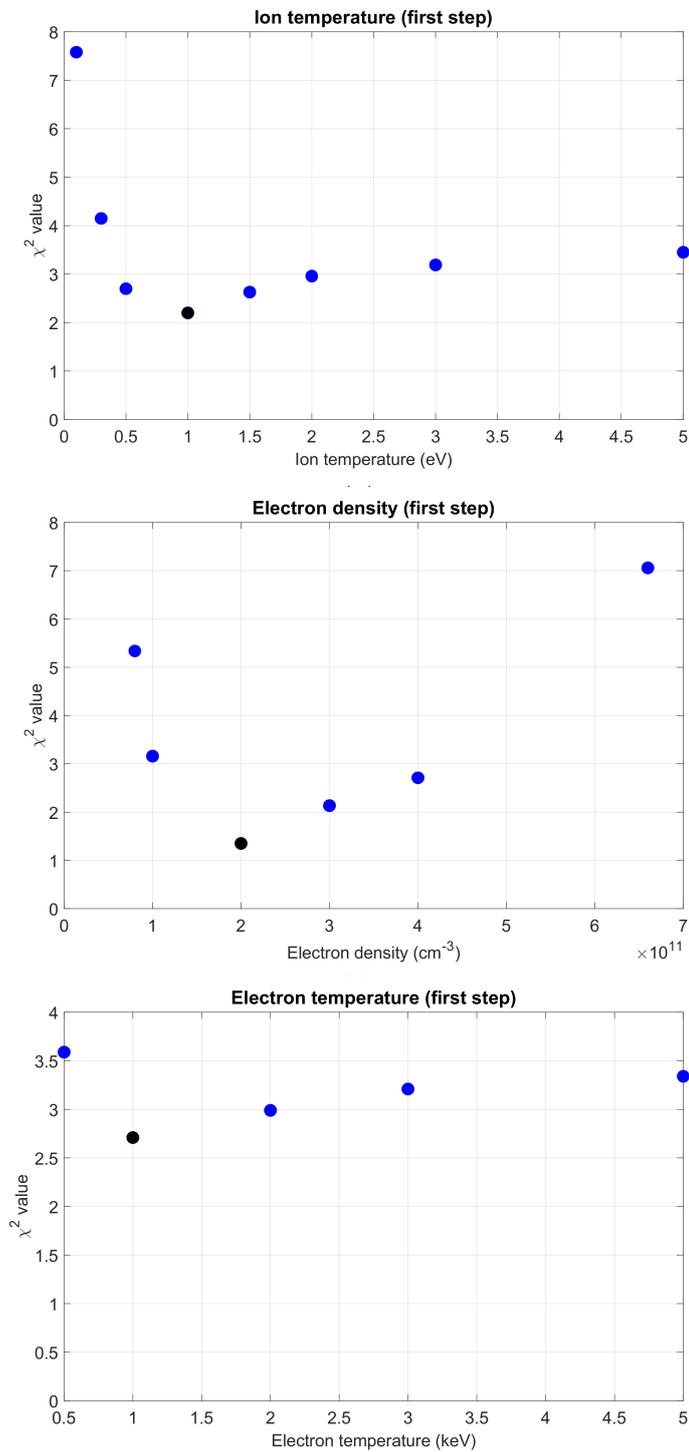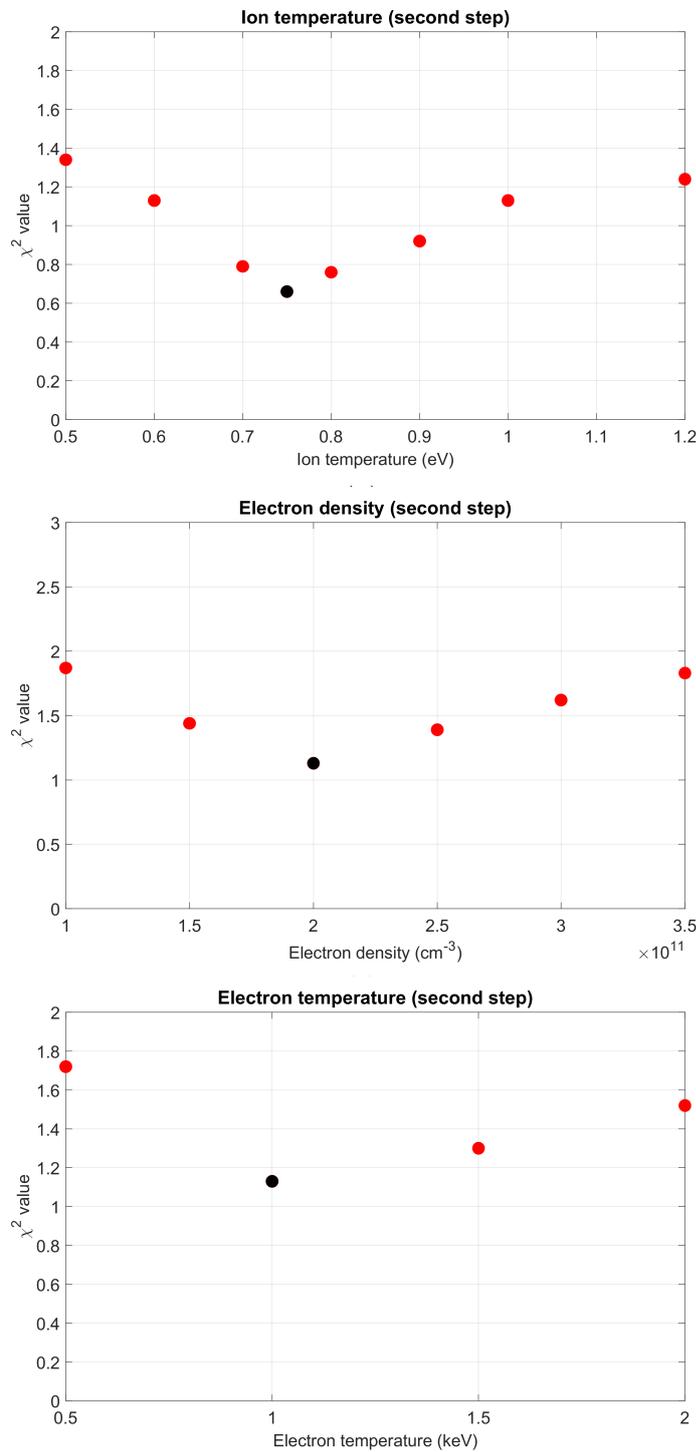
K + He (χ^2 calculation in second step)

FIGURE E.4: The χ^2 plots calculated in the second step: i) ion temperature, ii) electron density and iii) electron temperature. The minimum χ^2 value in each plot is considered as an optimum value of each plasma parameter. The minimum χ^2 value found in each parameter sweep is marked in black color.

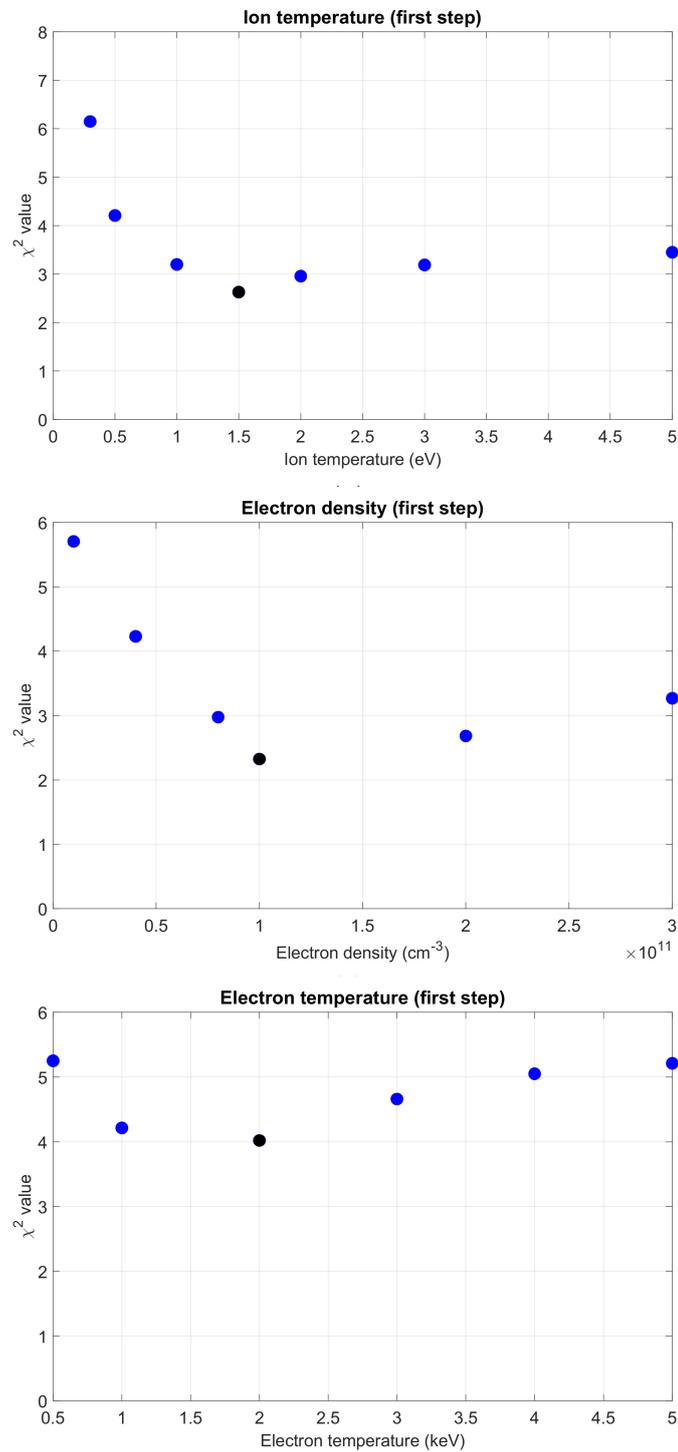## K + O_2 (χ^2 calculation in first step)

(C)

FIGURE E.5: The χ^2 plots calculated in the first step. The minimum χ^2 value in each plot is considered as an optimum value of each plasma parameter. The minimum χ^2 value found in each parameter sweep is marked in black color.
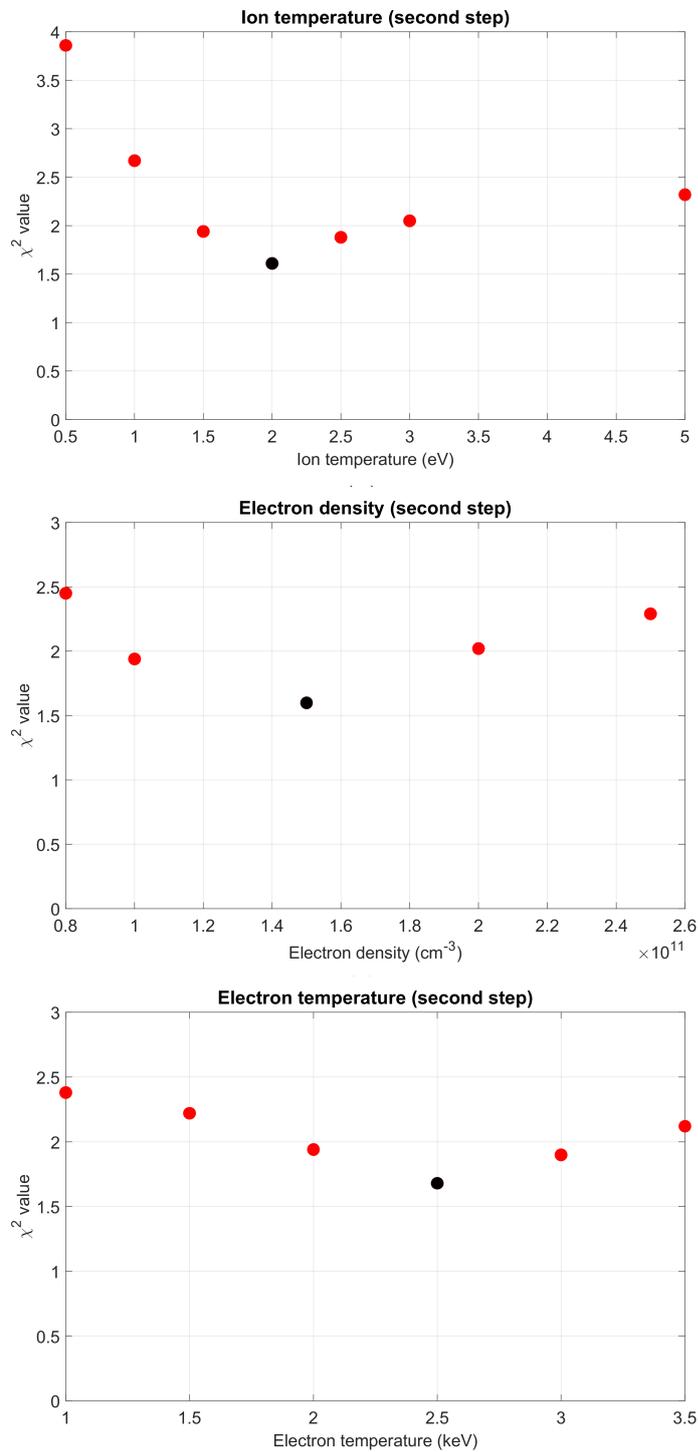
K + O_2 (χ^2 calculation in second step)

FIGURE E.6: The χ^2 plots calculated in the second step. The minimum χ^2 value in each plot is considered as an optimum value of each plasma parameter. The minimum χ^2 value found in each parameter sweep is marked in black color.

Bibliography

[1] Y. Blumenfeld , T. Nilsson and P. Van Duppen, Radioactive ion beam facilities, *Chalmers Publication Library*.

[2] P. Jardin, O. Bajeat, C. Couratin, P. Delahaye, M. Dubois, C. Feierstein, F. Pelle-moine, P. Lecomte, P. Lehérissier, L. Maunoury, M. G. Saint-Laurent, and E. Traykov, Status of the SPIRAL I upgrade at GANIL, *Review of Scientific Instruments* 83, 02A911 (2012).

[3] Claire Tamburella, *Projet P.I.A.F.E : Production d'etats de charges elevees pour des ions radioactifs*, PhD thesis, 27th juin 1996.

[4] P. Delahaye, A. Galatà, J. Angot, J. F. Cam, E. Traykov, G. Ban, L. Celona, J. Choinski, P. Gmaj, P. Jardin, H. Koivisto, V. Kolhinen, T. Lamy, L. Maunoury, G. Patti, T. Thuillier, O. Tarvainen, R. Vondrasek, and F. Wenander, Optimizing charge breeding techniques for ISOL facilities in europe: Conclusions from the EMILIE project, *Review of Scientific Instruments* 87, 02B510 (2016).

[5] L.Maunoury, P. Delahaye, M. Dubois, J. Angot, P. Sole, O. Bajeat, C. Barton, R. Frigot, A. Jeanne, P. Jardin, O. Kamalou, P. Lecomte, B. Osmond, G. Peschard, T. Lamy, and A. Savalle, Charge breeder for the SPIRAL1 upgrade: Preliminary results. *Review of Scientific Instruments* 87,02B508 (2016).

[6] O. Kamalou, J. Angot, O. Bajeat, F. Chautard, P. Delahaye, *et al*, GANIL Opera-tion Status and New Range of Post-Accelerated Exotic Beams. *13th International Conference on Heavy Ion Accelerator Technology (HIAT 2015)*, Sep 2015, Yokohama, Japan. pp.20-22.

[7] P. Van Duppen, Isotope Separation On Line and Post Acceleration, *The Eu-roschool Lectures on Physics With Exotic Beams*, Vol. II. 700. 2006.

[8] F. Chautard, G. Sénécal, Operation status of High Intensity Ion Beams at GANIL. *11th International Conference on Heavy Ion Accelerator Technology (HIAT09)*, Jun 2009, Venezia, Italy. pp.54-58

[9] L. Boy. Problèmes posés par l'accélération d'ions radioactifs dans le projet SPI-RAL. Réglage et stabilisation de l'accélérateur. *Physique des accélérateurs*. Uni-versité Pierre et Marie Curie - Paris VI, 1997. Français.

[10] P. Delahaye, M. Dubois, L. Maunoury, J. Angot, O. Bajeat, *et al*, New exotic beams from the SPIRAL 1 upgrade. *18th International Conference on Electromag-netic Isotope Separators and Related Topics*, Sep 2018, Geneva, Switzerland.

[11] T. Lamy, J. Angot, and T. Thuillier. European research activities on charge state breeding related to radioactive ion beam facilities. *Review of Scientific Instru-ments*, 79:02A909–1–5, 2008.

[12] Mélanie Marie-Jeanne. Investigation of the performances of an ECR charge breeder at ISOLDE: a study of the 1+ n+ scenario for the next generation ISOL

facilities. *Accelerator Physics*. Université Joseph-Fourier - Grenoble I, 2009. English.

[13] B. Hartmann, S. Kalbitzer, and Ch. Klatt. Energy spread of ion beams passing a gas stripper. *Nuclear Instruments and Methods in Physics Research B*, 124:490–499, 1997.

[14] Antonio C.C. Villari and the SPIRAL group. First results at SPIRAL-GANIL. *Nuclear Instruments and Methods in Physics Research B*, 204:31–41, 2003.

[15] F.Wenander. Charge breeding techniques. *CERN-AB-2004-035,*2004.

[16] Baron, Eric. (1979). The beam-stripper interaction studies for GANIL. Nuclear Science, IEEE Transactions on. 26. 2411 - 2413. 10.1109/TNS.1979.4329890.

[17] Hans-Dieter Betz. Charge states and charge-changing cross sections of fast heavy ions penetrating through gaseous and solid media. *Review of Modern Physics*, 44:465–539, 1972.

[18] Kunihiro Shima, Noriyoshi Kuno, Mikio Yamanouchi, and Hiroyuki Tawara. Equilibrium charge fractions of ions of Z = 4-92 emerging from a carbon foil. *Atomic Data and Nuclear Data Tables*, 51:173–241, 1992.

[19] Uwe Greife, Ellen Simmons, Luke Erikson, Cybele Jewett, Jake Livesay, and Kelly Chipps. Possibilities for beam stripping solutions at a rare isotope accelerator (RIA). *Nuclear Instruments and Methods in Physics Research B*, 261:9–12, 2007.

[20] P. Delahaye, O. Kester, C. Barton, T. Lamy, M. Marie-Jeanne and F.Wenander, Evaluation of charge-breeding options for EURISOL.*European Physical Journal A*, EDP Sciences, 2010, 46, pp.421-433.

[21] F. Ames, G. Bollen, P. Delahaye, O. Forstner, G. Huber, O. Kester, K. Reisinger, and P. Schmidt. Cooling of radioactive ions with the Penning trap at REXTRAP. *Nuclear Instruments and Methods in Physics Research A*, 538:17–32, 2005.

[22] P. Delahaye. ECRIS and EBIS charge state breeders: Present performances, future potentials. *16th International Conference on Electromagnetic Isotope Separators and Technique related to their Applications (EMIS2012)*, Dec 2012, Matsue, Japan. pp.389-394.

[23] Fredrik Wenander. EBIS as charge breeder for radioactive ion beam accelerators. *Nuclear Physics A*, 701:528c–536c, 2002.

[24] R. Geller, Electron Cyclotron Resonance Ion Sources and ECR Plasmas, IOP, London, 1996.

[25] T. Lamy, J. F. Bruandet, N. Chauvin, J. C. Curdy, M. Fruneau, R. Geller, G. Gimond, P. Sole, J. L. Vieux-Rochas, G. Gaubert, L. Maunoury, P. Sortais, and A. C. C. Villari, Production of multicharged radioactive ion beams: New results for the $1+ \rightarrow N+$ method with the MINIMAFIOS and SARA-CAPRICE electron cyclotron resonance ion sources, *Review of Scientific Instruments* 69, 741 (1998).

[26] A.C.C. Villari, C. Barué, G. Gaubert, S. Gibouin, Y. Huguet, *et al*, Ion source developments for RNB production at SPIRAL/GANIL. *Fifth International Conference on Radioactive Nuclear Beams (RNB5)*, Mar 2000, Divonne, France.

[27] M.P. BOURGAREL, SPIRAL facility: First results on the CIME cyclotron obtained with stable ion beams. *Proceedings of the 15th International Conference on Cyclotrons and their Applications*, Caen, France.

[28] F. Chautard, O. Bajeat, P. Delahaye, M. Dubois, P. Jardin,*et al*, GANIL operation status and upgrade of SPIRAL1. *12th International Conference on Heavy Ion Accelerator Technology*, Jun 2012, Chicago, United States. pp.51-53, 2012.

[29] T. Lamy et al. Charge breeding method results with the PHOENIX Booster ECR ion source. Proceedings of EPAC 2002, Paris, France, pages 1724–1726, 2002.

[30] G. Gaubert *et al.*, Direct 10 GHz rf feedthrough plasma device with the NANOGAN III ion source for SPIRAL, *Review of Scientific Instruments*, 77, 03A326 (2006).

[31] L. Penescu *et al.*, Development of high efficiency versatile arc discharge ion source at CERN ISOLDE, *Review of Scientific Instruments*, 81 (2010) 02A906.

[32] P. Chauveau, P. Delahaye, M. Babo *et al.*, A new FEBIAD-type ion source for the upgrade of SPIRAL1 at GANIL, Nucl. Inst. Methods Phys. Res. B, vol. 376, pp. 35– 38, 2016.

[33] L. Maunoury *et al.*, Charge breeding at Ganil: improvements, results and comparison with the other facilities, In the proceedings of ICIS 2019 conference.

[34] *https* : //*www.cathode.com*/

[35] J. Buon, Beam phase space and emittance, *General accelerator physics*, vol. 1* 89-115.

[36] I. G. Brown (Ed.), The physics and technology of ion sources, *John Wiley & Sons*, Inc., 2004.

[37] J. S. Humphries, Charged Particle Beams, *John Wiley & Sons*, Inc., 1990.

[38] Wiedemann, Helmut. (2015). Particle Accelerator Physics. 10.1007/978-3-319-18317-6.

[39] *https* : //*en.wikipedia.org*/*wiki*/*Einzel₁ens*

[40] H. Liebl. Applied Charged Particle Optics. *SpringerLink: Springer e-Books*. Springer, 2008.

[41] H.Wollnik, Optics of Charged Particles, *Academic Press, Inc.*, Orlando, Florida, 1987.

[42] J. A. Bittencourt. Fundamentals of Plasma Physics. *Springer (2004)*. ISBN 075030183X.

[43] Benjamin Bederson and L. J. Kieffer, Total Electron—Atom Collision Cross Sections at Low Energies—A Critical Review, *Rev. Mod. Phys.* 43, 601 – Published 1 October 1971

[44] R. J. Goldston AND P. H. Rutherford. Introduction to Plasma Physics. *Institute of Physics Publishing (1995)*. ISBN 0387209751.

[45] G. Melin *et al*, "Ion behavior and gas mixing in electron cyclotron resonance plasmas as sources of highly charged ions," *Journal of Applied Physics*, vol. 86, no. 9, pp. 4772–4779, 1999.

[46] M. Sakieldien, Characteristic Kα emission of electron cyclotron resonance ion source plasmas, PhD thesis, *Department of Physics, University of Jyväskylä*, 2018.

[47] G. D. Severn, A note on the plasma sheath and the Bohm criterion, *Dept. of Physics, University of San Diego*, California

[48] K. U. Riemann, The Bohm criterion and sheath formation, *J. Phys D.* 24, 493 (1991).

[49] M. A. Lieberman and A. J. Lichtenberg, Principles of plasma discharges and materials processing, *John Wiley and Sons Inc*, 2005.

[50] G. D. Shirkov, C. Mühle, G. Musiol, and Zschornack, "Ionization and charge dispersion in electron cyclotron resonance ion sources", *Nuclear Instruments and Methods in Physics Research Section A: Accelerators, Spectrometers, Detectors and Associated Equipment*, vol. 302, no. 1, pp. 1–5, 1991.

[51] D. H. Crandall, Electron impact ionization of multicharged ions, *Phys. Scripta* 23 (1981) 153 – 162.

[52] W. Lotz, Electron-impact ionization cross-sections and ionization rate coefficients for atoms and ions, *Astrophys. J. Suppl. Ser.* 14, 207 (1967).

[53] W. Lotz, Electron-Impact Ionization Cross-Section and ionization rate coefficients for atoms and ions from Hydrogen to Calcium, *Zeitschrift ftir Physik* 216, 241 – 247 (1968).

[54] D. N. Tripathi and D K. Rai, Cross Section for Double Ionization by Electron Impact: Li+, Na+, K+, *the Journal of Chemical Physics* 55, 1268 (1971).

[55] A. Müller, E. Salzborn, Scaling of cross sections for multiple electron transfer to highly charged ions colliding with atoms and molecules, *Phys. Lett.* A 62 (1977). 391 – 394.

[56] S. Gammino *et al*, *IEEE Transactions on Plasma Science* 36, 1552 (2008).

[57] I. Izotov *et al*, "Measurement of the energy distribution of electrons escaping minimum-B ECR plasmas", *Plasma Sources Science and Technology*, vol. 27, no. 2, p. 025012, 2018.

[58] C. Barue *et al*, *Journal of Applied Physics* 76, 2662 (1994).

[59] G. Douysset, H. Khodja, A. Girard, and J. P. Briand, "Highly charged ion densities and ion confinement properties in an electron-cyclotron resonance ion source", *Physical Review E*, vol. 61, no. 3, pp. 3015–3022, 2000.

[60] R. Kronholm *et al*, Spectroscopic method to study low charge state ion and cold electron population in ECRIS plasma, *Review of Scientific Instruments*, vol. 89, no. 4, p. 043506, 2018.

[61] C. Perret *et al*, Physics of Plasmas 6, 3408 (1999).

[62] O. Tarvainen *et al*, Limitations of electron cyclotron resonance ion source performances set by kinetic plasma instabilities, *Review of Scientific Instruments*, vol. 86, no. 2, p. 023301, 2015.

[63] FREDRIK J.C. WENANDER, Charge Breeding and Production of Multiply Charged Ions in EBIS and ECRIS

[64] O. Tarvainen *et al*, A new plasma potential measurement instrument for plasma ion sources, *Review of Scientific Instruments*, vol. 75, no. 10, pp. 3138–3145, 2004.

[65] T. Ropponen *et al*, Studies of plasma breakdown and electron heating on a 14 GHz ECR ion source through measurement of plasma bremsstrahlung, *Plasma Sources Science and Technology*, vol. 20, no. 5, p. 055007, 2011.

[66] G. Shirkov, Multicomponent consideration of electron fraction of electron cyclotron resonance source plasma, *Review of Scientific Instruments*, vol. 71, no. 2, pp. 850–855, 2000.

[67] V. P. Pastukhov. *Review of Plasma Physics,* 13:203, 1987.

[68] T.D. Rognlien and T.A. Cutler. Transition from pastukhov to collisional confinement in a magnetic and electrostatic well. *Nuclear Fusion*, 20(8):1003, 1980.

[69] O. Tarvainen *et al.*, Diagnostics of a charge breeder electron cyclotron resonance ion source Helium plasma with the injection of $^{23}Na^+$ ions. *Phys. Rev. Accel. Beams* 19, 053402, 2016.

[70] L. Maunoury *et al.*, SPIRAL1 Charge Breeder: Performances and Status. 22nd International Workshop on ECR Ion Sources (ECRIS2016), Aug 2016, Busan, South Korea. pp.35-38, 10.18429/JACoW-ECRIS2016-MOFO01.

[71] D. Hitz *et al*, Results and interpretation of high frequency experiments at 28 GHz in ECR ion sources, future prospects, *Review of Scientific Instruments*, vol. 73, no. 2, pp. 509–512, 2002.

[72] P. Sortais, J.L. Bouly, N. Chauvin, J.C. Curdy, R. Geller, T. Lamy, P.Sole, J.L.Vieux-Rochaz, "ECRIS as ion source and charge breeder", *Nuclear Physics A* 701 (2002) 537c–549c.

[73] T. Lamy, R. Geller, P. Sortais, and T. Thuillier, Status of charge breeding with electron cyclotron resonance ion sources, *Review of Scientific Instruments*, 77, 03B101 (2006).

[74] *http : //www.pantechnik.com*

[75] R. Geller, C. Tamburella, J. L. Belmont, The ISOL-MAFIOS Source, *Review of Scientific Instruments*, 68 (1997) 2319-232.

[76] J. Angot, T. Thuillier, M. Baylac, T. Lamy, P. Sole, et al.. Charge breeding time studies with short pulse beam injection. 23rd International Workshop on ECR Ion Sources (ECRIS 2018), pp.24-28, Sep 2018, Catane, Italy.

[77] J. Angot *et al.*, Recent improvements of the LPSC Charge Breeder, presented at ICIS17, Cern, Switzerland, October 2017.

[78] A. Annaluru *et al.*, 1+/N+ method: numerical simulation studies and experimental measurements on the SPIRAL1 ECR Charge Breeder. 23rd International Workshop on ECR Ion Sources, Sep 2018, Catania, Italy. pp.C01002.

[79] L. Maunoury *et al.*, SPIRAL1: a versatile user facility, *JINST* 13 (2018) no.12, C12022.

[80] A. Galata, G. Patti, C. Roncolato, J. Angot, and T. Lamy, "The new ECR charge breeder for the Selective Production of Exotic Species project at INFN—Laboratori Nazionali di Legnaro", *Review of Scientific Instruments 87*, 02B503 (2016).

[81] D. P. May, G. Tabacaru, F. P. Abegglen, and W. D. Cornelius, First operation of the charge-breeder electron-cyclotron-resonance ion source at the Texas A&M Cyclotron Institute,*Review of Scientific Instruments*, 81, 02A901 (2010).

[82] P. Delahaye, *Nucl. Instrum. Meth. B* 317 (2013) 389.

[83] R. Vondrasek, J. Clark, A. Levand, T. Palchan, R. Pardo, G. Savard, R. Scott, *Review of Scientific Instruments*, 85 (2014) 02B903.

[84] R.Vondrasek, Addressing contamination in ECR charge breeders, *Journal of Instrumentation*, Volume 14, January 2019

[85] T. Lamy *et al.*, "Beam injection improvement for electron cyclotron resonance charge breeders", *Review of Scientific Instruments*, 83, 02A909 (2012).

[86] K. Halbach, Design of permanent multipole magnets with oriented rare earth cobalt material, *Nucl. Instrum. Methods* 169 (1980) 1–10.

[87] E. Lienard, G. Ban, C. Couratin, P. Delahaye, D. Durand, X. Fabian *et al.*, Precision measurements with LPCTrap at GANIL, Hyperfine Interactions 236 (2015) 1.

[88] T. Kurtukian-Nieto *et al.*, SPIRAL2/DESIR high resolution mass separator, *Nucl. Instrum. Meth. B* 317 (2013) 284.

[89] R. Geller, T. Lamy, and P. Sortais, Charge breeding of isotope on-line-created radioactive ions using an electron cyclotron resonance ion trap, *Review of Scientific Instruments*, 2006 77:3.

[90] S. Chandrasekhar, The Astrophysical Journal 92, (1941), pp.285-304.

[91] S. Chandrasekhar, The Astrophysical Journal 97, (1943), pp.255-262.

[92] L. Spitzer, Jr., Physics of fully Ionized Gases, Interscience, Newyork, (1956).

[93] F. Wenander, Charge Breeding of Radioactive Ions. CAS-CERN Accelerator School: Ion Sources - Proceedings. 10.5170/CERN-2013-007.351 (2014).

[94] J. L. Delcroix and A. Bers, Physique des Plasmas, CNRS, New York,1994, Vol. 2, p. 357.

[95] L. Celona, Microwave Coupling to ECR and Alternative Heating Methods. CAS-CERN Accelerator School: Ion Sources - Proceedings. 10.5170/CERN-2013-007.443 (2014).

[96] R. Vondrasek *et al.*, "Charge Breeding Experiences with an ECR and an EBIS for CARIBU." (2016).

[97] R. Vondrasek, A. Kolomiets, A. Levand, R. Pardo, G. Savard and R. Scott, Performance of the argonne national laboratory electron cyclotron resonance charge breeder, *Review of Scientific Instruments*, 82 (2011) 053301.

[98] O.Tarvainen *et al.*, Injected 1+ ion beam as a diagnostics tool of charge breeder ECR ion source plasmas. *Plasma Sources Science and Technology*. 24. 10.1088/0963-0252/24/3/035014 (2015).

[99] A. Galatà, D. Mascali, L. Neri and L. Celona, A new numerical description of the interaction of an ion beam with a magnetized plasma in an ECR-based charge breeding device, *Plasma Sources Science and Technology*, Volume 25, Number 4 (2016).

[100] S. Chandrasekhar, Rev. Mod. Phys. 15 1 (1943).

[101] J. S. Kim, L. Zhao, B. P. Cluggish and Richard Pardo, Ion beam capture and charge breeding in electron cyclotron resonance ion source plasmas, *Review of Scientific Instruments*, 78, 103503 (2007).

[102] L. Zhao, B. P. Cluggish, J. K. Kim, R. C. Pardo and R. C. Vondrasek, "Simulation of charge breeding of rubidium using Monte Carlo charge breeding code and generalized ECRIS model, *Review of Scientific Instruments*, 81, 02A304 (2010).

[103] $https://www.far-tech.com/mcbc.php$

[104] $https://simion.com/$

[105] $http://irfu.cea.fr/dacm/logiciels/$

[106] B. A Trubnikov, *ReV. Plasma Phys.* 1, 105 (1965).

[107] $https://www.nrl.navy.mil/ppd/content/nrl-plasma-formulary$

[108] N. A. Krall & A. W. Trivelpiece, *Principles of Plasma Physics*, McGraw-Hill, New York, 1973.

[109] James D. Callen, Fundamentals of Plasma Physics, *University of Wisconsin*, 2006

[110] A. H. Boozer and G. Kuo-Petravic, *Phys. Fluids* 24, 851 (1981).

[111] A. H. Boozer, *Phys. Plasmas* 9, 4389 (2002).

[112] $https://en.wikipedia.org/wiki/Mu-metal$

[113] $http://www.esrf.eu/Accelerators/Groups/InsertionDevices/Software/Radia$

[114] $http://www.wolfram.com/mathematica$

[115] T. Lamy, J. L. Bouly, J. C. Curdy, R. Geller, A. Lacoste, P. Sole, P. Sortais, T. Thuillier, and J. L. Vieux-Rochaz, K. Jayamanna, M. Olivo, P. Schmor, and D. Yuan, Charge state breeding applications with the ECR PHOENIX source: From low to high current production, *Review of Scientific Instruments*, 73, 717 (2002).

[116] T. Lamy, J. Angot, T. Thuillier, P. Delahaye, L. Maunoury, et al.. Experimental activities with the LPSC charge breeder in the European context. 21st International Workshop on ECR Ion Sources (ECRIS 2014), Aug 2014, Nizhny Novgorod, Russia. pp.120-126.

[117] Richard Vondrasek, Charge Breeding with Electron Cyclotron Resonance Ion Sources, *ICFA Beam Dyn.Newslett.* 73 (2018) 86-101

[118] M. Martinen, Transient sputtering method for estimating ion confinement times in ECRIS plasma. *Master's thesis, University of Jyväskylä*, September 2018.

[119] M. Martinen, J. Angot, A. Annaluru, P. Jardin, T. Kalvas, H. Koivisto, S. Kosonen, R. Kronholm, L. Maunoury, O. Tarvainen, V. Toivanen, P. Ujic., Estimating ion confinement times from beam current transients in conventional and charge breeder ECRIS, *University of Jyväskylä*, Manuscript in preparation. 2019.

[120] O. Tarvainen, J. Angot, I. Izotov, V. Skalyga, H. Koivisto, T. Thuillier, T. Kalvas and T. Lamy, Plasma instabilities of a charge breeder ECRIS. *Plasma Sources Sci.Tech.*, 2017, 26 (10), pp.105002.

[121] A. A. Ivanov and K. Wiesemann, 2005 IEEE Trans. *Plasma Sci.* 33 1743-62.

[122] D. Mascali, S. Gammino, L. Celona and G. Ciavola, 2012, *Rev. Sci.* 83 02A336.

[123] V. Mironov, S. Bogomolov, A. Bondarchenko, A. Efremov, V. Loginov, "Simulations of charge-breeding processes in ECRIS", *AIP Conference Proceedings* 2011, 070003 (2018)

[124] $https://en.wikipedia.org/wiki/Pearson\%27s_chi-squared_test$

[125] S. Gammino, (2014). Production of High-Intensity, Highly Charged Ions. CAS-CERN Accelerator School: Ion Sources - Proceedings. 10.5170/CERN-2013-007.123.

[126] V. Mironov, S. Bogomolov, A. Bondarchenko, A. Efremov, and V. Loginov, Numerical model of electron cyclotron resonance ion source, *Phys. Rev. ST Accel. Beams* 18, 123401 (2015).

[127] R. Kronholm *et al.*, Spectroscopic study of ion temperature inminimum-B ECRIS plasmaSpectroscopic study of ion temperature in minimum-B ECRIS plasma, Manuscript in review. 2019.